TITLE PAGE

1. Report No.	2. Government Accession No.
FHWA/TX-81/8+208-2	

4. Title and Subtitle

BEHAVIOR OF POST-TENSIONED GIRDER ANCHORAGE ZONES

5. Report Date
April 1981

6. Performing Organization Code

7. Author(s)
W. C. Stone, W. Paes-Filho, and J. E. Breen

8. Performing Organization Report No.
Research Report 208-2

9. Performing Organization Name and Address
Center for Transportation Research
The University of Texas at Austin
Austin, Texas 78712

10. Work Unit No.

11. Contract or Grant No.
Research Study 3-5-77-208

12. Sponsoring Agency Name and Address
Texas State Department of Highways and Public Transportation; Transportation Planning Division
P. O. Box 5051
Austin, Texas 78763

13. Type of Report and Period Covered
Interim

14. Sponsoring Agency Code

15. Supplementary Notes
Study conducted in cooperation with the U. S. Department of Transportation Federal Highway Administration. Research Study Title: "Design Criteria for Post-Tensioned Anchorage Zone Bursting Stresses"

16. Abstract

Several large, thin-webbed box girder bridges, with post-tensioned anchorage zones designed in accordance with AASHTO and ACI requirements, have experienced large cracks along the tendon path in the anchorage zones at the design stressing load. Cracking of this nature provides a path for penetration of moisture and salts and thus presents a potential corrosion and frost damage threat. In addition, such cracking negates a major reason for the use of prestressed concrete, the minimization of service load cracking.

This report summarizes the observations noted in an extensive physical test program. A simplified test specimen was developed to accurately simulate the behavior of the post-tensioned box girder web. The experimental program investigated the primary variables affecting the formation of the tendon path crack: tendon inclination and eccentricity, section height and width, tensile splitting strength of the concrete, anchor width and geometry, and the effect of supplementary anchorage zone reinforcement, both active and passive. Behavioral trends are presented as determined from three sources. These include physical tests of 40 quarter-scale microconcrete models, physical tests of 9 full-scale prototype box girder web sections, and an extensive series of three-dimensional linear elastic finite element computer analyses.

17. Key Words	18. Distribution Statement
girder, post-tensioned, anchorage zones, bridges, AASHTO, ACI, cracks, tendon	No restrictions. This document is available to the public through the National Technical Information Service, Springfield, Virginia 22161.

19. Security Classif. (of this report)	20. Security Classif. (of this page)	21. No. of Pages	22. Price
Unclassified	Unclassified	276	

Form DOT F 1700.7 (8-69)

BEHAVIOR OF POST-TENSIONED GIRDER ANCHORAGE ZONES

by

W. C. Stone, W. Paes-Filho, and J. E. Breen

Research Report No. 208-2

Research Project No. 3-5-77-208

"Design Criteria for Post-Tensioned Anchorage Zone Bursting Stresses"

Conducted for

Texas
Texas Department of Highways and Public Transportation

In Cooperation with the
U. S. Department of Transportation
Federal Highway Administration

by

CENTER FOR TRANSPORTATION RESEARCH
BUREAU OF ENGINEERING RESEARCH
THE UNIVERSITY OF TEXAS AT AUSTIN

April 1981

The contents of this report reflect the views of the authors who are responsible for the facts and accuracy of the data presented herein. The contents do not necessarily reflect the views or policies of the Federal Highway Administration. This report does not constitute a standard, specification, or regulation.

PREFACE

This report is the second in a series which summarizes the detailed investigation of the effects and control of tensile stresses in the anchorage zones of post-tensioned girders. The first report summarizes the state-of-the-art and presents a three-dimensional finite element analysis procedure which is of great use in understanding the development of these tensile stresses. This report summarizes an extensive series of model and full-scale physical tests which were performed to document the problem and further explore the effect of variables. The third and final report in the series draws on the analytical and experimental results presented in the first two reports. It uses these results to develop design procedures and suggested AASHTO specification provisions to control the problem. The third report also contains several examples to illustrate the application of the design criteria and procedures.

This work is a part of Research Project 3-5-77-208, entitled "Design Criteria for Post-Tensioned Anchorage Zone Bursting Stresses." The studies described were conducted at the Phil M. Ferguson Structural Engineering Laboratory as a part of the overall research program of the Center for Transportation Research, Bureau of Engineering Research of The University of Texas at Austin. The work was sponsored jointly by the Texas Department of Highways and Public Transportation and the Federal Highway Administration under an agreement with The University of Texas at Austin and the Texas Department of Highways and Public Transportation.

Liaison with the Texas Department of Highways and Public Transportation was maintained through the contact representative Mr. Alan Matejowsky, the Area IV committee chairman Mr. Robert L. Reed and the State Bridge Engineer, Mr. Wayne Henneberger; Mr. Randy Losch was the contact representative for the Federal Highway

Administration. Special thanks are due to Messrs. Wanderlan Paes-Filho and John Sladek, assistant research engineers at the Phil M. Ferguson Structural Engineering Laboratory. They played key roles in the fabrication, testing, and data interpretation and shared responsibility for various stages of the physical testing. The Laboratory staff all contributed significantly with extra efforts throughout the project.

The overall study was directed by Dr. John E. Breen, the J. J. McKetta Professor of Engineering. The detailed analysis was carried out under the immediate supervision of Dr. William C. Stone, research engineer, Center for Transportation Research.

S U M M A R Y

Several large, thin-webbed box girder bridges, with post-tensioned anchorage zones designed in accordance with AASHTO and ACI requirements, have experienced large cracks along the tendon path in the anchorage zones at the design stressing load. Cracking of this nature provides a path for penetration of moisture and salts and thus presents a potential corrosion and frost damage threat. In addition, such cracking negates a major reason for the use of pre-stressed concrete, the minimization of service load cracking.

This report summarizes the observations noted in an extensive physical test program. A simplified test specimen was developed to accurately simulate the behavior of the post-tensioned box girder web. The experimental program investigated the primary variables affecting the formation of the tendon path crack: tendon inclination and eccentricity, section height and width, tensile splitting strength of the concrete, anchor width and geometry, and the effect of supplementary anchorage zone reinforcement, both active and passive. Behavioral trends are presented as determined from three sources. These include physical tests of 40 quarter-scale microconcrete models, physical tests of 9 full-scale prototype box girder web sections, and an extensive series of three-dimensional linear elastic finite element computer analyses.

I M P L E M E N T A T I O N

This report is the second in a series which summarizes a major experimental and analytical project aimed directly at developing specific recommendations to the State Department of Highways and Public Transportation and to AASHTO for inclusion in design specifications and in design manuals of practice. Those specific recommendations are included in the third and concluding report of this series.

This report contains detailed documentation of the physical tests on which the design recommendations are based. It is the necessary backup for those responsible for deciding on specifications and codes. In addition, it contains specific information regarding the behavior of complex anchorage zones which should be of great practical interest to designers who wish to cope with the problem. It presents documentation of the types of anchorage zone failures which can occur. Consideration of these failure patterns will lead to the pattern of reinforcement required to resist such failures.

C O N T E N T S

TABLES

F I G U R E S

CHAPTER 1

INTRODUCTION

1.1 Problems in Thin-Web Post-Tensioned Structures

Current trends in bridge construction show increased utilization of post-tensioned prestressed concrete. The problem of transferring the large post-tensioning force to the structure over a small local anchorage zone becomes a primary concern in the successful application of a post-tensioning system.

In the construction of cast-in-place box girders, it is feasible to use enlarged anchorage zones at the ends of the spans or at interior diaphragms to contain the tensile stresses which generally occur in the vicinity of the point of application of the post-tensioning forces. In construction of post-tensioned "I" beam type girders, it has been the general practice to provide a thickened end-block with substantial additional reinforcement to accommodate these anchorage zone stresses. Even in such enlarged sections, cover over edge tendons is small. However, in two very practical post-tensioning applications, segmentally constructed box girders and relatively thin laterally post-tensioned overhanging deck slabs, it is not economically practical to provide massive thickness to control anchorage zone stresses.

A number of problems have occurred in post-tensioned applications in both the bridge and the building field which indicate that the design procedures and design criteria for post-tensioned anchorage zone tensile stresses need further examination and refinement. The cracking which occurred in these anchorage regions was controlled by auxiliary reinforcement and the member strength was not appreciably

reduced. However harmless these cracks may appear, they do provide a path for penetration of moisture and salts and thus present potential corrosion and frost damage threats.

Major and contradictory changes have taken place in the AASHTO, ACI and PCI design specifications for anchorage zones in recent years, based more on the results of field experience and proprietary data than on published analyses or test procedures. Current design recommendations, while vague, seem both conservative and workable for many applications where massive end blocks with large cover can be used with relatively straight or gently curving tendons in cast-in-place post-tensioned construction. However, they do not give sufficient guidance for the wide range of thin-web post-tensioned applications currently in use today, or the many new applications being suggested as the industry develops. Thus, this study of the development and control of critical anchorage zone tensile stresses was undertaken. Its goal was to provide more specific guidance to bridge design and construction personnel regarding the behavior of anchorage systems so that they could better assess the performance of a post-tensioning system without having to rely wholly on the recommendations of the hardware supplier.

The first report in this series [1] summarized the published state-of-the-art in analysis, the applicable AASHTO and ACI design regulations, and presented a three-dimensional finite element analysis which shows great promise for use in this type application.

1.2 The Anchorage Zone Stress State

Application of linear, elastic theory shows that if a concentrated normal load is applied through a bearing plate and acts on a rectangular block, compressive and tensile stresses are set up. The distributions of radial stresses along the line of the load and along lines parallel to the load are shown in Fig. 1.1. Two important tension fields are shown in this figure: those acting along the

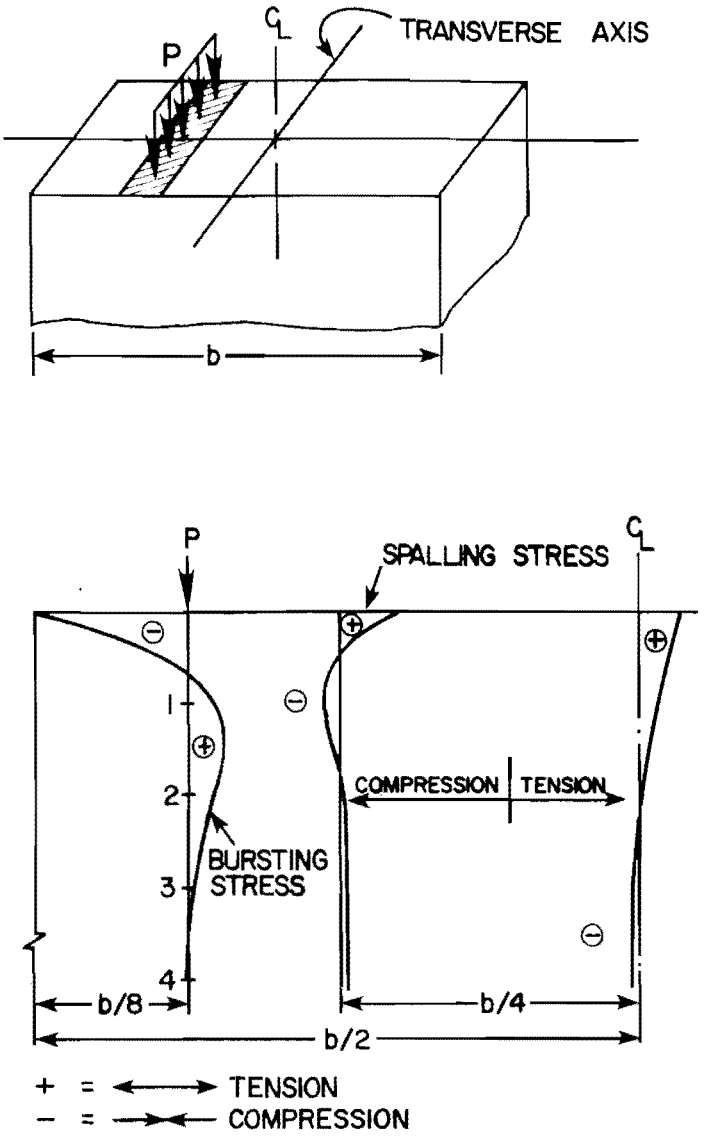

Fig. 1.1 Transverse stresses in a rectangular block loaded by a plate

line of the load, and those acting on or near the end face at points removed from the load. The two tensile stress zones are generally called:

(1) Bursting Stress--located along the line of loading, normal to it, and away from the point of loading.

(2) Spalling Stress--located along the loading surface, parallel to it and away from the point of loading.

The compressive stress immediately under the anchor is called:

(3) Bearing Stress--The load divided by the net bearing area.

The precise role that each of these three stresses plays in the behavior of the anchorage zone has not been fully understood. Positive prediction of cracking loads has been very difficult.

Distress in the anchorage zone is signalled by the sudden formation of a crack along the line of the load. As indicated in Fig. 1.2, the load at which this occurs depends not only on the size of the loaded area in relation to the geometry of the loaded surface, but additionally on the geometry of the system itself, i.e., the eccentricity, inclination, and curvature of the tendon. In addition, the shape of the anchorage device as well as the action of supplemental reinforcement affect the load at which crack formation occurs.

1.3 Overview of the Project

The overall research program was broken into six interactive phases which constitute its specific objectives. These were:

(1) To document the state-of-the-art based on an extensive literature study of all analytical, experimental, and design related papers and reports concerning anchorage zone stresses for post-tensioned applications. [Reported in Ref. 1.]

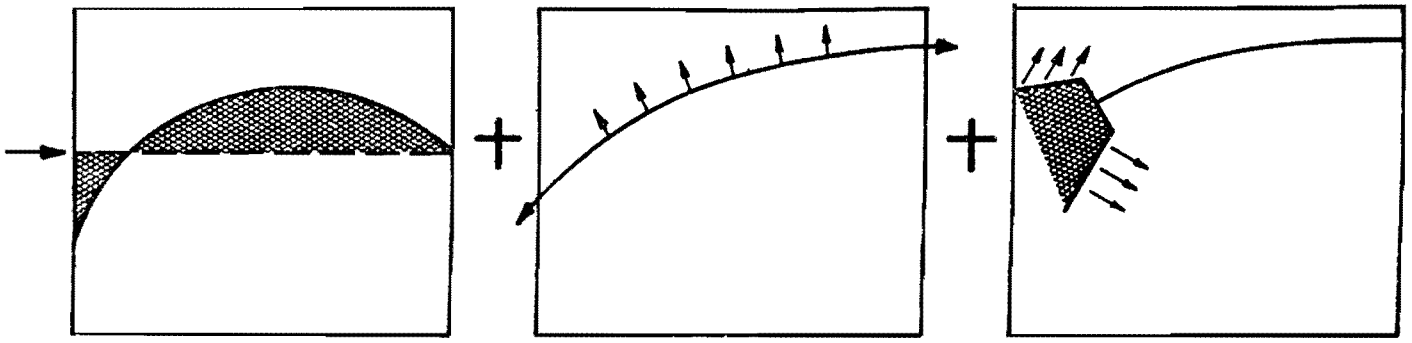

Fig. 1.2a Combination of end zone, radial, and inclined wedge effects

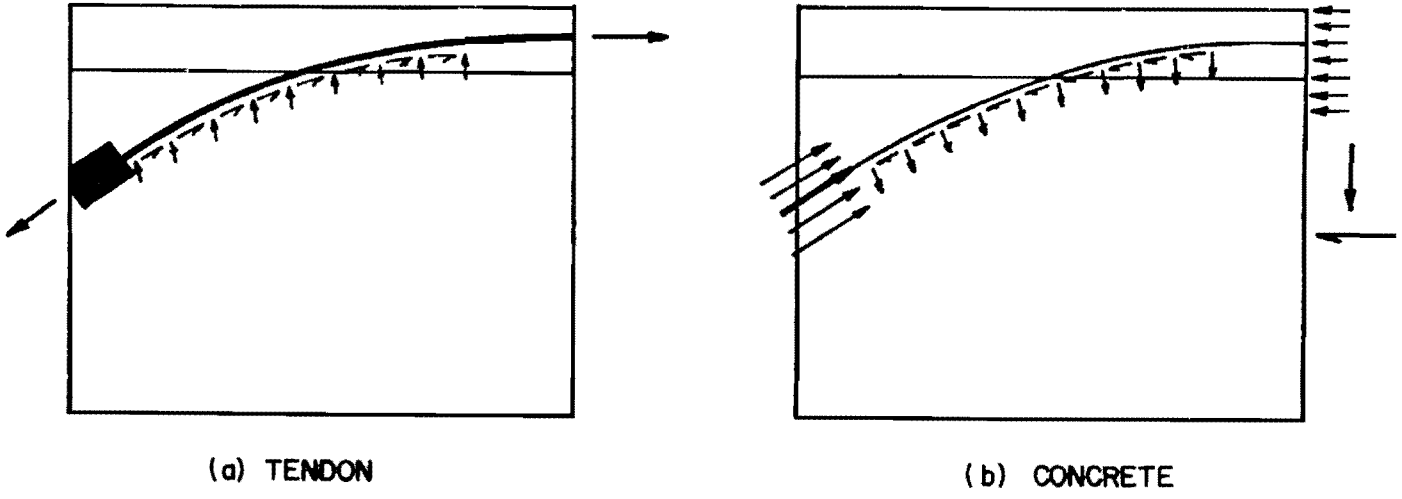

Fig. 1.2b Forces due to tendon curvature

(2) To survey the wide range of post-tensioning anchorage systems currently available in the United States and to make a classification according to general anchorage principles, sizes, and shapes. [Reported in Ref. 1.]

(3) To survey present and projected tendon path and anchorage zone characteristics in post-tensioned bridge applications. [Reported in Ref. 1.]

(4) To study systematically by both analytical and experimental procedures, the development of critical tensile stresses in the anchorage zone for typical applications using representative anchorage systems.

In essence this was the core of the project and is reported herein. In this phase the principal variables, inclination, cover (width), eccentricity, bearing areas, and anchorage type were examined using both accurate 1/4-scale models and full-scale prototype specimens in the laboratory. The two- and three-dimensional static, linear elastic finite element programs reported in detail in Ref. 1 were used to develop a behavioral model for first cracking for which the linear elastic assumption proved to be sufficiently accurate. Once calibrated the computer program could then be used to extrapolate beyond the range of the experimental tests. Ultimate strength trends were derived from physical specimen test data.

(5) To evaluate the efficiency of various types of active and passive reinforcement in anchorage zones, including spirals, conventional reinforcing bars and lateral prestressing.

This objective was an outgrowth of the experimental program but dealt with crack control rather than the behavioral mechanism by which the crack was initiated. If the cracking load could be altered and the ultimate load enhanced by the addition of reinforcement, then major design interest focuses on the most efficient scheme for placement of this reinforcement. Placement was the primary question concerning passive reinforcement. With lateral prestressing, or active reinforcement, a powerful new option was opened. This was due to the

fact that the stress field in the anchorage zone could be significantly altered by the addition of a transverse compressive force. Results are discussed in this report.

(6) To develop recommendations for specific design criteria for post-tensioned anchorage zone tensile stresses.

Based upon experimental and analytic data these recommendations can be broken down into two categories:

(a) If the structure is to be located in a highly corrosive environment where not even minor cracking can be tolerated, what is the maximum permissible stressing load, given the geometry of the anchorage zone?

(b) Given rigid geometric conditions and required load what is an "acceptable" crack and how can this be controlled through an active or passive reinforcing scheme?

In either case the structure must be capable of performing satisfactorily under service load conditions and with an adequate factor of safety under failure conditions. The design recommendations and examples based on this investigation are contained in the final report.

1.4 Experimental Program

The overall experimental program consisted of three major series. Because specimen geometry and some of the instrumentation varied from series to series, the procedures and results in each series will be presented in separate chapters.

The basic series were:

(1) Quarter-scale rectangular models--this series consisted of tests and accompanying analytical evaluations of 34 rectangular sections of approximately one-quarter scale. It was the major series for examination of the variables and included specimens designed to illustrate the effects of:

(a) Anchorage Geometry

(b) Side Cover

(c) Tendon Eccentricity

(d) Tendon Inclination

(e) Efficiency of both orthogonal and spiral passive reinforcement

(2) Full-scale I-section girder anchorage zones--this series consisted of tests and accompanying evaluations of 9 full-scale prototype box girder web sections. The specimens had small flanges and were of an I section. The major variables were selected to illustrate the effects of:

(a) Anchorage Bearing Area

(b) Tendon Inclination

(c) Percentage of Spiral Reinforcement

(d) Lateral Post-tensioning (active reinforcement)

(e) Method of Reinforcement

(3) Quarter-scale models of the I section tests--this series consisted of 6 tests of highly accurate one-quarter scale models of the prototype test specimens. Its purpose was to verify the applicability of the model series as well as to provide further behavioral information. The main variables examined in this series included:

(a) Anchorage Bearing Area

(b) Tendon Inclination

(c) Tendon Curvature

The major trends noted in each series are reported herein. A survey of the overall behavioral trends which influence development of design procedures is given in Ref. 2.

CHAPTER 2

QUARTER-SCALE RECTANGULAR MODEL TESTS

2.1 Introduction

The primary reason for using quarter-scale structural models was to efficiently use the time and resources available to examine a broad spectrum of anchorage zone geometries and reinforcing schemes. Complete use of full-scale box girder sections was prohibitive in cost.

Models are widely used in structural engineering when the structure or material is too complex to represent analytically, when the test structure is too large for laboratory conditions, or as in this study, where a verification is required of a complex analytical procedure.

Similitude requirements can be derived to relate the prototype to the model structure. If the requirements are accurately met the model can be tested and its results used to predict the behavior of the prototype. In direct modeling where the material properties for the prototype and the model are the same, then the prototype and model are related by only the linear scale factor S_1.

2.2 Quarter-Scale Model of Box Girder Anchorage Zone

2.2.1 General. The post-tensioned anchorage zone problem is aggravated in thin web sections such as in precast segmentally constructed box girder bridges. The finite element analyses outlined in Ref. 1 indicated that the anchorage zone stress state was a sufficiently localized phenomenon so that the entire box section need not be cast for testing purposes. In fact, as long as the tendon was not

anchored at the web-flange interface, only the web section was of primary importance. To simplify fabrication, the first series of quarter-scale models was cast so as to replicate a rectangular web section for a typical box girder bridge segment (see Figs. 2.1 and 2.2). Part way through this series of tests, problems were encountered in developing full tendon capacity in specimens with curved tendons. This was due to splitting off of cover concrete at the specimen dead end opposite the anchorage. In order to avoid this problem in the full-scale tests (which dealt primarily with curved tendons), a portion of the top and bottom flange was retained (see Fig. 3.1) so that the specimens had an "I" cross section. In order to ensure that similitude was developed between the quarter-scale models and prototype specimens, a second series of model tests was performed (see Chapter 4) precisely replicating the I-section prototype details as well as having companion rectangular specimens for comparison.

2.2.2 Specimen Design

2.2.2.1 Type of Specimen Chosen. Based upon an extensive examination of box girder geometries used in a number of segmental bridges both in the U.S. and abroad (see Fig. 2.1), a reduced web section representing a typical geometry (Fig. 2.2) was chosen to serve as a prototype. The model was directly scaled using the scale factor $S_L = 1/4$ for linear dimensions and $S_L^2 = 1/16$ for loads and areas. The quarter-scale model thus consisted of a 20 in. high, 3 in. thick web section, usually 48 in. in length.

2.2.2.2 Specimen Details and Materials. For record keeping, the following alphanumeric sequence was used to designate the specimen type for all model specimens:

MJKL-N

where M: represents a quarter-scale model and F a prototype specimen

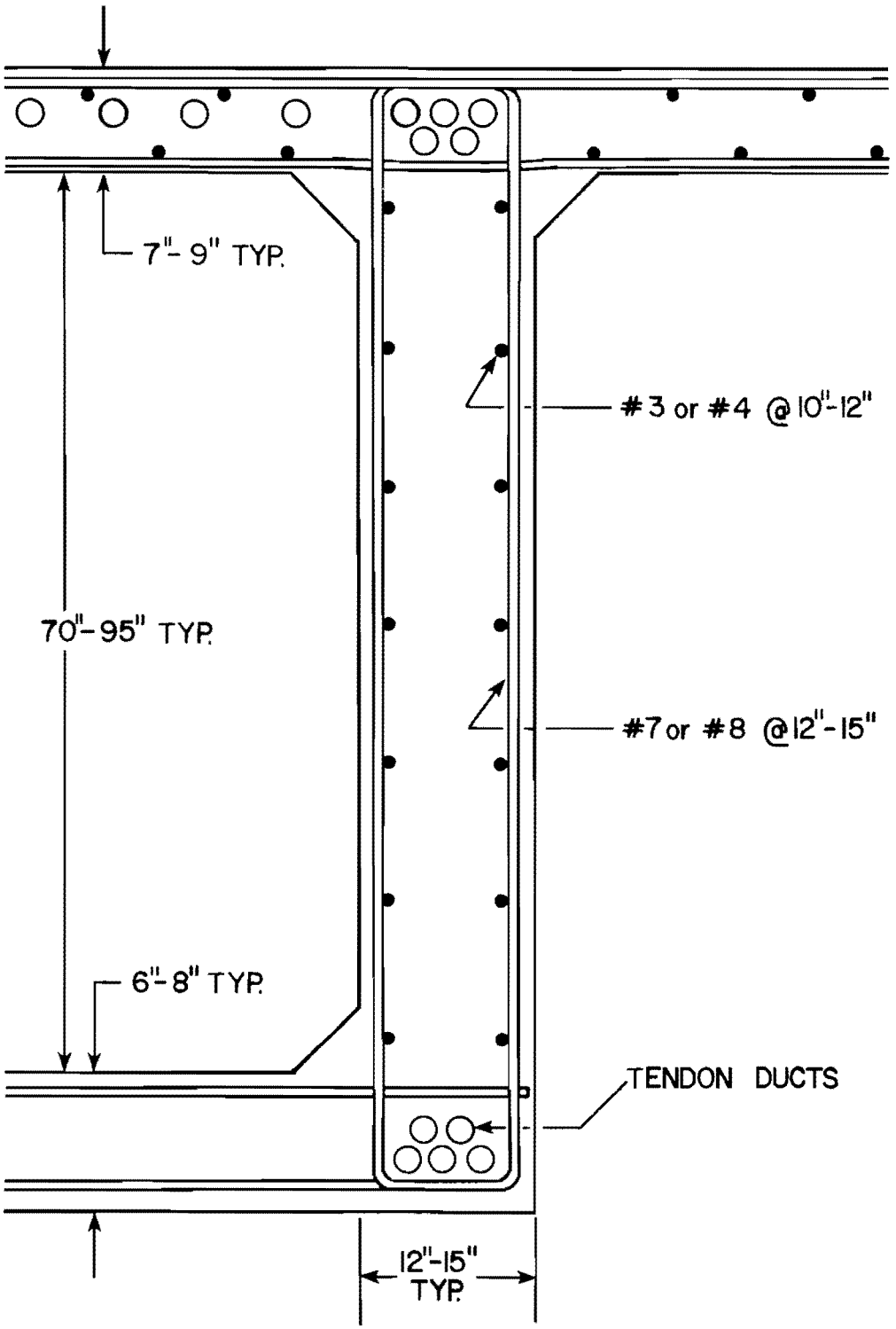

Fig. 2.1 Typical box girder details

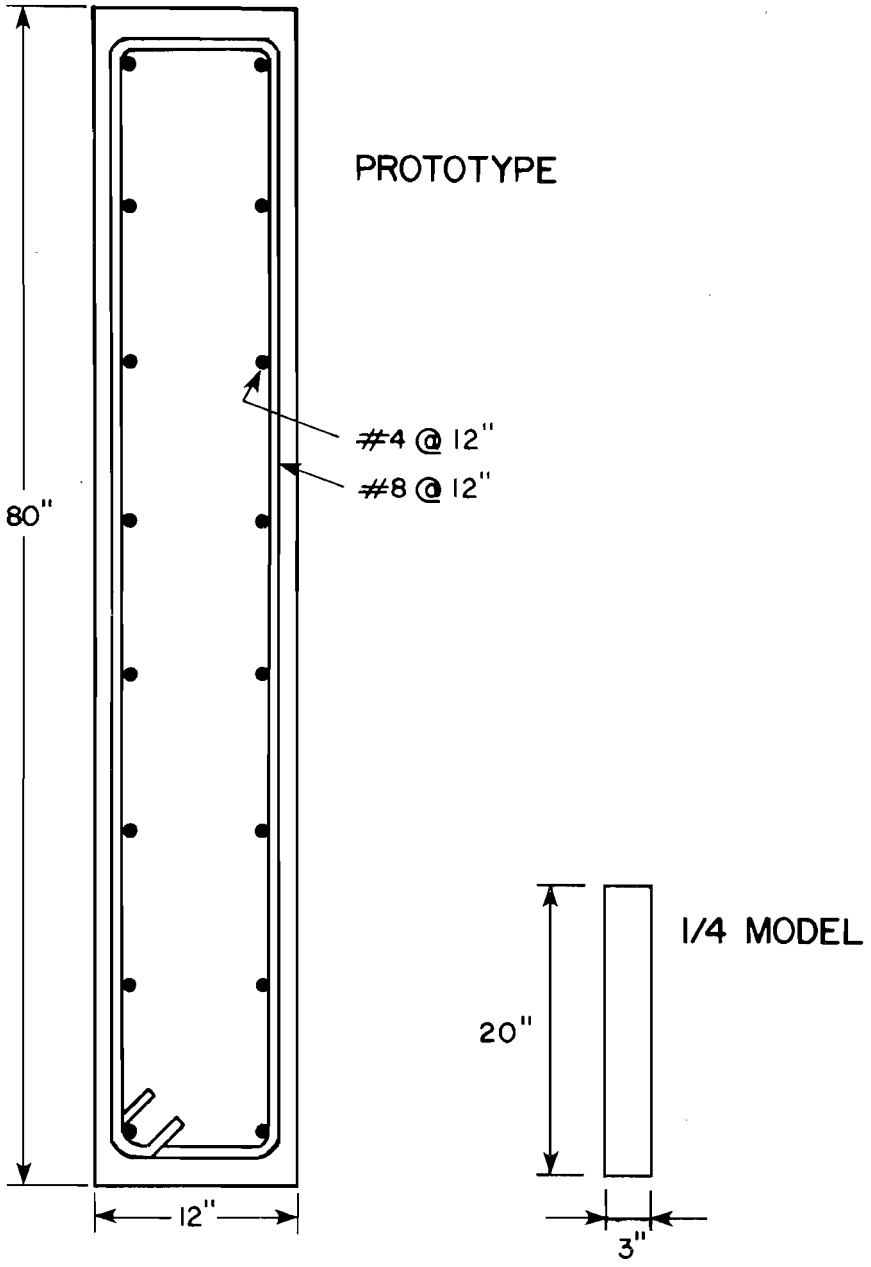

Fig. 2.2 Idealized prototype for rectangular model series

J: used for second model series to designate specimen geometry I = I-section, R = rectangular section. All tests in first model series were rectangular and hence no J term was used

K: specimen number in a particular series

L: end specimen tested. For most model tests it was possible to perform one test at each end of the specimen, designated end A or end B. Occasionally an identical rerun specimen was cast which used the letters C and D

N: series designation when used. 2 = cover, 3 = inclination, 4 = eccentricity.

As an example, specimen M5B-4 indicated a microconcrete quarter-scale model, the fifth cast in series number 4 (an eccentric tendon), side B.

The selection of microconcrete as the modeling material for this series greatly simplified the fulfillment of similitude requirements. It has been shown [3] that microconcrete mechanical properties can be very similar to those of the prototype concrete. Using this microconcrete with carefully selected reinforcing steel results in reinforced concrete models with material stress and strain scale factors close to unity. The value of $S_L = 1/4$ was chosen based upon previous experience at The University of Texas at Austin and general recommendations from the ACI Committee on Structural Models [4].

By applying the similitude requirements to the idealized prototype shown in Fig. 2.2, the model dimensions are as shown in Fig. 2.3. The microconcrete mix design was based on direct scaling of the prototype aggregate gradation curve as suggested by Frantz [3]. Microconcrete indirect tensile strength, as measured by split cylinder tests, is usually significantly higher than that of the prototype concrete despite the fact that compressive strengths are nearly identical. This trend has frequently been reported in the literature [3,5,6] and is attributable to a more solid bond in tension as a result of the finer aggregate. The substantial number of tests in this investigation indicate that normalized cracking loads

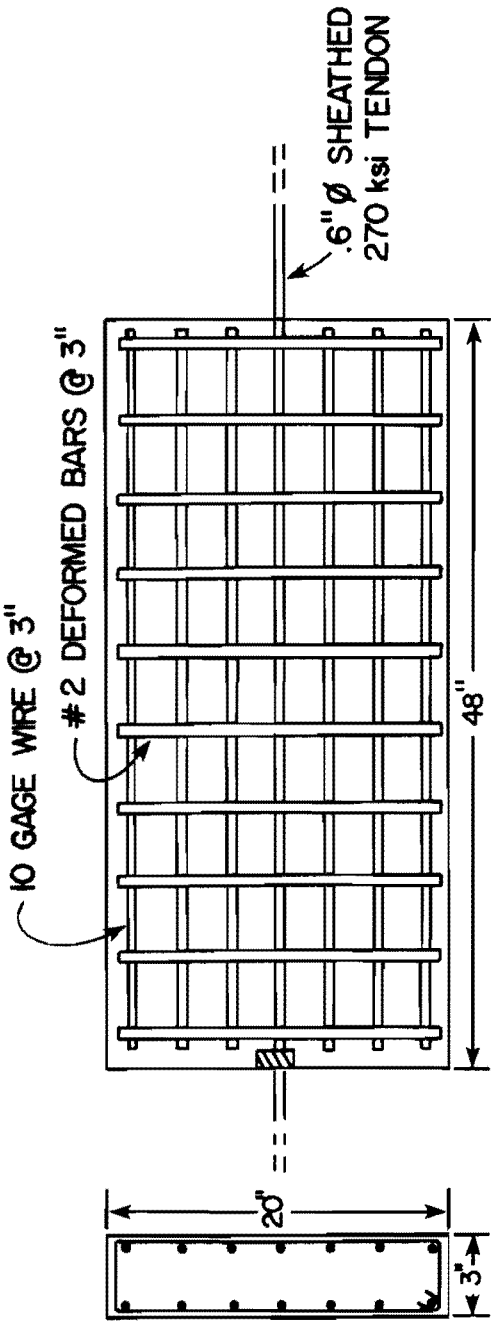

Fig. 2.3 Model dimensions and reinforcement

(adjusted by the scale factor S_L^2) are nearly identical in model and prototype when they are adjusted by the measured split cylinder tensile strength.

4.2.2.3 Microconcrete. Microconcrete is based on geometric scaling of the prototype aggregate gradation curve with some modification of the scaled curve to reduce the water requirements created by the presence of very small particles.

The prototype concrete for this study was based upon the Texas Department of Highways and Public Transportation Type H mix design for superstructure concrete.

The final mix design was based on a trial batch basis. Type III high early strength cement was used in order to allow a reduction in curing time. An ASTM C494 retarding admixture approved by the Texas Department of Highways and Public Transportation was used to delay initial set and improve workability. The following quantities per cubic foot were used:

TABLE 2.1 FINAL MIX DESIGN

TCM 1/8 Aggregate	41.0 lb
OTTAWA Silica Sand	36.8 lb
No. 1 Blast Sand	33.8 lb
Type III Cement	21.25 lb
Retarder	0.51 fl. oz.
Water	14.8 lb
Water/cement = 0.7	
Cement ratio = 6.1 sack/cu. yd.	

Three trial batches were required to determine an adequate water-cement ratio. The final batch had a 7-day compressive strength of approximately 4000 psi using 3 in. × 6 in. cylinders. For most specimens, split cylinder tests were performed to determine the indirect tensile strength of the microconcrete. Previous tests by

Leyendecker [7] and Aldridge [8] have shown that the modulus of elasticity for these types of microconcretes could be reasonably approximated using the ACI Building Code formula:

$$E_c = 33w^{1.5}\sqrt{f'_c}$$

where E_c = modulus of elasticity, psi
w = weight per cubic foot of concrete, lb/ft^3
f'_c = compressive strength of concrete, psi

2.2.2.4 Passive Reinforcement. Excluding special reinforcement added for the anchorage zone (spirals, mats, etc.), typical web reinforcement for box girders, as shown in Fig. 2.1, consists of #7 or #8 vertical stirrups. These are usually "U" shaped at the bottom and flare out into the top flange mat reinforcement. Horizontal reinforcement consists of #3 or #4 bars at 12 in. to 15 in. spacing. Figure 2.2 shows the details of an idealized prototype used as the basis for the model design. Reinforcement for a direct model would be scaled by a factor of 1/4 from that shown. Availability of reinforcing bars and wires led to the reinforcing cage shown in Fig. 2.3. Deformed 6 mm bars were used for the stirrups, while 10 gage wires were employed for horizontal bars. Vertical bars were exactly the diameter required while horizontal bars were within 8 percent which was a very acceptable figure since the initial reinforcement design was quite arbitrary. The reinforcement had nearly identical stress-strain characteristics to the prototype reinforcement achieved by using specially developed 60 ksi bars.

2.2.2.5 Fabrication. Three sets of forms were used for simultaneous casting of three models to minimize variations in compressive strength. All forms were plywood with differing end forms for straight tendon specimens and for curved tendon specimens. A small wedge of wood was attached to the end form to create a 30 degree blockout in the anchorage zone for those specimens with inclined, curved tendons.

Reinforcing cages were fabricated by hand using wire ties in special jigs, then insertion strain gages were wired into position and checked electronically. The finished cage was positioned in the form. Wooden chairs were provided to ensure the proper bottom cover. The post-tensioning tendon was adjusted to the correct smooth profile as shown in Fig. 2.4. The final location of the internal strain gages was recorded and the forms closed.

Concrete was placed in several layers with both internal and external vibration. Ten to twenty cylinders were cast for each mix. Specimens and cylinders were covered with plastic sheets to prevent loss of moisture. After three days, the forms were removed and the curing process continued until the desired compressive strength was reached.

2.3 Experimental Parameter Study

2.3.1 Objectives and Variables. There were two main objectives of this model series. The first objective was to provide data for the calibration of the analytical program, as detailed in Ref. 1. The second objective was more general in scope. The models were designed to investigate the wide range of variables which affect the performance of the anchorage zone, to find out what general trends were occurring, and to determine the critical conditions requiring further study using the more limited number of full-scale prototype specimens. The major model variables fell into four categories:

(1) Anchorage zone geometry

   a. cover (width)
   b. tendon eccentricity
   c. tendon inclination

(2) Hardware geometry

   a. plate
   b. cone
   c. bell

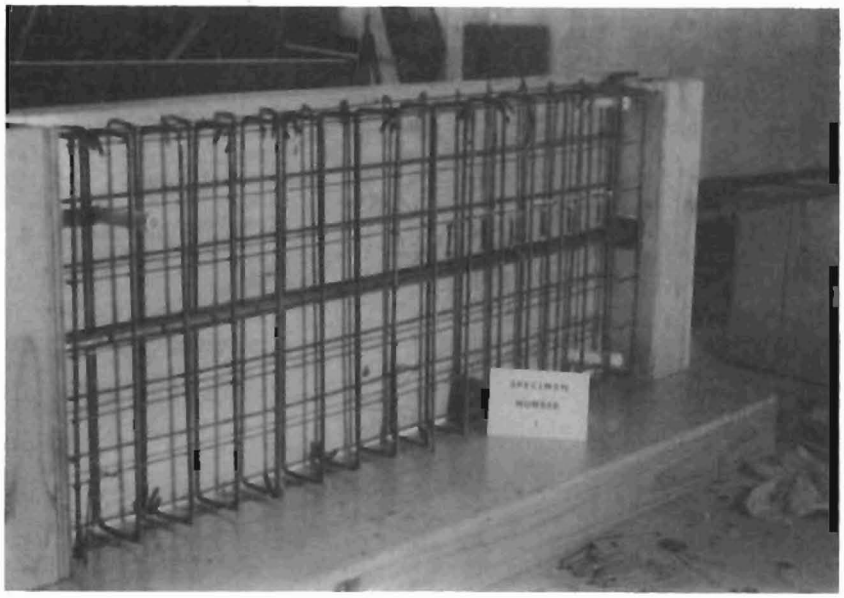

(a) Straight tendon

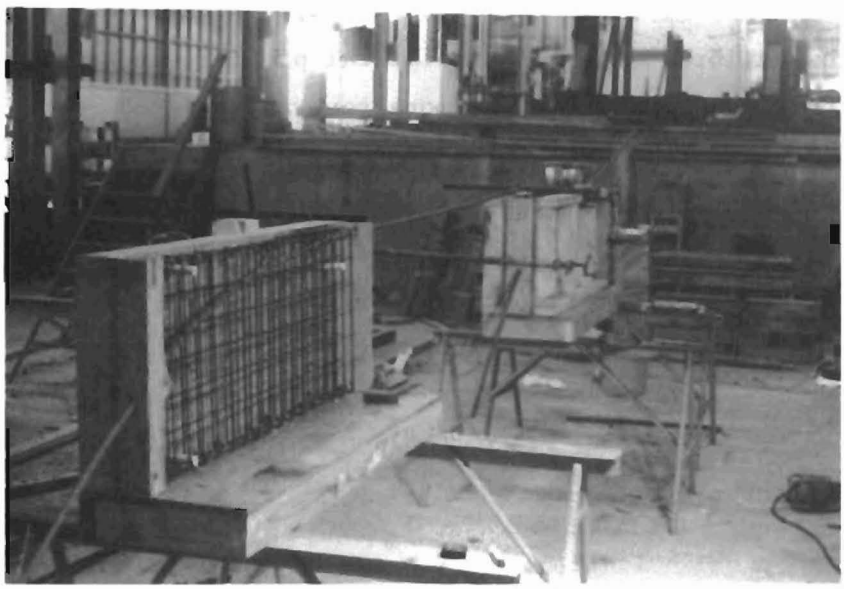

(b) Curved tendon

Fig. 2.4 Aligning tendon profile prior to casting

(3) Tendon Profile

a. curved
b. straight

(4) Reinforcement (passive)

a. orthogonal (mat)
b. spiral

Table 2.2 lists the specific properties and designations for the specimens in this model series. Not covered in this table are the specific dimensions of the anchorage hardware which will be presented in Sec. 2.3.4.

2.3.2 Instrumentation

2.3.2.1 Micro Insertion Strain Gages. The most difficult experimental obstacle was development of a reliable means of measuring the strain inside the specimen without disrupting the stress field with bulky gages that would act as additional reinforcement. For the models, this meant that insert gages would have to be quite small and made of a material which had a modulus similar to concrete so as to pick up the small strains at low force. A simple insert strainmeter was developed, as shown in Fig. 2.5. 1/32 in. foil gages were used. The "foil" backing was actually a very flexible polyamide compound which permitted the gage to be glued to a round surface. The gage was mounted on a 2 in. long 10 gage aluminum bar of 0.135 in. diameter using Eastman 910 two-part adhesive. The gage occupied a 45 degree segment on the circumference. The bars were prethreaded for 1/4 in. on each end, so that the gage would be measuring the average strain across a 1-1/2 in. unbonded length of the bar. The gages were waterproofed with BLH Barrier B epoxy sealant after the lead wires had been soldered in place. The gage was then encased in a thin shell of BLH Barrier E--a flexible epoxy sheet--and wrapped with teflon tape. A washer and nut were then attached to the lead wire end and the central portion of the gage was inserted into a 1-3/4 in. piece of 1/4 in. diameter heat shrink tubing which abutted against the washer. A heat gun was used to

TABLE 2.2

RECTANGULAR MICROCONCRETE MODEL SPECIMENS

(QUARTER SCALE)

Specimen	t Width (in.)	2a Depth (in.)	e Eccentricity (in.)	θ Inclination (deg.)	2a' Anchor Width (in.)	Anchor Type	Reinforcement
M-1	4	20	0	0	2	plate	none
M1-2	4	20	0	0	2	plate	none
M2-2	3	20	0	0	2	plate	none
M3-2	2	20	0	0	2	plate	none
M3-2r	2	20	0	0	2	plate	none (rerun of M3-2)
M1-3	3	20	0	30	2	plate	none
M2-3	4.5	20	0	30	2	plate	none
M1A-4	3	20	6	0	2	plate	none
M1B-4	4.5	20	6	0	2	plate	none
M2B-4	4.5	20	6	0	2	cone	none
M3A-4	3	20	6	0	2	cone	10 gage orthogonal ρ=0.48
M3B=4	3	20	6	0	2	cone	6mm deformed ρ=1.83
M4A-4	4.5	20	6	0	2	cone	10 gage orthogonal ρ=0.32
M4B-4	4.5	20	6	0	2	cone	6mm deformed ρ=1.96
M5A-4	4.5	20	6	0	2	cone	13 gage spiral ρ=0.39
M5B-4	4.5	20	6	0	2	cone	10 gage spiral ρ=0.85
M6A-4	3	20	6	0	2	cone	13 gage spiral ρ=0.58
M6B-4	3	20	6	0	2	cone	10 gage spiral ρ=1.27
M7A-4	3	20	3	0	2	plate	none
M7B-4	3	20	3	0	2	cone	none
M7C-4	3	20	3	0	2	plate	none

TABLE 2.2 (Continued)

Specimen	t Width (in.)	2a Depth (in.)	e Eccentricity (in.)	θ Inclination (deg.)	2a' Anchor Width (in.)	Anchor Type	Reinforcement	
M7D-4	3	20	3	0	2	cone	none	
M8B-4	3	20	6	0	2	plate	none	
M8D-4	3	20	6	0	2	plate	10 gage spiral	ρ =1.27
MR1A	3	20.5	0	0	2.625	plate	none	
MR1B	3	20.5	0	0	2.125	plate	none	
MI1A	3	20.5	0	0	2.625	plate	none	
MI2	3	20.5	0	30	2.625	plate	none	
MI3	3	20.5	0	30	2.625	plate	13 gage spiral	ρ = 0.42
MR2A	4.5	20	0	0	2.75	bell	none	
MR2B	4.5	20	0	0	2.	cone	none	
MR3	4.5	20	6	0	2.75	bell	none	

NOTE: Reinforcement ratio

$$\rho = \frac{A_s}{s\ t}$$

where s = stirrup spacing or spiral pitch

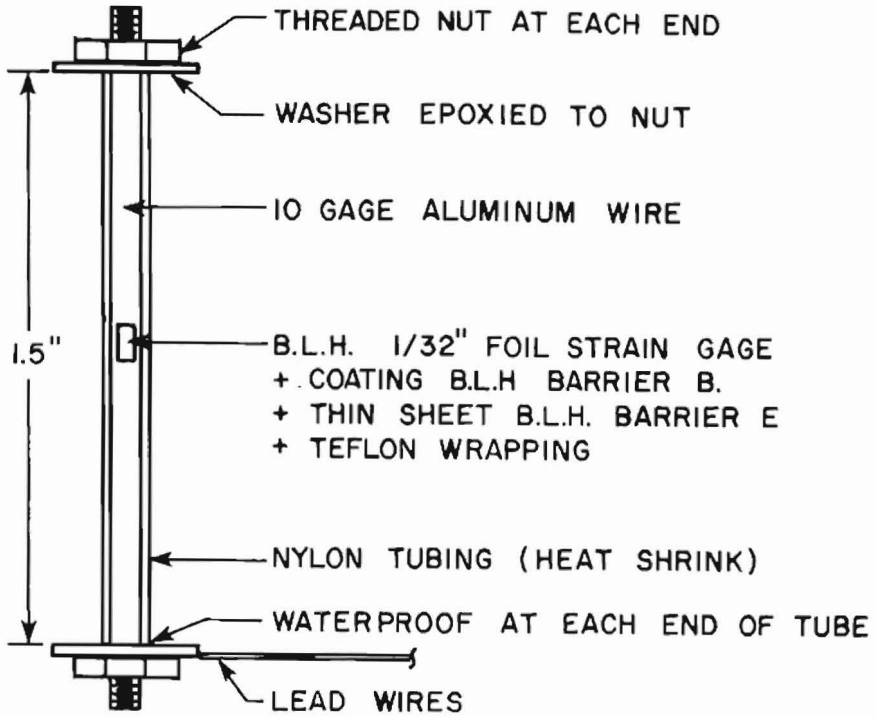

Fig. 2.5 Insert strainmeter details

reduce this outer shell to give a durable waterproof shell encasement of the gage. The washer and nut were tightened on the opposite end and the gage tested to ensure proper electronic functioning. Before using these gages in the model specimens a number of trial runs were performed. 3 in. by 6 in. microconcrete cylinders were cast with insert gages positioned parallel to the longitudinal axis in the center of the cylinder. The cylinders were loaded in compression and the strain recorded. Direct tension tests were also performed on a gage suspended from the two washers. Both types of tests showed acceptable linear behavior up to yield of the aluminum bar.

When placed in the model these internal strain meters can be classed as: (a) Bursting gages which follow the tendon path and are oriented so as to measure the transverse strain, and (b) spalling gages which are attached to the end face. Figures 2.6 and 2.7 show the actual locations of the bursting gages. Although the spalling gages are shown here for contrast and definition, it should be noted that none was used in the rectangular model test series. At the time of testing of these models the preponderance of information from the literature indicated that the bursting stress (strain) distribution was of primary importance. Spalling gages were later used in the full-size and second model series.

The gages were read at each successive load stage using a VIDAR automated data acquisition unit. The gages were oriented in directions parallel to the loaded face. Thus, vertical or transverse stresses obtained by using a formula such as

$$\sigma = \epsilon_t E_c \tag{2.1}$$

where σ_t = transverse stress (bursting or spalling, psi)

ϵ_t = gage direct strain

E_c = modulus of elasticity of concrete, psi

are only approximate. A more rigorous solution would be

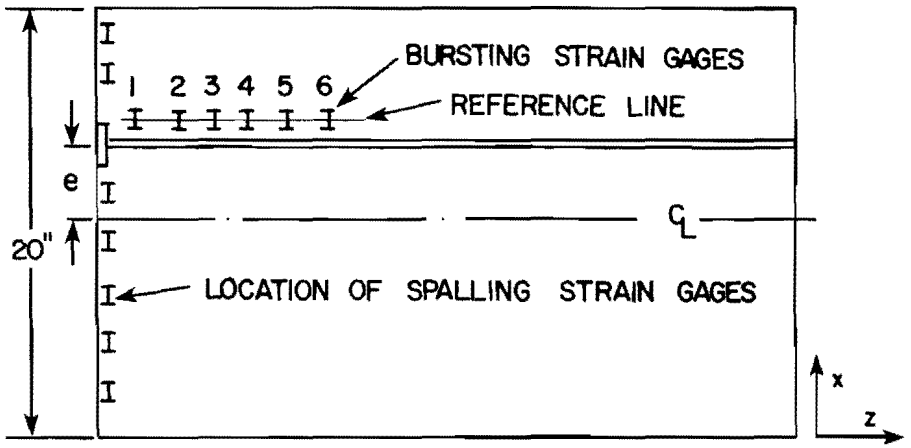

Gage ID	z (inches)	x (inches)
1	4	10 7/8 + e
2	7	10 7/8 + e
3	10	10 7/8 + e
4	13	10 7/8 + e
5	16	10 7/8 + e
6	19	10 7/8 + e

Fig. 2.6 Insert gage locations for straight tendon specimens. Eccentric tendon models used only the first four bursting strain gages. (Spalling strain gages were not used for this particular model series. Their relative location as used in later models is indicated for reference.)

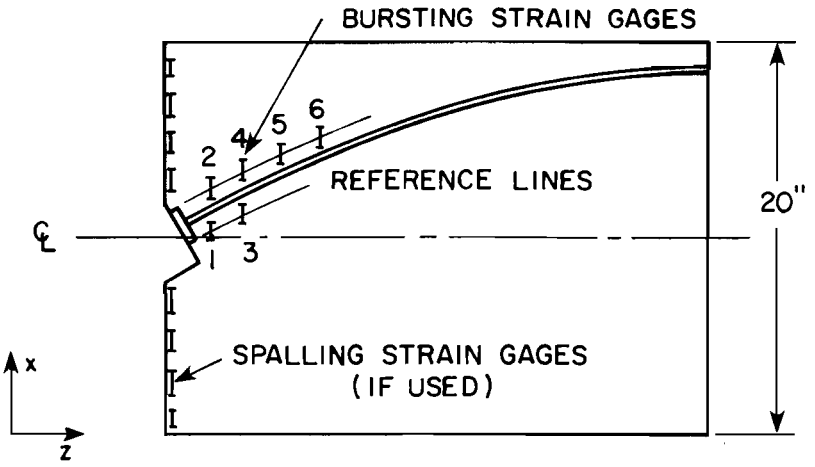

	Specimen M1-3		Specimen M2-3	
Gage ID	z(inches)	x(inches)	z(inches)	x(inches)
1	4	8.375	4	8.875
2	4	12.125	4	12.125
3	7	9.75	7	9.75
4	7	13.125	7	13.25
5	10	14.125	10	14.25
6	13	15.25	13	15.25

Fig. 2.7 Insert gage locations for curved tendon model specimens. (No spalling gages were used in this particular series)

$$\sigma_t = \epsilon_t E_c - \nu\epsilon_\ell \; E_c - \nu\epsilon_{lat} \; E_c \qquad (2.2)$$

where ϵ_ℓ = longitudinal strain
ϵ_{lat} = transverse strain
ν = Poisson's ratio

Generally ϵ_{lat} is nearly zero for a thin web problem. ϵ_ℓ, however, should be considered in calculating the bursting stresses. For the spalling stresses, ϵ_ℓ is approximately zero on the end face and thus Eq. 2.1 can be used. For this reason, and since for simplicity no horizontal gages were placed corresponding to the transverse gages, all comparisons made between the analytical model and the physical specimen are done on a basis of direct transverse strain and not stress. As the analytical program outputs both stress and strain and accounts for the effects described in Eq. 2.2 the design stresses can be obtained from the program.

2.3.2.2 External Strain Gages. Transverse (bursting) surface strains along the tendon path were measured using a 2 in. gage length Demec mechanical extensometer. The spacing of gage stations was typically 3 in. along the tendon path as shown in Fig. 2.8. These surface strains were usually very small, the resulting data were somewhat erratic, and in many cases were unusable.

2.3.2.3 Crack Measurements. Crack patterns were observed and marked on the side faces of the specimens, as shown in Fig. 2.8. Where cracks intersected grid lines, the crack widths were measured to the nearest 1/1000 in. with the aid of an illuminated 60 power microscope. A detailed description of the propagation and formation of the cracks is given in Sec. 3.4.

2.3.2.4 Loading and Load Monitoring. The post-tensioning load was applied in the same fashion that it would be in a typical installation, i.e., through a tendon post-tensioning system. This is in contrast to many other investigations where external compressive loads were applied in testing machines. The post-tensioning load was

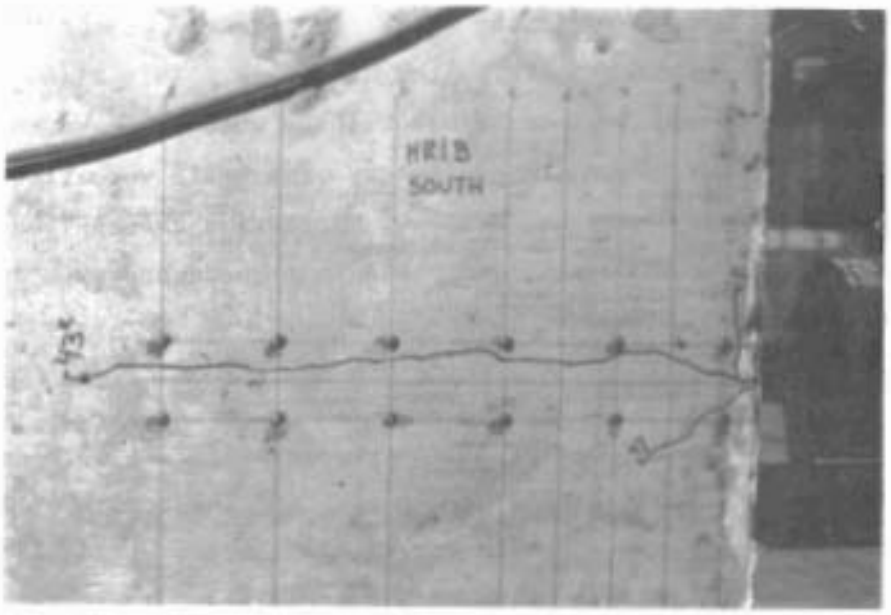

(a)

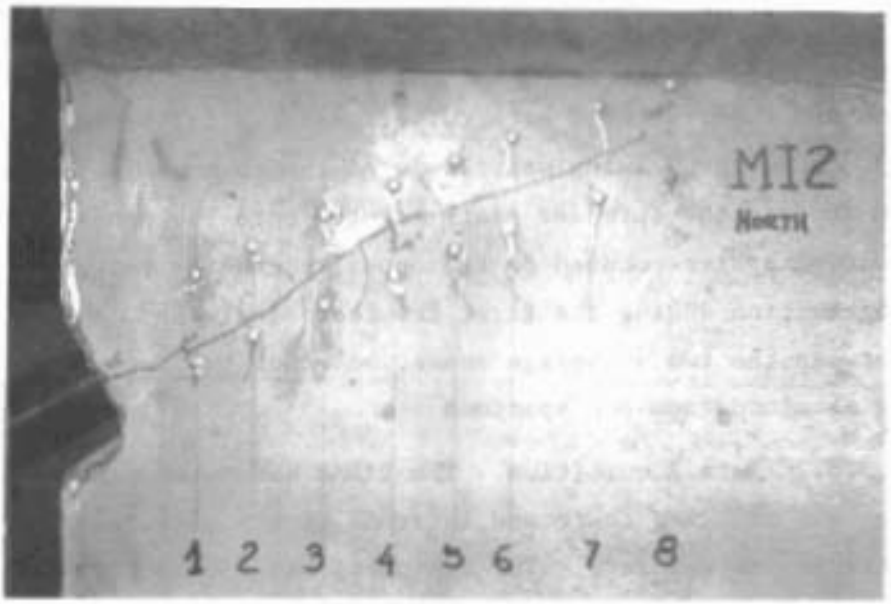

(b)

Fig. 2.8 Typical Demec gage stations and vertical grids for crack measurement

controlled and monitored using three independent systems. Calibrated load cells were placed between the anchor and the ram on the loading face and behind a spreader plate on the rear face. This allowed any friction across the specimen to be determined, which is particularly important for the curved tendon specimens. The cells were frequently recalibrated and were the prime means of monitoring the applied load. Pressure gages (0 to 10000 psi) and pressure transducers provided check systems.

2.3.3 Test Procedures

2.3.3.1 Loading System. Post-tensioning forces were applied using centerhole hydraulic rams, hand pumps, and load cells at both ends of the specimens, as shown in Fig. 2.9a. A very stiff load spreader was fabricated which was set firmly in place against the noncritical face using hydrostone grout. The rear (dead end) load cell was set between this spreader and the dead end anchor. The live end anchor was embedded in the concrete and the ram rested against this anchor. Once testing had been completed on one end, the specimen was removed and the fractured area cut off using a carborundum saw (Fig. 2.9). After the sawing was completed the specimen was cleaned up, turned around, the spreader plate grouted onto the newly cut end and the loading system mounted on the opposite end for testing. Careful observation during the first few tests indicated no interference between the two anchorage zones, and thus two independent tests were obtained from one specimen.

2.3.3.2 Data Acquisition. The VIDAR automated data acquisition system was utilized to record internal strain gage readings and pressure transducer readings. The equipment has a capacity of 400 data channels at a scan rate of 33 channels per second. A digital strainmeter was used to monitor the load cells and pressure transducers. Data were recorded on magnetic tape and echo printed on a teletype terminal at the test site. This permitted rapid detection of any faulty gages or wiring before the test reached a critical stage, i.e., cracking.

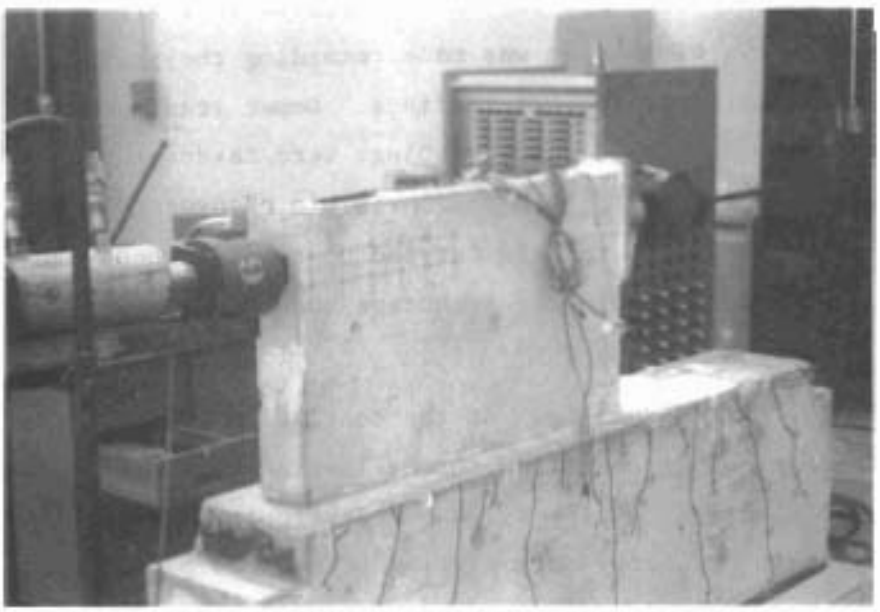

(a) Typical two-sided specimen ready for testing

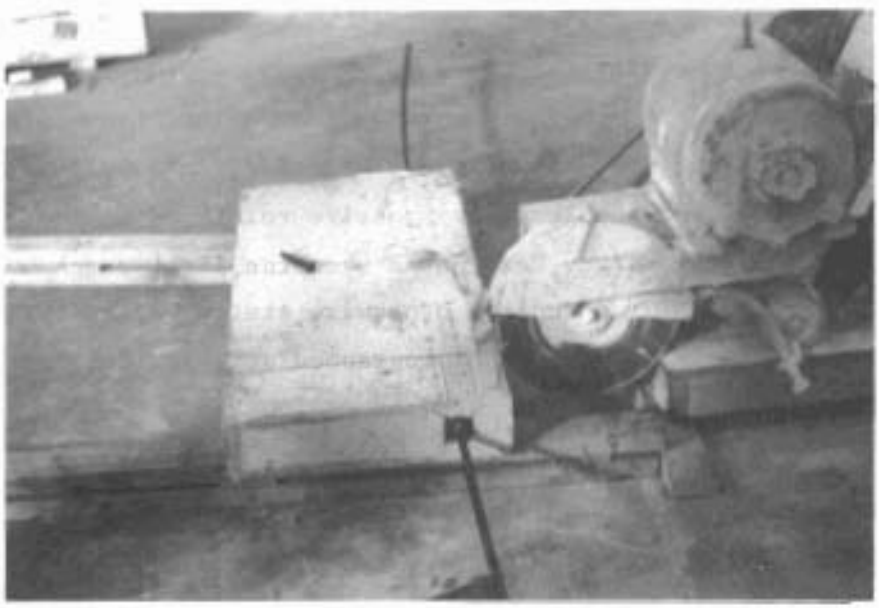

(b) Cutting off destroyed anchorage zone prior to testing of far end

Fig. 2.9 Testing of two-sided model specimens

2.3.3.3 Test Procedures. Prior to loading a set of zero readings were taken. The load was then increased in 1 kip increments. At each load stage a VIDAR scan was made recording the pressure transducer and insert strainmeter readings. Demec readings were taken at 10 kip increments. Crack width readings were taken at the onset of first cracking and at load stages where visible changes took place in the crack pattern. All tests were carried up to failure of the specimens which occurred either in the anchorage zone or (rarely) in the post-tensioning tendon.

2.3.3.4 Data Reduction. At the conclusion of each test the magnetic data tape was transferred to the laboratory's NOVA computer and reduced to a series of plot files. A Tektronix plotting routine was used to obtain hard copy data plots. Data could be assembled on a channel-by-channel basis (strain gage versus load) or as a string of channels for a given load stage. The latter was used to obtain the bursting and spalling plots used in this report.

2.4 Test Results

This section details the observed behavior of the test specimens under load. The results are broken down into five categories: anchor geometry, cover (web thickness), tendon inclination, tendon eccentricity, and varied supplementary passive reinforcement. First cracking as used in this study designates when the first crack was observed by the naked eye and unless otherwise stated refers to the tendon path crack. Specimens were photographed at important load stages to illustrate behavioral mechanisms.

2.4.1 Anchorage Geometry Series. After tendon path cracking occurred on the segmental bridge at Corpus Christi, serious questions were raised concerning the role which the anchorage device had played [9]. Basically, three distinct types of anchors were generally available in the U.S. at the time: the plate, cone, and bell configurations shown in Fig. 2.10. (Note the plate type has a lightweight

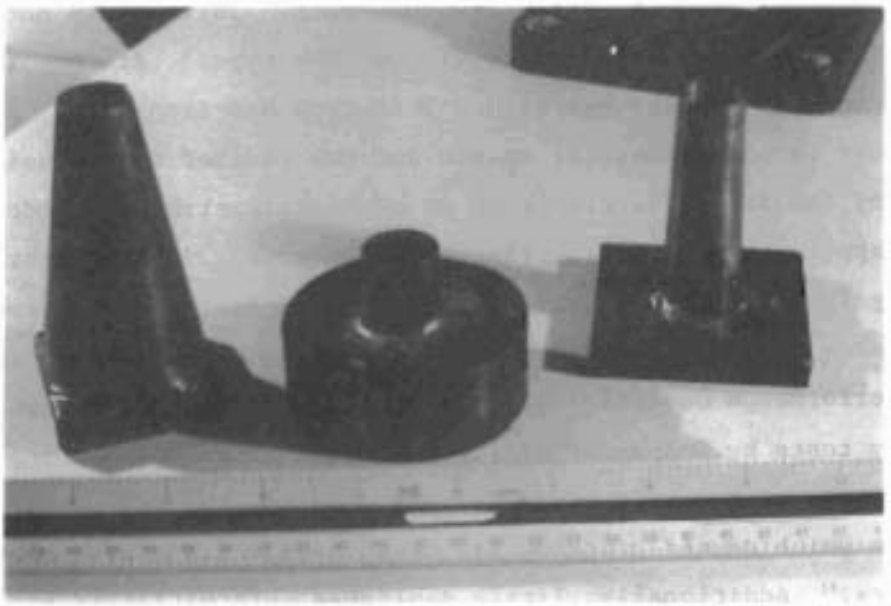

Cone Bell Plate

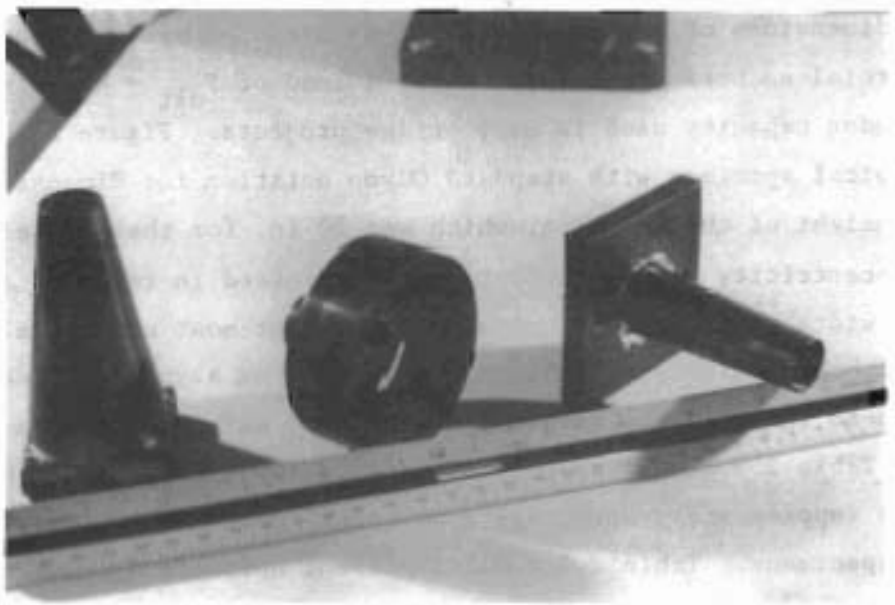

Fig. 2.10 Models of typical anchors used in post-tensioned construction

conical trumpet to connect to the tendon sheath. This should not be confused with the rigid heavy walls of the cone type.) At Corpus Christi a cone-type anchor was used. This type had seen considerable use on the commercial market and was claimed to be "quite adequate" by the manufacturers based on concentric straight tendon tests and applications. Conflicting opinions appear in the literature. Gergely [10] claimed that since a cone of concrete was seen to appear under a plate-type anchor near cracking load, it should exhibit the same performance under load as a conical-shaped anchor. However, exploratory tests by Cooper et al. [9] indicated a vast discrepancy when "specimens with bearing-type anchors cracked at loads nearly twice those which caused cracking in identical specimens with cone-type anchors." Additionally, little published information is available concerning special anchors such as the "bell" anchor.

The shortage of independent published data on the effect of anchorage configuration led to a series of 14 tests. Figure 2.11 shows the dimensions of the model anchorages used. These were scaled from commercial anchors designed to carry a load of P_{ult} = 496 kips, a typical tendon capacity used in many bridge projects. Figure 2.12 shows a typical specimen with standard Guyon notation for dimensions. 2a is the height of the specimen, which was 20 in. for these models; e is the eccentricity of the tendon and is expressed in terms of a; $2a'$ is the width of the anchor, usually square for most commercial anchors, although this is not always the case. For asymmetric anchors, $2b'$ is used to indicate the vertical dimension. All tendons are straight. Table 2.3 gives the general details for specimens in this series. No supplementary anchorage zone reinforcement was provided for these specimens. Table 2.4 and 2.5 present normalized cracking and ultimate load data. Comparisons of the three anchorage type cracking and ultimate loads are presented in Figs. 2.13 and 2.14 for tendon eccentricities of e = 0 and e = 0.6a, respectively. In Fig. 2.13 the value for M1-2 was extrapolated from data for the cover

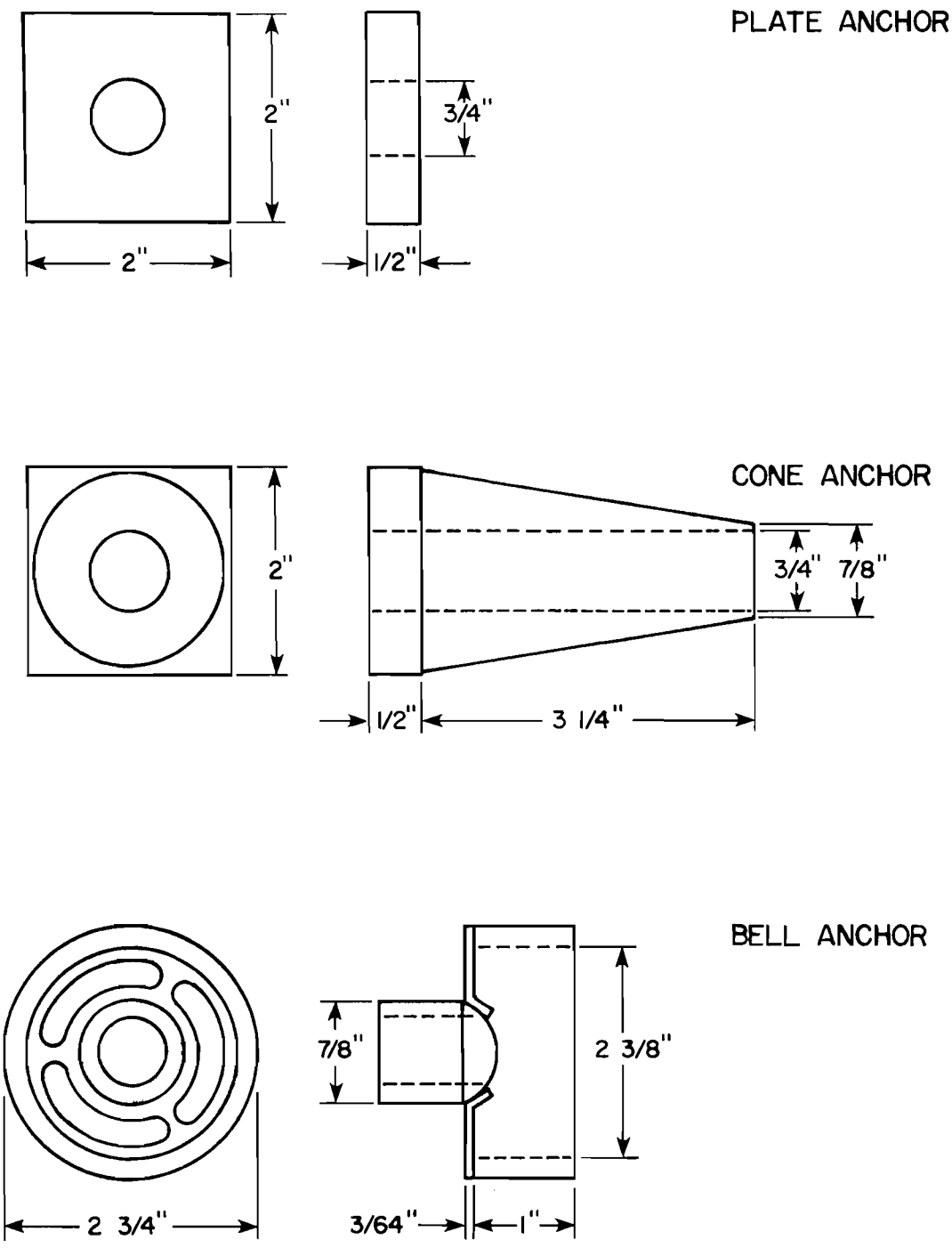

Fig. 2.11 Model anchorage geometries

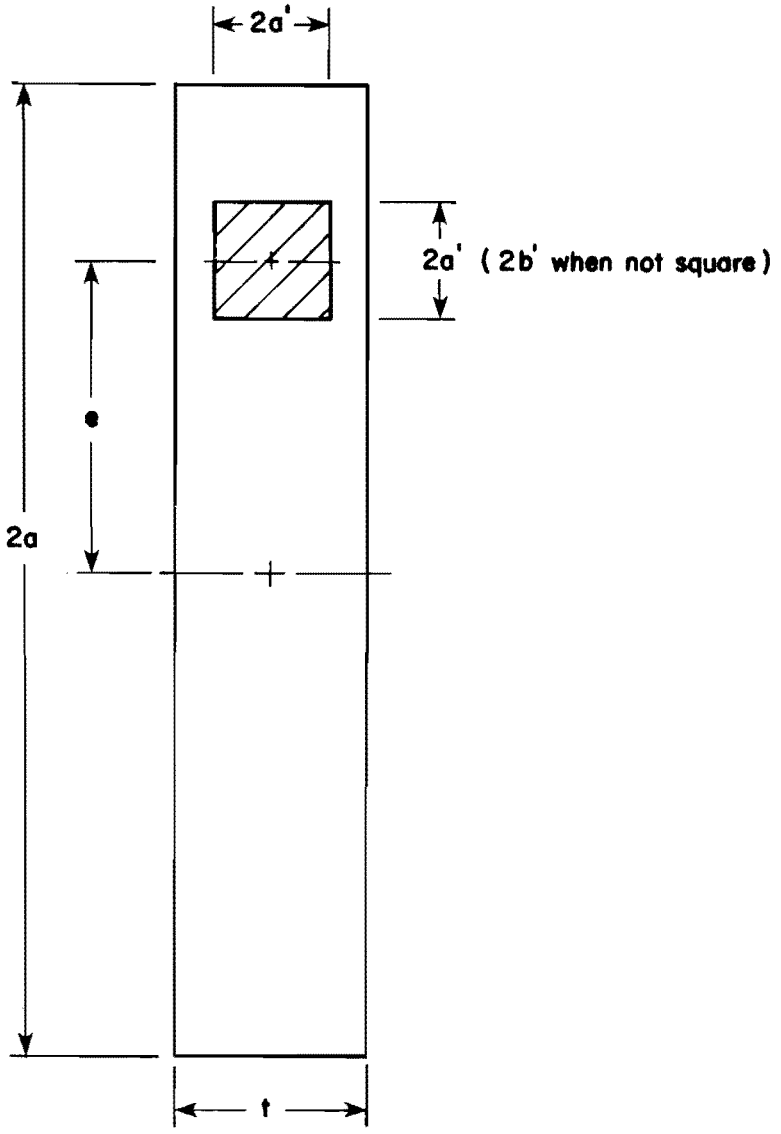

Fig. 2.12 Specimen geometry general notation

TABLE 2.3

BASIC SPECIMEN INFORMATION FOR ANCHORAGE GEOMETRY SERIES

	Specimen Name	P_{cr}(k)	P_{ult}(k)	Eccentricity e (in.)	Width t (in.)	f'_c (psi)	f_{sp}(psi)
Cone Anchors	MR2B	28	31	0	0.45a (4-1/2)	4272	516
	M7B-4	12	13	0.3a (3)	0.3a (3)	2400	327
	M7D-4	22	26	0.3a (3)	0.3a (3)	3631	51]
	M1B-4	10	14	0.6a (6)	0.3a (3)	3583	495
	M2B-4	13	13	0.6a (6)	0.45a (4-1/2)	3583	495
Bell Anchors	MR2A	44	53	0	0.45a (4-1/2)	3360	534
	MR3	24	50	0.6a (6)	0.45a (4-1/2)	4668	495
Plate Anchors	M2-2	34	34	0	0.3a (3)	4250	627
	M1-2	43	43	0	0.4a (4)	4250	627
	M7A-4	15	17	0.3a (3)	0.3a (3)	2400	327
	M7C-4	32	36	0.3a (3)	0.3a (3)	3960	548
	M8B-4	41	35	0.6a (6)	0.3a (3)	4244	707
	M1A-4	18	18	0.6a (6)	0.3a (3)	3583	495
	M2A-4	22	22	0.6a (6)	0.45a (4-1/2)	3583	495

TABLE 2.4

NORMALIZED CRACKING LOADS--ANCHORAGE GEOMETRY SERIES

	Specimen Name	P_{cr}/f'_c	$P_{cr}/\sqrt{f'_c}$	P_{cr}/f_{sp}
	MR2B	6.55	428	54.2
CONE	M7B-4	5.0	244.9	36.7
ANCHORS	M7D-4	6.06	365	42.96
	M1B-4	2.79	167	20.2
	M2B-4	3.63	217	26.3
BELL	MR2A	13.1	759	82.4
ANCHORS	MR3	5.14	351	48.4
	M2-2	8.0	521	54.2
	M1-2	10.1	660	68.6
PLATE	M7A-4	6.25	306	45.0
ANCHORS	M7C-4	8.08	508	58.4
	M8B-4	7.30	476	43.8
	M1A-4	5.02	301	36.4
	M2A-4	6.14	367	44.4

TABLE 2.5

NORMALIZED CRACKING AND ULTIMATE LOADS--ANCHORAGE GEOMETRY SERIES

	Specimen ID	Tendon Path P_{cr}	Tendon Path P_{cr}/f_{sp}	Upper Diagonal P_{ud}	Upper Diagonal P_{ud}/f_{sp}	Lower Diagonal P_{ld}	Lower Diagonal P_{ld}/f_{sp}	Ultimate P_{ult}	Ultimate P_{ult}/f_{sp}
Cone Anchors	MR2B	28	54.2	31	60.1	31	60.1	31	60.1
	M7B-4	12	36.7	12	36.7	12	36.7	13	39.8
	M7D-4	22	42.9	26	50.8	26	50.8	26	50.8
	M1B-4	10	20.2	14	28.3	14	28.3	14	28.3
Bell Anchors	MR2A	44	82.4	52	97.4	52	97.4	53	99.3
	MR3	24	48.4	48	76.9	33	66.6	50	100.0
Plate Anchors	M2-2	34	54.2	--	----	--	----	34	54.2
	M1-2	43	68.6	--	----	--	----	43	68.6
	M7A-4	15	45.9	15	45.9	15	45.9	17	52.0
	M7C-4	32	58.4	--	----	--	----	36	65.7
	M8B-4	31	43.8	34	48.1	34	48.1	35	49.5
	M1A-4	18	36.4	18	36.4	18	36.4	18	36.4
	M2A-4	22	44.4	23	46.5	23	46.5	23	46.5

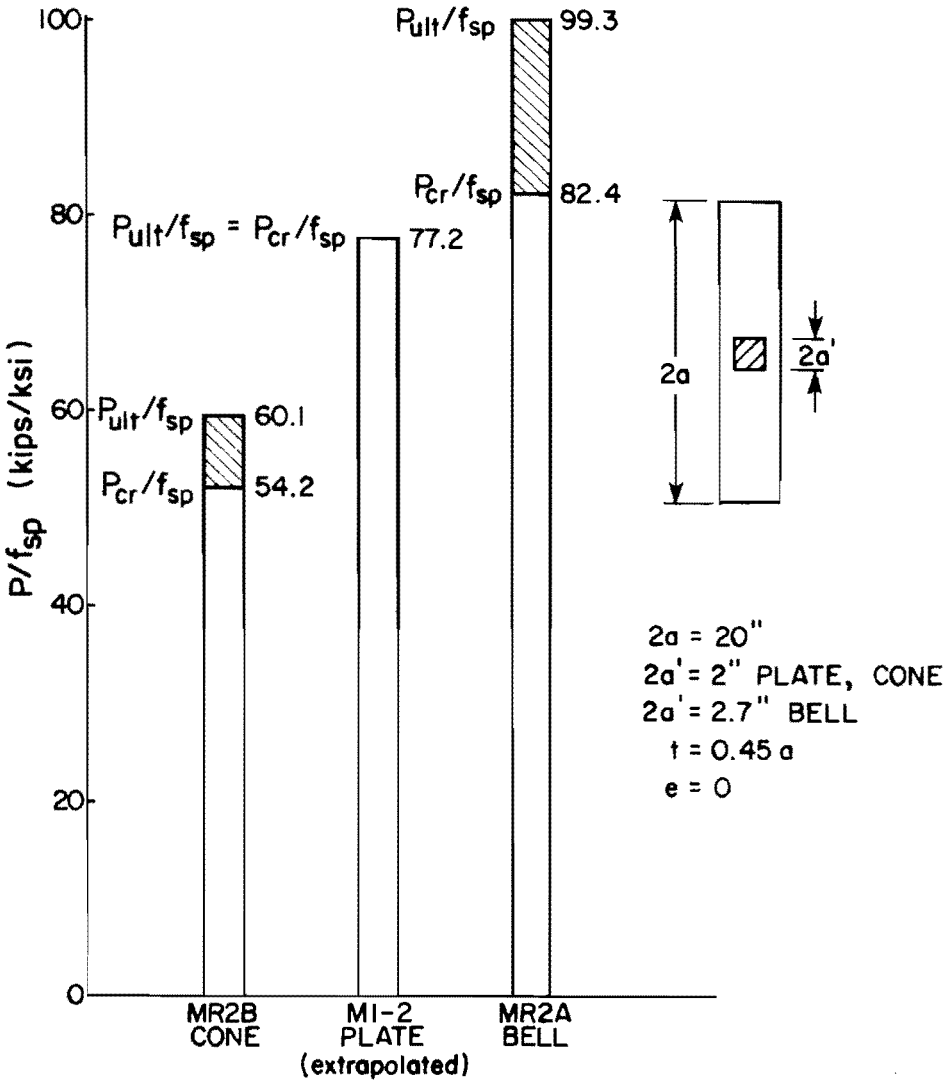

Fig. 2.13 Cracking and ultimate loads at e = 0 for different anchor geometries

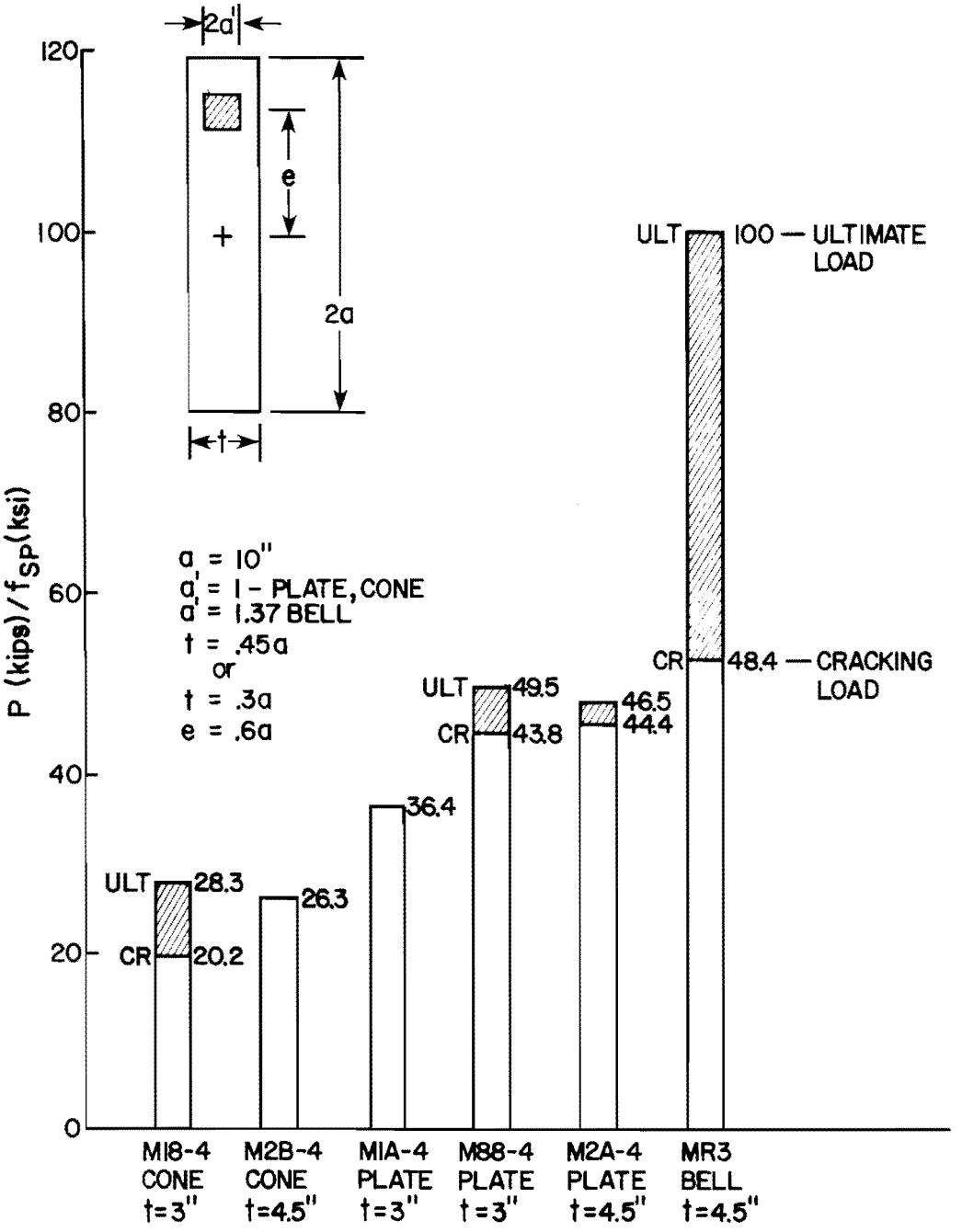

Fig. 2.14 Cracking and ultimate loads at e = 0.6a for different anchor geometries

series tests with thickness of 0.3a and 0.4a, as no test was performed for a thickness of 0.45a with a plate anchor at zero eccentricity.

The following four sections discuss behavioral patterns observed for the three types of anchors and present a quantitative summary of comparative performance.

2.4.1.1 Plate (Bearing) Anchors. Plate anchors tend to exhibit a very distinct behavior when loaded as shown in Fig. 2.15. For a concentrically loaded specimen at initial cracking, a crack will form along the tendon path (see Fig. 2.15a) beginning at a point roughly $2a'$ (the width of the anchor) in front of the loaded face. As the load increases this crack extends, both towards the loaded face and away from it. Further increases in load lead to the formation of diagonal cracks emanating from the four corners of the bearing plate (assumed rectangular) toward the side faces, as shown in Fig. 2.15b. Still further increases in load allow these diagonal cracks to propagate along the side faces. Since the diagonal cracks stem from the corners of the anchorage, each side will have two of them, one upper and one lower. Once the upper and lower diagonal cracks form on the side face the anchorage is on the verge of an explosive failure (see Fig. 2.15c). Figure 2.16 illustrates the above sequence as observed experimentally and Fig. 2.17 shows the explosive nature of final failure. For all geometric conditions investigated (straight, inclined, or eccentric) it was observed that the load range between first cracking and ultimate could be extremely small. Many times failure occurred at the same load which caused cracking (see Figs. 2.13 and 2.14). This observation applies only to sections with no supplementary anchorage zone reinforcement. As will be pointed out in Sec. 2.4.5, such reinforcement plays a twofold role:

(a) to raise the cracking load

(b) to provide a significant amount of reserve strength between cracking and ultimate

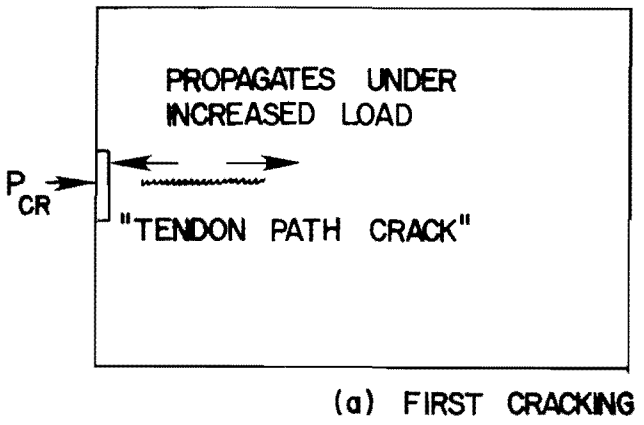

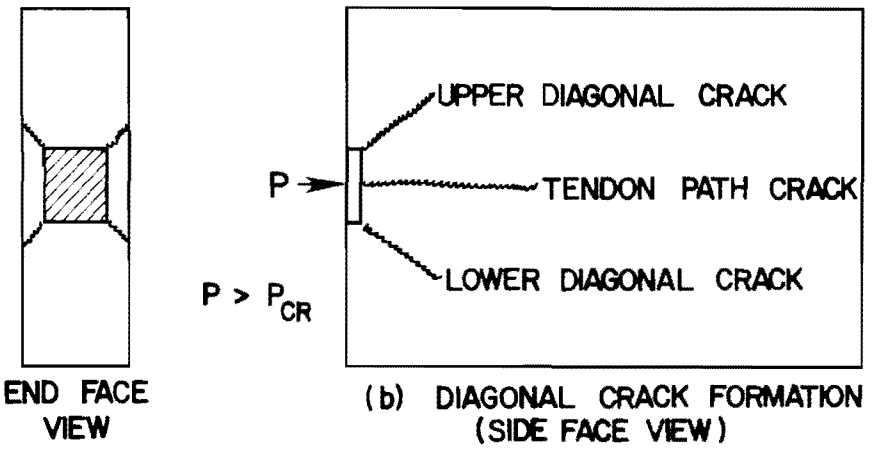

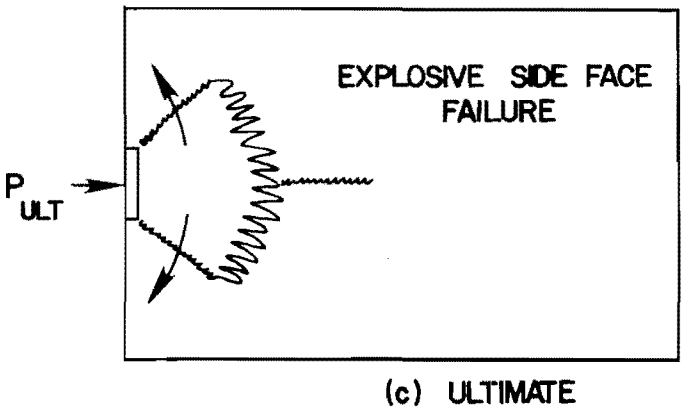

Fig. 2.15 Failure sequence for plate anchors

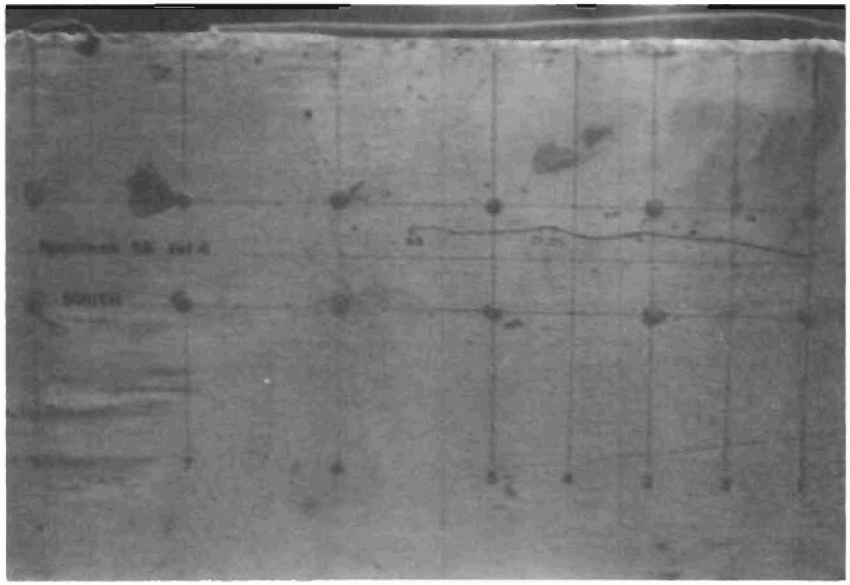

(a) Tendon path crack

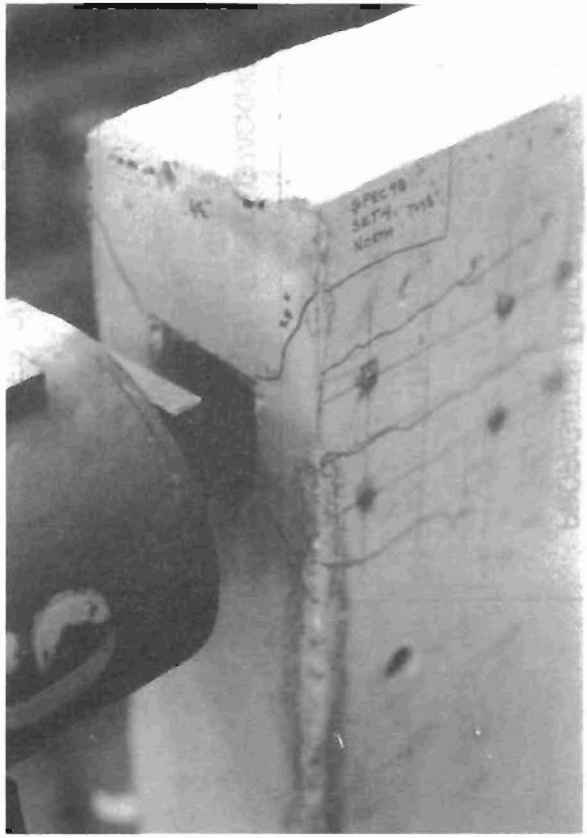

(b) Diagonal cracks at anchor

Fig. 2.16 Failure sequences--plate anchors

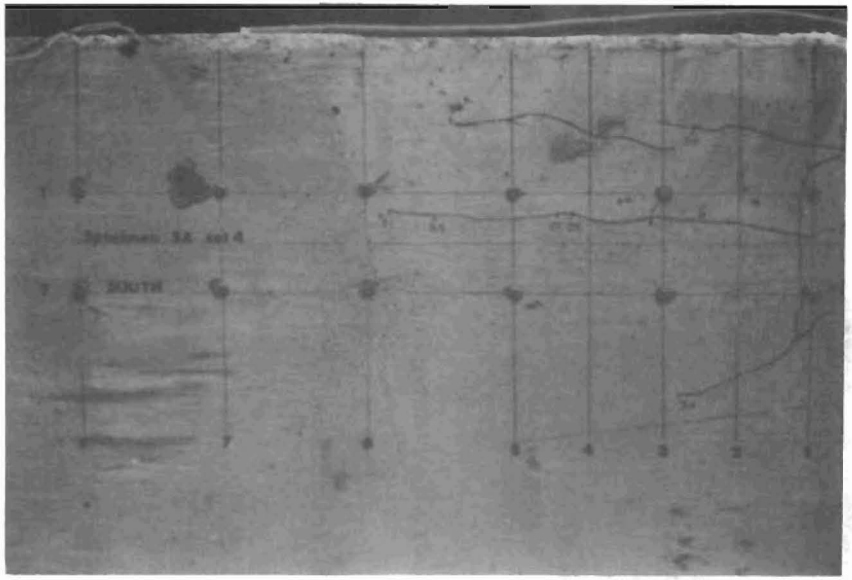

(c) Diagonal cracks propagate

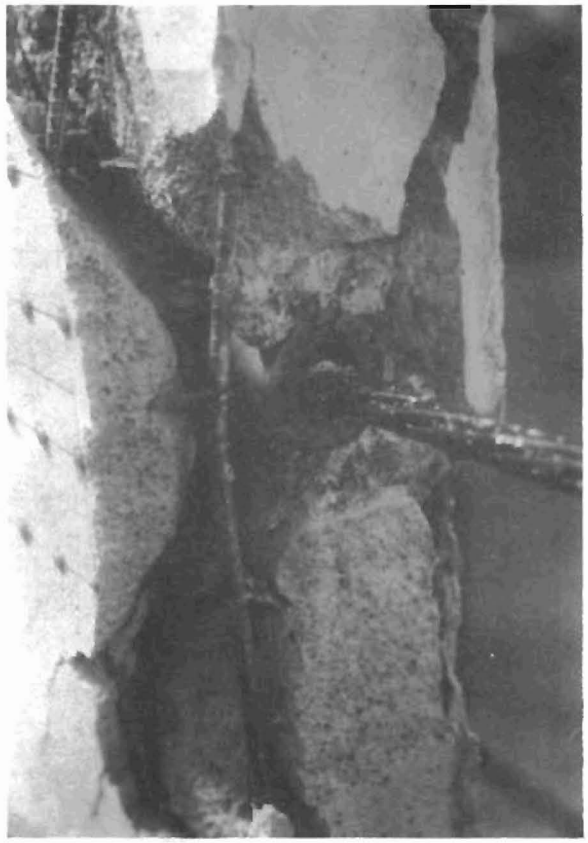

(d) Ultimate failure

Fig. 2.16 (continued)

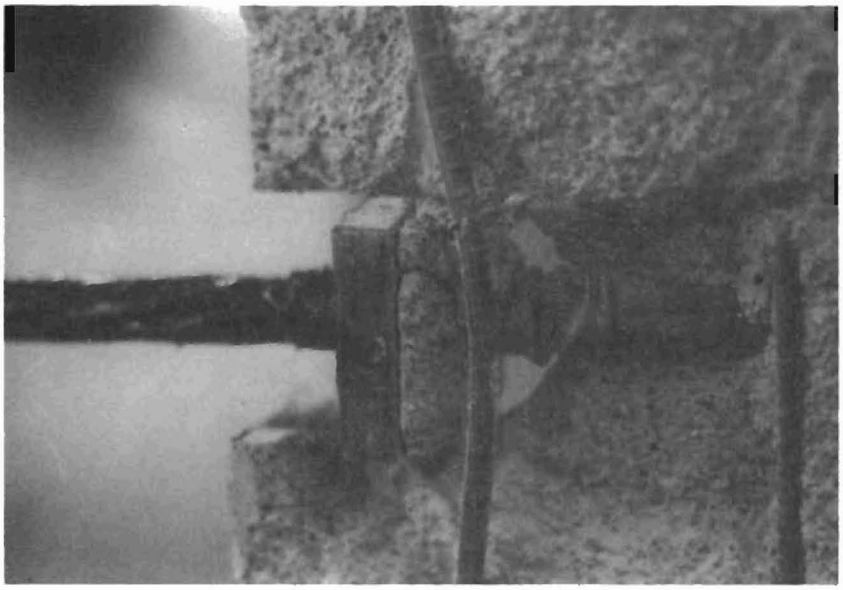

(e) Cone of crushed concrete

Fig. 2.16 (continued)

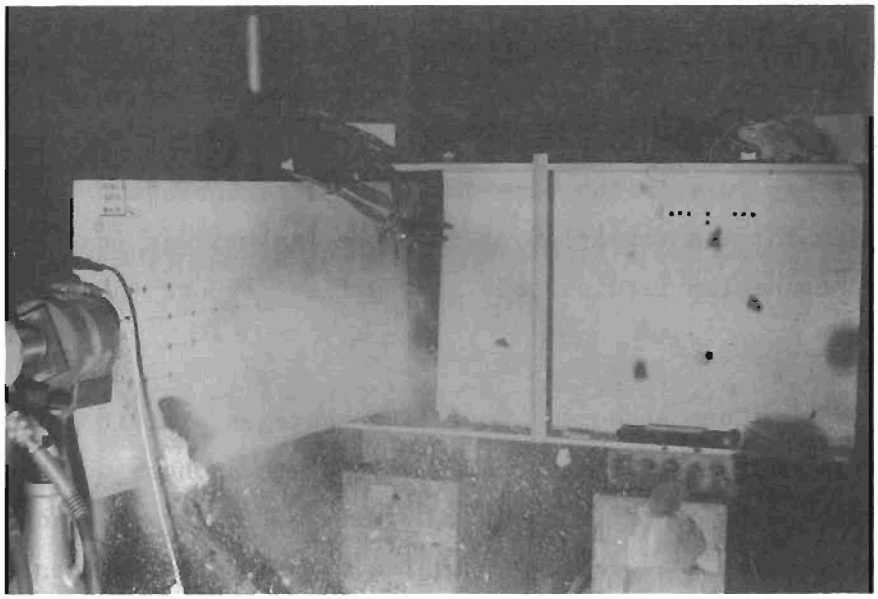

(a) Specimen M3-2

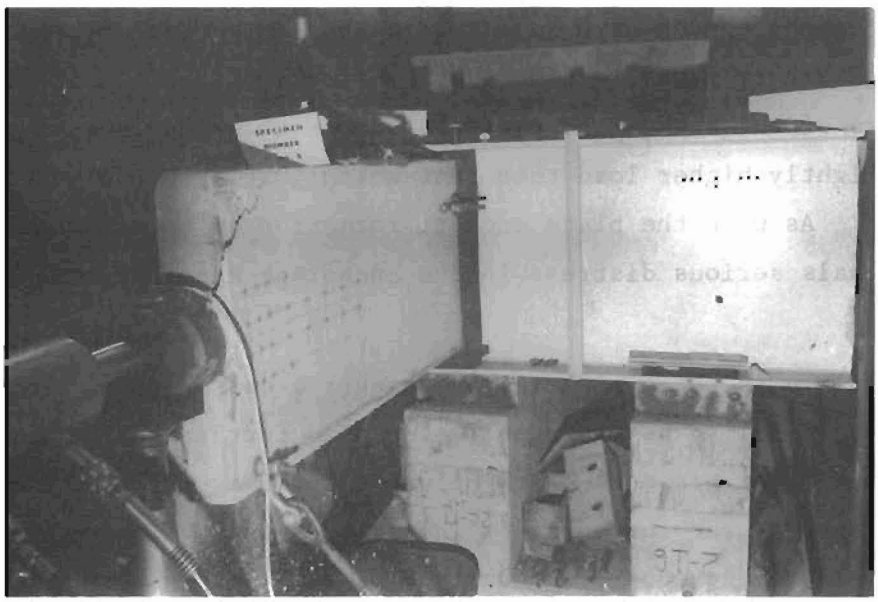

(b) Specimen M1-2

Fig. 2.17 Explosive failure of anchorage zone with plate anchors

Finally, one of the most striking characteristics of plate anchor failures is the formation of a "cone," more specifically a pyramid, of crushed concrete beneath the anchor. A powdering of mortar was exhibited along the sides of the cone indicating that a shear-type failure had taken place (see Fig. 2.16e). It is apparent that this cone plays a key role in the behavior of plate anchorages. A possible mechanism for the formation of the cone, as well as its role in the failure mechanism is discussed in the final report in this series.

2.4.1.2 Cone Anchors. Conical anchorages exhibit cracking behavior very similar to that observed for plate anchors which have the same base plate geometry except that all actions take place at substantially lower load levels. The failure sequence is identical to that shown in Fig. 2.15, with the exception that failure is usually not explosive for specimens without supplementary anchorage zone reinforcement. As with the plate-type anchor, the first crack to form is always along the tendon path. In most cases, this crack begins at a distance of $2a'$ from the loaded face. Diagonal cracks emanate from the corners of the anchor and progress across the side face at the same or slightly higher load than that which initiated the tendon path crack. As with the plate anchor, formation of the diagonal cracks signals serious distress in the anchorage zone, or impending failure.

Failure is not explosive, but rather a cessation of increased load-carrying ability as the anchor is pushed further and further into the specimen. The diagonal cracking was thus always visible and usually occurred near the onset of failure. A typical experimentally observed failure sequence is shown in Fig. 2.18. In general, cracking loads for the conical anchorages investigated in this series were on the order of 30 to 50 percent lower than those of identical specimens using plate anchors. Also no "cone" of concrete was present at failure.

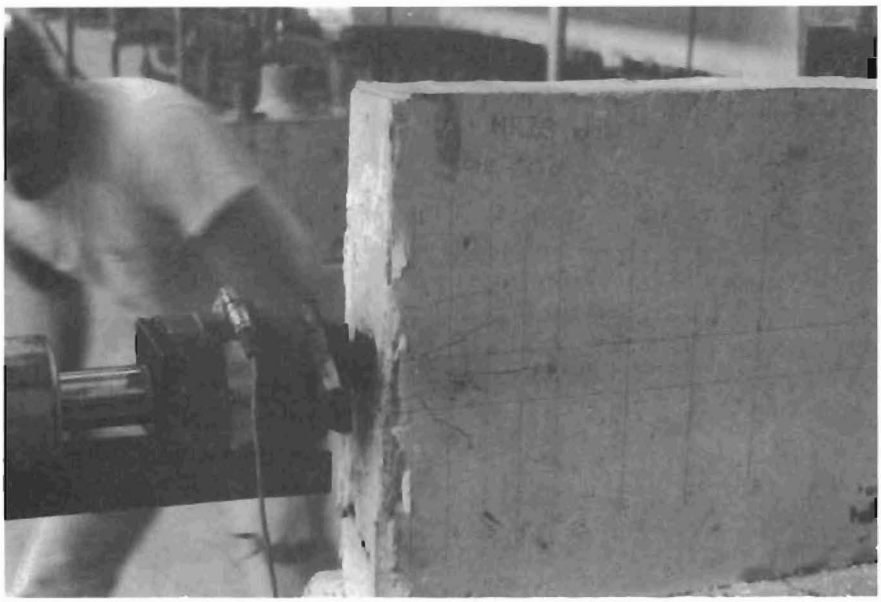

(a) t = 4-1/2 in., e = 0--showing upper, lower and tendon path cracking immediately prior to failure

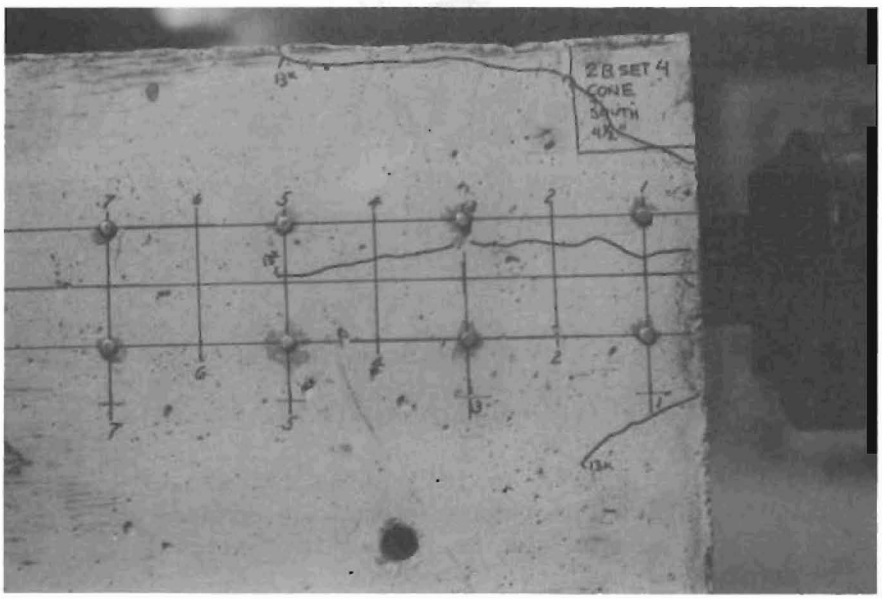

(b) t = 4-1/2 in., e = 0.6a (6 in.) immediately prior to failure

Fig. 2.18 Cone anchorage failure

(c) t = 3 in., e = 0.6a (6 in.) after failure. Diagonal cracks propagate from four corners of anchor. Anchorage is forced into web, nonexplosive failure

Fig. 2.18 (continued)

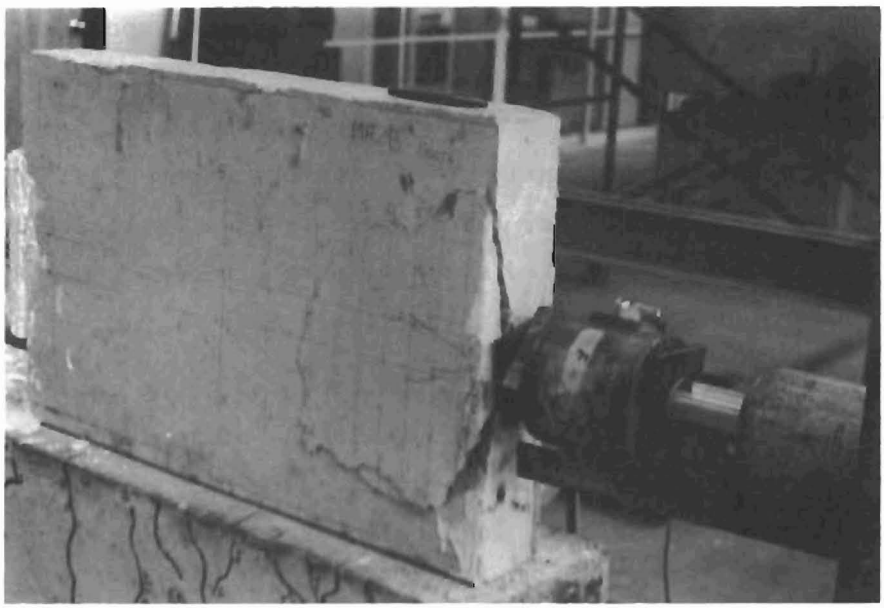

(d) t = 4-1/2 in., e = 0 in. ultimate failure after cone has been forced 2-1/2 in. into web

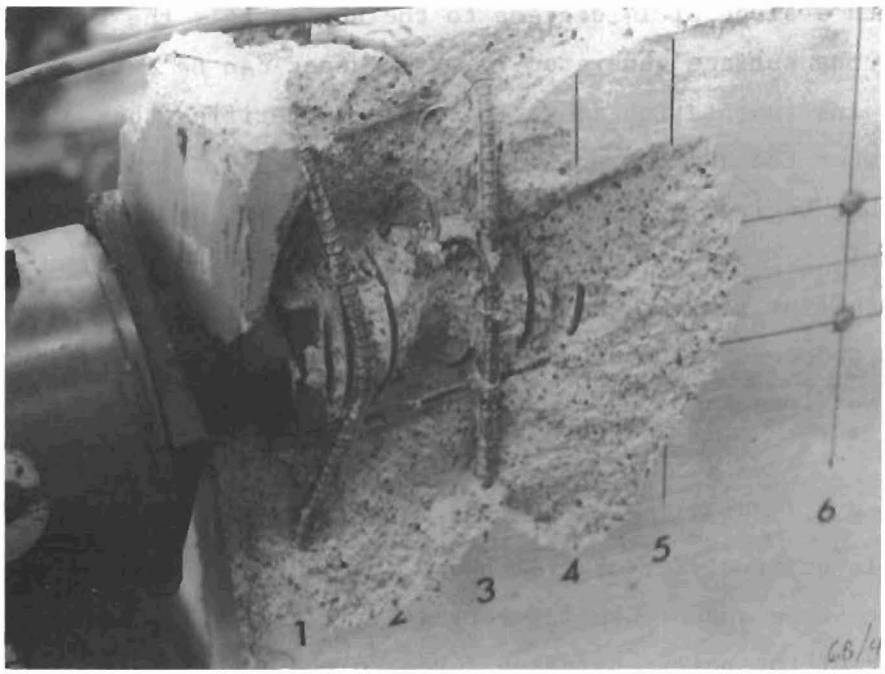

(e) Explosive failure of spiral reinforced cone t = 3 in., e = 0.6a (6 in.)

Fig. 2.18 (continued)

An interesting note on conical anchors which have special supplementary anchorage zone reinforcement (spirals specifically) is that both the cracking and ultimate loads are significantly raised, as much as twice those for unreinforced cones (but still less than 70 percent of that for a similarly reinforced plate anchor). Additionally, as shown in Fig. 2.18e, the failure is then explosive instead of the gradual wedging associated with the unreinforced cone. Reinforcement effects will be discussed in detail in Sec. 2.4.5.

Another difference between the cone and plate anchors is the actual mechanism of load transfer. While the plate anchor applies the post-tensioning load to the anchorage zone through direct bearing, the cone anchor achieves load transfer principally through bond, friction, and normal forces along the cone surface (Fig. 2.19a). Once the bond has been broken and the friction forces overcome, the load must be sustained by the horizontal component of the normal force acting on the side of the cone (Fig. 2.19b). For this type cone with a slope of 14 degrees to the horizontal, the forces normal to the cone surface generated in this manner can be extremely large. Special instrumentation shown in Fig. 2.20 verified that cracking occurs when the anchor begins to slip. Figure 2.21 shows that once the anchor begins to slip, cracking and then failure occurs with only a nominal increase in load. The basic difference between cone and plate behavior would thus appear to lie in the higher load required to form the cone of crushed concrete for the plate anchor versus the much lower load required to initiate slip along the face of the cone anchor.

2.4.1.3 Bell Anchors. The bell anchor seems to operate on a principle quite different from the plate and the cone anchor. While the plate-type anchor usually represents a very rigid and stiff transfer of the post-tensioning force to the loaded face, the bell anchor shown in Fig. 2.10 basically consists of an apparently flimsy piece of sheet metal spot-welded to a relatively thin (in comparison

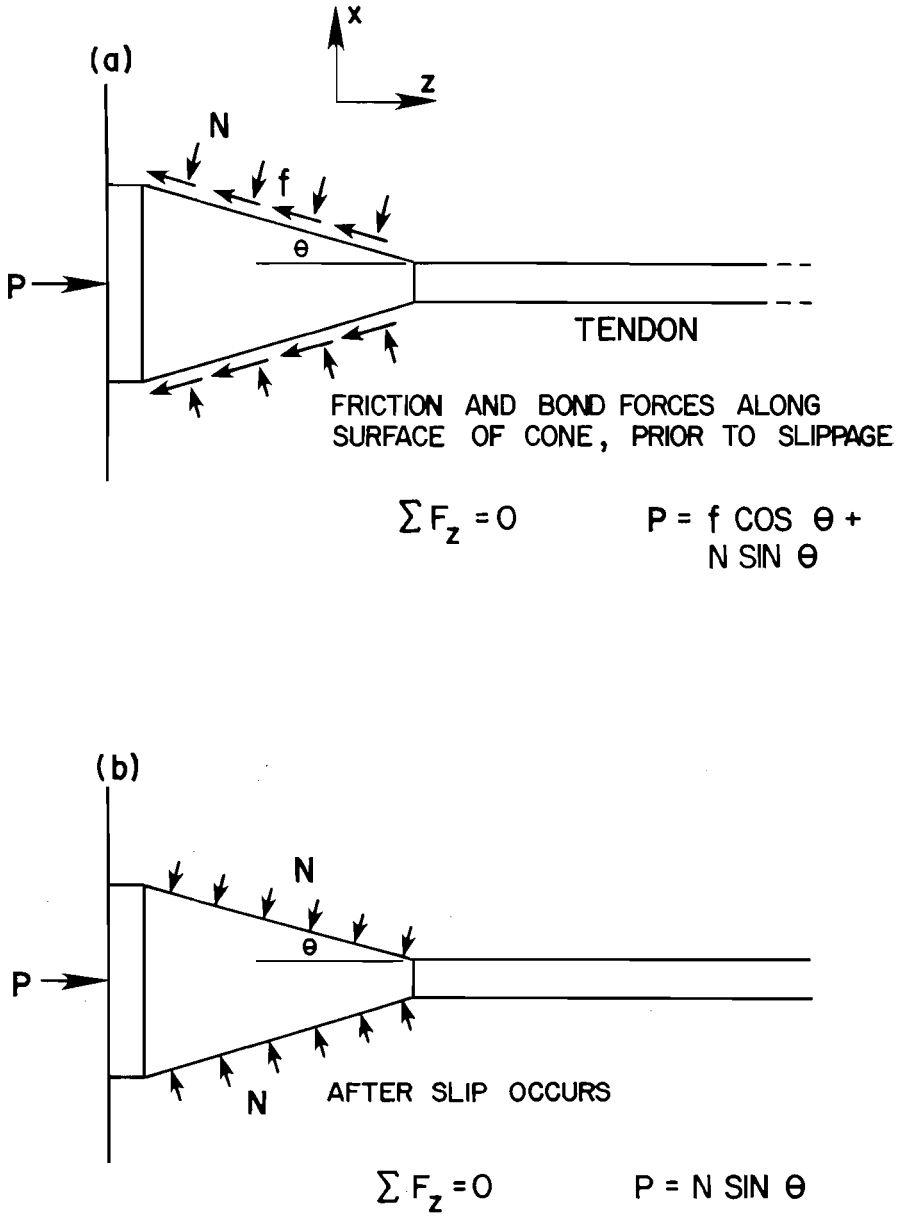

Fig. 2.19 Possible load transfer mechanism for cone anchors

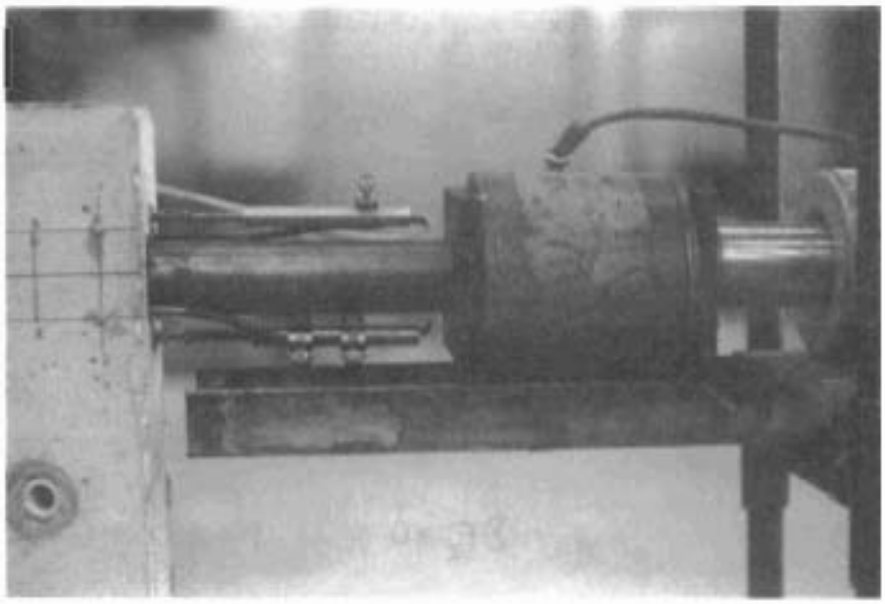

(a) System used to measure slip of cone anchors

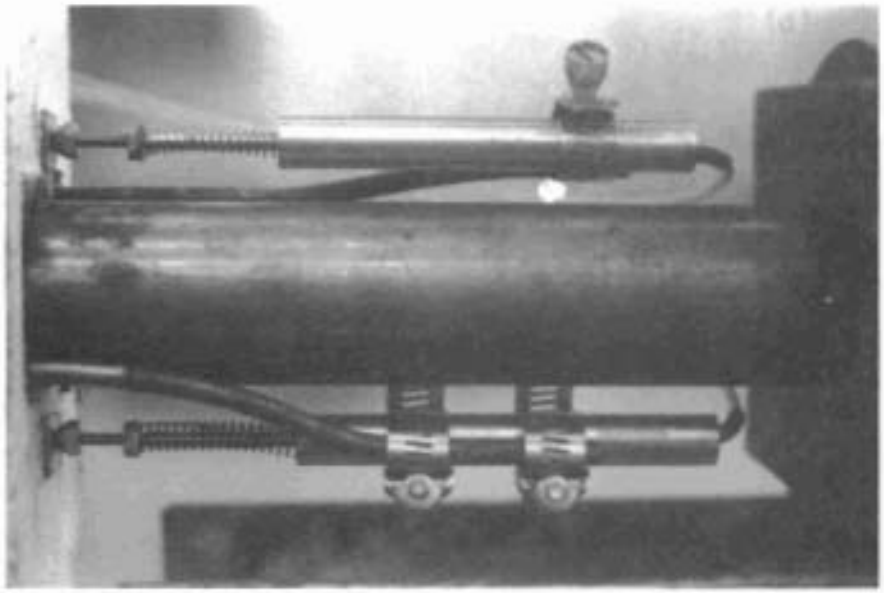

(b) Close up of LVDT slip gages mounted to anchor

Fig. 2.20 Slip gages for cone anchors

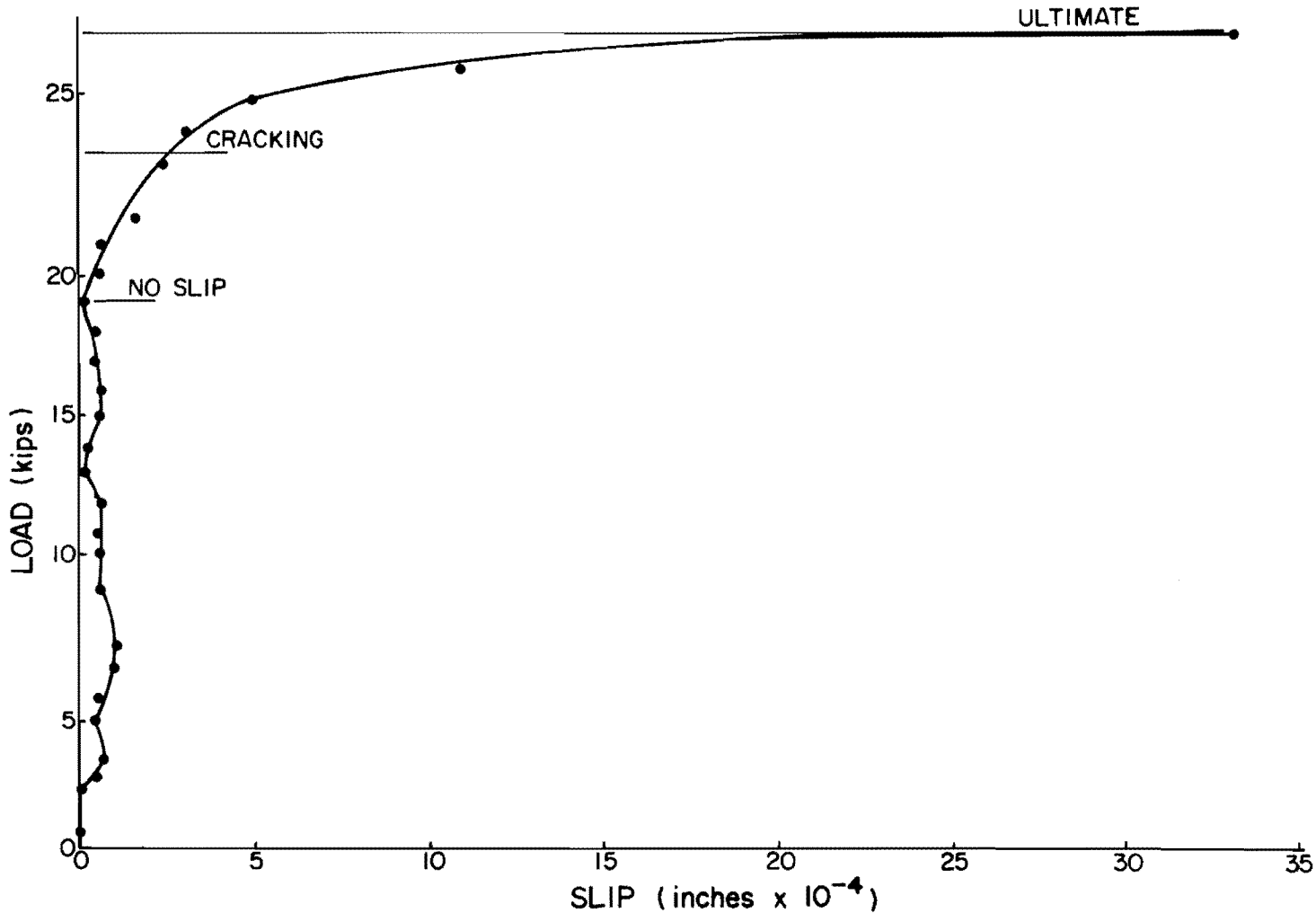

Fig. 2.21 Typical load-slip plot for cone-type anchors

with the thickness of the average bearing plate) hoop of wide bar stock. The key to the bell seems to be that the load is transferred to this flimsy sheet metal covering via a large threaded nut which has a hemispherical head. As the load is applied through the nut the spherical head acts much like the cone anchor, creating large lateral pressures. These lateral expansive forces are confined by the hoop, setting up a state of triaxial compression ahead of the nut. The result is that the entire mechanism behaves as if it were a bearing anchor of about the same equivalent area as confined within the hoop. Since the bell anchor appears less expensive to fabricate than a plate anchor, it can usually be designed for a greater capacity at a given cost. The anchorage used in these tests was scaled based upon the manufacturers rate P_{ult} so that each anchor would present the same rated capacity. As can be seen from Fig. 2.11, the bell anchor had a significantly larger diameter than either the plate or the cone.

Notable differences occurred in the cracking pattern. Rather than the progression of tendon path crack, diagonal cracks on the loaded face, and upper and lower diagonal cracking on the side faces prior to failure as exhibited with the plate and cone anchors, the bell anchor exhibited variation in cracking before failure. As shown in Fig. 2.22, at roughly the same load a single tendon path crack formed at one end, while upper and lower diagonal cracks formed at the other end without the presence of the tendon path crack. These occurred at approximately 0.8 P_{ult}. Just before failure three major cracks usually opened on the end face, one vertical crack above the anchor and two diagonal cracks below the anchor. Failure was explosive for both specimens tested and usually occurred on the side with the single tendon path crack. Although no evidence of diagonal cracking (on the tendon path crack side) was present before specimen MR2A failed, specimen MR3 formed both the upper and lower diagonal cracks prior to failure on that side. Figure 2.25 shows a typical experimentally observed failure.

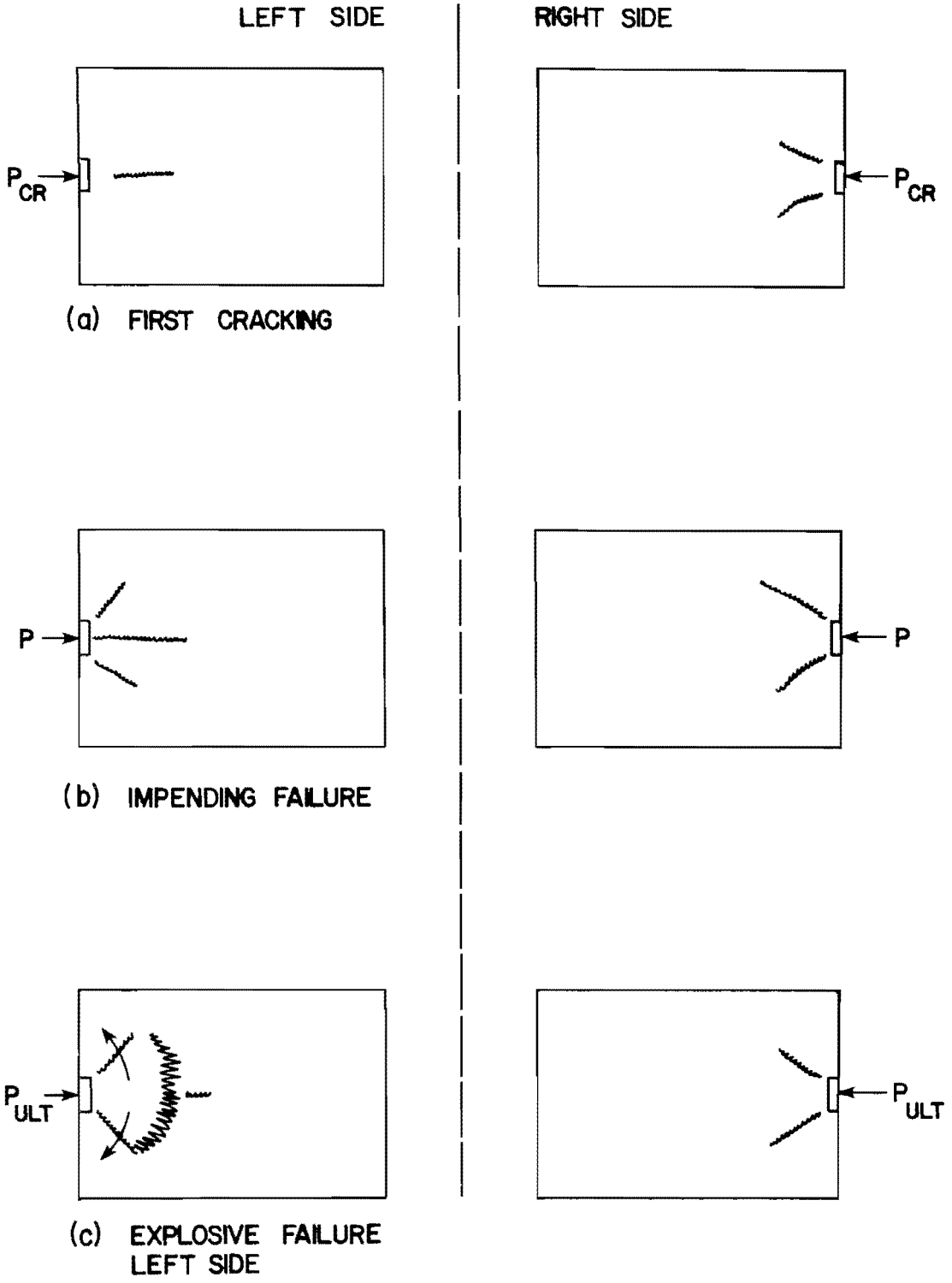

Fig. 2.22 Failure sequence for bell anchors

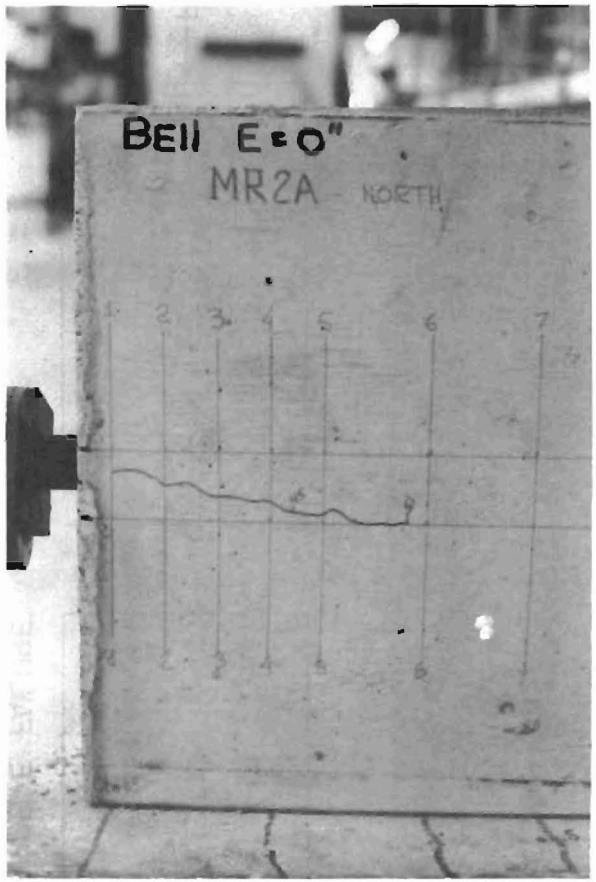

(a) North side--single tendon path crack prior to failure

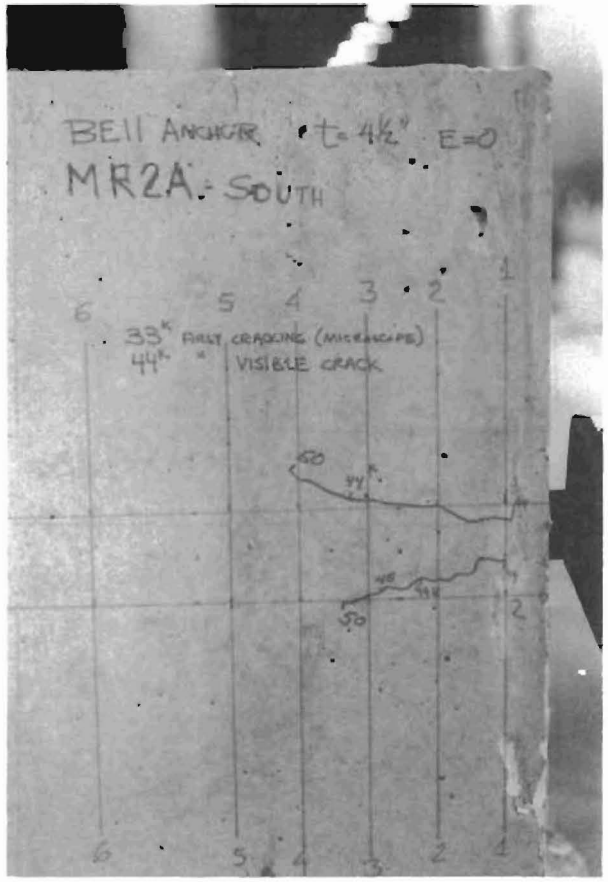

(b) Upper and lower diagonal cracks on south side illustrate asymmetry caused by circular anchor

Fig. 2.23 Bell anchorage failure

(c) End view after failure--three major cracks

(d) Explosive failure of north side

Fig. 2.23 (continued)

A possible failure theory for the bell anchor would be that it behaves the same as would a rigid circular plate anchor of the same circular cross section. A shear cone would thus form ahead of the bell prior to failure. Solid evidence of a shear cone for bell anchors was not available from the tests as explosive failures left little material in front of the anchorage for examination. Further study of the behavior of the bell would appear to be warranted considering its attributes of low cost and high ultimate load capacity.

2.4.1.4 Comparison of Anchorage Types. The general trend apparent from Figs. 2.13 and 2.14 was that conical anchorages cracked at loads 30 to 50 percent lower than those for plate anchors tested under identical circumstances. The somewhat larger but equivalent bell anchors cracked at loads 7 to 9 percent above those observed for plate anchors. Ultimate load data indicated that for plate and conical anchors without supplemental anchorage reinforcement specimens failed at loads at or only slightly above the cracking load. The bell anchors developed substantially higher loads beyond cracking: 20 percent higher for an eccentricity of $e = 0$, and 106 percent higher for an eccentricity of $e = 0.6a$.

2.4.2 Cover Series. Three-dimensional finite element studies indicated that tensile stresses in the anchorage zone could be reduced significantly by increasing the section width for a given load and anchorage system. This test series consisted of eight specimens designed to investigate the effects of cover concrete on anchorage zone behavior. Plate-type anchors, as detailed in Fig. 2.11, were used for six specimens. Two specimens with cone-type anchors were also included to verify that similar trends with respect to cover thickness occur regardless of anchorage type. Web thicknesses of $t = 2$, 3, 4, and 4.5 in. were investigated. The experimental results were compared with predicted strains from the 30 FEM analytical program. Tables 2.6 and 2.7 give pertinent details of the tests. Cracking trends are presented in Fig. 2.24. In general, specimens with a given type of anchorage exhibited failure sequences as described in the previous section. No supplementary

TABLE 2.6

BASIC SPECIMEN INFORMATION FOR COVER SERIES f_{sp}

	Specimen ID	P_{cr} (kips)	P_{ult} (kips)	Eccentricity e^*	Width t^*	Cover c/t	f'_c (psi)	f_{sp} (psi)
Concentric Plate	M1-2	43	43	0	0.4a (4")	0.25	4250	627
	M2-2	34	23	0	0.3a (3")	0.17	4250	627
	M3-2	24	24	0	0.2a (2")	0.0	4250	627
	M4-2	18	19	0	0.2a (2")	0.0	2923	460
Eccentric Plate	M1A-4	18	18	0.6a	0.3a (3")	0.17	3583	495
	M2A-4	22	23	0.6a	0.45a (4-1/2")	0.28	3583	495
Eccentric Cone	M1B-4	10	14	0.6a	0.3a (3")	0.17	3583	495
	M2B-4	13	13	0.6a	0.45a (4-1/2")	0.28	3583	495

*See Fig. 2.12 for definitions of e, t, a.

TABLE 2.7

NORMALIZED CRACKING AND ULTIMATE LOADS (COVER SERIES)

Specimen ID	P_{cr}/f'_c	$P_{cr}/\sqrt{f'_c}$	P_{cr}/f_{sp}	P_{ult}/f'_c	$P_{ult}/\sqrt{f'_c}$	P_{ult}/f_{sp}	2a'/t
M1-2	10.1	659	68.6	10.1	659	68.6	0.5
M2-2	8.0	521	54.2	8.0	521	54.2	0.66
M3-2	5.65	308	38.3	5.65	368	38.3	1.0
M4-2	6.16	332	39.1	6.5	351	41.3	1.0
M1A-4	5.02	301	36.4	5.02	301	36.4	0.66
M2A-4	6.14	367	44.4	6.42	383	46.5	0.44
M1B-4	2.79	167	20.2	3.90	233	28.3	0.66
M2B-4	3.63	217	26.3	3.63	217	26.3	0.44

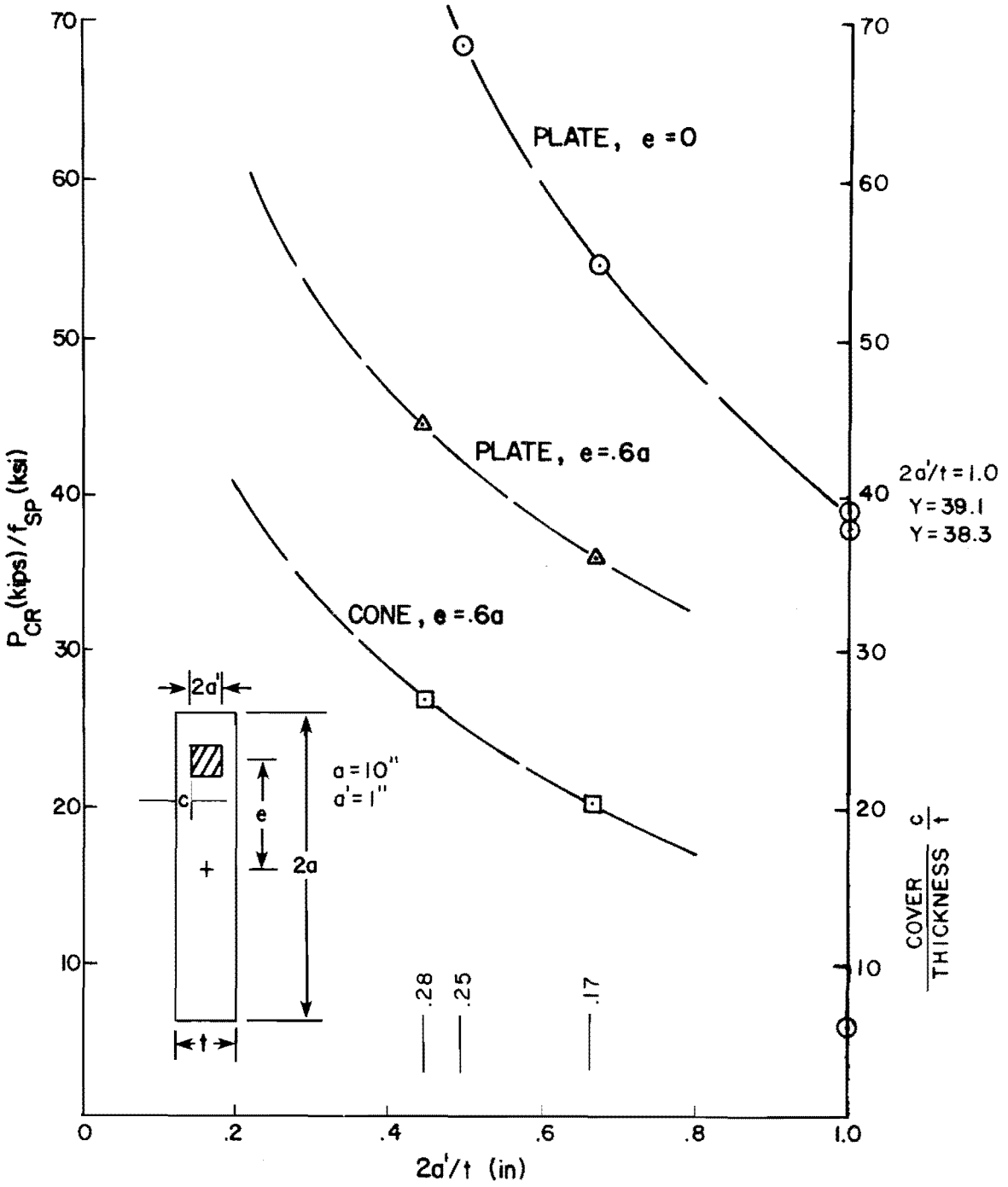

(a) Normalized for f_{sp}

Fig. 2.24 Cover effects on cracking load

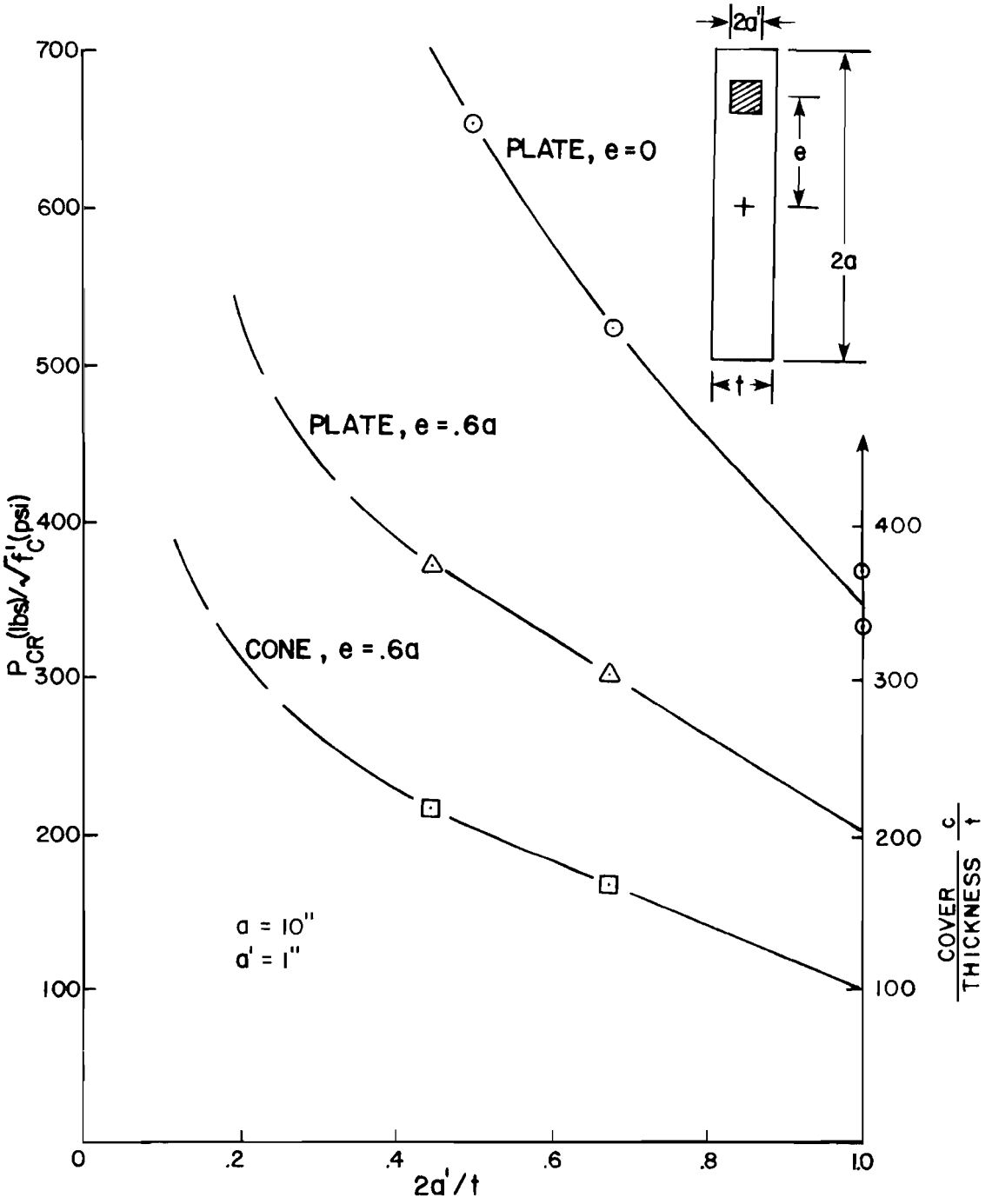

(b) Normalized for $\sqrt{f'_c}$

Fig. 2.24 (continued)

anchorage zone reinforcement was provided in this series and thus emphasis was placed on the load to cause first cracking since most specimens failed at loads at or only nominally above the cracking load.

The most striking result shown in Fig. 2.24 is that for a given anchor geometry and eccentricity increased cover yielded increasingly higher cracking loads. This is what one would expect intuitively, since larger forces would be required to set up sufficient tensile stresses to split the section longitudinally for a thicker section. In fact, for a fixed anchor size one would expect an exponential rise in the cracking load as the value $2a'/t$ goes to zero. Most practical anchorage situations for thin web sections fall between $2a'/t = 0.4$ to $2a'/t = 1$. ($c/t = 0.3$ to $c/t = 0$) The limiting case of $2a'/t = 1$ ($c/t = 0$) would be the same as the idealized strip loading condition.

Figure 2.25 shows the measured distribution of transverse strain along the tendon path. The analytical comparison shown in Ref. 1 shows good agreement. The trend indicates that for increasing cover and hence specimen width and cross section area, the transverse bursting strain decreases substantially. For straight, concentric tendons, it appears that the maximum bursting strain follows the cracking trends of Fig. 2.24, and thus theoretically could be used as the key parameter for design of tensile reinforcement in the anchorage zone. In fact, this is what has been done in the past with procedures such as Guyon's method. However, other series will show that with eccentric and inclined tendons the correlation between bursting strain and cracking load becomes highly erroneous, leaving doubt as to the merits of design on the basis of bursting stress. It is very important to note the magnitude of the strains measured. An elastic tensile strain agreeing with f_{sp} would be on the order of 150-200 microstrain. In almost all cases the maximum bursting strain at cracking was substantially below this tensile strain which would be a very conservative limit.

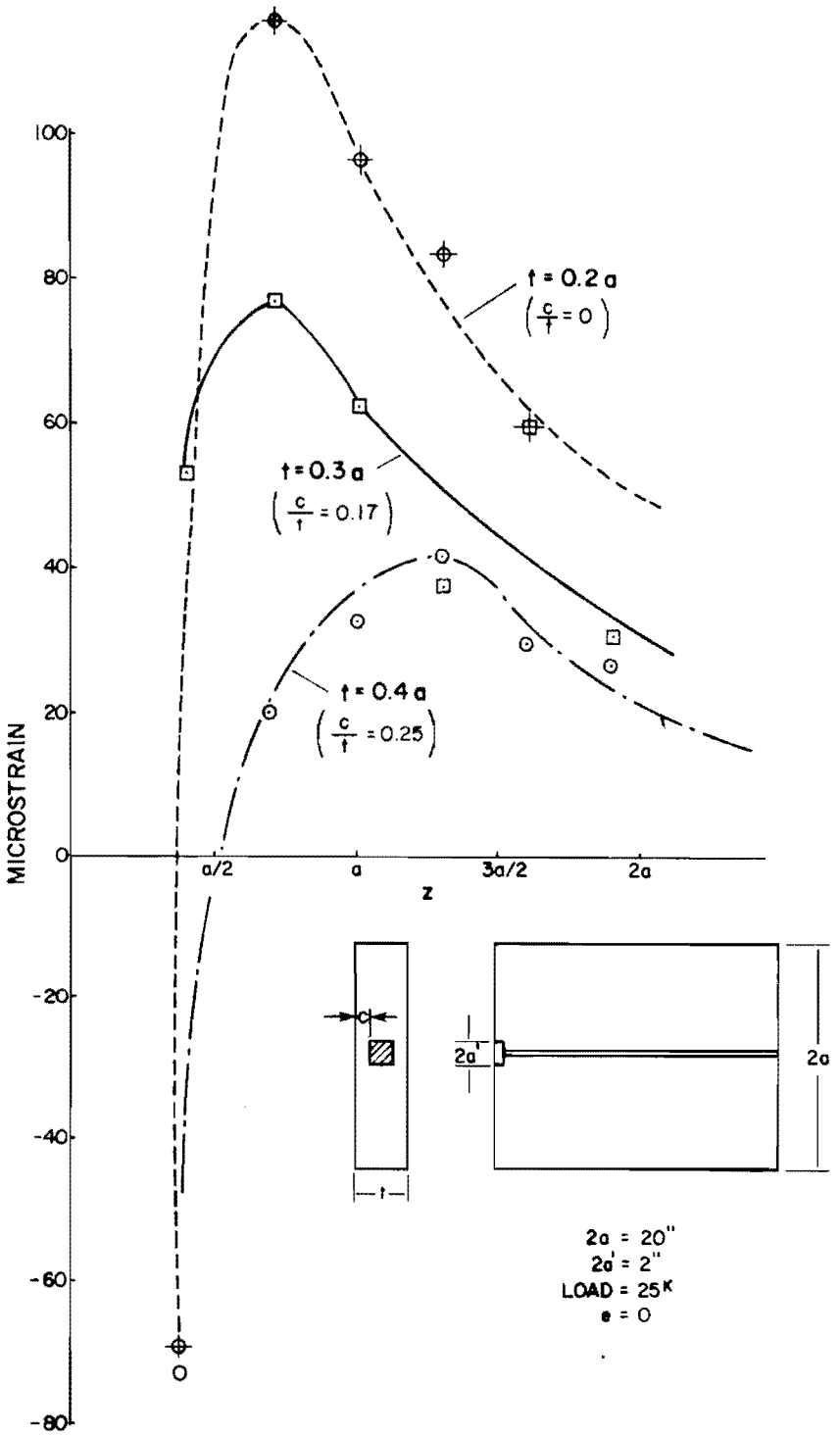

Fig. 2.25 Experimental bursting strain distribution--cover series

2.4.3 Eccentricity Series. This test series consisted of comparison of 13 specimens designed to investigate the effects of tendon eccentricity on the stress state as well as the load performance of the anchorage zone. Specimens were also used for study of other variables and basic data were also reported in Tables 2.3 through 2.7. Eccentricities varied from zero (concentric loading) to 0.6a (or 6 in. for a 20 in. high specimen). Figure 2.26 shows the initial cracking load trends for various specimen widths and anchorage types under increasing eccentricity. The general trend for all anchor types and covers is of decreasing cracking load with increasing eccentricity. For most anchorage types investigated, the cracking load at an eccentricity of e = 0.6a was approximately 50 percent of that for similar concentrically loaded specimens.

Fairly obvious trends are indicated with respect to anchorage types, with the best performance being exhibited by the bell. The cone, as shown before, cracked at considerably lower loads than the other anchorages tested.

Looking at the ultimate strength trends in Fig. 2.27, it can be seen that the bell anchor is the only one to carry substantially greater loads above cracking, and at ultimate it demonstrated an apparent insensitivity to eccentricity. Whether or not this is an absolute trend should be the subject of further study. Further discussion on eccentricity and possible cracking mechanisms is presented in the final report.

Figure 2.28 shows the general bursting strain trends in the linear-uncracked range for increased eccentricity. Only a slight difference in maximum strain was observed, with eccentric tendons exhibiting the lower values. This is a trend of substantial significance and has been reproduced using the analytical program. Figure 2.26 clearly shows that the cracking load for a plate anchor with an eccentricity of e = 0.6a is only half that of its concentrically loaded companion specimen. The analytically predicted (and

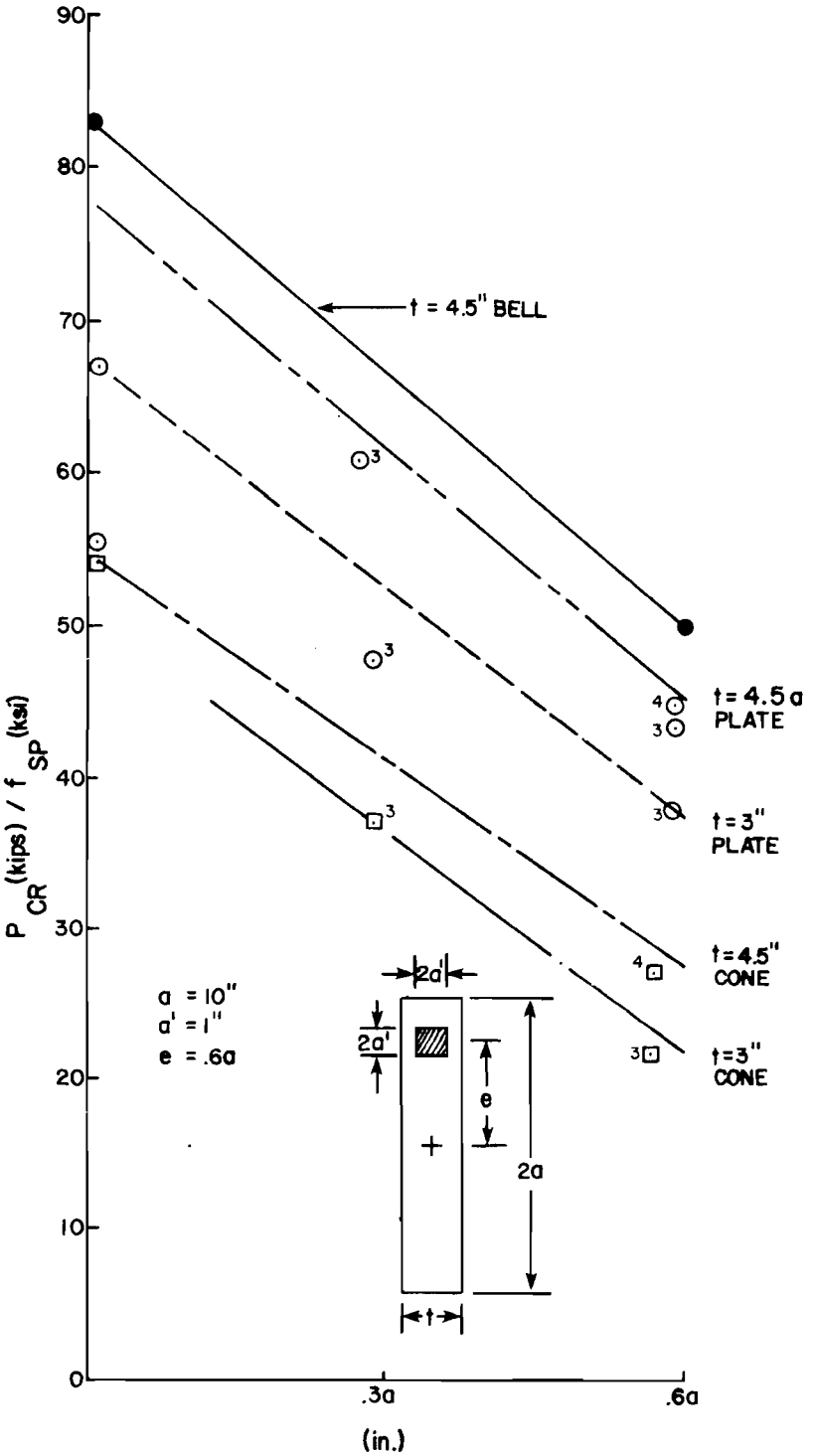

Fig. 2.26 Crack loads normalized to f_{sp}--eccentricity series

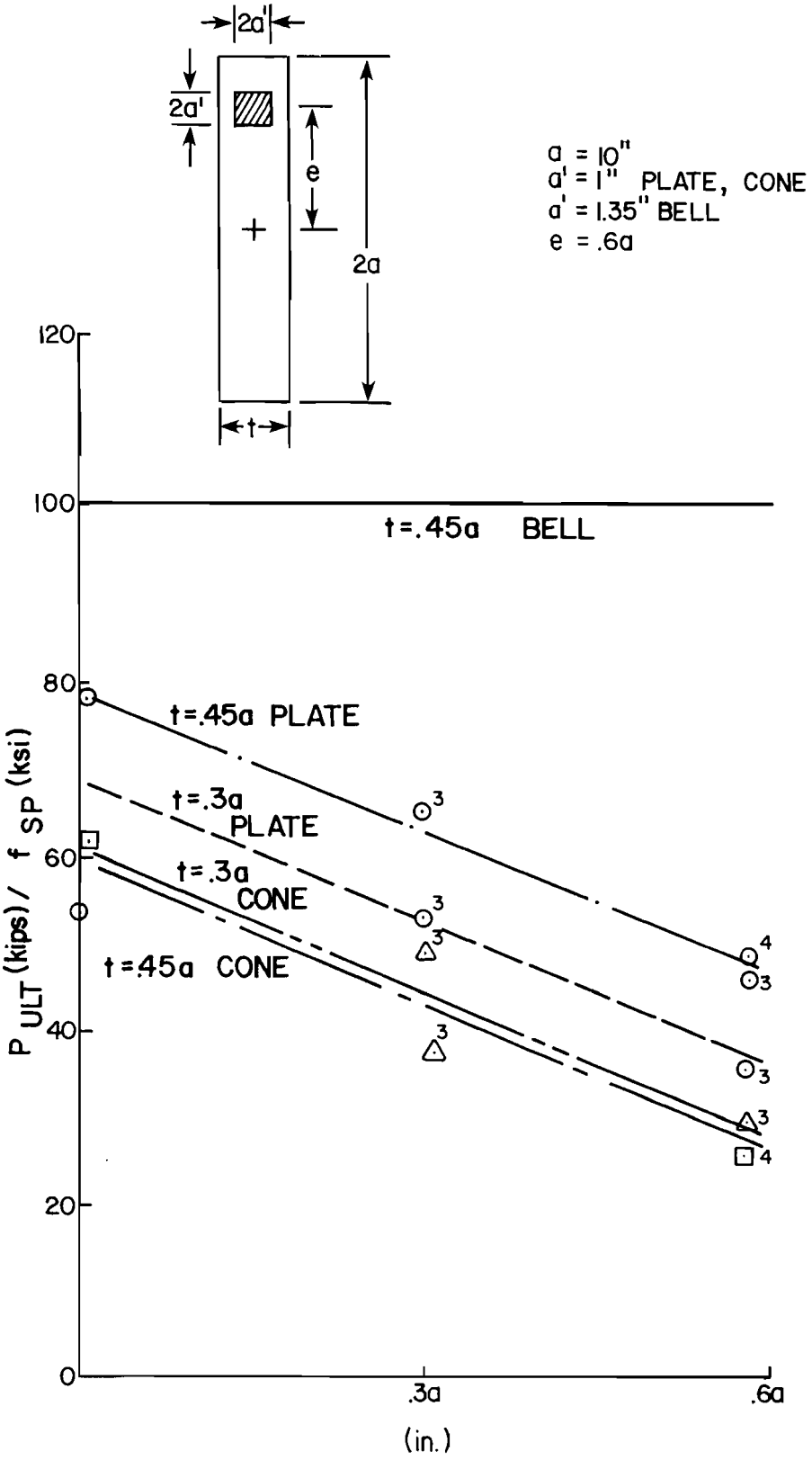

Fig. 2.27 Ultimate load normalized to f_{sp} -- eccentricity series

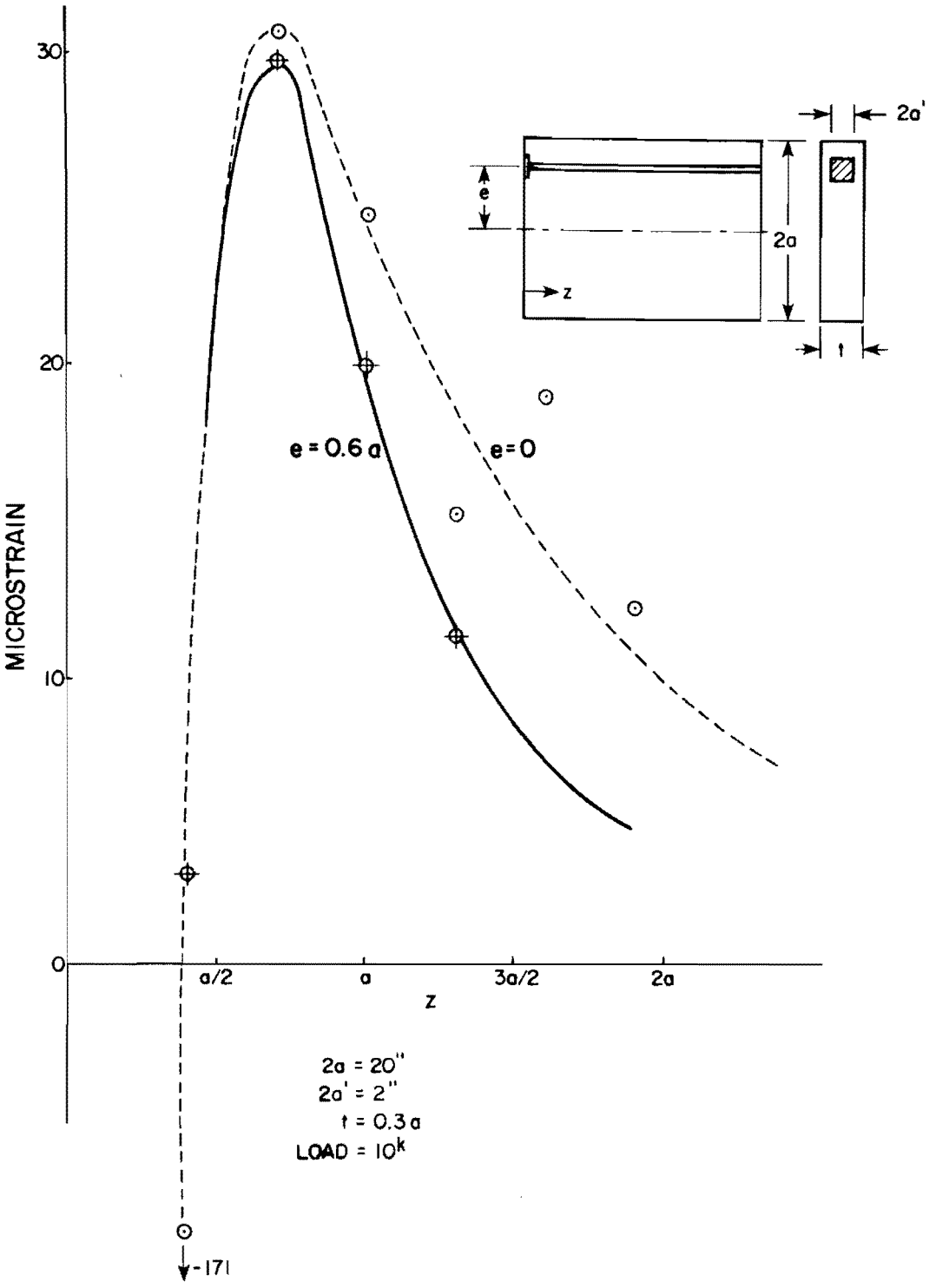

Fig. 2.28 Experimental bursting strain distribution--eccentricity series

physically observed) decrease in the bursting stress (strain) distribution due to increased eccentricity contradicts the observed cracking and ultimate load trends which showed a marked load decrease with increased eccentricity. This contradiction spurred a search, using the 3D FEM computer program, for possible alternative indicators which would more accurately follow the experimental data. These are outlined in the final report.

2.4.4 Inclined Tendon Series. An exploratory series of two specimens with tendons inclined at a 30 degree angle were cast in two widths ($t = 0.45a$ and $t = 0.3a$) for comparison with previously reported specimens with horizontal tendons. Table 2.8 presents the additional experimental data used for the plots in Fig. 2.29. The general trend is that for increasing inclination the cracking load drops. There is a fair amount of scatter between the results for the two widths, as evidenced by the skew of the curves. The "flattest" is for the width $t = 0.3a$ (3 in.) and indicates a 17 percent drop in cracking load for the 30 degree inclined tendon when compared to the straight tendon model. For the $t = 0.45a$ case the difference is 35 percent. The analytical results showed an approximately 1 percent drop in cracking load per degree of tendon inclination.

The measured bursting strain distribution for the $t = 0.3a$ case is plotted in Fig. 2.30 along with that for its companion specimen with zero inclination. Again, a very important trend is shown. The maximum tensile bursting strain drops rapidly with increasing tendon inclination. This directly contradicts the cracking and ultimate load trends seen in Fig. 2.29. Again, it is apparent that some other mechanism than the bursting stress is initiating the cracking.

2.4.5 Passive Reinforcement Series. Passive reinforcement is a term used for ordinary nonprestressed reinforcement. It does not develop much stress until some action cracks the concrete. This is in contrast to active reinforcement such as prestressing

TABLE 2.8

INCLINED TENDON MODEL DATA

Specimen ID	P_{cr} (kips)	P_{ult} (kips)	Eccentricity e	Width t	Inclination θ (deg.)	f'_c (psi)	f_{sp} (psi)
M1-3	28	32	0	0.3a	30	3572	610
M2-3	32	26	0	0.45a	30	4129	637

Specimen ID	P_{cr}/f'_c	$P_{cr}/\sqrt{f'_c}$	P_{cr}/f_{sp}	P_{ult}/f'_c	$P_{ult}/\sqrt{f'_c}$	P_{ult}/f_{sp}	Θ
M1-3	7.84	468	45.9	8.96	535	52.4	30°
M2-3	7.75	498	50.3	8.72	560	56.5	30°

Note: Upper and lower diagonal cracking did not appear until failure.

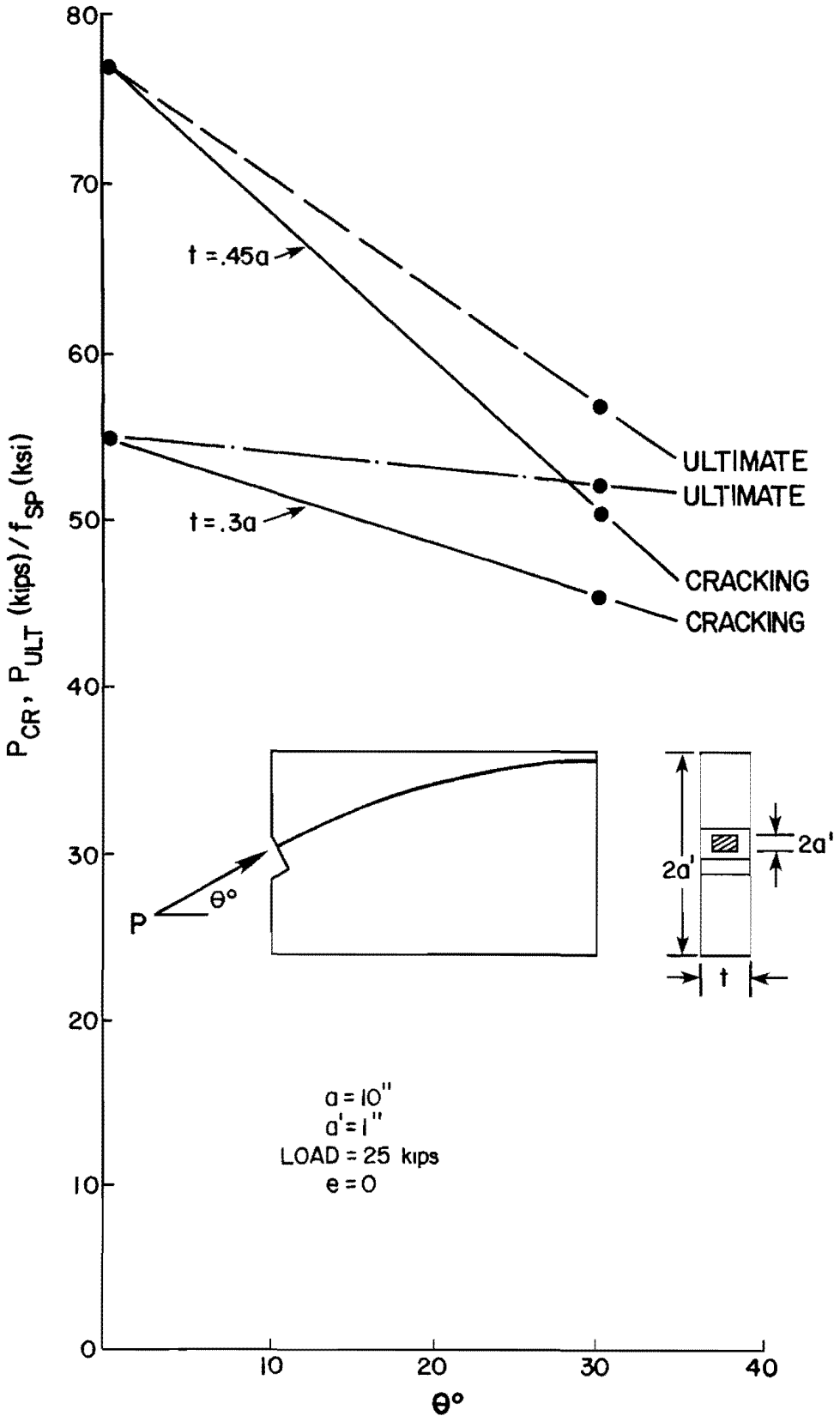

Fig. 2.29 Cracking and ultimate loads--tendon inclination series

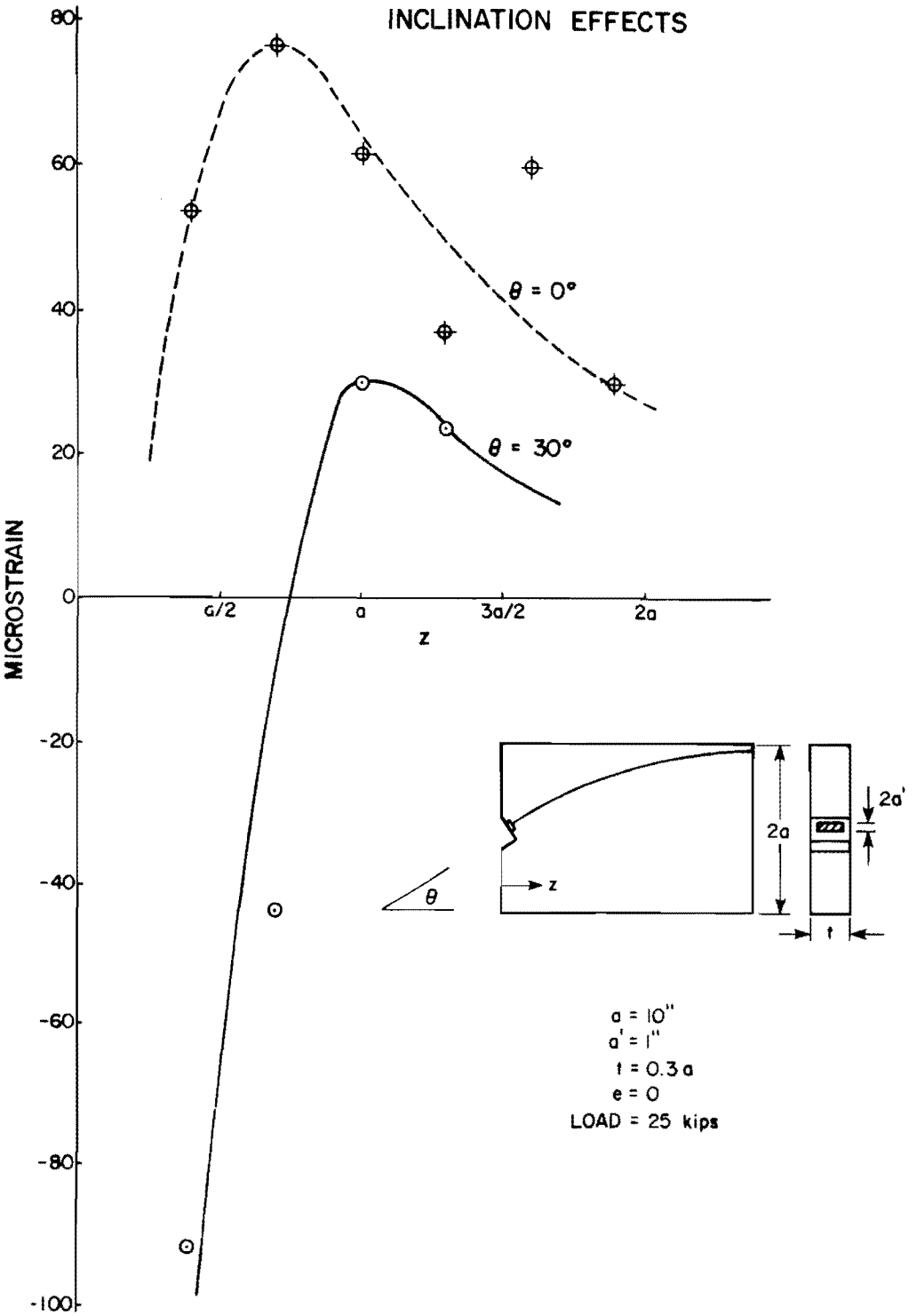

Fig. 2.30 Experimental bursting strain distribution--inclination series

steel which is given high stress by special construction operations. There are two current methods for providing passive reinforcement for anchorage zones. These consist of orthogonal meshes of standard reinforcing bars or of spirals. In the early stages of this research study, the recommendations of Guyon and Leonhardt (summarized in Ref. 1) were available for design of orthogonal reinforcement based on elasticity bursting stress distributions. Similarly, the experimentally based method of Rhodes and Turner was also available. These methods dealt principally with orthogonal type reinforcement design. They determined the necessary reinforcing to carry a tensile force calculated by an approximate method based on the area under the tersile portion of the bursting stress distribution. Reinforcement was provided in those areas where the tensile stress exceeded the tensile capacity of the concrete.

Design of the passive orthogonal reinforcement for the test specimens of this series was based on a bursting stress criterion. However, because good correlation between the experimental and 3D FEM bursting strain distributions had been obtained in the early nonreinforced concentric models, it was felt at that time that the orthogonal reinforcement could be more accurately designed for this test series by utilizing a finite element derived bursting stress curve. The details of this procedure are presented in Sec. 2.4.5.1. For the design of spiral reinforcement, a procedure based on the general philosophy used for design of column spirals was used and is detailed in Sec. 2.4.5.2.

2.4.5.1 Design of Orthogonal Reinforcement. The 3D FEM calculated bursting stress distributions for the specimens with $t = 0.3a$ (3 in.) and $t = 0.45a$ (4-1/2 in.) are shown in Fig. 2.31. Based on a diagonal tension analogy it is assumed that the plain concrete will be able to carry a tensile stress of at least $2\sqrt{f'_c}$. Any sections where the bursting tensile stress exceeds this value

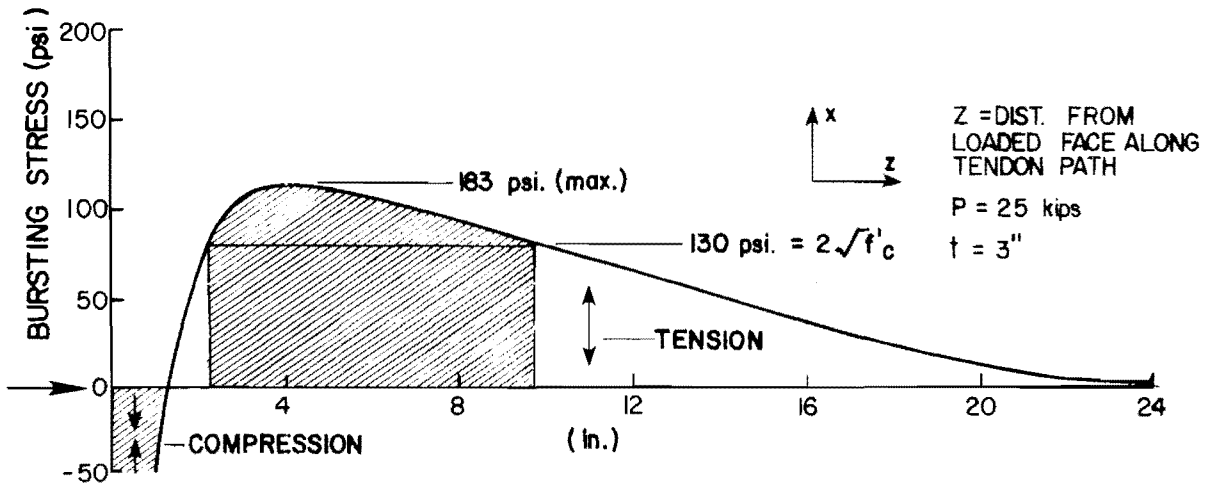

(a) Bursting distribution for t = 3 in. specimen along tendon path

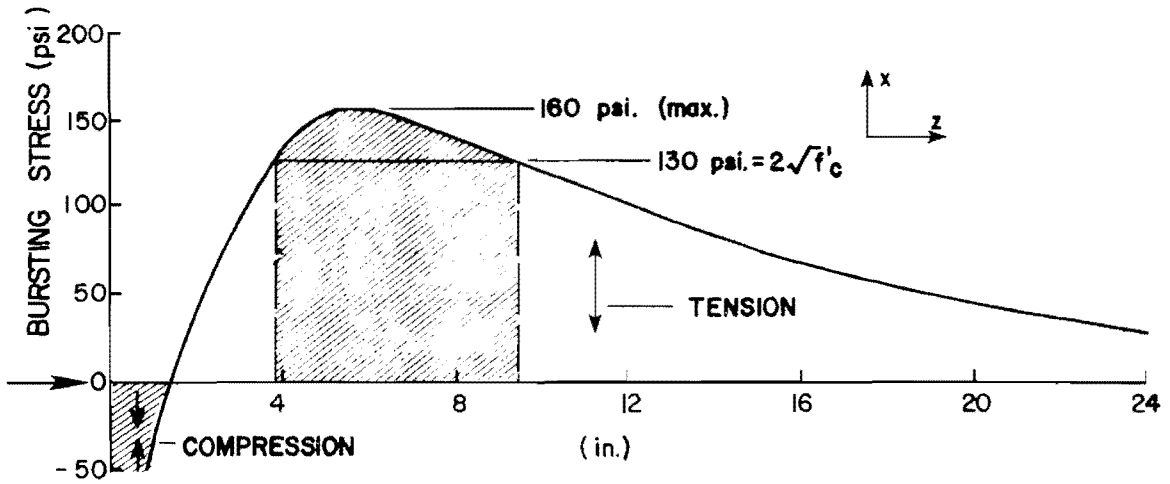

(b) Bursting stress distribution for t = 4-1/2 in. specimen along tendon path

Fig. 2.31 Orthogonal reinforcement design using 3D FEM analysis

were assumed cracked and required supplementary reinforcement capable of carrying the full tension to prevent further propagation of the tendon path crack. The reinforcement was designed to resist the force corresponding to the shaded portion of the bursting curve. To obtain a numerical value for this force, the shaded area was numerically integrated with the use of a polar planimeter and multiplied by the section width to obtain the total tensile force. Since the bursting stress decreases from a maximum along the tendon path to a lower value at the web face, the force thus calculated will be conservative. For example a 3-in. thick specimen with the bursting stress distribution for a tendon load of 25 kips, as shown in Fig. 2.31a, f'_c = 4300 psi, $2\sqrt{f'_c}$ = 130 psi would have an area of the shaded section of A = 1229 lb./in. The total force to be resisted is then F = 1229 × 3 in. = 3687 lb. Since the bursting stress distribution was calculated for a service load of 25 kips, the reinforcement was proportioned based on an allowable service load stress of $0.6f_y$. Using Grade 60 reinforcement (f_y = 60 ksi) the required steel area is

$$A_{steel} = 3687 \text{ lb}/36000 \text{ psi} = 0.102 \text{ in.}^2$$

The U-shaped stirrups were fabricated from 10 gage wire so that the area of each stirrup crossing the tendon path was

$$A_{stirrup} = [(0.135)^2\pi/4]2 = 0.02863 \text{ in.}^2$$

A spacing of 2 in. max was desired. Five 10 gage stirrups at 2 in. spacing from z = 2 in. to z = 10 in. would provide

$$A_{st\ total} = 5(0.02863) = 0.143 > 0.102 \text{ in.}^2 \quad \underline{OK}$$

By similar calculation, the same reinforcement was chosen for the 4-1/2 in. section.

For comparison, an alternate bursting stress curve from the two-dimensional finite element program was used to design the orthogonal reinforcement for a second set of specimens. Figure 2.32 shows

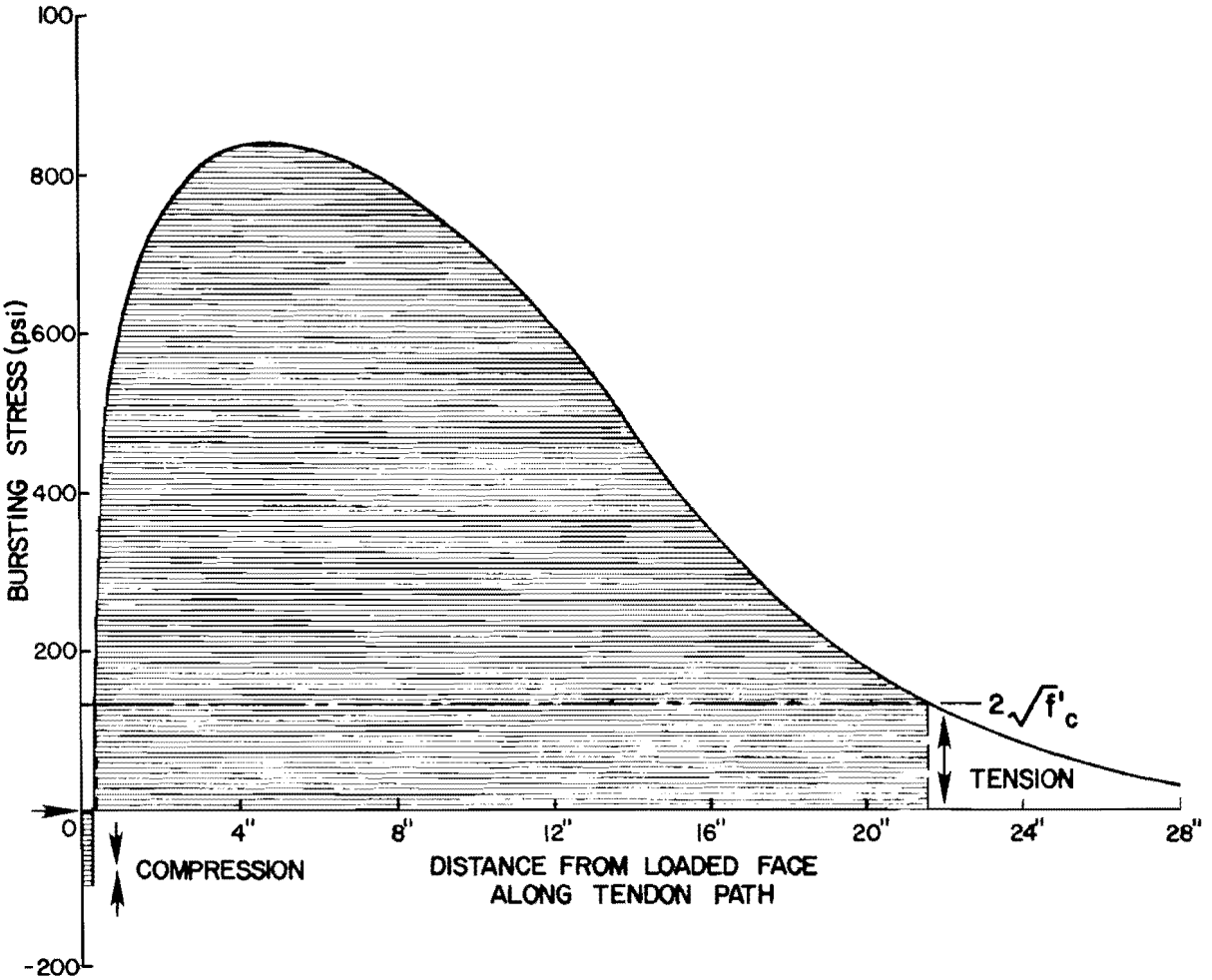

Fig. 2.32 2D-FEM analysis bursting distribution

the 2D bursting distribution used. The design procedure was the same otherwise. For the 3 in. thick section the total force to be resisted was 35,300 lb., a value nearly ten times that calculated using the three-dimensional analysis. This required eleven 6 mm (60 ksi) U-stirrups at 1.6 in. spacing. Similar calculations indicated the 4-1/2 in. section needed seventeen 6 mm U-stirrups at 1 in. spacing.

2.4.5.2 Spiral Reinforcement Design. In contrast to orthogonal reinforcement, spiral design for the anchorage zone could be likened to that of a spirally reinforced concrete column (see Fig. 2.33a and b) for which a detailed design procedure was readily available [11].

Figures 2.33c and d show that a lateral compressive confining stress f_2 will increase the allowable primary compressive stress f_1. The allowable value is given by:

$$f_1 = 0.85f'_c + 4.1f_2 \tag{2.3}$$

Figures 2.33e and f show that for a spiral of diameter D and pitch s the value for f_2 obtained from summation of forces is:

$$f_2 Ds = 2A_s f_s \tag{2.4}$$

$$\text{thus} \quad f_2 = \frac{2A_s f_s}{Ds} \tag{2.5}$$

combining this with Eq. 2.3 yields:

$$f_1 = 0.85f'_c + \frac{8.2A_s f_s}{Ds} \tag{2.6}$$

In the post-tensioned anchorage zone shown in Fig. 2.33b, f_1 is the post-tensioning load divided by the bearing area of the anchorage. For the 3-in. thick specimen a spiral diameter of 2 in. and a pitch of 3/4 in. were chosen somewhat arbitrarily for concrete placement. The tendon design load of P = 25 kips and the 2 in. square bearing plate require:

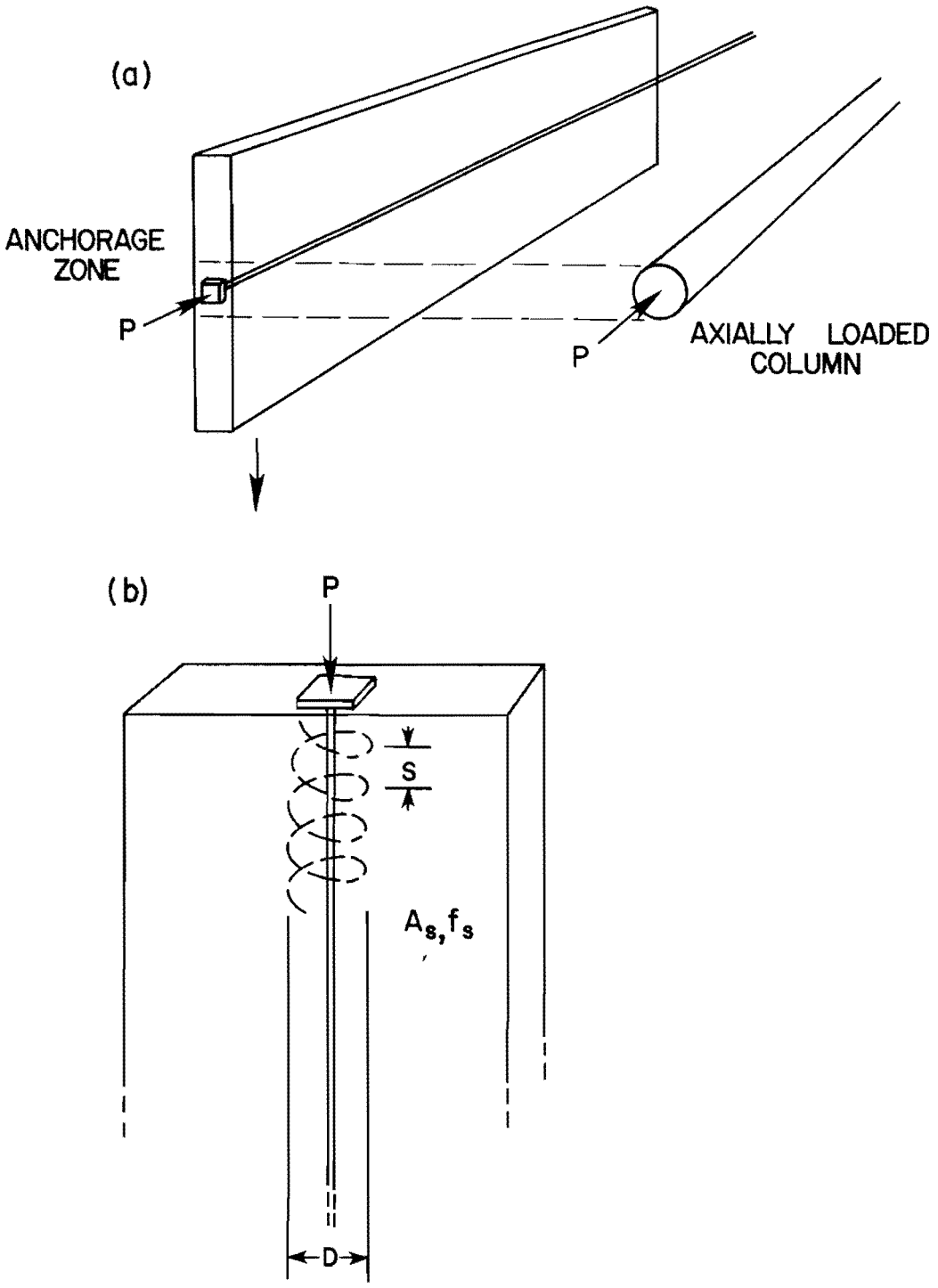

Fig. 2.33 Design of spiral reinforcement

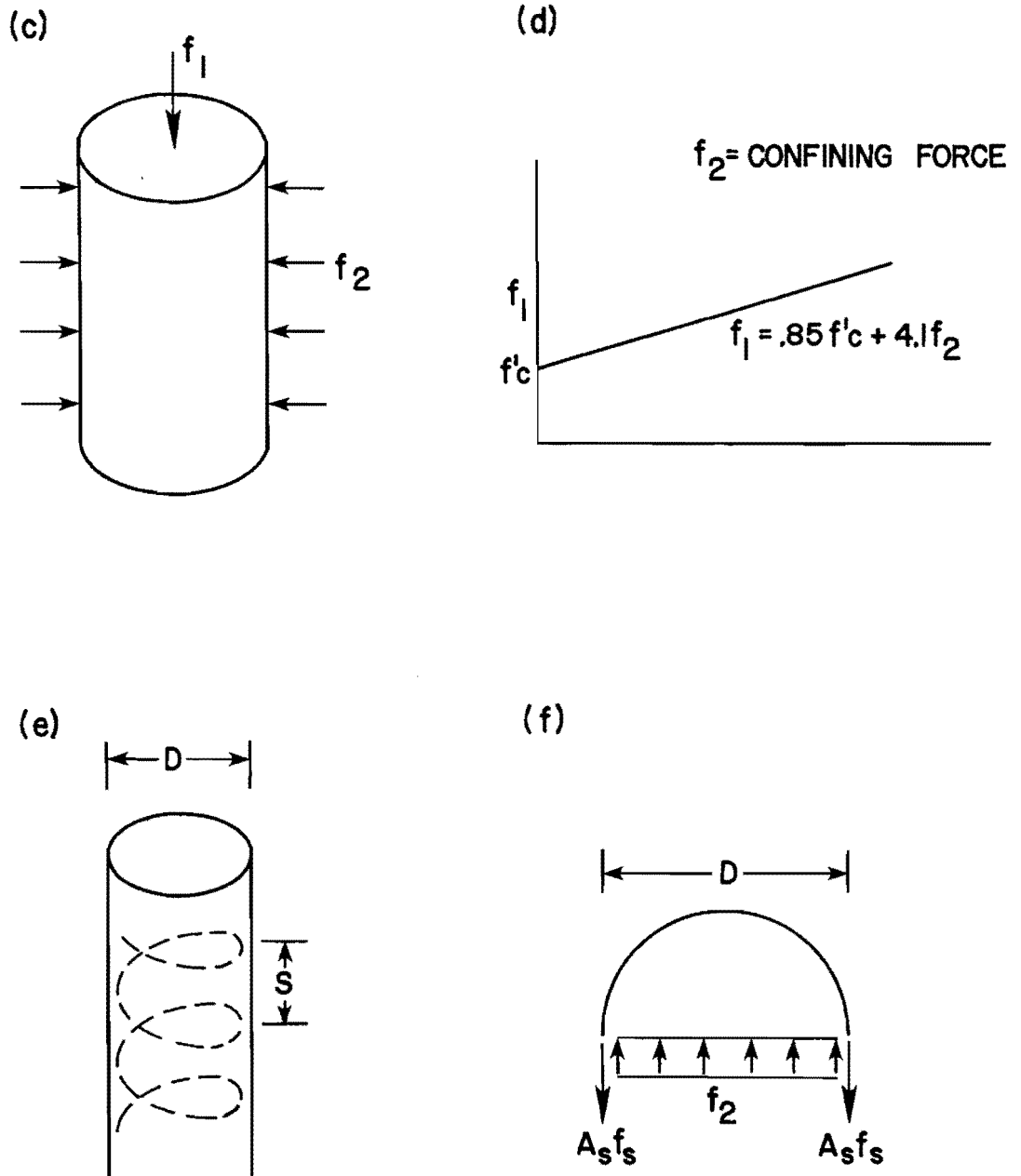

Fig. 2.33 (Continued)

$f_1 = 25k/4 \text{ in.}^2 = 6250 \text{ psi}$ (for a 2 in. × 2 in. anchor plate)

$f'_c = 4300 \text{ psi}$

$$A_s \text{ reqd.} = \frac{f_1 - 0.85f'_c}{8.2f_s} (Ds) \qquad (2.7)$$

for Grade 60 reinforcement $f_s = 0.6(60000 \text{ psi}) = 36000 \text{ psi}$

$$A_s = \frac{6250 - 4300(0.85)}{8.2(36000)} (2)(0.75) = 0.0132 \text{ in.}^2$$

The required diameter of the bar to be used in fabricating the spiral is thus

$$\frac{\pi d_{bar}^2}{4} = 0.0132 \text{ in.}^2$$

$d_{bar} = 0.130$ in. or approximately 10 gage.

Use 10 gage wire (60 ksi), 2 in. diameter spiral at 3/4 in. pitch. The spiral was arbitrarily chosen to be 6 in. long for this series.

Identical reinforcement was used for the 4-1/2 in. section. As a comparison, a spiral with the same diameter, pitch and length, but fashioned from 13 gage wire instead of 10 gage was used in two companion specimens. This represented a 50 percent reduction in reinforcement.

2.4.5.3 Passive Reinforcement Series. It was believed that the addition of the supplementary reinforcement would substantially increase the ultimate loads. There was a strong possibility the increase might be enough to rupture the tendon before failure of the anchorage zone. To minimize the ultimate loads to prevent the tendon capacity from being exceeded, it was decided to choose the specimen configuration which had yielded the lowest cracking and ultimate loads. This was the cone-type anchorage at an eccentricity

of e = 0.6a with a straight tendon. Other specimen details were identical.

Reinforcement and test data are given in Tables 2.9, 2.10, and 2.11. Figure 2.34 shows typical placement of orthogonal and spiral reinforcement prior to casting. Note that considerably more supplementary steel is provided in the orthogonal reinforcing scheme.

Figure 2.35 shows the cracking trends observed for the varied reinforcing schemes as a function of the total ultimate load capacity of the supplementary reinforcement crossing the tendon axis. This places the results in perspective as to the efficiency of the reinforcement. Note that minor amounts of reinforcement significantly increase the cracking load. For the thinner web section, the spiral shows a markedly better performance than orthogonal reinforcement. In fact, a relatively light spiral (13 gage) cracked at a 23 percent higher load than a companion orthogonal reinforcement specimen with seven times as much tensile force capacity. ($A_s f_y$ = 38.5 kips vs. 5.52 kips for the spiral). For the t = 0.45a case, the difference between spiral and orthogonal reinforcement is lessened somewhat, possibly since the spiral confines less of the anchorage zone. For both reinforcing schemes the maximum achievable cracking loads are being approached asymptomatically and extremely large amounts of reinforcement appear to be unwarranted.

Figure 2.36 illustrates the ultimate behavior of specimens with supplementary anchorage zone reinforcement. Addition of supplementary reinforcement greatly enhanced ultimate loads and ductility. The spiral clearly outperformed conventional orthogonal reinforcement. The light spiral (13 gage) developed an ultimate load 52 percent higher than the heaviest orthogonal mesh used in companion specimens for a thickness of t = 0.3a. For the case of t = 0.45a the 13 gage spiral developed an ultimate load 18 percent higher than the orthogonal maximum even though eleven times as much supplementary steel

TABLE 2.9

PASSIVE REINFORCEMENT SERIES DATA

	Specimen ID	Anchor Type	Supplemental Reinforcement	t	P_{cr} (kips)	P_{ult} (kips)	f'_c (psi)	f_{sp} (psi)
ORTHOGONAL	M3A-4	Cone	5-10 Gage Stirrups @ 2" spacing	0.3a*	19	21	3766	509
	M3B-4	Cone	11 6 mm Stirrups @ 1.6" spacing	0.3a	19	22	3766	509
	M4A-4	Cone	5-10 Gage Stirrups @ 2" spacing	0.45a	24	26	4140	534
	M4B-4	Cone	17 6 mm Stirrups @ 1" spacing	0.45a	28	32	4140	534
SPIRAL	M5A-4	Cone	13 Gage Wire 3/4" Pitch 2" Diameter	0.45a	25	37	4250	521
	M5B-4	Cone	10 Gage Wire 3/4" Pitch 2" Diameter	0.45a	25	36	3696	486

Table 2.9 (continued)

	Specimen ID	Anchor Type	Supplemental Reinforcement	t	P_{cr}	P_{ult}	f'_c	f_{sp}
	M6A-4	Cone	13 Gage Wire 3/4" Pitch 2" Diameter	0.3a	24	34	4250	521
SPIRAL	M6B-4	Cone	10 Gage Wire 3/4" Pitch 2" Diameter	0.3a	25	32	3696	486
	M8D-4	Plate	10 Gage Wire 3/4" Pitch 2" Diameter	0.3a	46	49	4244	707

*a = 10" all specimens.

TABLE 2.10

NORMALIZED RESULTS-PASSIVE REINFORCEMENT SERIES

Specimen ID	Tendon Path		Upper Diagonal		Lower Diagonal			
	$P_{cr}/\sqrt{f'_c}$	P_{cr}/f_{sp}	P_{cr}	P_{ud}/f_{sp}	P_{cr}	P_{ud}/f_{sp}	$P_{ult}/\sqrt{f'_c}$	P_{ult}/f_{sp}
M3A-4	309	37.3	21	41.2	21	41.2	342	41.0
M3B-4	309	37.3	22	43.0	22	43.0	358	43.0
M4A-4	373	44.8	25	46.8	25	46.8	404	48.6
M4B-4	435	52.0	28	52.4	28	52.4	497	59.9
M5A-4	383	48.0	34	65.2	34	65.2	567	71.0
M5B-4	411	51.4	33	67.9	36	74.0	592	74.0
M6A-4	368	46	33	63.3	32	61.4	522	65.2
M6B-4	411	51.4	31	63.7	31	63.7	526	65.8
M8D-4	706	65.0	46	65.0	46	65.0	752	69.4

TABLE 2.11

REINFORCEMENT RATIOS--MODEL SERIES*

Specimen ID	Reinforcement	t	Reinforcement Ratio (%) ρ	$A_s f_y$ (kips)
M3A-4	10 Gage Stirrups	0.3a	0.48	8.58
M3B-4	6 mm Stirrups	0.3a	1.83	38.5
M4A-4	10 Gage Stirrups	0.45a	0.32	8.58
M4B-4	6 mm Stirrups	0.45a	1.95	59.5
M5A-4	13 Gage Spiral	0.45a	0.39	5.52
M5B-4	13 Gage Spiral	0.45a	0.85	11.08
M6A-4	13 Gage Spiral	0.3a	0.58	5.52
M6B-4	10 Gage Spiral	0.3a	1.27	11.08
M8D-4	10 Gage Spiral	0.3a	1.27	11.08

$$\rho = \frac{A_s}{t \cdot s} \quad ; \qquad A_s = \text{total steel area}$$

t = web thickness

s = spiral pitch or stirrup spacing

*Percent steel crossing tendon axis in bursting region.

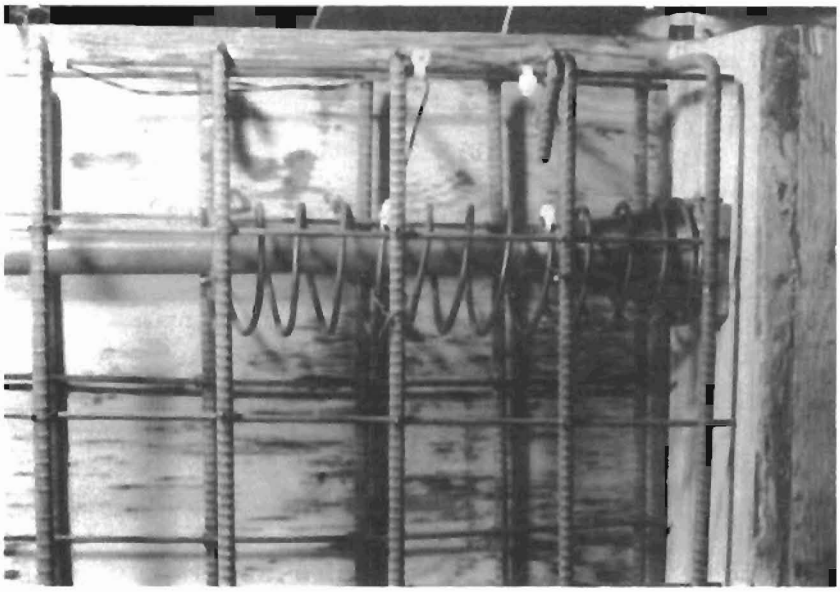

(a) "Heavy" spiral reinforcement

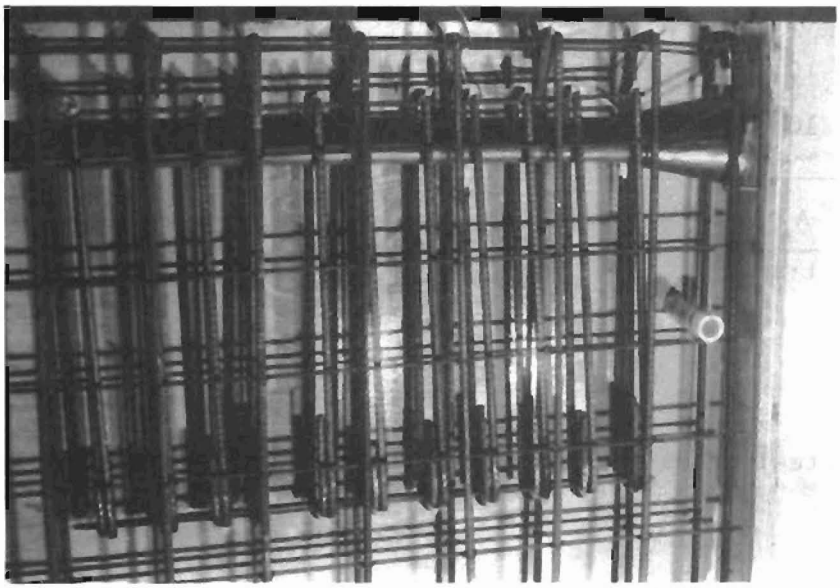

(b) "Heavy" orthogonal reinforcement

Fig. 2.34 Passive reinforcement for models

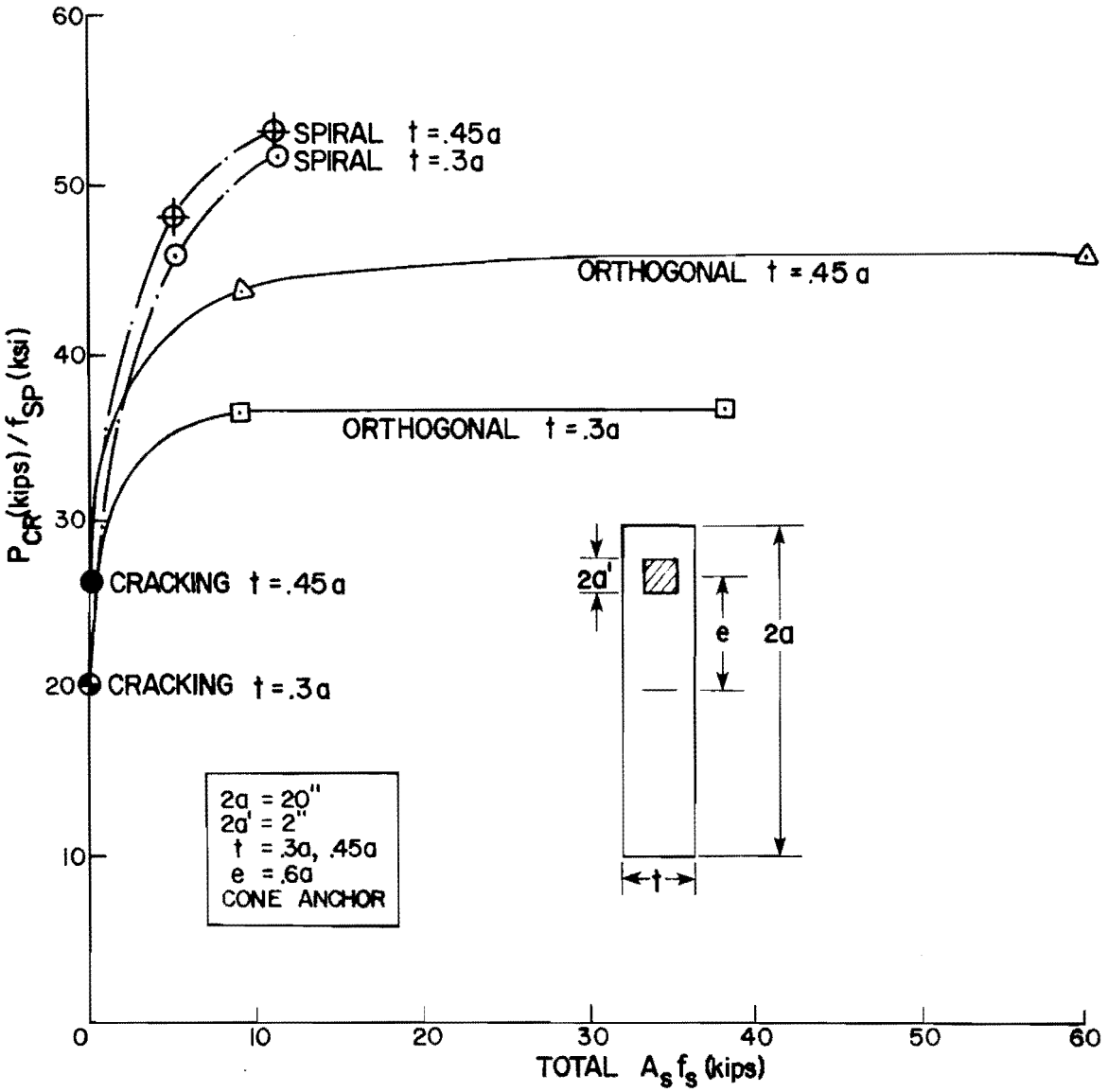

Fig. 2.35 Normalized cracking loads--reinforcement series

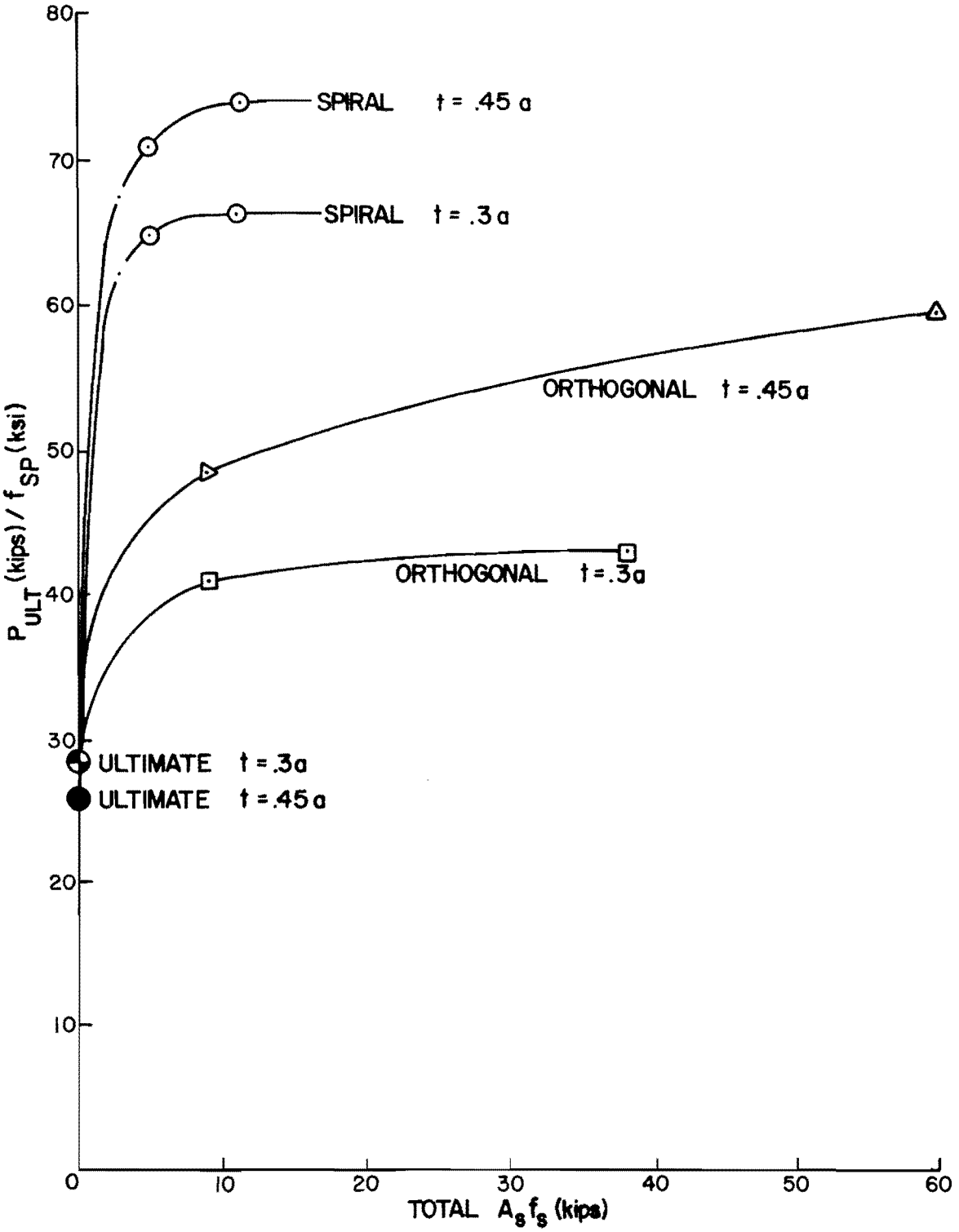

Fig. 2.36 Normalized ultimate loads--reinforcement series

area was used in the orthogonal specimen. Spiral reinforced specimens, on the average developed ultimate loads 248 percent greater than those required to fail the unreinforced specimens. The asymptotic effect--i.e., decreased gains for larger amounts of reinforcement--is also evident in the ultimate strength trends. Two conclusions that are readily apparent are:

(1) Spiral reinforcement is the safest and most efficient passive method of reinforcement that can be used to control anchorage zone failures.

(2) The spiral need not be extremely heavy. The 13 gage spiral with less than half the steel area performed nearly as well as the 10 gage spiral.

Table 2.12 presents crack width data taken at the beginning of tendon path cracking and recorded for every load stage where a change in the crack pattern was noted. Crack readings were taken on both sides of the specimen, and as the pattern was usually symmetric, the data at similar grid lines were averaged. Due to the fact that for different reinforcing schemes cracking occurred at widely dissimilar loads, the only way to objectively examine the performance of one reinforcing scheme with respect to another was to normalize the crack widths at P_{cr} by the cracking load. These normalized crack widths are listed in Table 2.13. Figures 2.37 and 2.38 illustrate the effect of supplementary reinforcement on crack width distributions along the tendons.

The results are quite interesting. Crack widths are clearly lowest for spiral reinforcement and the lighter spiral apparently performs quite well. Orthogonal reinforcement does not do as well as the spiral, although increasing the amount of orthogonal steel does reduce the crack widths even if it does not reduce the cracking load significantly. The light spiral appeared to perform best when the cover concrete was at a minimum. This seems to echo results from

TABLE 2.12

AVERAGE CRACK WIDTHS--REINFORCEMENT SERIES

(In 1/1000 in. Units)

Specimen	Load(kips)	GRID LINE 1	2	3	4	5	6
M1B-4	10	1.75	2	1.5	.5		
	12	2.75	3	2.25	.75		
M2B-4	13	2	2.5	1.5	2	.5	
M3A-4	19	1.5	3	2	1	.5	
	20	2.75	3	2.75	1.5	.5	
M3B-4	19	2.25	1.5	1.5	.625		
	20	2.5	1.75	1.75	1	.25	
	21	3	2	2	1.25	.5	
M4A-4	24	2	2	3	2.5	2.25	.75
	25	2	2.25	3.5	2.5	2.5	.75
M4B-4	28	1.5	1.75	1.5	1		
	30	2	2	2	1.5	1	.25
M5A-4	25	.25	1.5	.875	.5		
	27	1	2	1	.75		
	29	1.5	3	2.5	1.5	.5	
	31	2	3	2.75	1.75	.75	
	33	2.25	3.75	2.5	2	.75	
	34	2.5	3.75	2.5	2	.75	
	36	3	4.38	2.5	2.5	.75	
M5B-4	25	.625	1.5	.5	.25		
	27	.75	1.75	1	.25		
	30	1.25	2.5	1.5	1	.25	
	33	2	2.5	2	1.5	1	
M6A-4	25	1	.125	.25			
	27	1.5	.75	1.5	2		
	29	2.25	1.5	1.75	2		
	31	2.5	2	1.75	2.5		
	33	4	2.5	2.75	.125		
M6B-4	25	1.25	1.75	1.25	.75		
	27	2	2.5	1.25	1		
	29	2.25	2.75	1.75	1.5	.25	
	31	7	4	2.25	1.75	1	

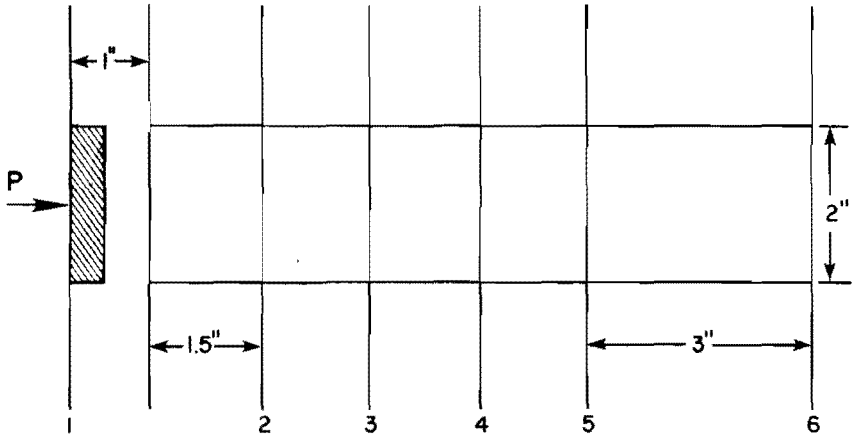

GRID LINE SYSTEM FOR CRACK REFERENCE

TABLE 2.13

AVERAGE CRACK WIDTHS NORMALIZED TO P_{cr}
(ALL CRACK WIDTHS IN 1/1000 IN. UNITS)

	Average Crack Width ÷ P_{cr} (kips)			t = 0.3a all specimens	
Grid Line	M1B-4	M3A-4	M3B-4	M6B-4	M6A-4
1	0.175	0.079	0.118	0.05	0.042
2	2.0	0.158	0.079	0.07	0.005
3	0.15	0.105	0.079	0.05	0.011
4	0.05	0.053	0.033	0.03	
5		0.026			
6					

	Average Crack Width ÷ P_{cr}			t = 0.45a all specimens	
	M2B-4	M4A-4	M4B-4	M5B-4	M5A-4
1	0.154	0.083	0.054	0.025	0.01
2	0.192	0.083	0.0625	0.06	0.06
3	0.115	0.125	0.054	0.02	0.035
4	0.154	0.104	0.036	0.01	0.02
5	0.038	0.094			
6		0.031			

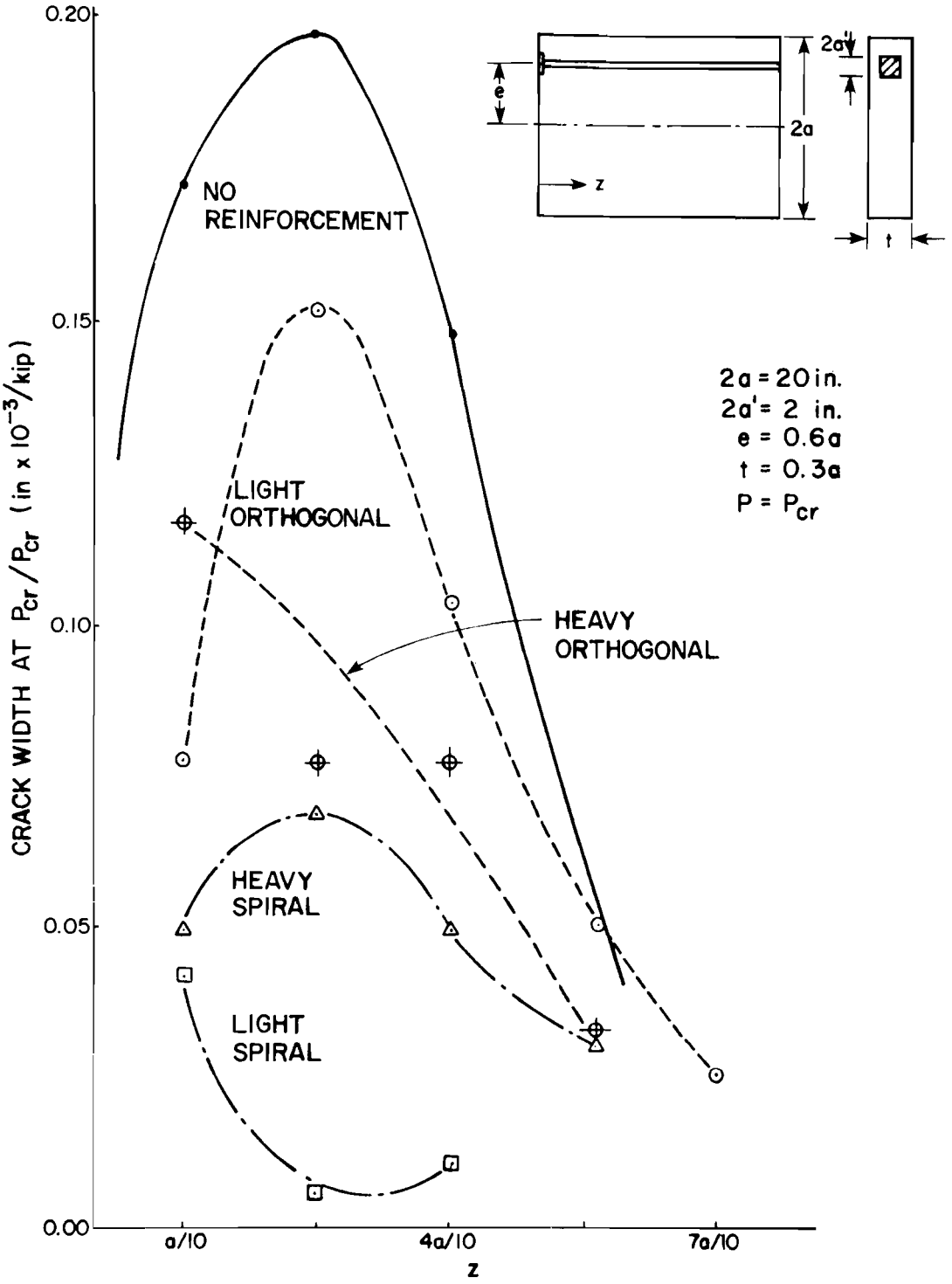

Fig. 2.37 Crack widths normalized to P_{cr}, t = 0.3a

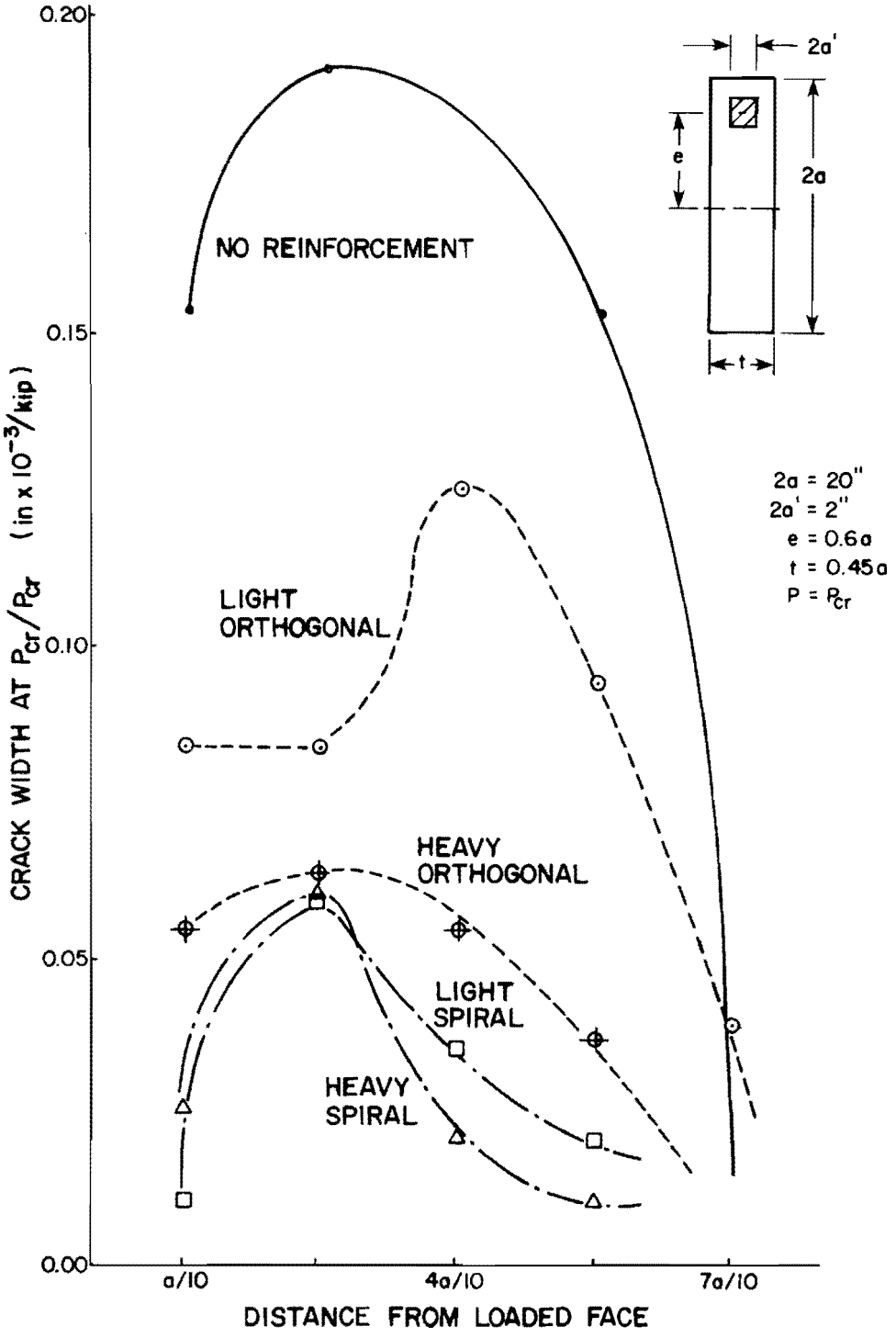

Fig. 2.38 Crack widths normalized to P_{cr}, t = 0.45a

other concrete crack control studies, which indicate the reinforcement for controlling side face crack widths should be placed as close as possible to the face while satisfying cover requirements. Such studies [12] also indicate that large numbers of smaller diameter bars produce a finer distribution of smaller cracks. Bearing this in mind it would seem that the optimal spiral would be one having a confining effect to satisfy Eq. 2.7 but using a finer pitch. In actual practice the clear pitch could not be less than the maximum aggregate size. For the $t = 0.3a$ tests the 2 in. diameter spiral was the maximum diameter that would fit in the shear reinforcement cage, and as such represents the optimum diameter. For wider cages the spiral diameter should be increased so as to place the reinforcement closer to the face. This analogy is limited to thin web applications.

CHAPTER 3

FULL-SCALE I-SECTION TESTS

3.1 Introduction

After completion of the rectangular model series reported in Chapter 2 and the calibration of the 3D FEM analytical program reported in the first report [1], a series of full-scale tests using prototype hardware and dimensions was run. Variables were selected to examine in greater detail certain behavioral patterns observed in the models. Spiral reinforcement, particularly for inclined tendons, was of primary interest. Since many commercial anchors apparently successfully developed over twice the bearing stress permitted by American codes, that variable was examined. Finally, the use of transverse prestressing to precompress the anchorage tension zones showed great promise and were investigated.

For identification a specimen numbering system similar to that used in the first model series was employed:

FS(N)(M)

where FS = full-scale test.

N = specimen number (1 through 5).

M = end of specimen being tested; each specimen had two ends--A and B.

3.2 Design of Prototype Specimen

3.2.1 Dimensions. The prototype specimen used for full-scale testing differed slightly from that shown in Fig. 2.2. For stability during testing, a wider base flange was provided. Since during the tests of the curved tendon models a crushing problem had

arisen at the dead end where the tendon was highly eccentric, this was controlled by an enlarged reinforced top flange. To maintain a consistent relationship with the box girder segment shown in Fig. 2.1, the redesigned prototype consisted of an "I" section, with the enlarged top and bottom flanges proportioned as in the box girder. The final geometry is detailed in Fig. 3.1.

3.2.2 Reinforcement. In detailing the reinforcement, minor changes were made from procedures used in the models. To minimize difficulties with bends and tolerances, slightly smaller bars at a closer spacing to maintain the same percentage were desirable. The final choice of reinforcement consisted of #7 U-stirrups at 13 in. rather than #8 U-stirrups at 15 in. with #3 longitudinal bars at 10.5 in. spacing (Fig. 3.1c). All reinforcing was Grade 60 (f_y = 60 ksi).

3.2.2.1 Supplemental Anchorage Zone Reinforcement. Four specimens with 30 degree inclined tendons also had Grade 60 non-deformed spiral reinforcement along the tendon path. Two of the spirals were fabricated from 3/8 in. ϕ rods and two from 1/2 in. ϕ rods (both f_y = 60 ksi). As shown in Fig. 3.2 the diameter of the completed spirals was 8 in. with a pitch of 2 in. "Short" spirals had an overall length of 13 in. while "long" spirals were 26 in. in length. The base of the spirals was positioned against the face of the anchor.

Two specimens, also with 30-degree inclined tendons, were supplemented using active reinforcement by the use of vertical (transverse) web prestressing tendons. Two 0.5 in. ϕ 270 ksi tendons were used for each specimen and were located side by side (straddling the main tendon duct) at predetermined distances from the end face.

3.2.3 Fabrication. The forms were constructed of 3/4 in. plywood with 2 x 4 studs and whalers and 12 in. snap ties at 2 ft. spacing both horizontally and vertically. The shear reinforcement cage was assembled using standard wire twist ties. Insert

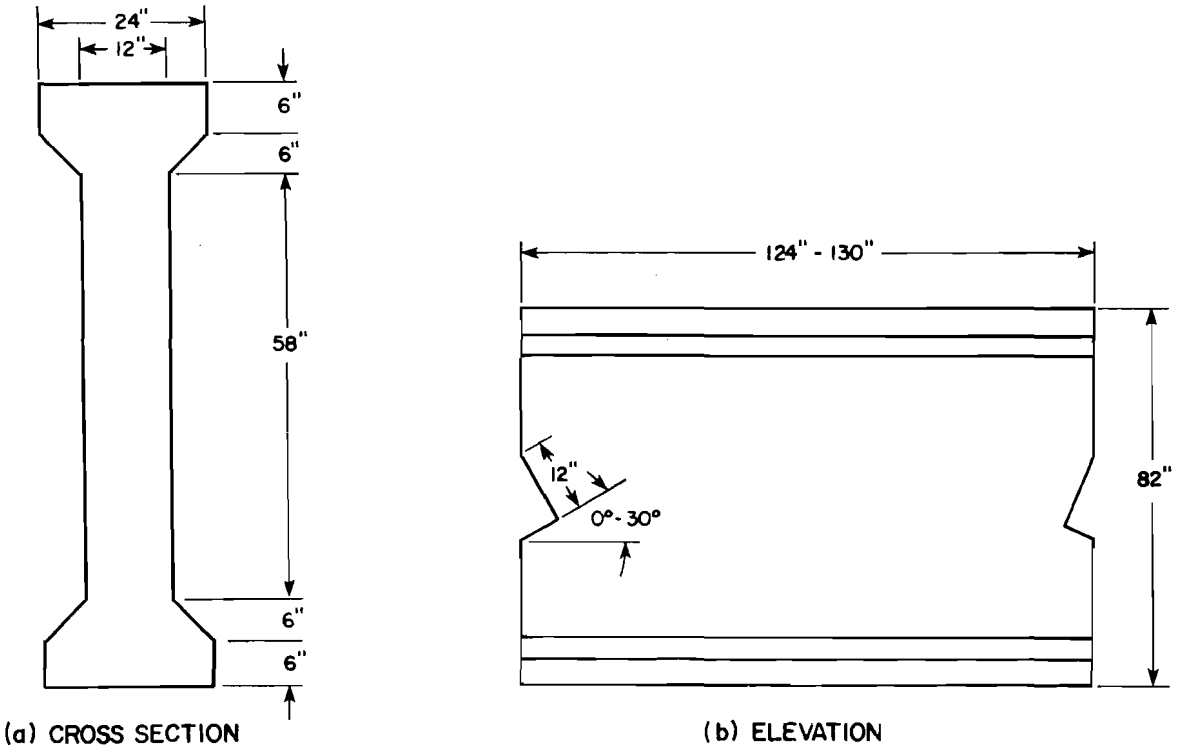

Fig. 3.1 Full-scale specimen details

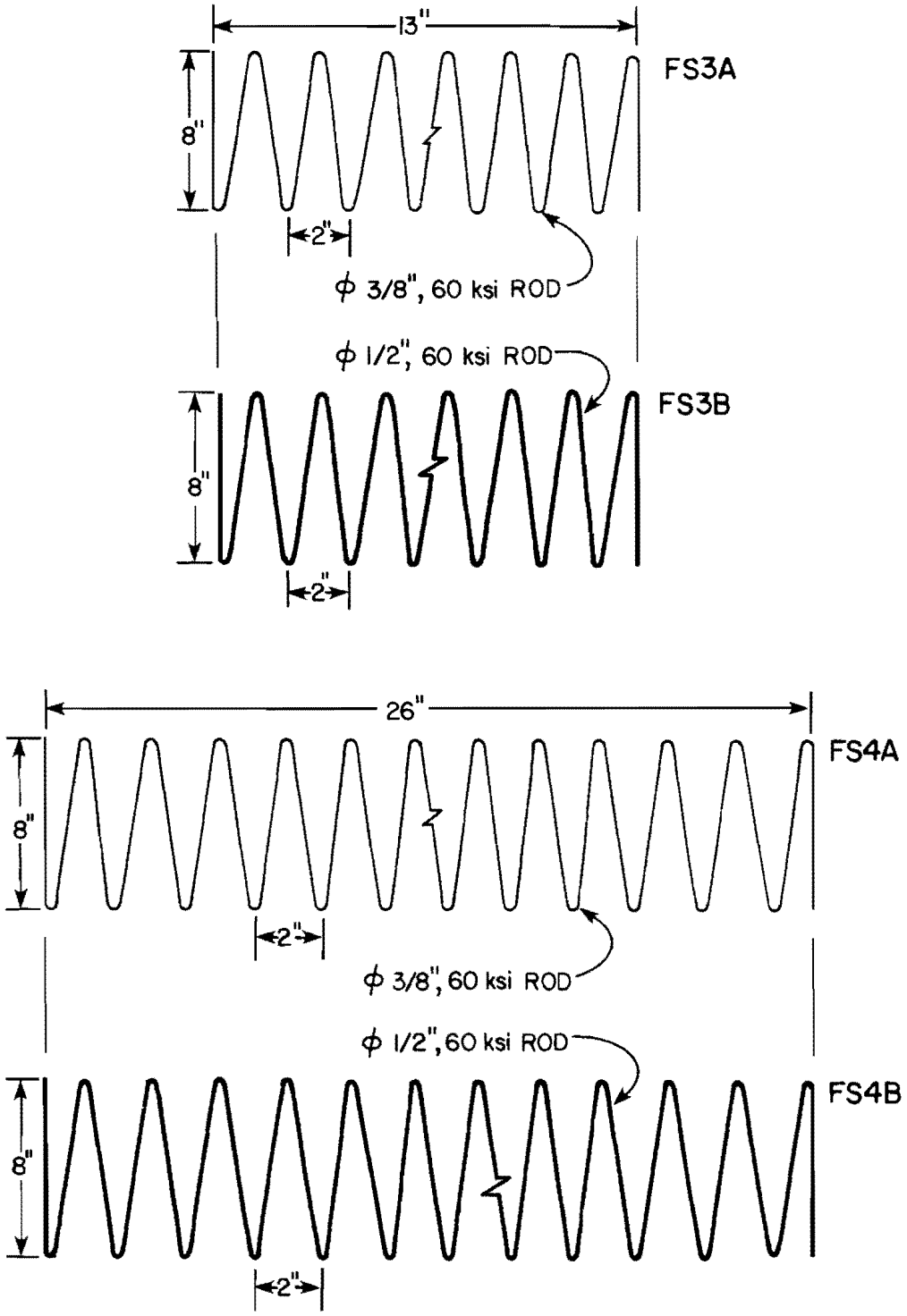

Fig. 3.2 Spiral reinforcement details

strainmeters were wired into the cage at predetermined locations. The cage was placed in the form with only one side form erected. Tendon ducts were then inserted and the end forms with the pre-attached anchorage hardware were bolted into place. All anchors were commercial bearing-type anchors with a lightweight trumpet, as shown in Fig. 3.3. The anchors were rated for 12-1/2 in. ϕ 270 ksi strands. The tendon duct was aligned in a continuous curve and wired into position. The entire form was sealed and bolted. Casting was done in five lifts using external and internal form vibration. The concrete mix used was Texas Highway Department Type H superstructure concrete with a maximum aggregate size of 3/4 in. Proportions were:

Mix Proportions of Concrete

Water	312 lb./cu. yd.
Cement (Type I)	520 lb./cu. yd.
Fine Aggregate	1179 lb./cu. yd.
Coarse Aggregate (max 3/4 in.)	1930 lb./cu. yd.
ASTM C494 Retarder	25 oz. (fluid)

Required Slump 5 in.

Required Strength $f'_{c_{28\text{-day}}}$ = 4000 - 4500 psi

Twenty standard test cylinders were cast for each specimen. Following a 7 to 10 day curing period, the forms were stripped and the specimen moved either to the testing location or a holding yard. All specimens were allowed to cure a full 28 days before testing. Figure 3.4 illustrates the fabrication sequence.

3.3 Experimental Procedures

3.3.1 Variables. The major variables investigated in the full-scale tests were:

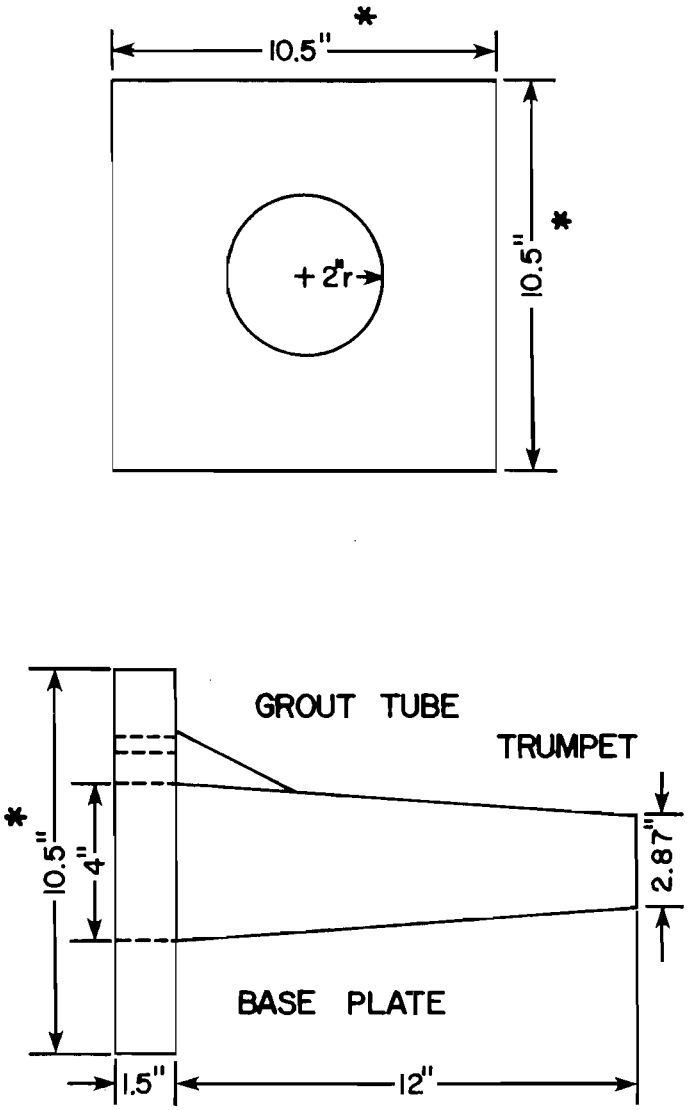

Fig. 3.3 Commercial plate anchor details for full-scale tests

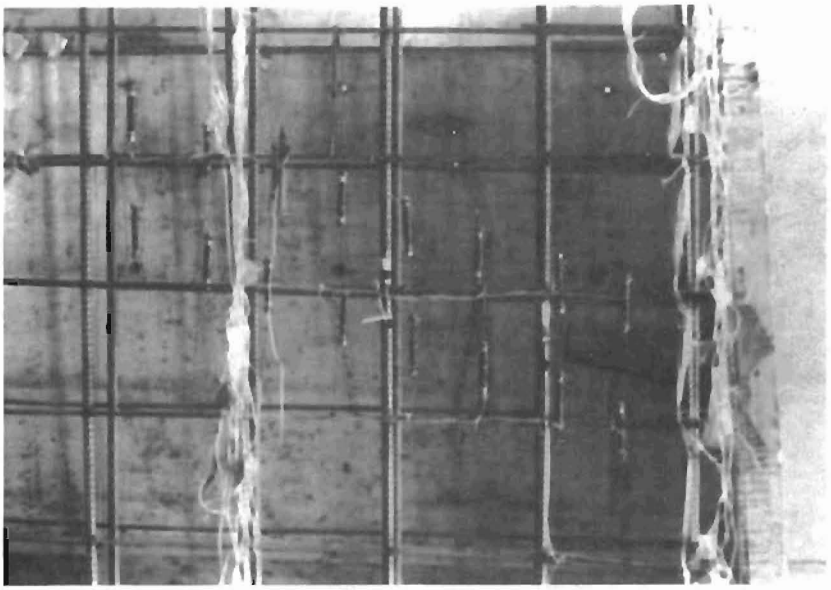

(a) Insert strainmeters

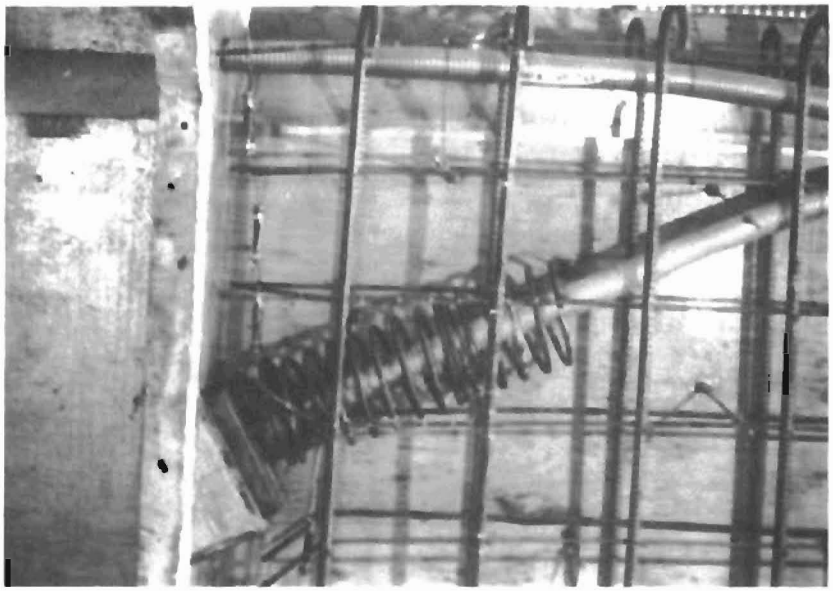

(b) Spiral reinforcement

Fig. 3.4 Fabrication of full-scale specimens

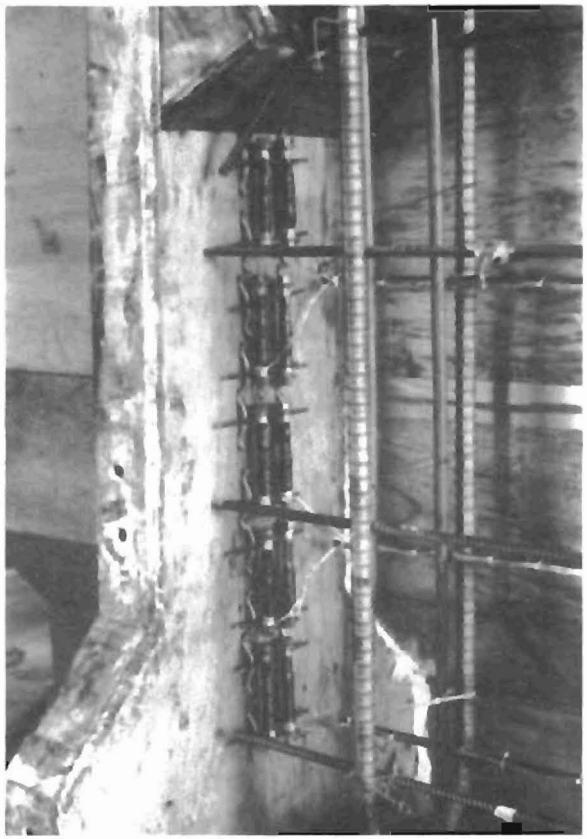

(c) Spalling strainmeters mounted on end form

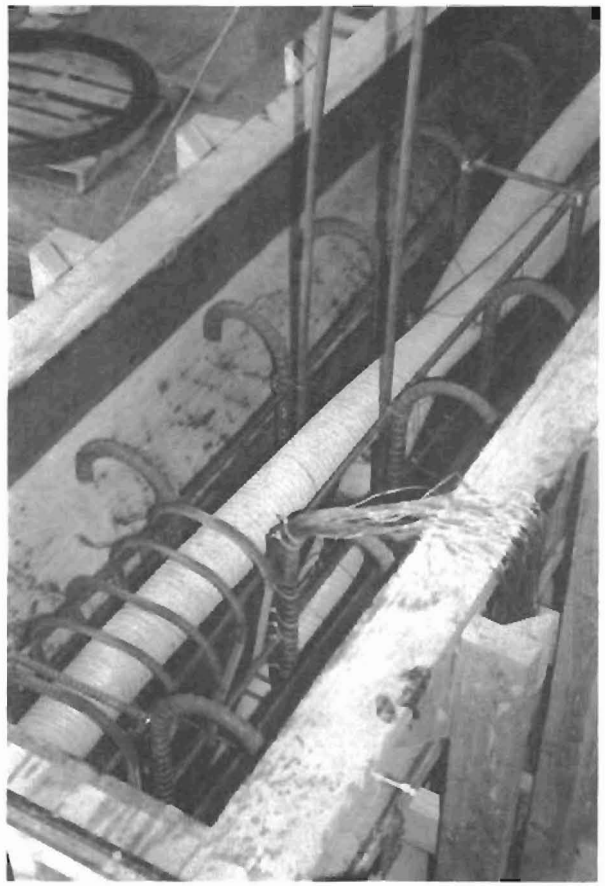

(d) Top view of closed forms showing lateral post-tensioning tendons and primary tendon duct

Fig. 3.4 (continued)

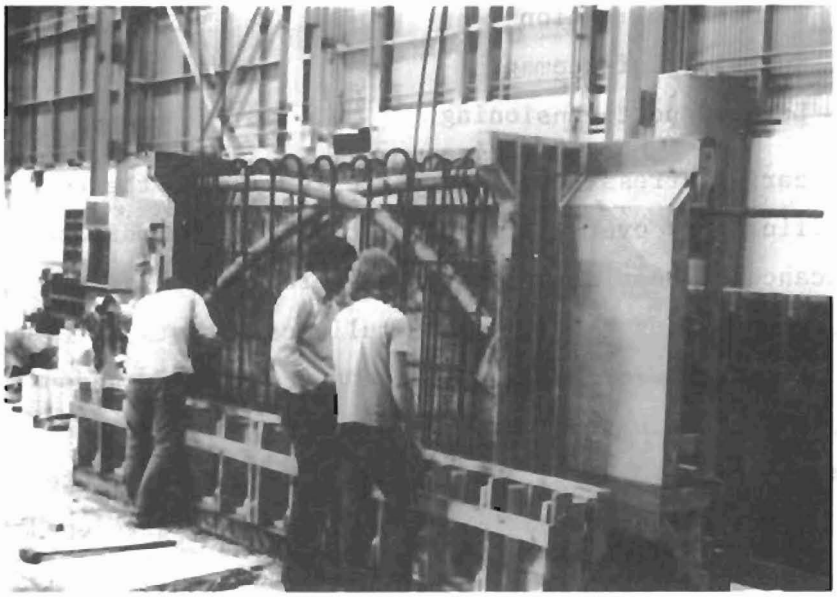

(e) Bottom of side form closed

(f) Top of side form lifted into place

Fig. 3.4 (continued)

a. Bearing stress
b. Tendon inclination
c. Spiral reinforcement
d. Lateral post-tensioning

a) Bearing stress--The literature review and the conflict in design specifications over allowable bearing stress indicated that the significance of bearing stress on anchorage behavior was not fully understood. Thus the first two full-scale tests were designed to investigate the performance of straight concentric tendon anchors with widely different bearing areas. At a prototype design tensioning load of 396 kips ($0.8f_{pu}$), the standard commercial plate anchor (10-1/2 in. × 10-1/2 in.) used in one test specimen developed a rated bearing stress of 4053 psi. For the second specimen the same type commercial plate anchor was cut down to 8-1/2 in. × 8-1/2 in. At the design load of 396 kips, the reduced anchor would develop 6635 psi or 1.64 times the commercially rated bearing stress. Both values were substantially greater than the AASHTO 3000 psi maximum.

b) Tendon inclination--A series of three specimens was designed to study in further detail the performance of the commercial anchorage hardware as affected by inclination. Angles of 0, 15, and 30 degrees were chosen.

c) Spiral reinforcement--Passive reinforcement in the form of spirals were used to check findings from the model specimens concerning the volumetric spiral percentage, and to examine the effect of the length of the spiral.

d) Active reinforcement in the form of lateral post-tensioning was investigated with a twofold purpose. The first was to compare its efficiency in controlling anchorage zone cracking with that of passive reinforcement such as provided by the spiral. Secondly, it was used to confirm a spalling initiation failure which will be presented in the final report. An extensive series of computer analyses was

performed to locate the optimum position for lateral prestress to achieve the following conditions in the anchorage zone:

(1) To precompress the bursting stresses as much as possible, while permitting end face spalling stresses to remain virtually unaltered.

(2) To precompress the tensile spalling stresses as much as possible, while permitting the tendon path bursting stresses to remain the same.

These tests were designed to directly address the major questions suggested by the behavior observed in the first model series and accompanying computer simulations. Were transverse bursting tensile stresses initiating tendon path cracking as believed by most previous researchers or was, in reality, a more complex mechanism triggered by end face tensile stresses which formed a wedging cone of concrete after an internal shear failure?

3.3.2 Instrumentation

3.3.2.1 Insert Strainmeters. With the success of the micro insert strainmeters in the model series, a larger version was developed for use in the full-scale specimens, as shown in Fig. 3.5. The details were identical to those used in the micro strainmeters except that a 4 in. long gage length 3/8 in. diameter aluminum bar and 3/8 in. paper-backed strain gages were used. This made fabrication of the gages much easier, and lead wire connections were more dependable. All specimens were instrumented to measure spalling and bursting distributions and an average of 30 to 40 gages were used per specimen (test). Calibration curves showed that for most actual tests gage strain never exceeded the linear region.

3.3.2.2 Surface Strain Gages. A grid of mechanical extensometer points was glued along the tendon path using an 8 in. gage length rather than the 2 in. used in the models. An 8 in. Berry gage was used in testing. Although this gage has a supposed accuracy of 12.5

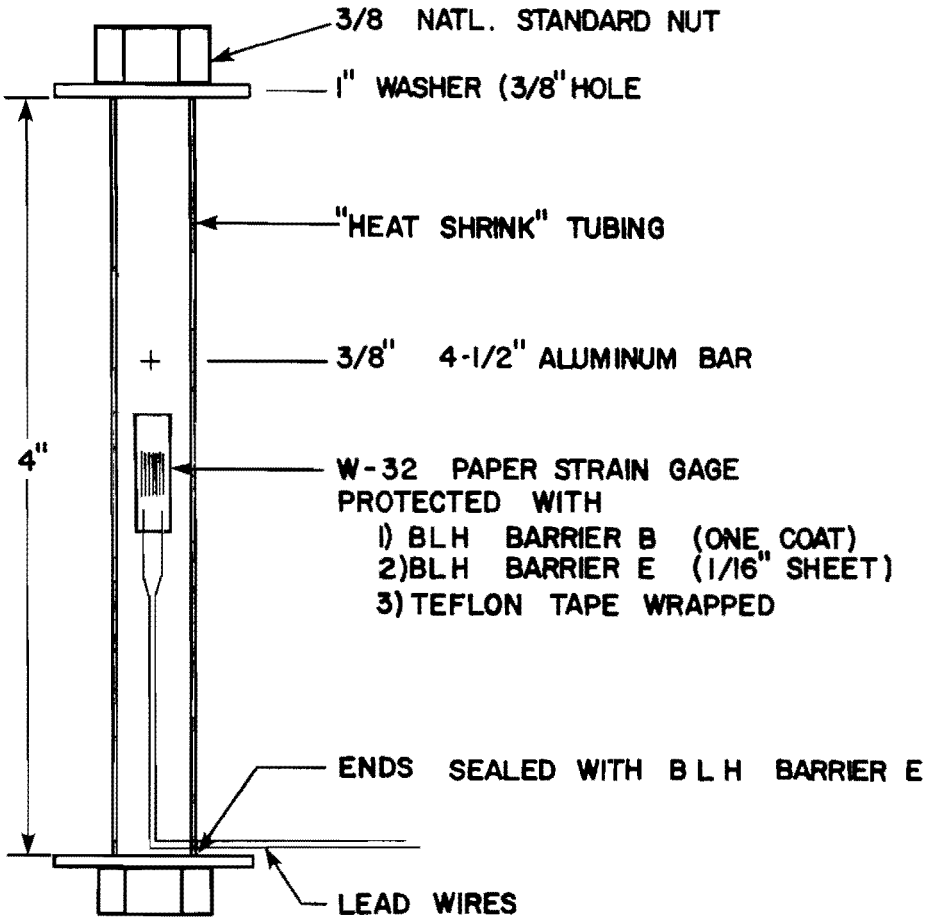

Fig. 3.5 Full-scale insert strainmeter details

microstrain, variations of as much as 100 microstrain between successive readings of a particular set of points for a given load were observed. This made the results of the surface gages so unreliable they are not included in this report.

3.3.2.3 Crack Readings. A grid work of vertical lines at 8 in. horizontal spacing was marked on both sides of the specimens and crack widths recorded to the nearest 1/1000 in. using a 60 power microscope. Crack readings were recorded whenever a visible change took place in the crack pattern.

3.3.2.4 Load Monitoring. The primary post-tensioning load was controlled using two calibrated 10,000 psi pressure transducers and two 10,000 psi helicoid pressure gages. In order to determine friction loss along the tendon, a load cell bank was incorporated in the far end dead man anchor. Lateral post-tension loads were monitored using centerhole load cells and checked by pressure gage readings.

3.3.3 Test Procedures

3.3.3.1 The Loading System. The anchors were again loaded as in actual usage by stressing of a tendon passing through the specimen. The full-scale specimens were designed to replicate a typical box girder web section, and hence the post-tensioning hardware was chosen on the same basis. For the commercial bearing type anchor used, the maximum tendon size was a 12 strand (F_{pu} = 496k) tendon in a 2-1/2 in. ID flexible duct. This was the same size tendon used in the Corpus Christi bridge project where the cracking problem was first noticed. Since cracking in those box sections had occurred at a load level below the maximum tensioning load (P = $0.8F_{pu}$), and since most of the orthogonally reinforced models had failed at loads only slightly above cracking, it was felt that this loading system, together with an available 200 ton ram would be sufficient to achieve ultimate load. However, shortly after cracking

occurred in the first two specimens (FS1A, FS1B), the ram capacity was reached and the test had to be stopped. A 500 ton centerhole ram was obtained and the tests continued. Upon reloading, the tendon failed at the conical grips in the pulling head. A new pulling head and different chucks were tried but with the same results. At this point, a careful reassessment was made of the anticipated ultimate loads, and the changes in the loading system which would be required to achieve them. The duct system was enlarged to 3-1/2 in. ID (sufficient for twenty-six 1/2 in. strands) for all new specimens to be cast. For those specimens which had already been cast using the 2-1/2 in. ID duct, it was found that by removing the flexible metal tubing, seventeen 1/2 in. strands could be drawn through to develop nearly 50 percent more load. The final loading system is shown in Fig. 3.6. The main ram was driven by a continuous flow electric console pump, while lateral post-tensioning rams used hand-operated pumps.

3.3.3.2 Data Acquisition. Data acquisition for the full-scale tests was similar to the model studies, but on an expanded basis. Strain gages were connected to a VIDAR data acquisition system. Gage scans were taken at each load stage (10 kip increments), recorded on magnetic tape and displayed on a portable teletype at the test site. Two key gages were used to detect the onset of internal cracking before visual cracks appeared on the surface. One was located approximately $4a'$ from the anchor along the tendon path (max bursting point) and the other directly below the anchor along the end face. Both gages were connected to X-Y plotters. A large deformation would signal the need to begin intensive examination for cracks. A surface crack was always spotted following a large jump in these gages, indicating that internal microcracking (such as would cause the shear cone to form) is not pronounced prior to formation of the visible tendon path crack. Load cells and pressure transducers for load control were read on a BLH digital strainmeter. The overall instrumentation setup is shown in Fig. 3.7a.

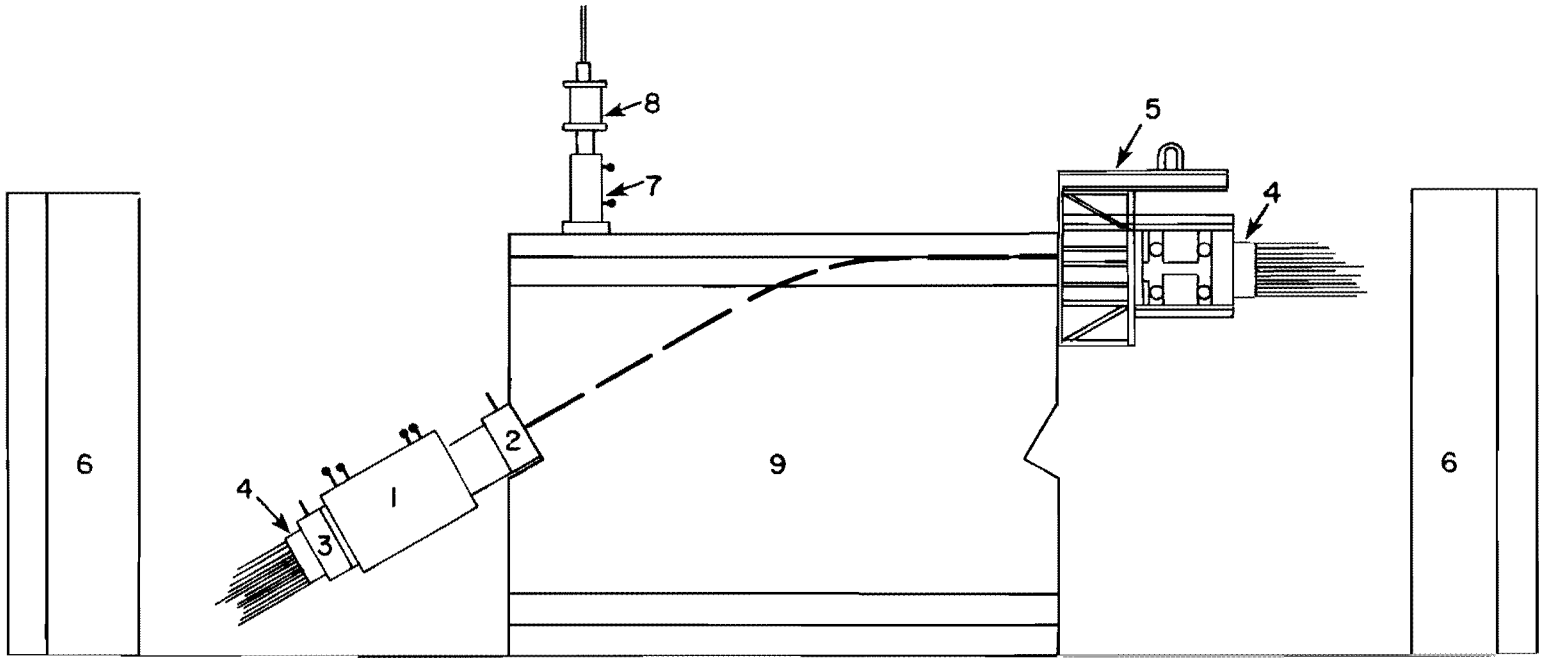

(1) 500 TON CENTER HOLE RAM
(2) SPACER BLOCK
(3) REAR SPACER BLOCK
(4) 26 STRAND ANCHOR HEAD
(5) DEAD MAN - FRICTION LOAD CELLS
(6) TENDON BACKSTOP
(7) LATERAL POST-TENSIONING JACK
(8) LOAD CELL FOR 7
(9) FULL SCALE CURVED TENDON SPECIMEN

Fig. 3.6 Full-scale testing frame

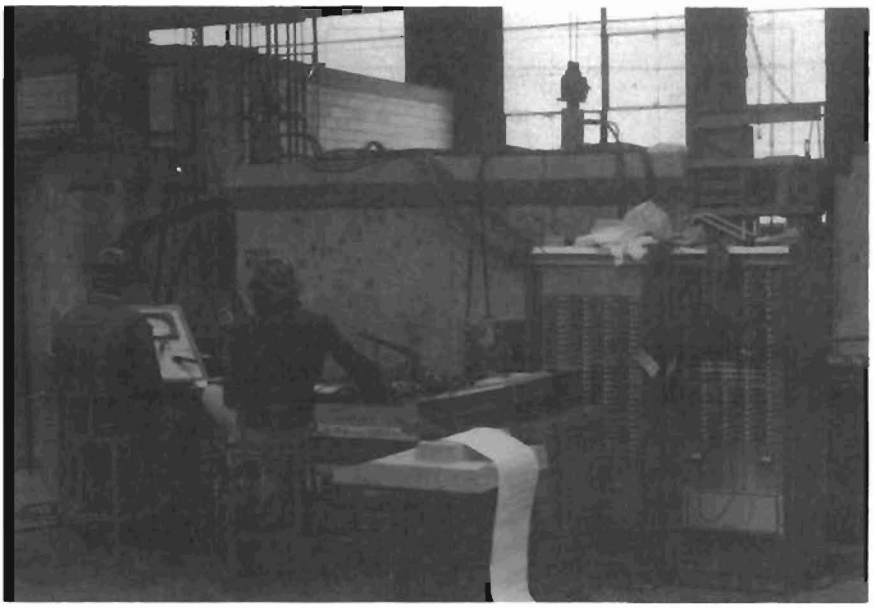

(a) Data acquisition equipment

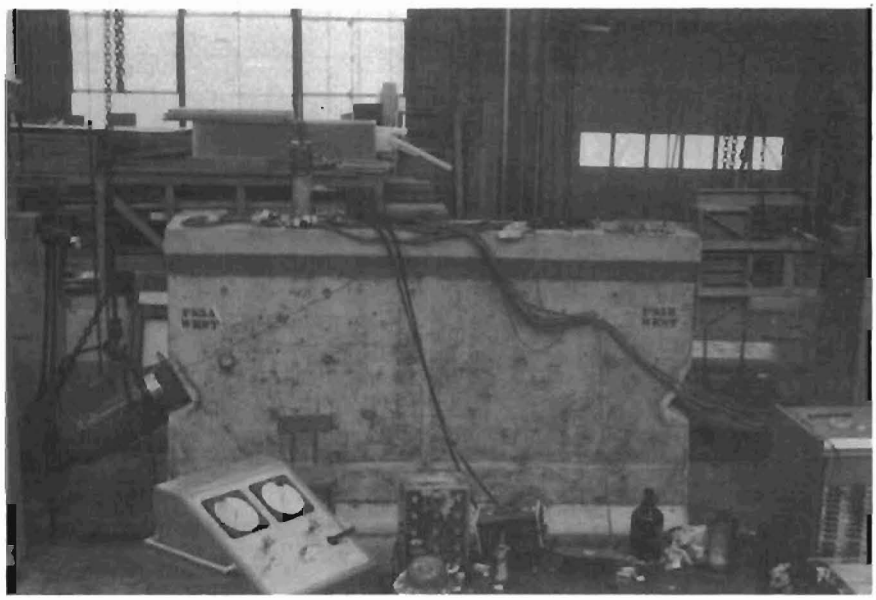

(b) Loading systems

Fig. 3.7 General test setup for full-scale specimens

3.3.3.3 Test Procedure. Testing procedure for the full-scale specimens was identical to that used for the quarter-scale models (Sec. 2.3.3.3) except that load stages consisted of 10 kip increments rather than 1 kip increment and surface strain measurements were taken using an 8 in. Berry gage at 50 kip intervals. Figure 3.7b shows the overall test setup.

3.3.3.4 Data Reduction. Data reduction was identical to the technique employed for the models as described in Sec. 2.3.3.4 in detail.

3.4 Test Results

3.4.1 Bearing Stress Series. Two straight tendon, concentric load tests were performed to investigate the performance of plate-type anchors which would develop widely different bearing stresses for a given load. The standard anchor (Test FS1B) consisted of a commercial 10.5 in. × 10 in. × 1.5 in. thick plate with a 12 in. long light trumpet. A "high bearing stress" anchor (test FS1A) was fabricated from a standard anchor by sawing 1 in. off all sides to form an 8.5 in. × 8.5 in. anchor, thus presenting a substantial reduction in bearing area.

Table 3.1 gives the data summary for tests FS1A and FS1B. Initial cracking loads were identical for the two specimens. This is even more surprising when considered in relation to the concrete compressive strength. The smaller plate anchor was tested first and the compressive strength was lower. The larger plate anchor was tested later and the concrete had matured and was stronger. In spite of this the actual cracking load was the same. Note the split cylinder test data contradict the strength gain. Figure 3.8 shows the cracking trends normalized to f_{sp} with respect to the square root of net bearing areas (A_b). It can be seen that if split tensile cylinder strength is accepted the larger anchor had a cracking load only 12 percent above that for the small anchor, indicating that there is no major change in behavior between the two different

TABLE 3.1

CRACKING DATA FOR BEARING STRESS SERIES

Specimen ID	Eccentricity e	Inclination Θ	Width t	f'_c	f_{sp}	P_{cr}	P_{ult}
FS1A	0	0	0.146a (12")	5034 psi	451 psi	400^k	Tendon failure at 450^k
FS1B	0	0	0.146a (12")	5783 psi	401* psi	400^k	Tendon failure at 460^k

*f_{sp} of 401 psi slightly low. Average value to be expected for prototype concrete is $6.5\sqrt{f'_c}$ or approximately 490 psi.

Specimen ID	$P_{cr}/\sqrt{f'_c}$	P_{cr}/f_{sp}	$P_{ult}/\sqrt{f'_c}$	P_{ult}/f_{sr}	Anchorage Type	Net Bearing Area A_b
FS1A	5638	887	----	----	8-1/2 x 8-1/2" Plate	59.7 in^2
FS1B	5260	997.5	----	----	10-1/2 x 10-1/2" Plate	97.7 in^2

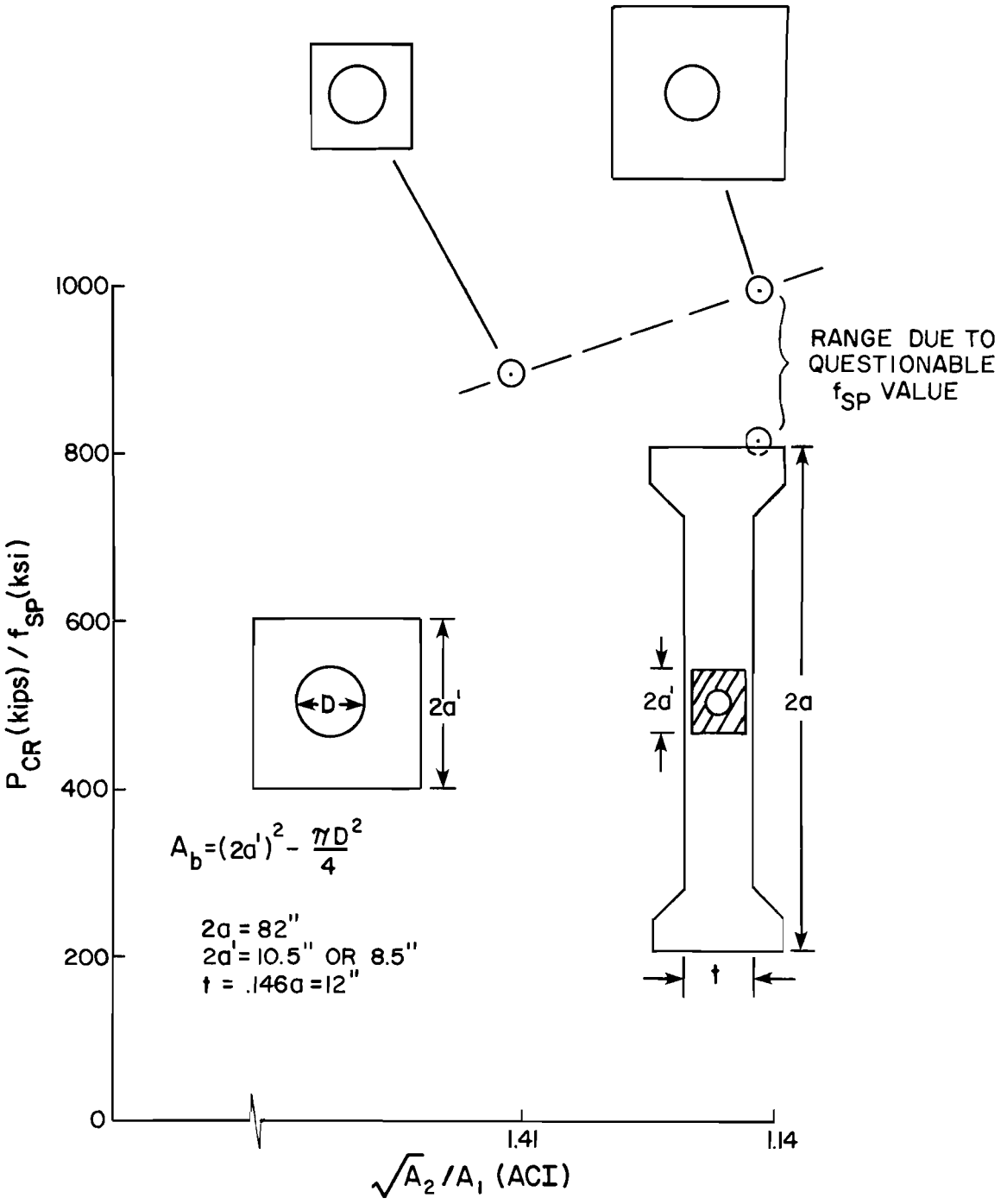

Fig. 3.8 Normalized cracking loads for bearing stress series

plate sizes. Assuming the more probable f_{sp} of 490 psi there is no difference in normalized load. This can be brought into sharper perspective when it is realized that the net bearing area of the large plate (97.7 in.^{2}) is nearly twice that of the reduced anchor (59.7 in.^{2}), yet the normalized cracking load differs by only 12 percent. The effect of surrounding concrete might be considered to be a major one. The $\sqrt{A_2/A_1}$ (ACI) values differ by 24 percent--1.41 for the small plate, 1.14 for the large plate, as illustrated in Fig. 3.8. The ACI Commentary Sec. 18.11 value of $P_{allow} = f_{cp}A_{net} = A_{net}(0.6)f'_{ci}\sqrt{A_2/A_1}$ would be 254 in. for FS1A and 386 in. for FS1B. For these two plates, the ACI allows a 47 percent higher load for the larger bearing plate, when in fact both cracked at identical loads. Due to full development of the tensile ultimate of the tendons inserted, neither specimen could be taken to an ultimate based on concrete failure. For this reason, and the fact that there apparently was little difference in the performance of the anchorage zone for anchors with widely differing bearing areas, a series of four quarter-scale models was cast to investigate the phenomena in further detail. Results for these model tests are presented in Chapter 4.

A large number of internal strain gages were used to determine strain distributions in the bursting and spalling zones. Plots of the bursting strain distribution for specimen FS1A with the reduced size bearing plate are shown in Fig. 3.9, while those of FS1B are shown in Fig. 3.10. The two plots in each figure indicate strains read at a load of 200 kips and at the cracking load, respectively.

Both plots show the expected tensile bursting profile with the maximum tensile strain occurring at a distance of $3a'$ to $4a'$ ($2a'$ = width of the anchor) from the loaded face. A typical full range load-strain plots for a gage measuring the maximum tensile strain is shown in Fig. 3.11. Note the generally linear behavior of the data up to cracking.

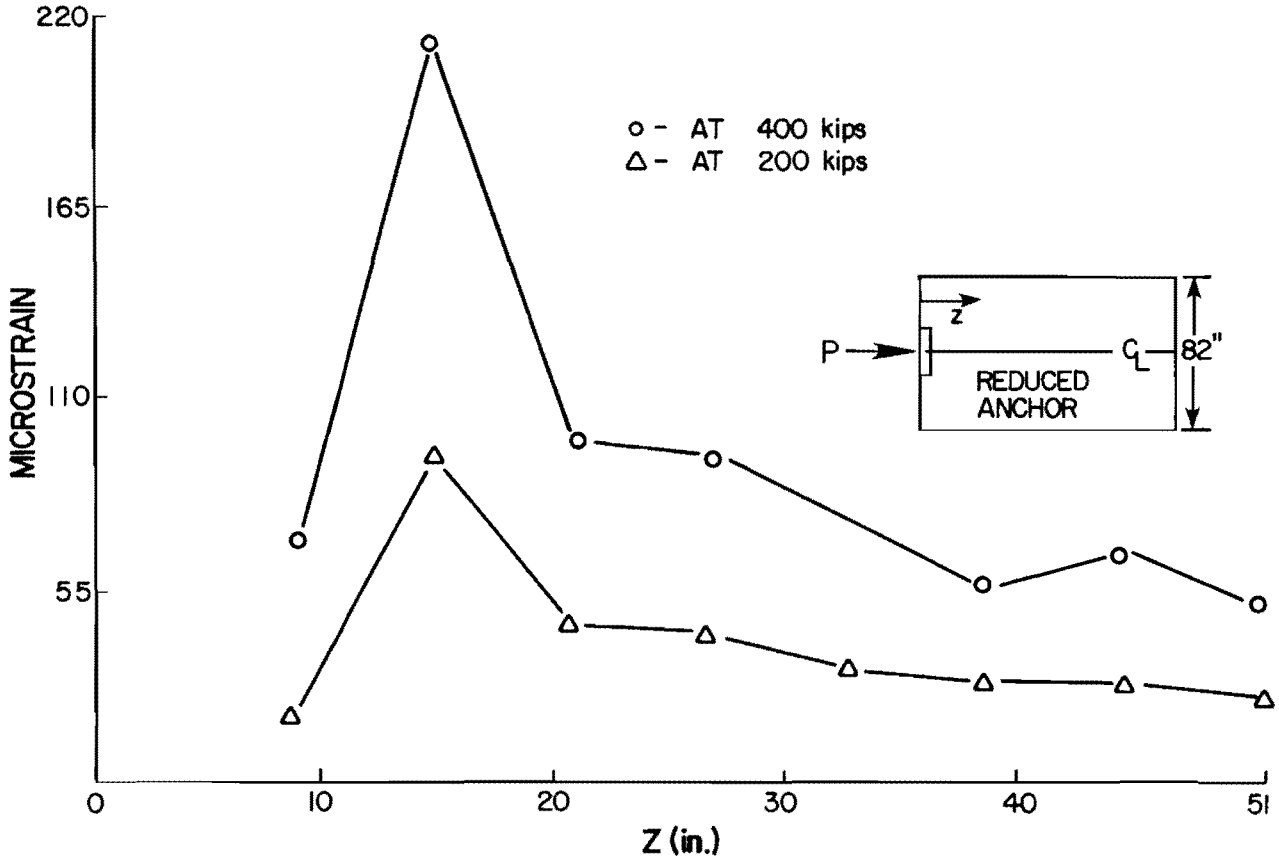

Fig. 3.9 FS1A experimental bursting strain distribution

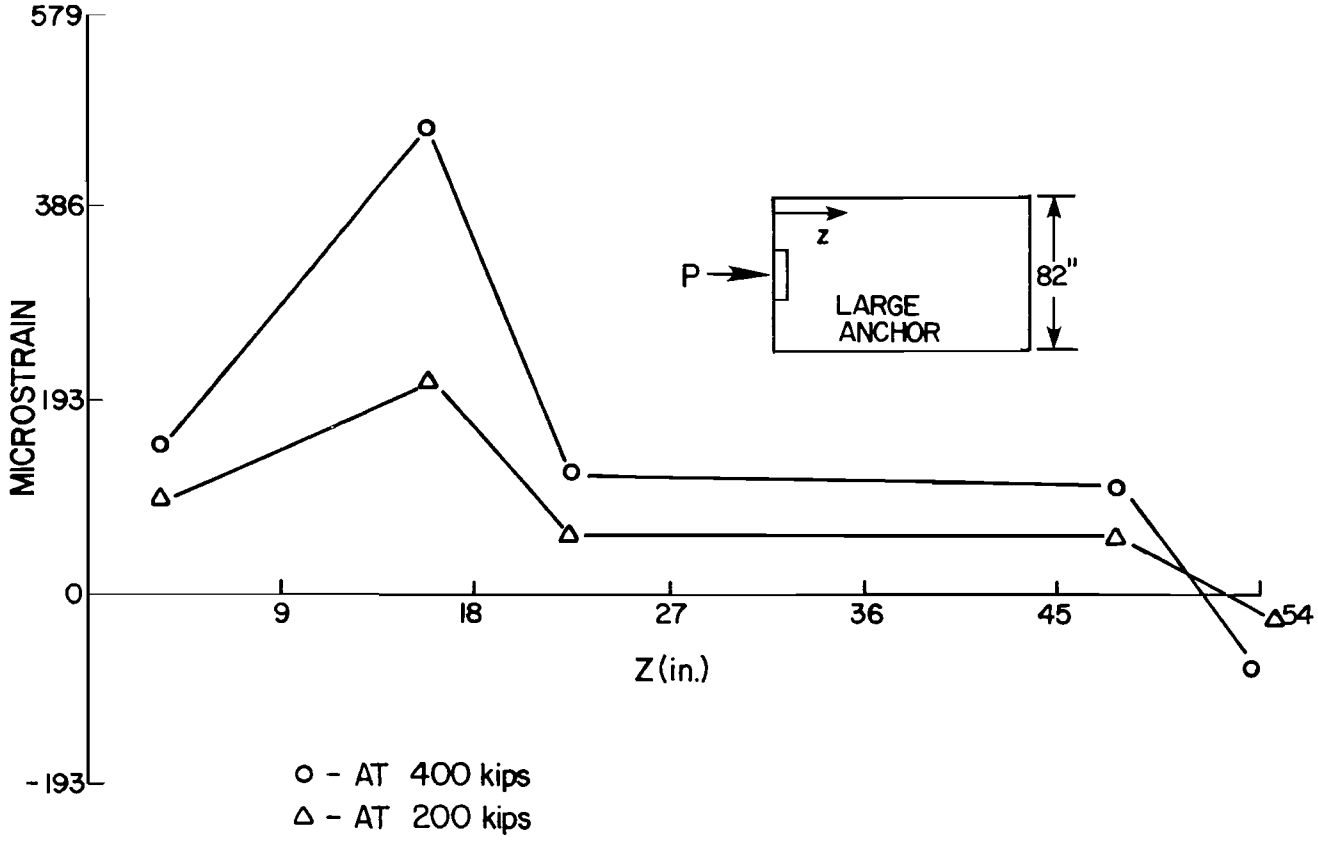

Fig. 3.10 FS1B experimental bursting strain distribution

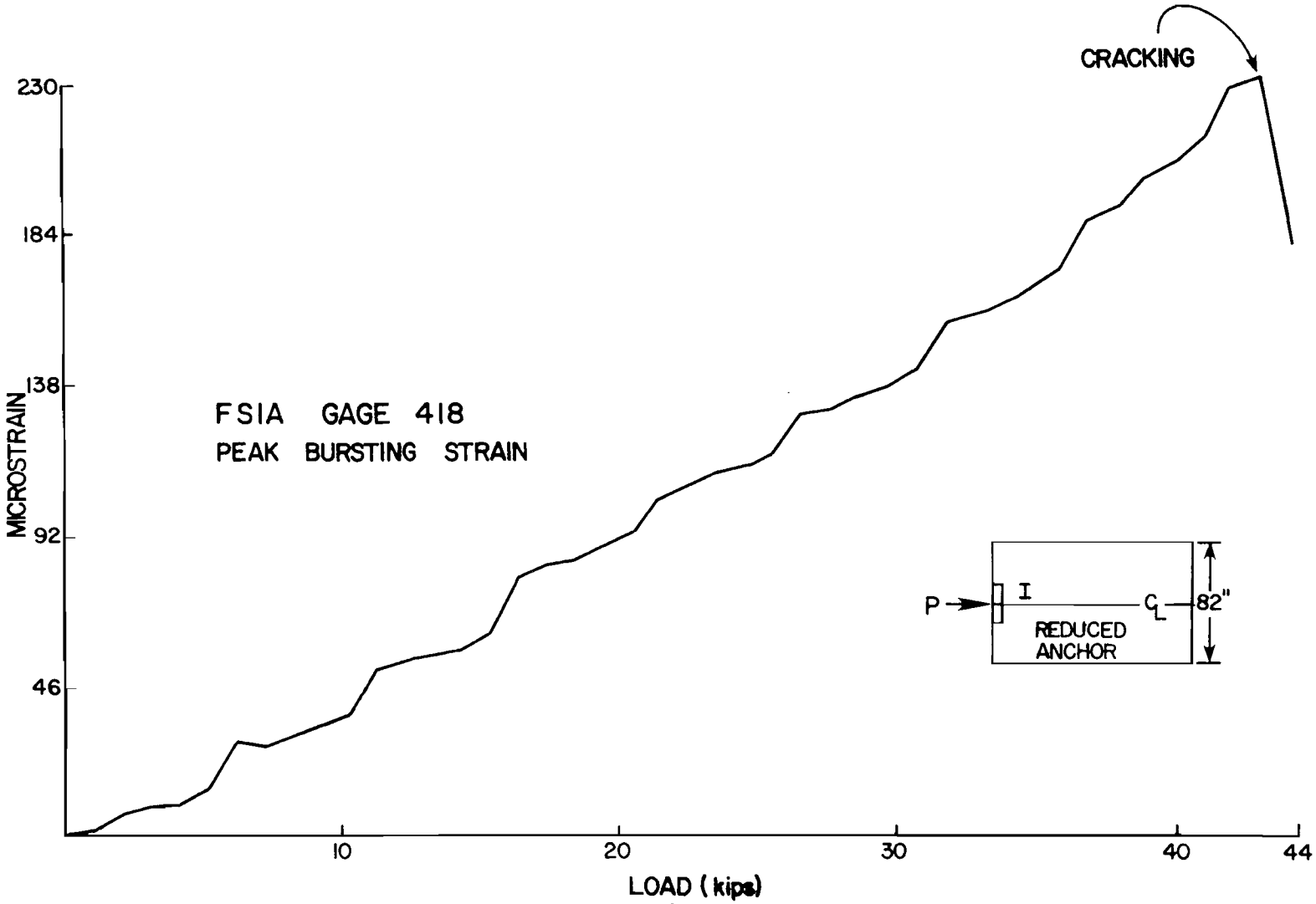

Fig. 3.11 Load-strain plot--typical gage FS1A

A comparison of the bursting strain distribution in Fig. 3.12 for specimens FS1A and FS1B shows the peak tensile strain for FS1B ($2a' = 10.5$ in.) to be more than twice that for FS1A ($2a' = 8.5$ in.). This seems unreasonably high, particularly in view of the fact that the 3D FEM computer program predicted nearly identical peak strains (see Fig. 3.13).

The majority of the spalling gages for both specimens FS1A and FS1B proved to be either defective or yielded such erratic data as to be unusable. Those gages which did function properly are plotted in Fig. 3.14b against the 3D FEM spalling distribution for specimen FS1B and seem to follow the general trend. Maximum tensile spalling strains predicted using the program showed that specimen FS1A (small anchor) would develop a maximum approximately 15 percent above that for FS1B (large anchor). Further discussion on the effects of bearing stress is presented in Chapter 4 and in the final report.

3.4.2 Inclination Series. Three specimens--FS1B, FS2A, and FS2B--were cast to investigate in greater detail the effect of tendon inclination. Angles of 0, 15, and 30 degrees to the horizontal were used, respectively. Anchorages consisted of the standard (10.5 in. × 10.5 in. × 1.5 in.) commercial bearing-type anchor with a twelve 1/2 in. diameter 270 ksi strand tendon. No supplementary anchorage zone reinforcement was provided.

Table 3.2 gives the data summary for these specimens. Figure 3.15 shows the normalized cracking load as a function of the tendon inclination. This indicates a drop in initial cracking load of 27.5 percent between the straight concentric tendon and the 30-degree inclined tendon, or roughly 1 percent per degree of inclination over the range investigated. This compares favorably with the results reported by Cooper et al. [9].

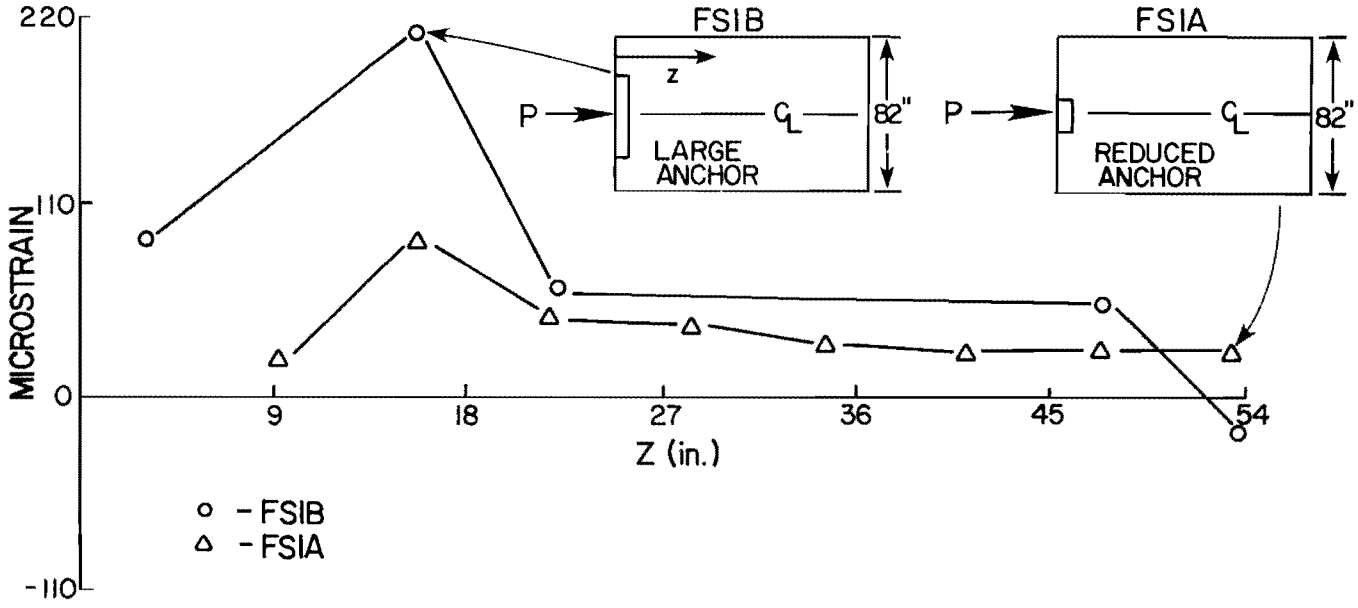

Fig. 3.12 FS1A/FS1B bursting strain distribution comparison at P = 200 kips

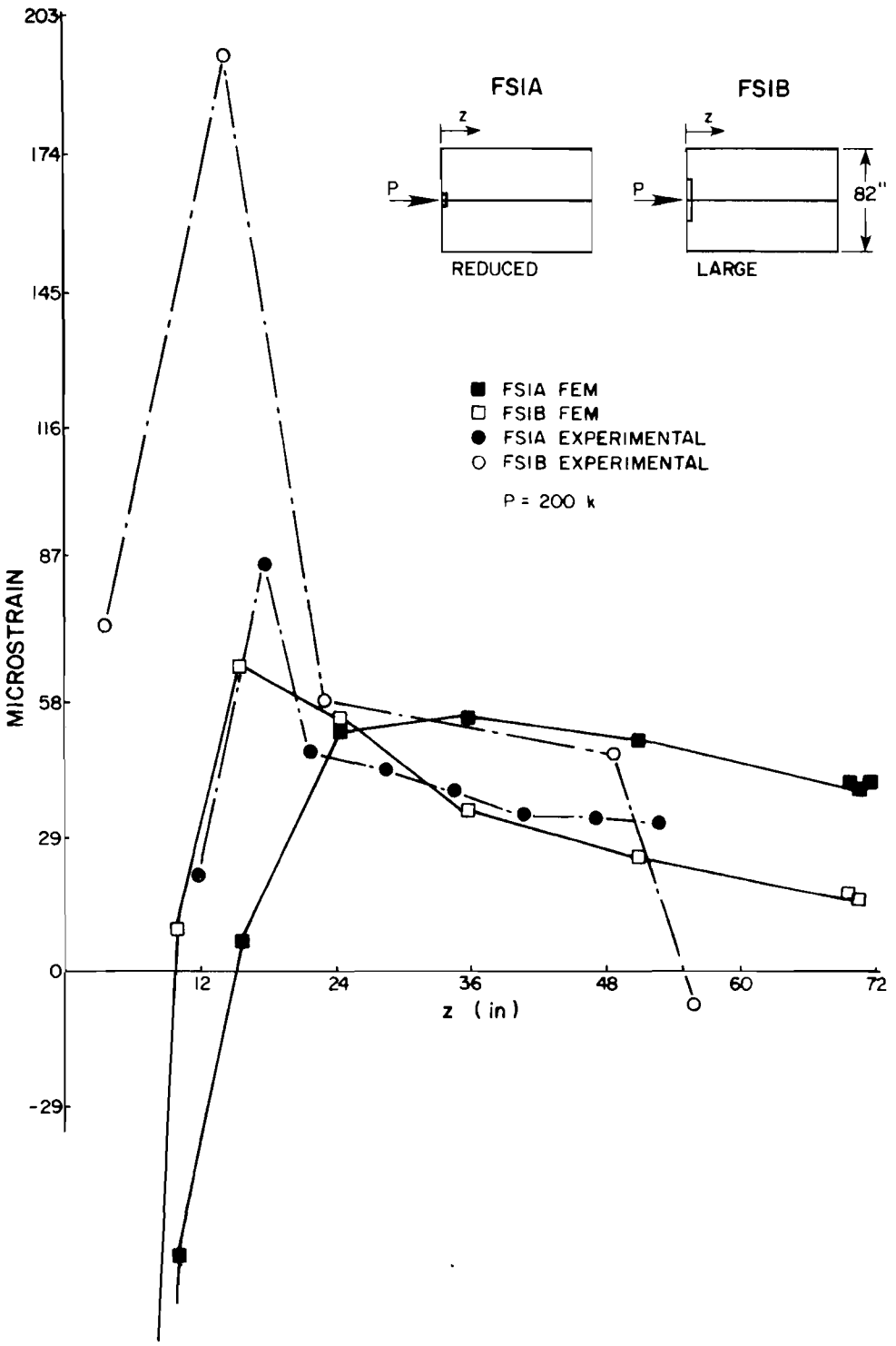

Fig. 3.13 Comparison FS1A/FS1B vs 3D FEM bursting strain distribution

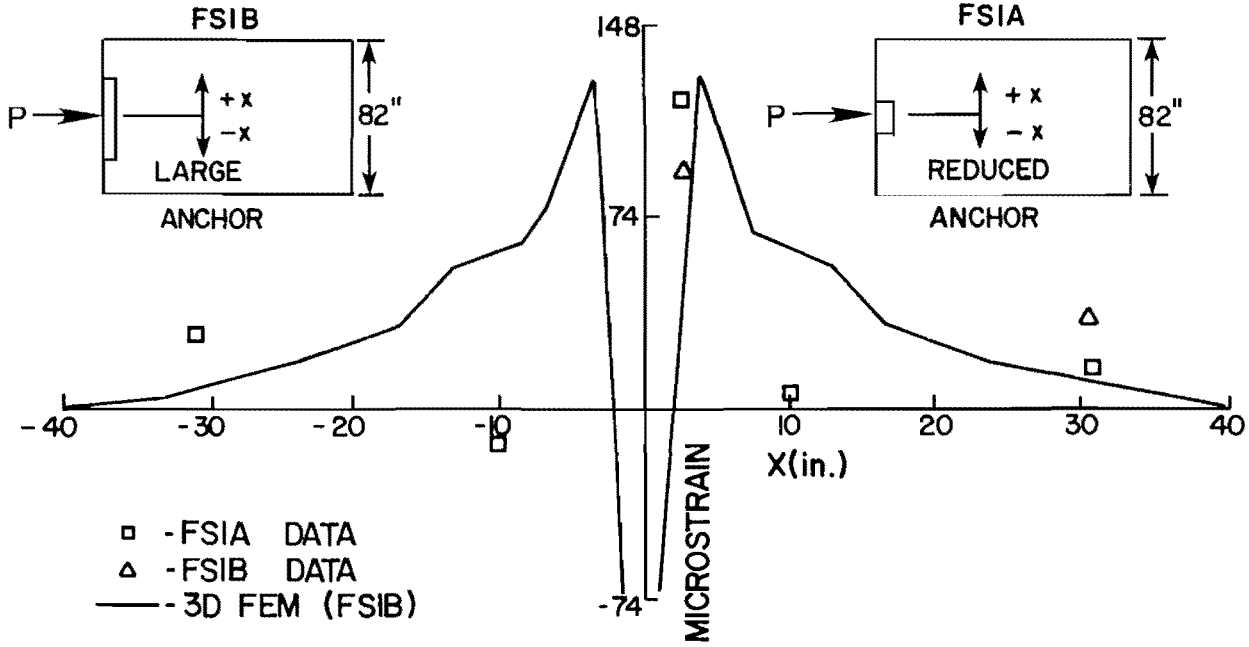

Fig. 3.14 Comparison FS1A/FS1B vs 3D-FEM spalling distribution

TABLE 3.2

INCLINED TENDON SPECIMENS

Specimen ID	Eccentricity e	Inclination θ	f'_c (psi)	f'_{sp} (psi)	P'_{cr} (kips)	P_{ult}
FS1B	0	0°	5783	401*	400	Tendon failure at 450^k
FS2A	0	15°	5040	532	440	Tendon failure at 610^k
FS2B	0	30°	4627	455	330	Tendon failure at 620^k

Specimen ID	$P_{cr}/\sqrt{f'_c}$	P_{cr}/f_{sp}	P upper diagonal	P_{ud}/f_{sp}	P lower diagonal	P_{ld}/f_{sp}
FS1B	5260	997.5	---	---	---	---
FS2A	6198	827.0	490	921	510	958
FS2B	4851	725.0	---	---	340	747

*f_{sp} of 401 psi slightly low. Average value to be expected for prototype concrete is $6.5\sqrt{f'_c}$ or approximately 490 psi.

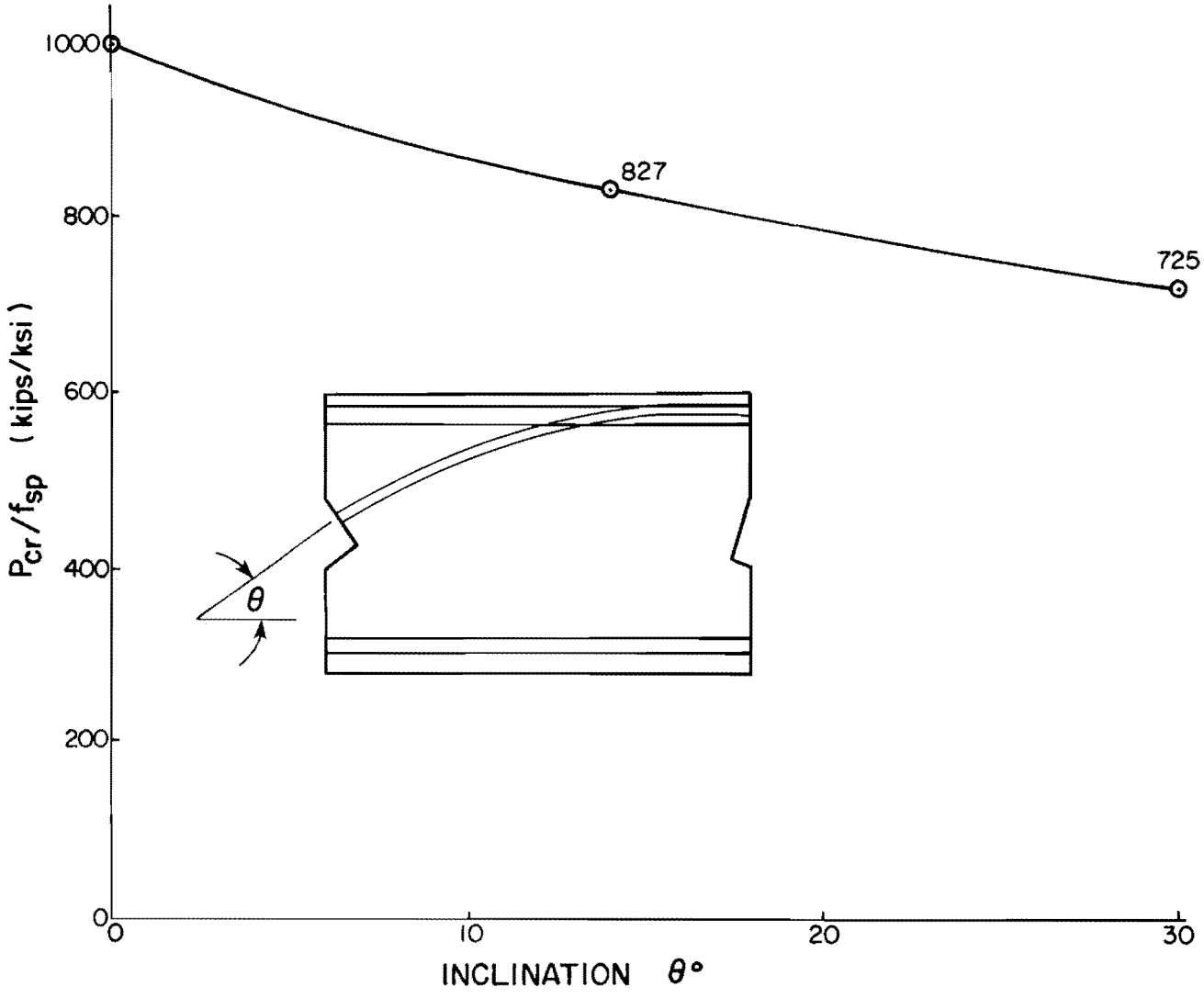

Fig. 3.15 Normalized cracking loads--inclined tendon series

First cracking occurred along the tendon path as illustrated in Fig. 3.16. As with the first two specimens, the tendon strength was the load limit, so that the anchor zone limit was not attained. However, using seventeen 1/2 in. 270 ksi strands through the same tendon duct, a load of approximately 600 kips was achieved before rupture of the tendon. No major diagonal side face cracks were seen to form. It is unfortunate that data could not be obtained for a full load history of these first four specimens. However, it is clear that the cracking problem encountered at Corpus Christi did not endanger the capacity of the tendon anchorages. The tendon ultimate was 500 kips, so that ultimate failure would have occurred in the tendon rather than the concrete.

Based on experience with the gages used in the first two specimens, twin gages were mounted at each spalling strain location and over-under gages were wired into place along the tendon path in subsequent specimens in an effort to reduce the impact of faulty gages in key locations.

Figures 3.17 through 3.20 show bursting and spalling strain distributions for specimens FS2A and FS2B in the uncracked state and compare them to the 3D finite element solutions. In general, the bursting strain for inclined tendons is lower than that for a concentric straight tendon, as illustrated in Fig. 3.21. A precise relationship would be difficult to define but it appears that moderate inclinations (i.e., 15 degrees) tend to decrease the bursting strain significantly, while large inclinations (i.e., 30 degrees) seem to have about the same effect as the moderate inclination due to higher normal and friction forces along the tendon duct. The maximum bursting strain for both inclined tendon specimens is well below that for the straight concentric tendon specimen. On the other hand, Fig. 3.22 and the experimental data show that the calculated peak spalling strain, which occurs directly below the anchor plate and on the end face, rapidly increases for increasing

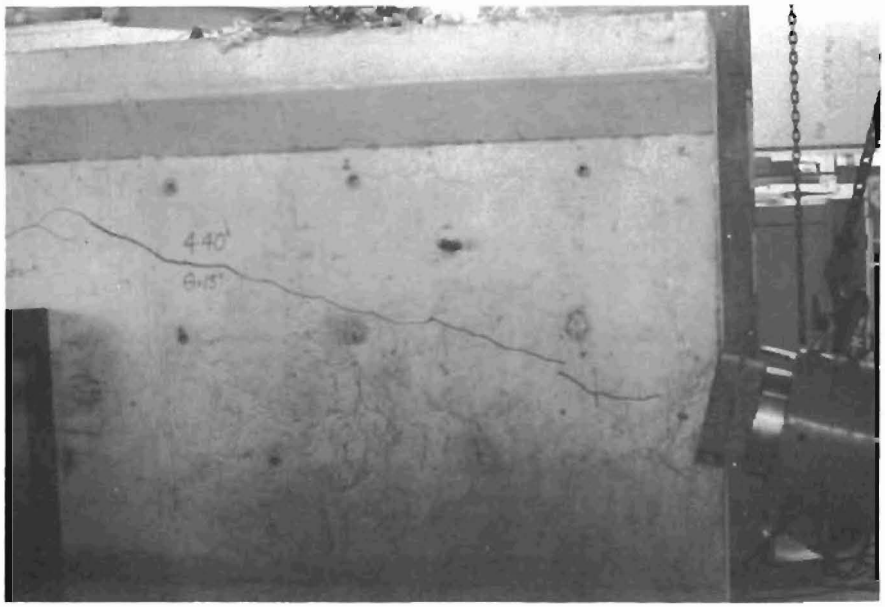

FS2A, 15 degree inclination, P_{cr} = 440 kips

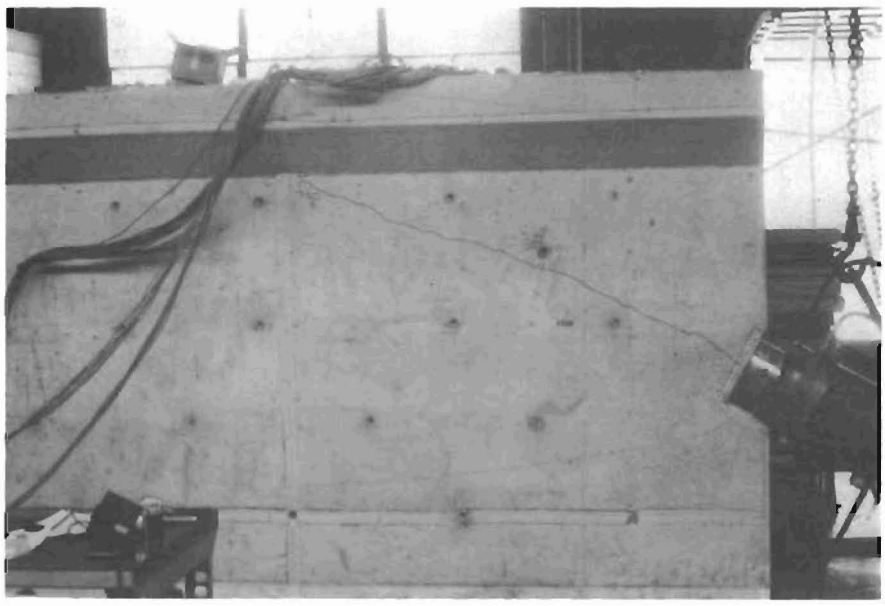

FS2B, 30 degree inclination, P_{cr} = 330 kips

Fig. 3.16 Specimens FS2A and FS2B at first cracking

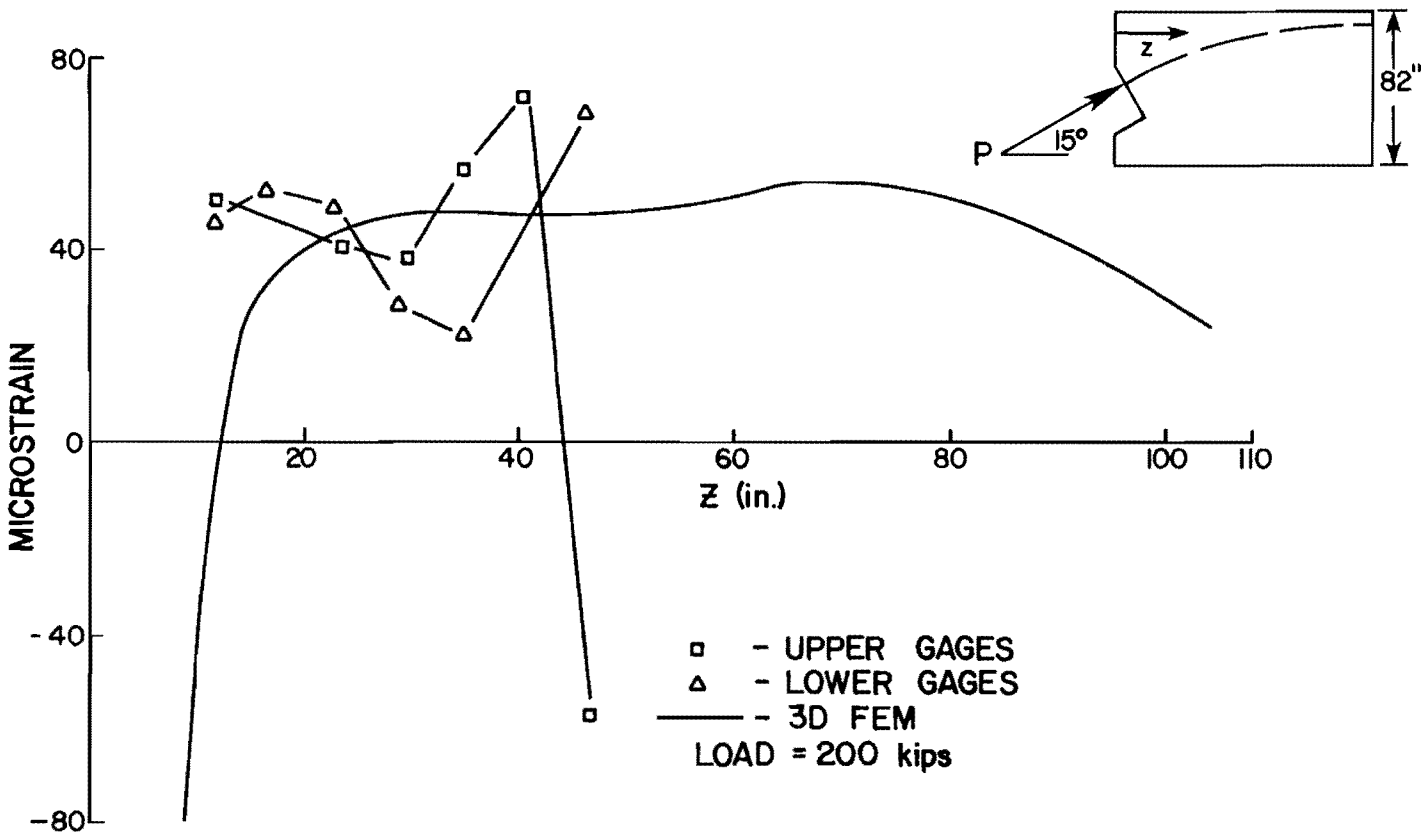

Fig. 3.17 FS2A--3D-FEM vs experimental bursting strain distribution

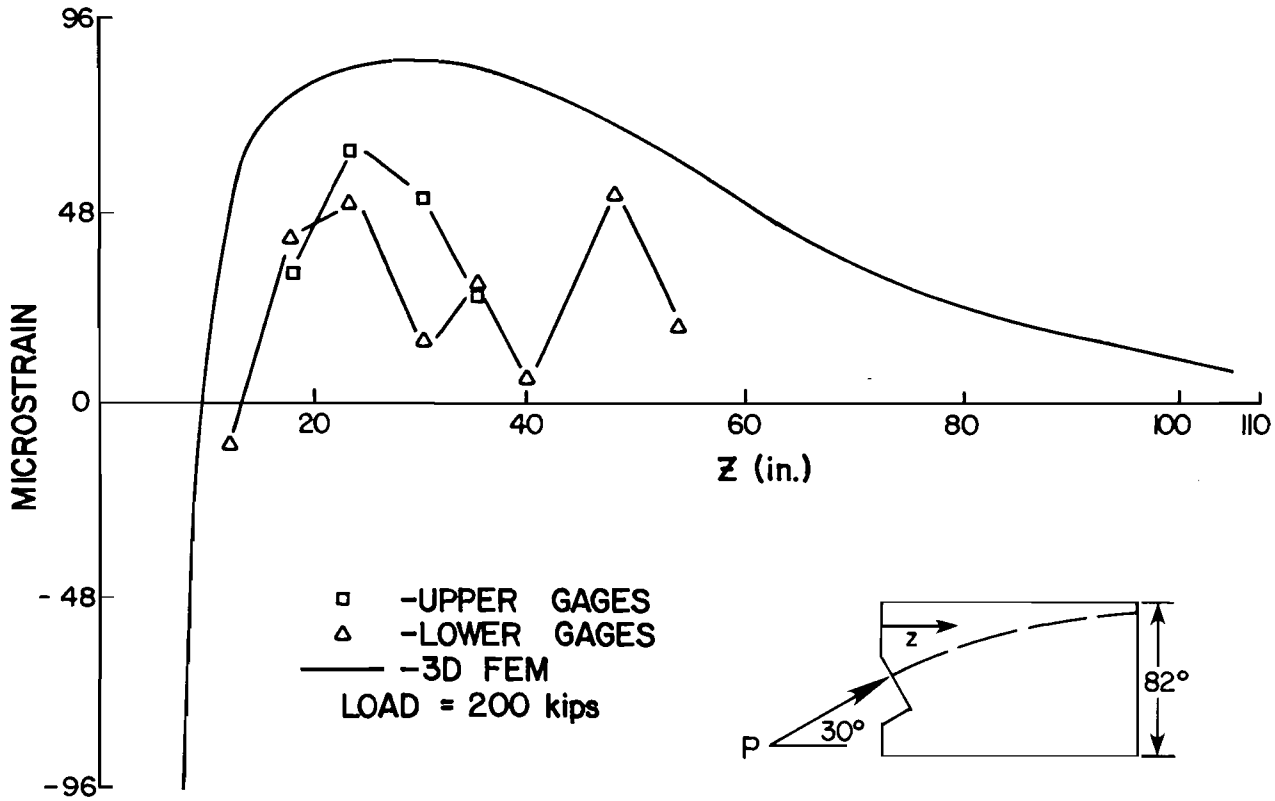

Fig. 3.18 FS2B--3D-FEM vs experimental bursting strain distribution

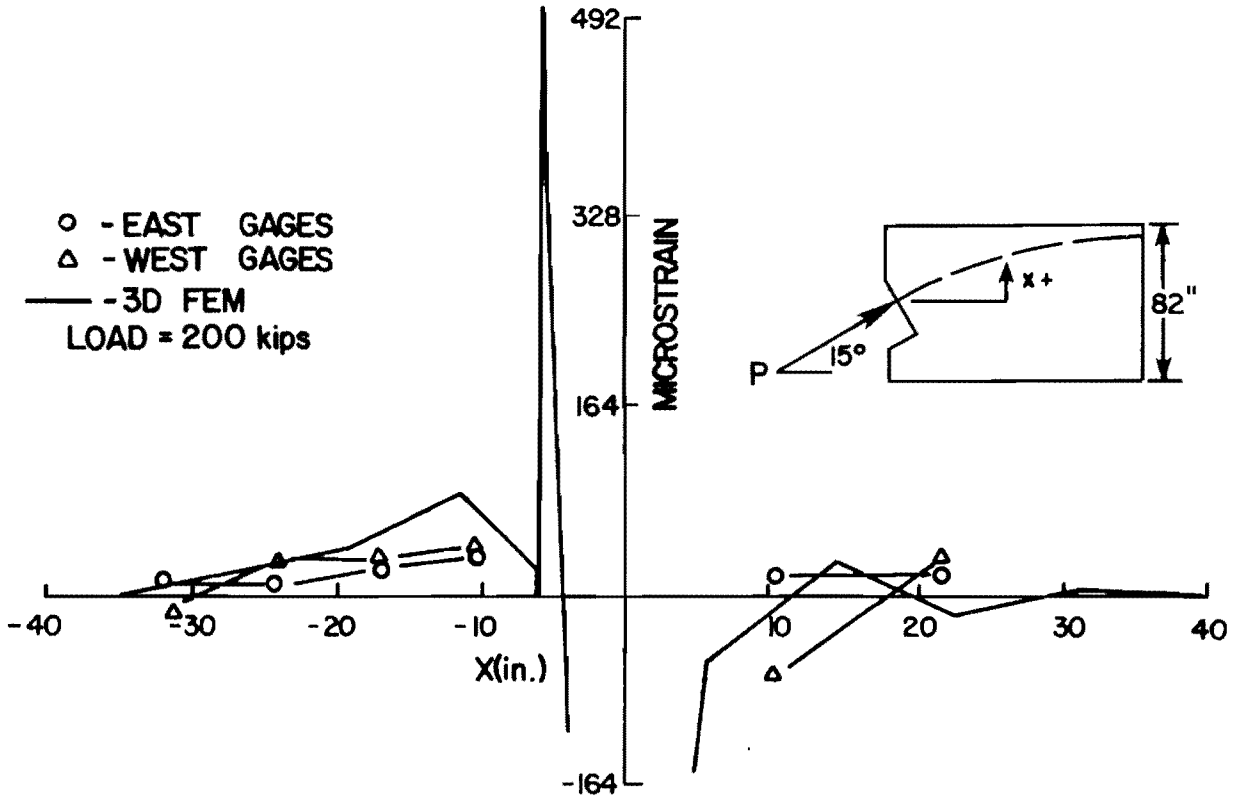

Fig. 3.19 FS2A--3D-FEM vs experimental spalling strain distribution

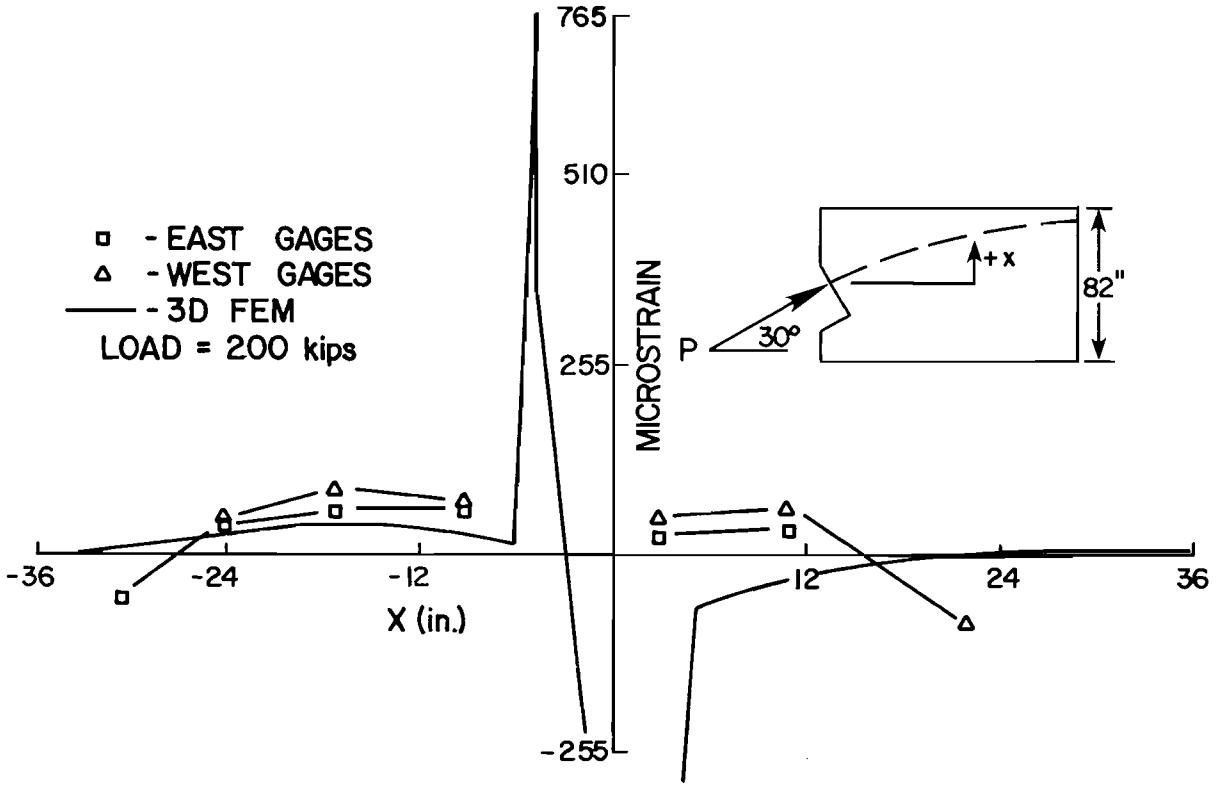

Fig. 3.20 FS2B--3D-FEM vs experimental spalling strain distribution

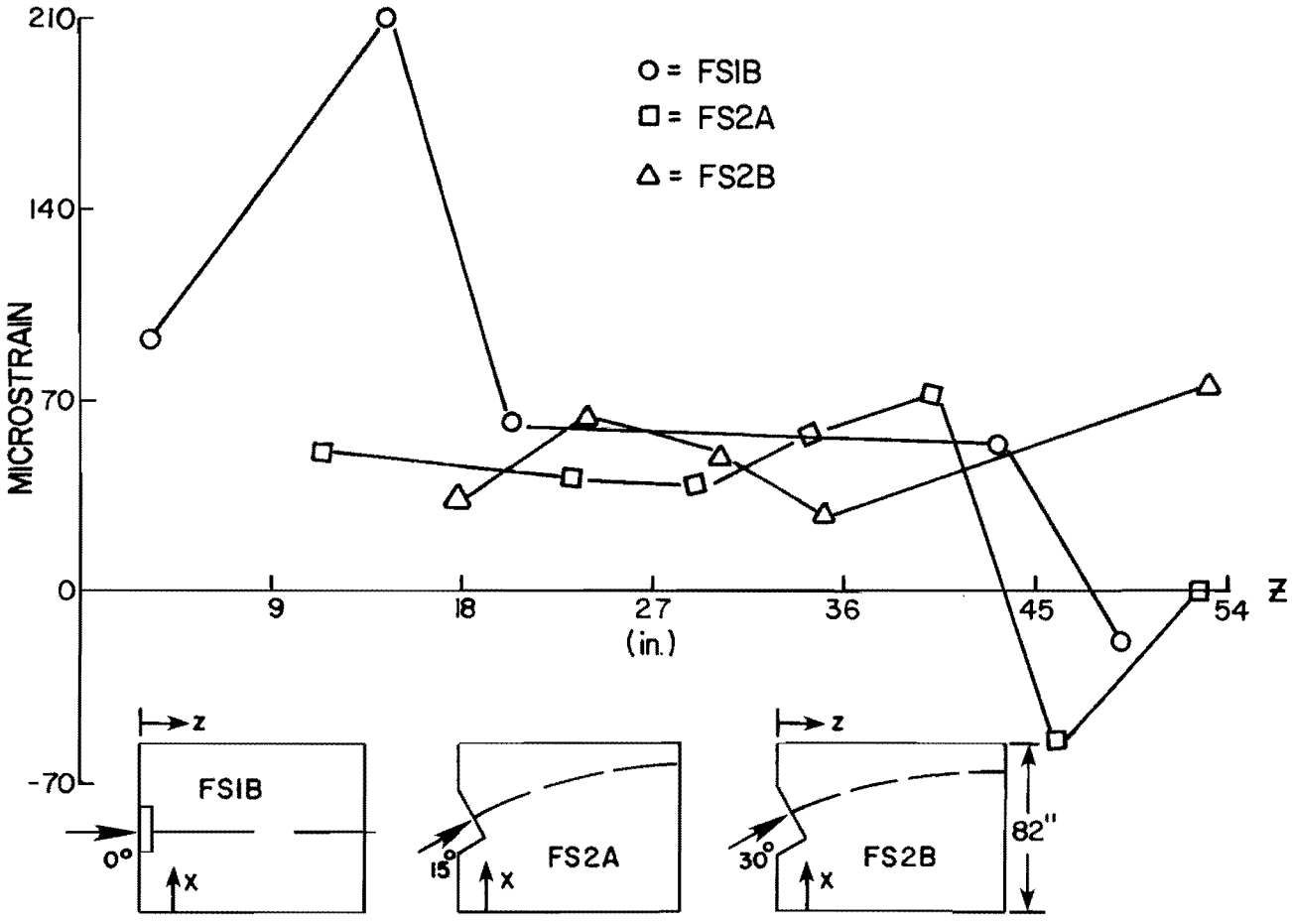

Fig. 3.21 Experimental bursting strain distribution for inclined tendon specimens

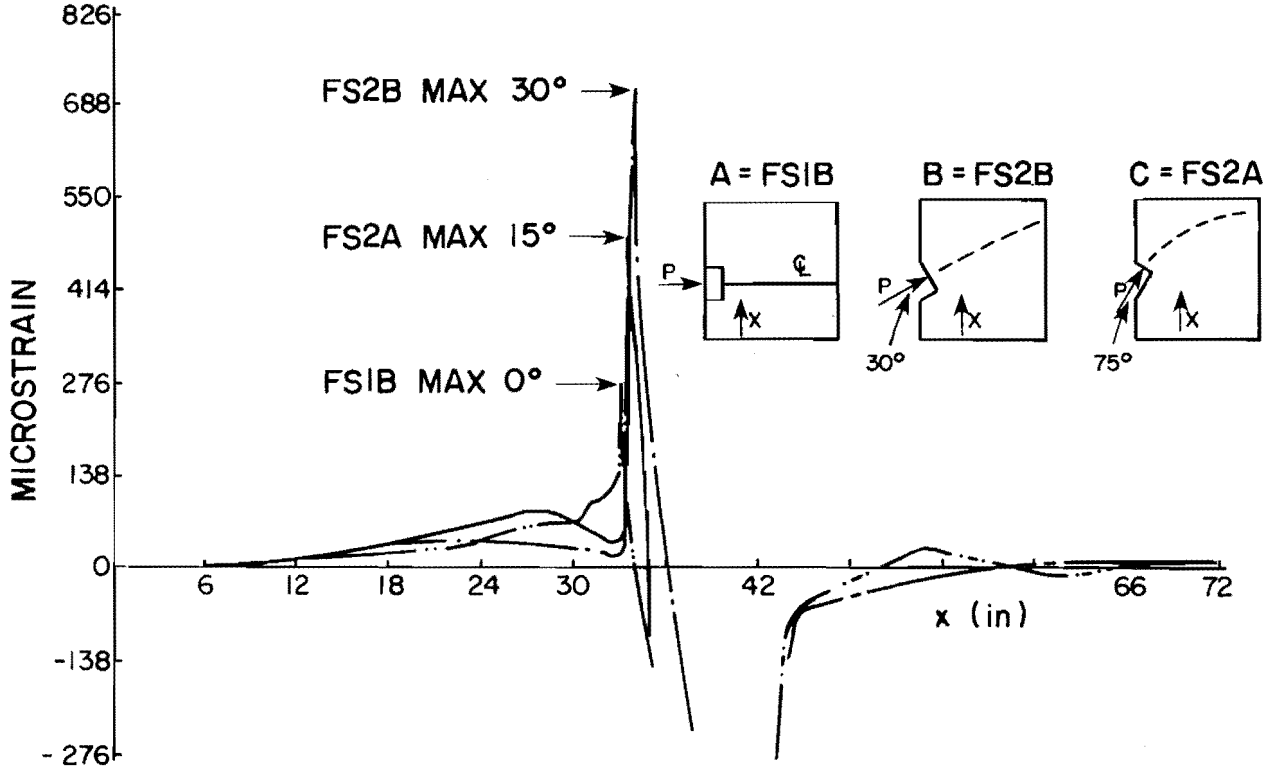

Fig. 3.22 3D-FEM spalling strain distribution for inclined tendons

inclination. Since the peak spalling strains are calculated to occur between the corner of the blockout and the edge of the anchor (see Fig. 3.23), it was impossible to place an accurate strain-measuring device at that location. Relatively good correlation between the 3D FEM program and the experimental gage data had been achieved in other locations so that the maximum values shown in Fig. 3.22 are assumed to be reasonably accurate, although unconfirmed by experimental measurements.

In summary, the full-scale specimens exhibited similar cracking trends with respect to tendon inclination as those observed in the models. First visible cracking occurred along the tendon axis, usually initiating at a distance of approximately $2a'$ from the loaded face and extending to the web-flange junction. No audible sounds were heard prior to formation of the visible tendon path crack and internal gages indicated that internal cracking occurred simultaneously with visible cracking. Increased angles of inclination decreased the cracking load substantially. Specimen FS2B (30-degree inclination) cracked when only 83 percent of the design maximum temporary tensioning load was reached. The cracking load was in close agreement to the cracking load levels experienced in the similarly inclined tendons in the Corpus Christi prototype bridge. Unlike the model specimens, the upper and lower diagonal side face cracks (the indicators of impending failure) did not form due to insufficient load capacity in the loading system. Despite these problems, a significant (over 40 percent) increase in load above first cracking was sustained without further visible cracking, despite the fact that no supplementary anchorage zone reinforcement was provided in these full-scale specimens. Observed cracking loads of model and prototype (normalized by f_{sp} and multiplied by the load scale factor $1/S^2 = 16$) were nearly identical. This would suggest that the full-scale specimens are not as sensitive to a lack of supplemental reinforcing as were the microconcrete models which usually failed at loads only nominally above cracking when supplemental reinforcing was not used.

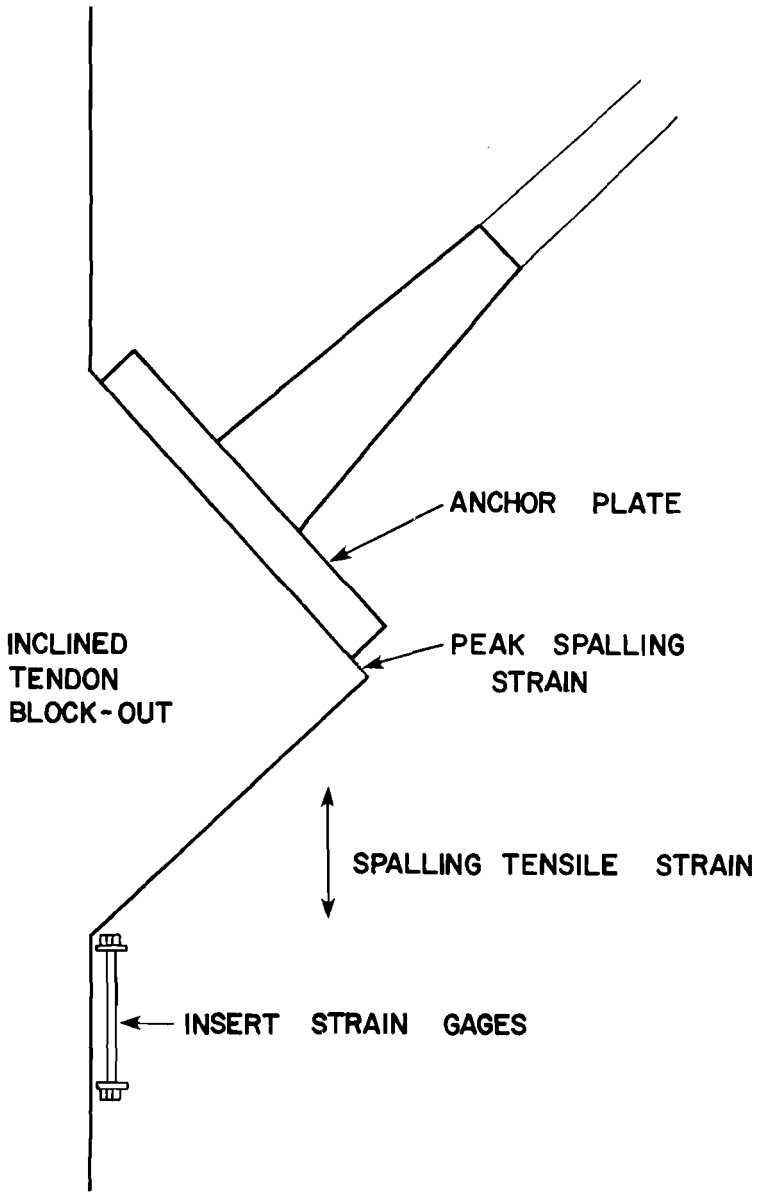

Fig. 3.23 Location of maximum spalling strain for inclined tendon specimens

Internal strain gages as well as the analytical program showed a decrease in the bursting strain for increased inclination. Likewise, the maximum spalling strain appeared to increase with tendon inclination.

3.4.3 Spiral Reinforcement Series. The model studies reported in Chapter 2 indicated that confining spirals along the tendon path were the most efficient passive means of anchorage zone reinforcement. This superior performance over orthogonal mat reinforcement was attributed to several factors:

(1) The spiral provided a lateral confining force which tended to prevent formation of the shear cone beneath the anchor.

(2) Initial cracking load was greatly increased, while crack widths were reduced after cracking.

(3) Ultimate failure usually occurred when the spiral steel failed in tension at loads well above those for conventionally reinforced specimens.

(4) Light spirals (fabricated from small diameter rods) seemed to yield equal performance to those fashioned from heavier rod stock.

In view of this, two variables were investigated in the full-scale tests of spiral reinforcement:

(1) The size of the spiral wire for a given spiral outer diameter and pitch.

(2) The length of the spiral.

The spirals were designed to have the maximum possible outside diameter which still allowed concrete placement and satisfied cover requirements. This was a diameter of 8 in. for the full-scale specimens which had a web thickness of 12 in. A pitch of 2 in. was used to allow concrete to flow freely into the core. The "short" spirals used in specimens FS3A and FS3B were 13 in. in length, while

the "long" version used in specimens FS4A and FS4B were 26 in. in length. All were fabricated from 60 ksi smooth rod stock. Each spiral was instrumented with 14 strain gages and affixed against the anchor plate as shown in Fig. 3.24. Due to the congestion, no bursting strain gages could be placed in specimens with spiral reinforcement. All specimens used 30-degree inclined tendons.

3.4.3.1 Test Results. FS3A--This specimen had a 13 in. long 3/8 in. ϕ spiral (see Fig. 3.24c). First cracking occurred at 370 kips along the tendon path, beginning at a distance of approximately 16 in. (3a′) from the loaded face and propagating to the web-flange junction as shown in Fig. 3.25a. Further increase in load to 580 kips initiated formation of the upper and lower diagonal cracks, radiating from the corners of the anchor plate. At 620 kips, a massive (0.125 in.) longitudinal crack appeared 10 in. below the previous tendon path crack extending from 18 in. to about 60 in. from the loaded face. The widest part occurred at the point of sharpest curvature and a wide vertical crack connected it to the upper tendon path crack, as illustrated in Fig. 3.25b. A side face blowout appeared imminent and the load was released to permit testing of specimen FS3B. Strainmeter data are reported in the next subsection for ease of comparison.

FS3B--This specimen was reinforced with a 13 in. long spiral identical to the one used in specimen FS3A but fabricated from 1/2 in. ϕ stock rather than 3/8 in. (see Fig. 3.24c for details). As shown in Fig. 3.26a first cracking occurred along the tendon path at a load of 300 kips, with the maximum crack width at a distance of 50 in. from the loaded face. A second longitudinal crack formed at a load of 470 kips beginning at a distance of 30 in. from the end face and stopping at 54 in. Upper and lower diagonal cracks formed at the anchor at a load of 480 kips. At 590 kips a vertical crack formed at the point of sharpest curvature, connecting the upper and lower longitudinal cracks. As shown in Fig. 3.26c, an attempt to

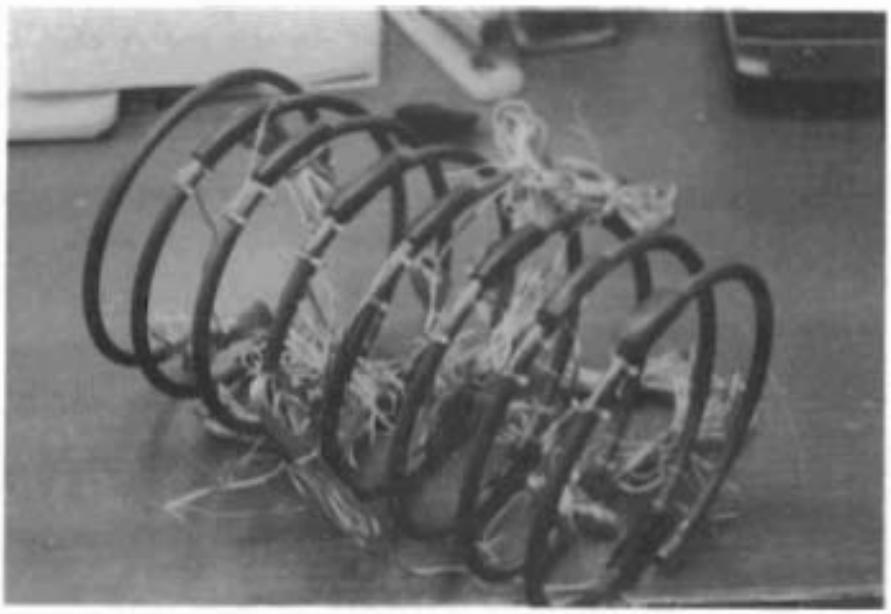

(a) Spirals with strain gages on opposing sides

(b) Positioning of spiral in the reinforcing cage

Fig. 3.24 Spiral instrumentation and placement

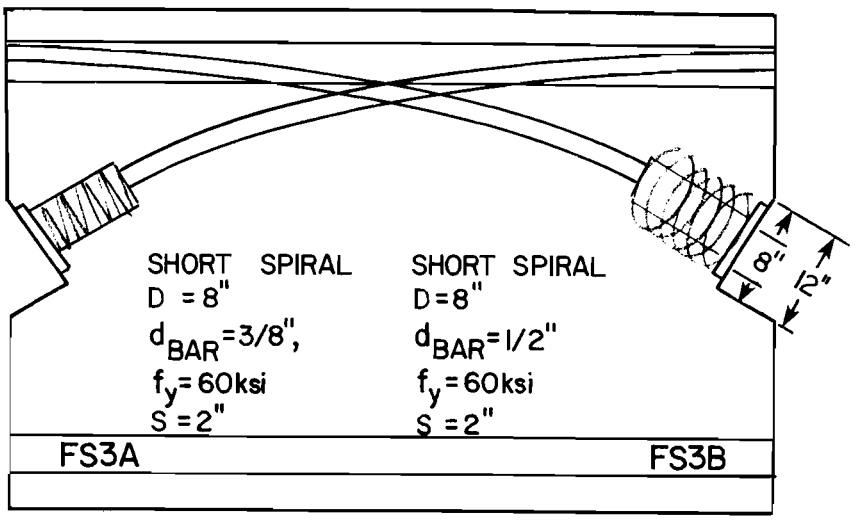

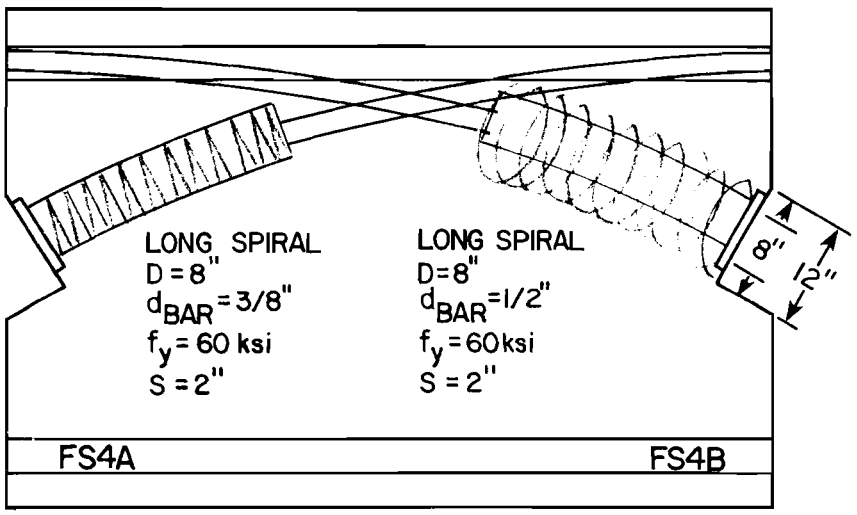

(c) Spiral reinforcement details

Fig. 3.24 (Continued)

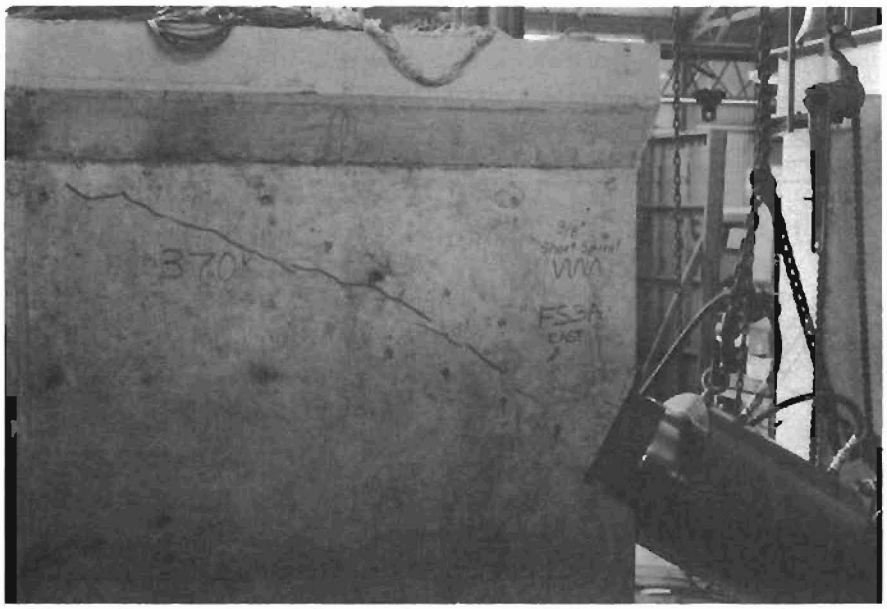

(a) First cracking along tendon path

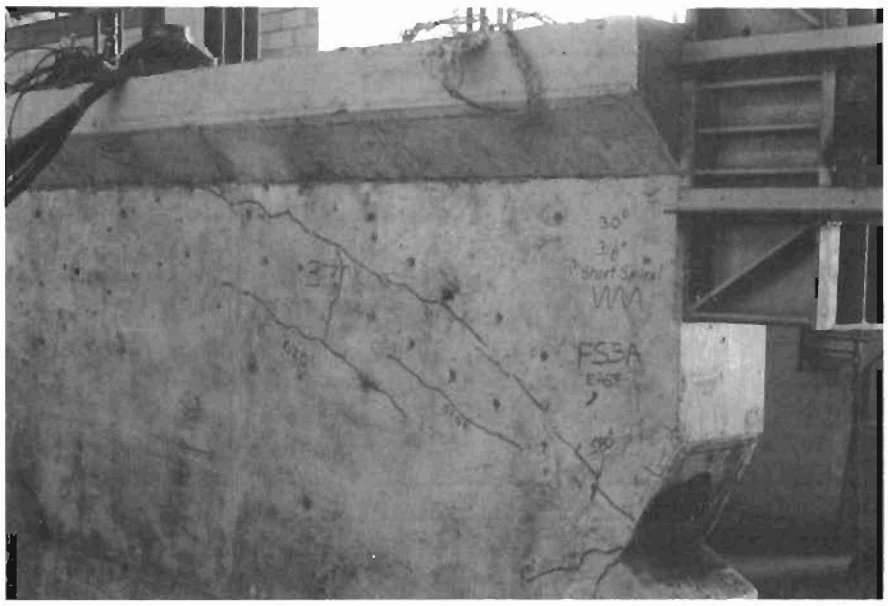

(b) At failure, impending side face rupture. Note vertical connecting crack (arrows)

Fig. 3.25 Failure sequence: specimen FS3A

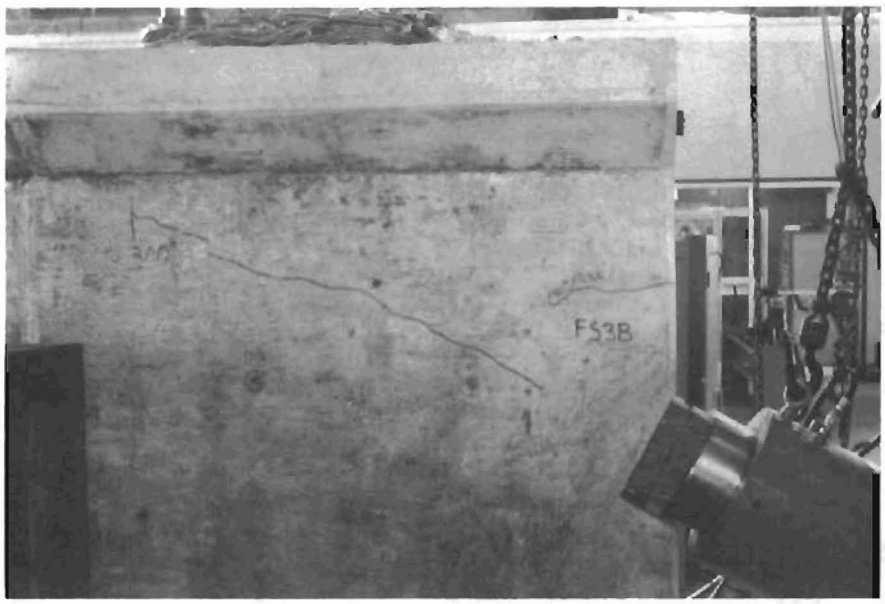

(a) First cracking along tendon path

(b) Lower longitudinal crack forms at point of maximum curvature. Upper and lower diagonal cracks form shortly thereafter

Fig. 3.26 Failure sequence: specimen FS3B

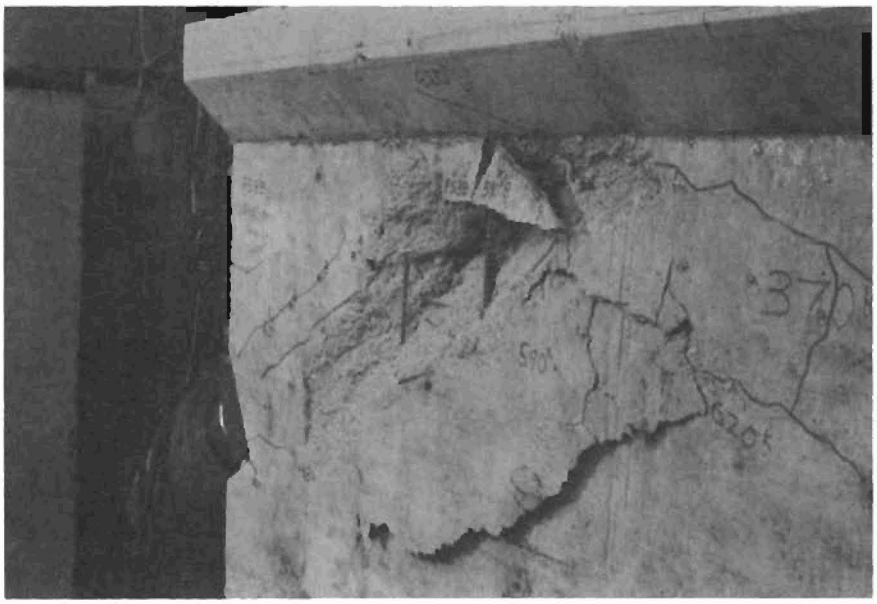

(c) Ultimate load: 590 kips. Side face rupture at point of maximum curvature

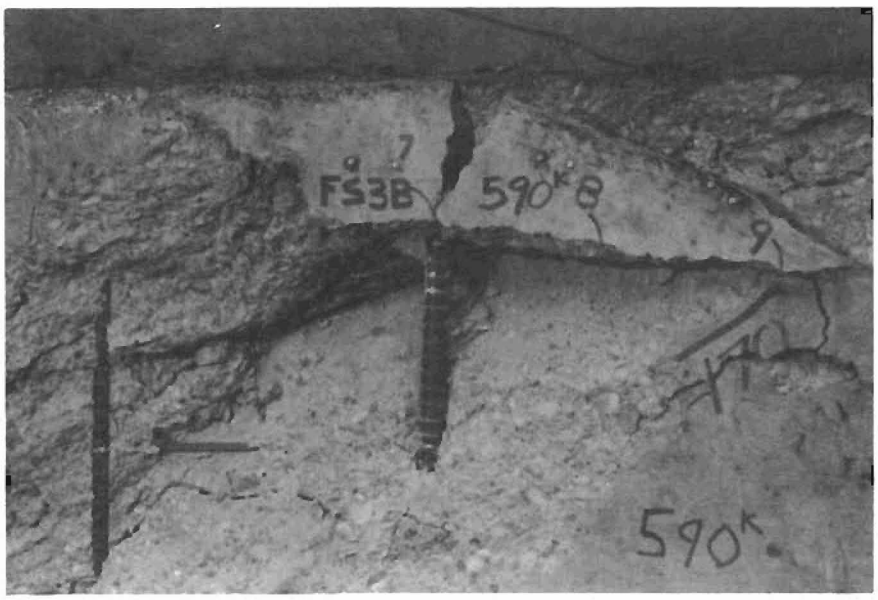

(d) Close up of failure zone. Vertical bar in center has been forced outward

Fig. 3.26 (continued)

increase the load beyond 590 kips met with a sudden rupture of the side face at the point of sharpest curvature at a point 50 in. from the loaded face--well removed from the anchorage zone. A close inspection of the failure area showed the vertical shear reinforcement to be significantly bent outward, as shown in Fig. 3.26d. Furthermore, prior to failure it was noted that a small ledge had formed on the lower side of the tendon path crack on both sides of the specimen. Since this was evidenced on both sides of the specimen, it could only be attributed to the multiple strand tendon flattening out and creating large lateral forces on the tendon duct and side walls. Thus, the failure which was prevented in the anchorage zone by the spiral, was governed by a different mechanism than had been seen in any of the model specimens.

It is important to note here that the multistrand effect and the effect of radial outward forces due to tendon curvature are significant and cannot be found by tests similar to those performed by Zielinski and Rowe [13,14], or Hawkins [15,16] where an external compressive force was applied to the concrete. This was a reason why, when the tendon limit was reached in full-scale series tests FS2A and FS2B, it was decided to not switch to an external load device to continue the test.

Representative plots of the strain along the spiral in FS3A and FS3B are presented in Fig. 3.27. At ultimate load the peak strain in the lighter spiral at FS3A was only 150 microstrain, or approximately 4500 psi--thus it did not yield. The explanation may lie in the fact that failure was impending at the point of maximum curvature at a distance well beyond the end of the spiral. Figure 3.25b with the heavier spiral, on the other hand, indicated that most gages observed considerably higher strains, averaging between 700 to 1400 microstrain (21,000 to 42,000 psi) at ultimate, still below yield. One gage out of 14 registered a peak strain of 3100 microstrain at ultimate--sufficient to yield the spiral steel--but

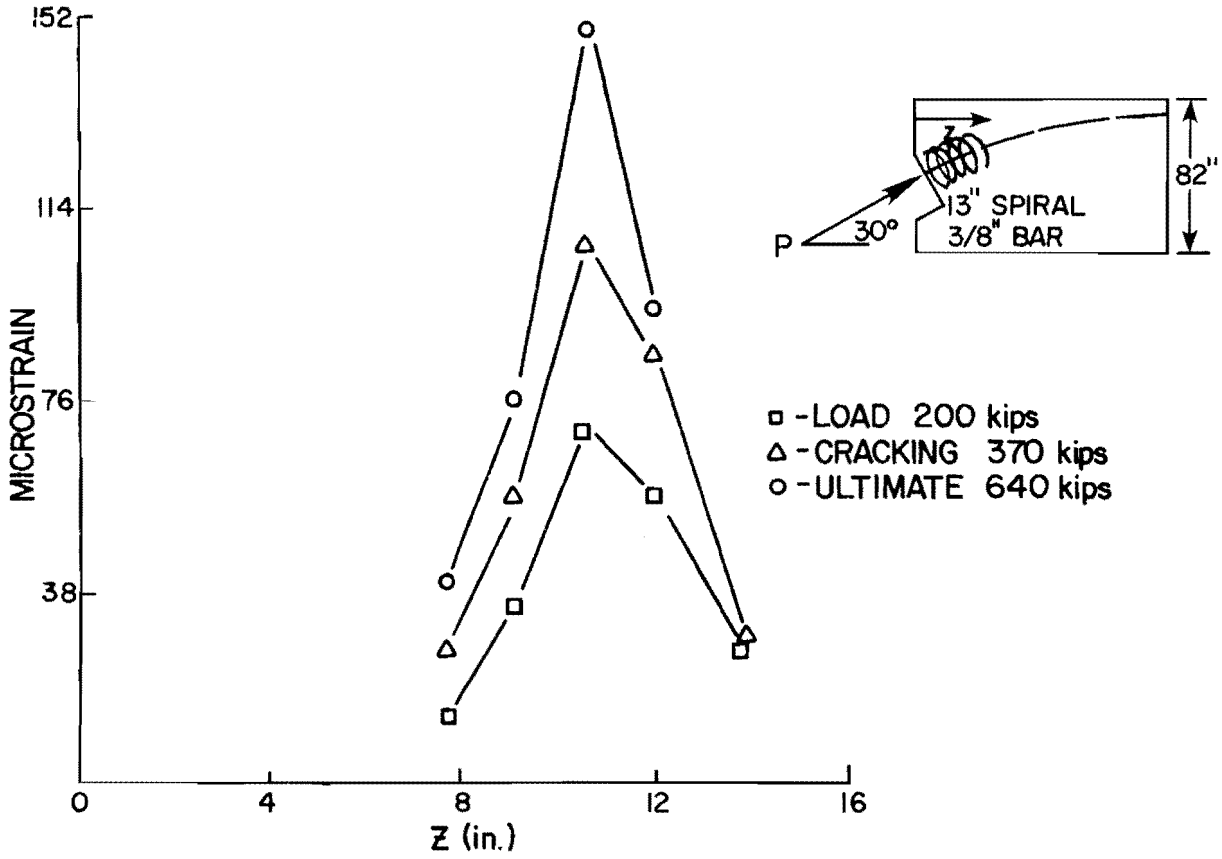

(a) FS3A

Fig. 3.27 Measured spiral strain distribution

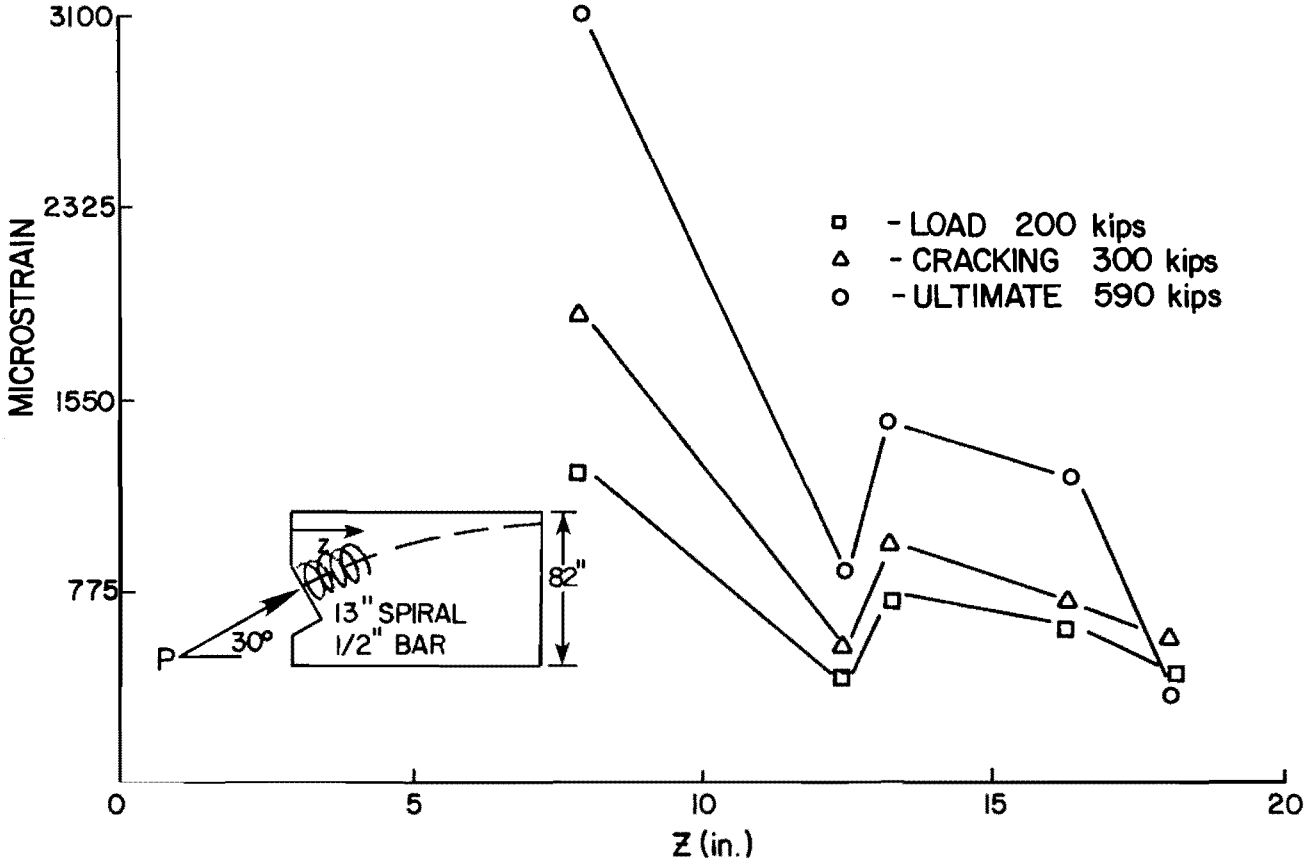

(b) FS3B

Fig. 3.27 (continued

this may have been due to a faulty gage, since gages to either side registered values only one-third as high.

Spalling strain distributions for different load levels are shown in Fig. 3.28. The spalling strains were significantly lower in the specimen with the smaller diameter spiral.

FS4A. Supplemental reinforcement for this specimen consisted of a 3/8 in. ϕ spiral as used in specimen FS3A except 26 in. long. As shown in Fig. 3.29a, the first crack occurred at a load of 400 kips along the tendon path centered 50 in. from the loaded face in the immediate vicinity of the point of maximum curvature. Unlike first cracking in the two previous specimens, the crack was well removed from the anchorage zone. In fact, closer observation revealed that it apparently began at the point where the spiral reinforcement stopped and propagated along the tendon path to the web-flange junction. Crack width measurements were widest near the point of sharpest curvature. At 440 kips, the tendon path crack extended from the anchor plate to the web-flange junction, as shown in Fig. 3.29b. Upper and lower diagonal cracks appeared at a load of 530 kips, emanating from the anchor plate corners. At 550 kips, parallel sets of longitudinal cracks formed roughly 6 in. above and 6 in. below the original tendon path crack, as shown in Fig. 3.29c. A vertical connecting crack between upper and lower longitudinal cracks at the point of maximum curvature also formed at 550 kips. As shown in Fig. 3.29d, ultimate failure occurred at 650 kips and was so catastrophic that it destroyed the entire specimen (FS4A and FS4B). An anchorage zone failure occurred similar to that seen in the models, as shown in Fig. 3.29e, but, in addition, a 2 in. wide crack ran along the entire top of the specimen from end to end. A large longitudinal crack beginning at the corner of the anchorage blockout propagated to the far end web-flange junction, indicated a web shear failure as well. It should be noted that the large longitudinal crack along the top of the specimen would not

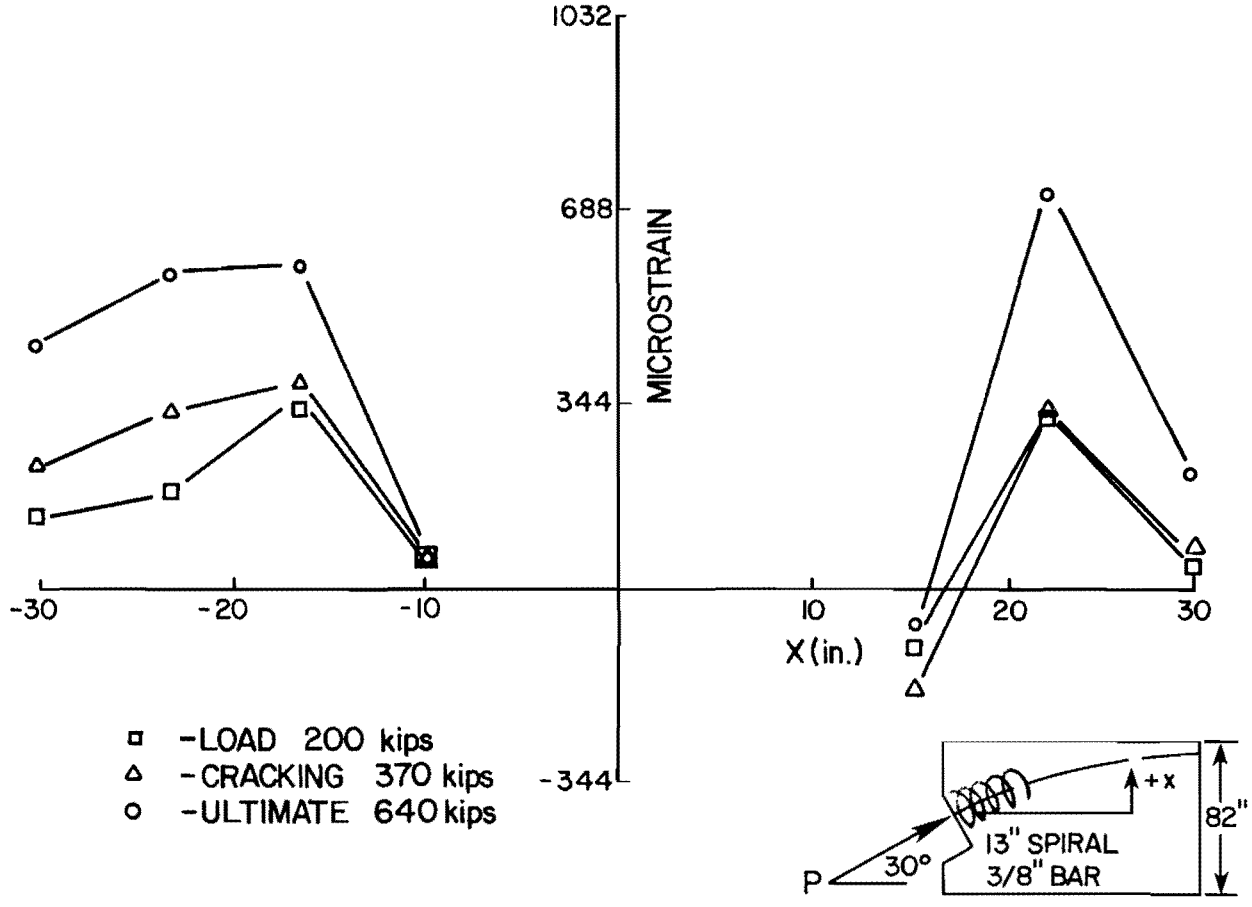

(a) FS3A

Fig. 3.28 Measured spalling strain distribution

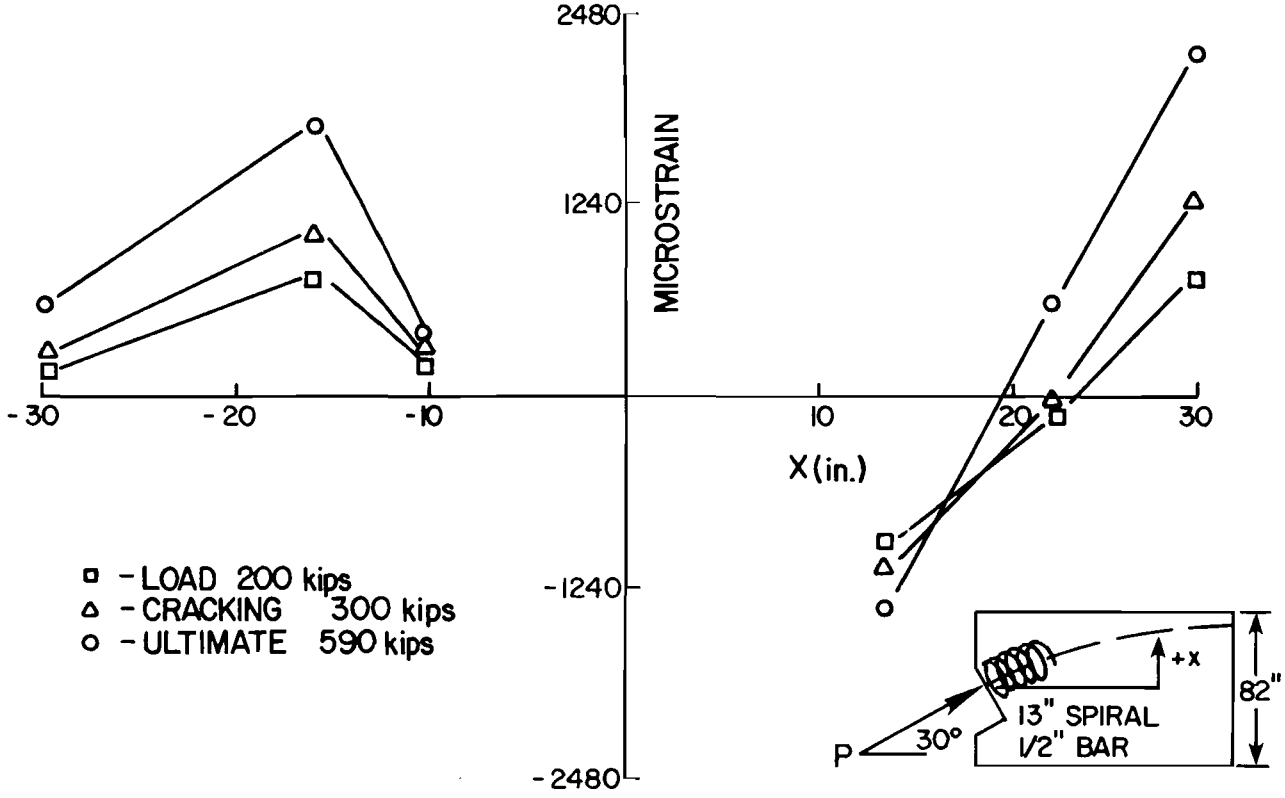

(b) FS3B

Fig. 3.28 (continued)

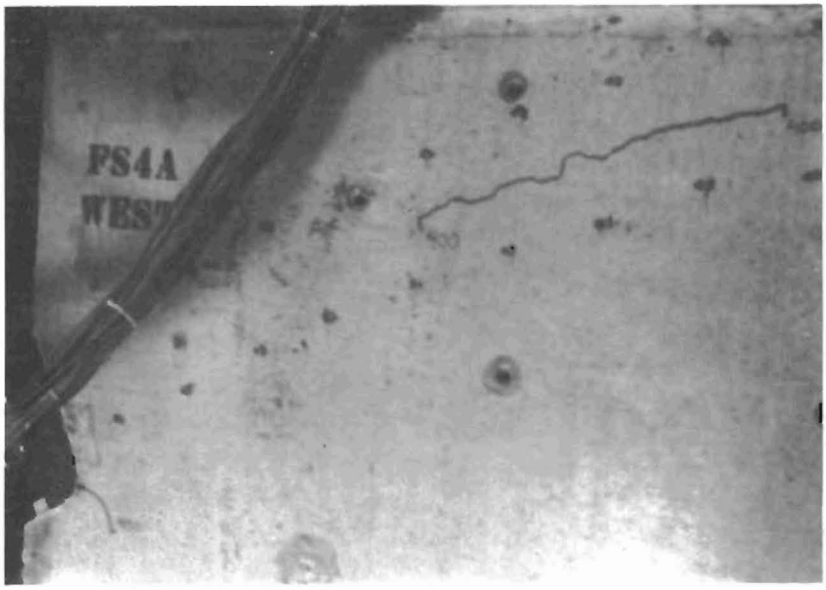

(a) First cracking at point of maximum curvature

(b) Progression of tendon path crack into anchorage zone with increased load

Fig. 3.29 Failure sequence--specimen FS4A

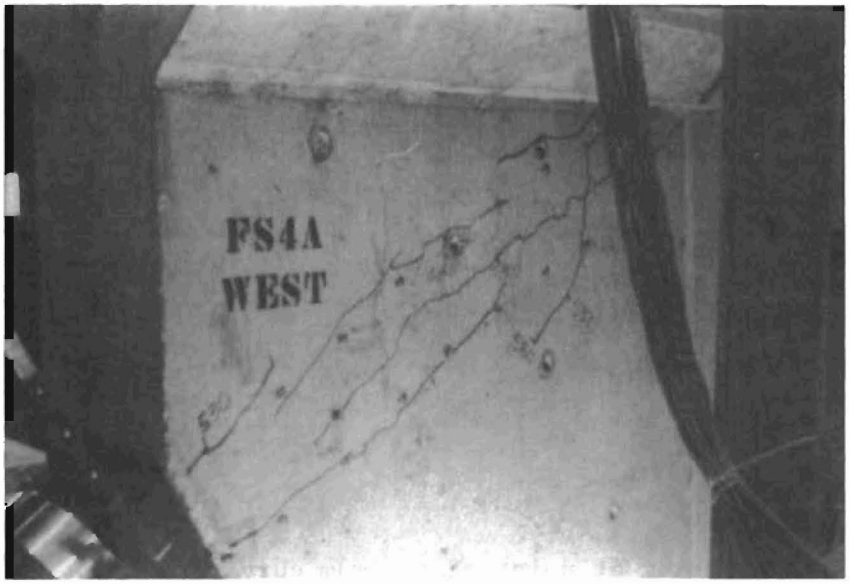

(c) Multiple longitudinal cracks prior to failure

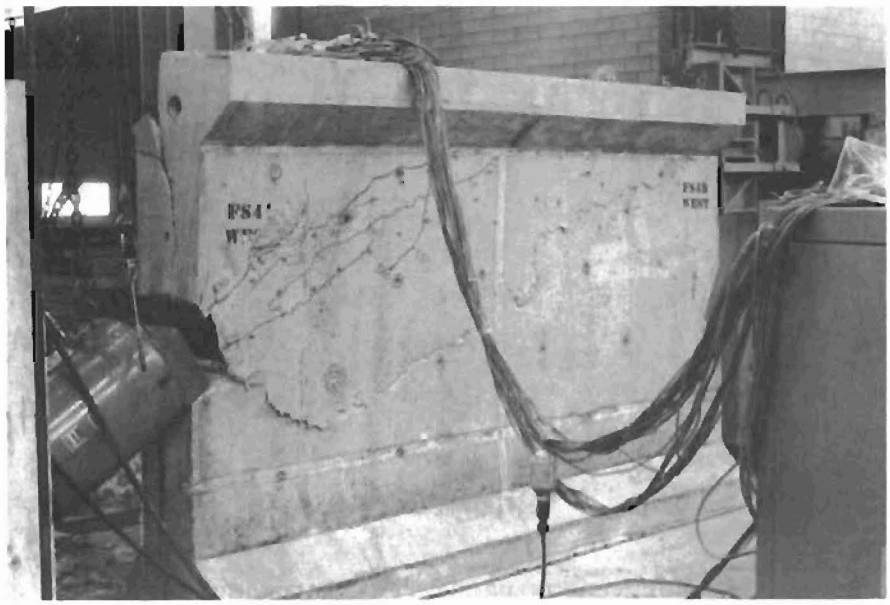

(d) Ultimate failure, 650 kips

Fig. 3.29 (continued)

(e) Ultimate load (650 kips) FS4A.
Close up of anchorage area

Fig. 3.29 (Continued)

have formed in a full box section due to the presence of the top deck steel.

Plots showing strain in the spiral and the spalling distribution at various key load stages are given in Figs. 3.30 and 3.31. Again the highest spiral strain measured is below the yield strain. Although the anchorage zone failure for specimen FS4A was fairly explosive, it should be noted that, as with specimen FS3A, the spiral reinforcement did not yield prior to failure. The maximum stress of 24,300 psi occurred near the far end of the spiral, 25 in. from the loaded face.

A comparison of all full-scale specimens with supplementary anchorage zone reinforcement follows in Sec. 3.4.5. Due to the difficulties encountered in analytically modeling the spiral reinforcement in the anchorage zone, no direct analytical solution was attempted.

3.4.4 Active Reinforcement Series--(Lateral Prestress)

3.4.4.1 Specimen Design. In one of his more recent texts [17] Guyon made the following observation concerning inclined tendons used in cantilevered box girder bridges:

> If either the thickness or the strength of the concrete is inadequate, the section will crack along the line of the tendon. Cracking of this kind is not prevented by means of ordinary untensioned "passive" stirrups. Up to a point, cracking of this nature can be prevented either by placing the anchors on load spreading plates or better, by the use of active reinforcement; that is, by creating a sufficient vertical prestress behind the anchors by means of tensioned stirrups.

Other than this brief statement, no mention is made of the qualitative details of how much vertical prestress should be used for a given situation, nor where it should be placed for optimum performance.

A model test performed by Cooper [9], in which the web section was uniformly laterally post-tensioned along its length, indicated that cracking and ultimate loads were significantly

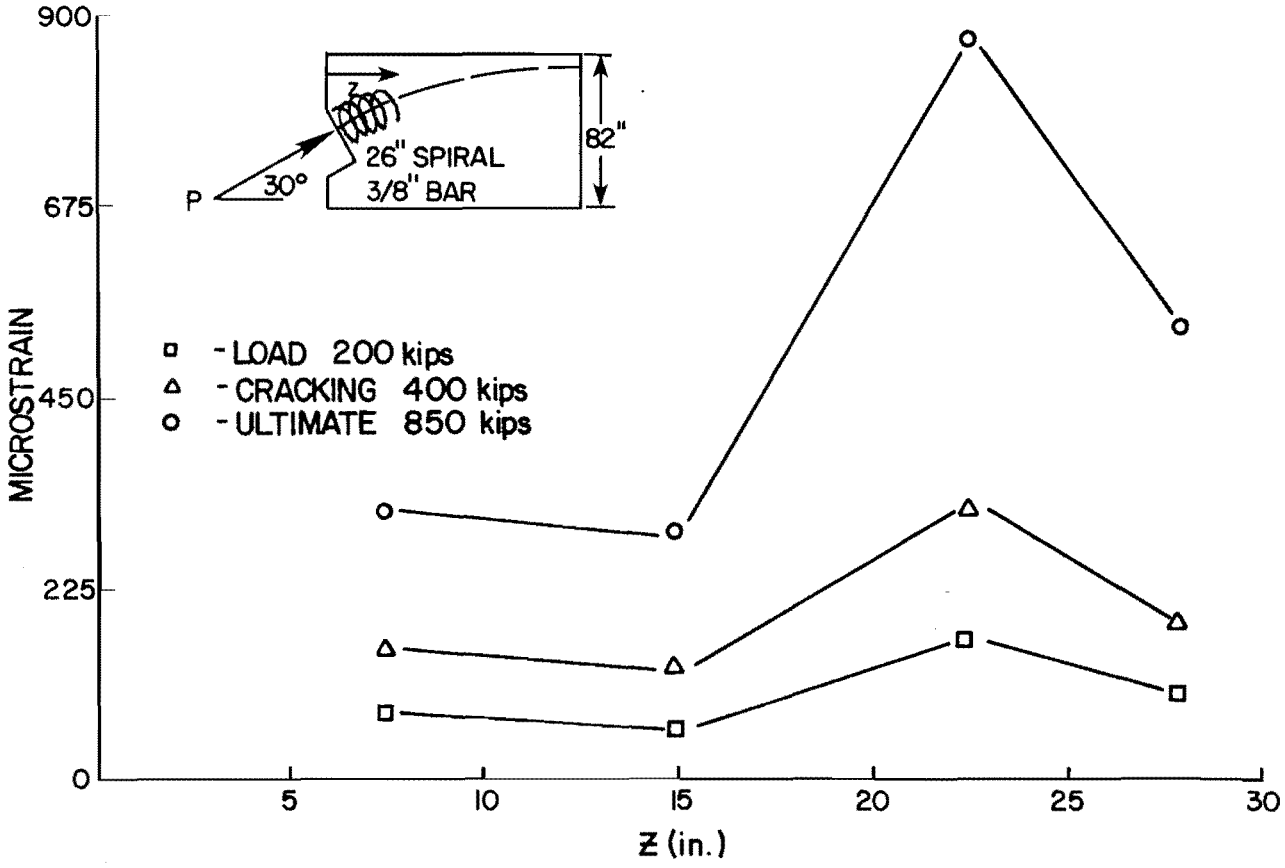

Fig. 3.30 FS4A measured spiral strain distribution

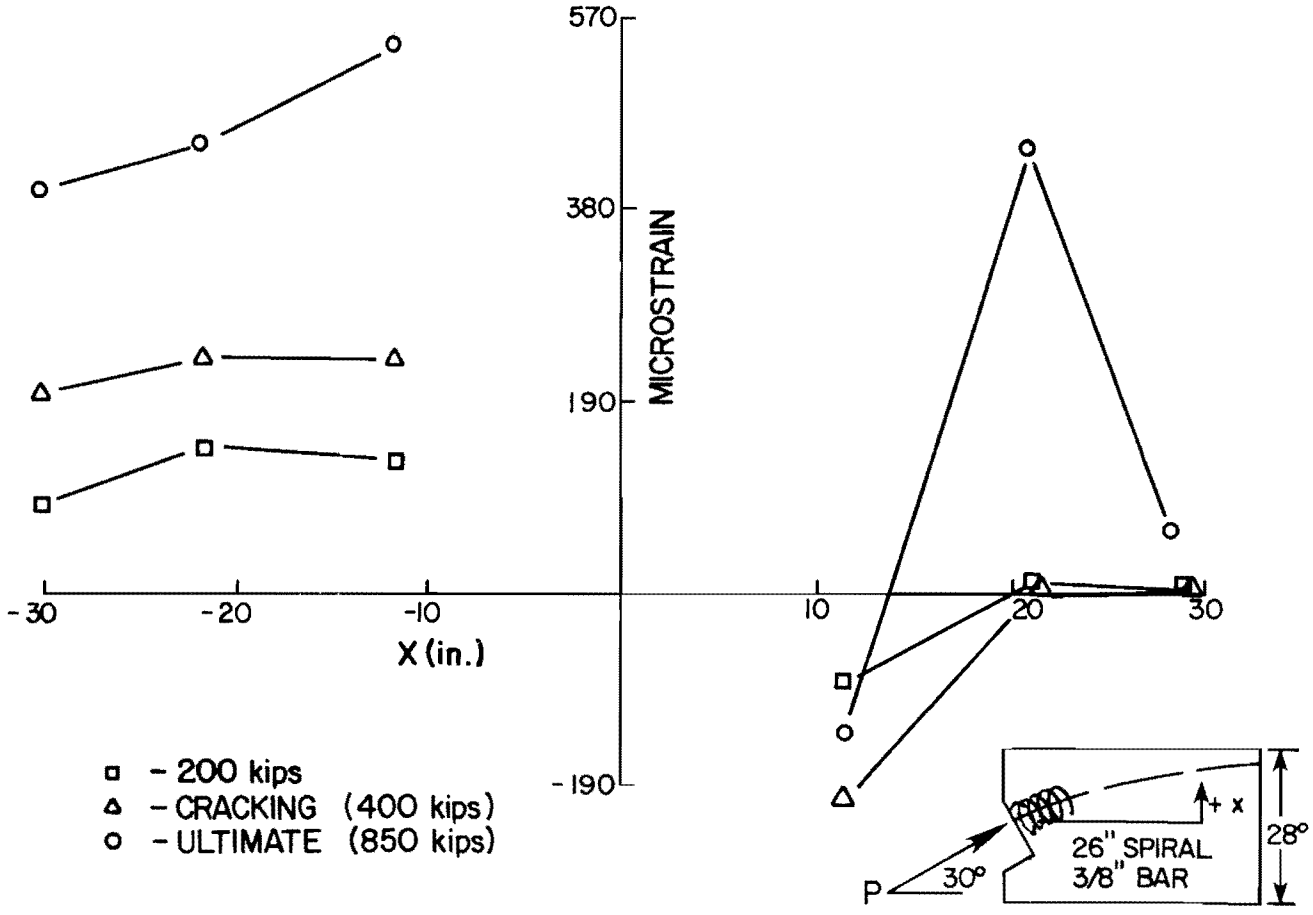

Fig. 3.31 FS4A experimental spalling strain distribution

raised by this technique. Since Cooper's test was a crude approach to the problem (i.e., vertically post-tension the entire web), and Guyon's recommendations were vague, a practical approach for designing lateral prestress to control anchorage zone cracking was not available. The full-scale specimens FS5A and FS5B were thus designed to accomplish a twofold purpose:

(1) To locate the optimum location for the placement of the lateral prestress, thus minimizing the amount to be used.

(2) To provide a means of isolating the crack initiating mechanism.

In order to accomplish this, an extensive series of 3D FEM analyses was performed using the previously developed mesh [1] for the curved tendon prototype, but with application of the lateral prestress at certain key mesh points. In order to prevent a twisting moment from being set up in the web section, two vertical prestress tendons were placed symmetrically on opposite sides of the tendon duct. The results of the analysis presented in Figs. 3.32 and 3.33 indicate:

(1) Locating the lateral prestress tendons at a distance of approximately $z = 0.8a$ from the loaded face achieves maximum precompression of the tensile bursting stress. For full-scale specimens this was at a distance of 32 in. from the end face. At this particular location, the maximum tensile spalling stress is reduced only slightly.

(2) Locating the lateral prestress tendons as close as possible to the loaded face achieves maximum precompression of the spalling tensile stresses, while compressing the bursting stress only slightly.

(3) Performance of the vertical prestress is not affected by the spacing across the width of the web, i.e., two tendons placed next to the tendon duct yield the same stress distribution as two tendons

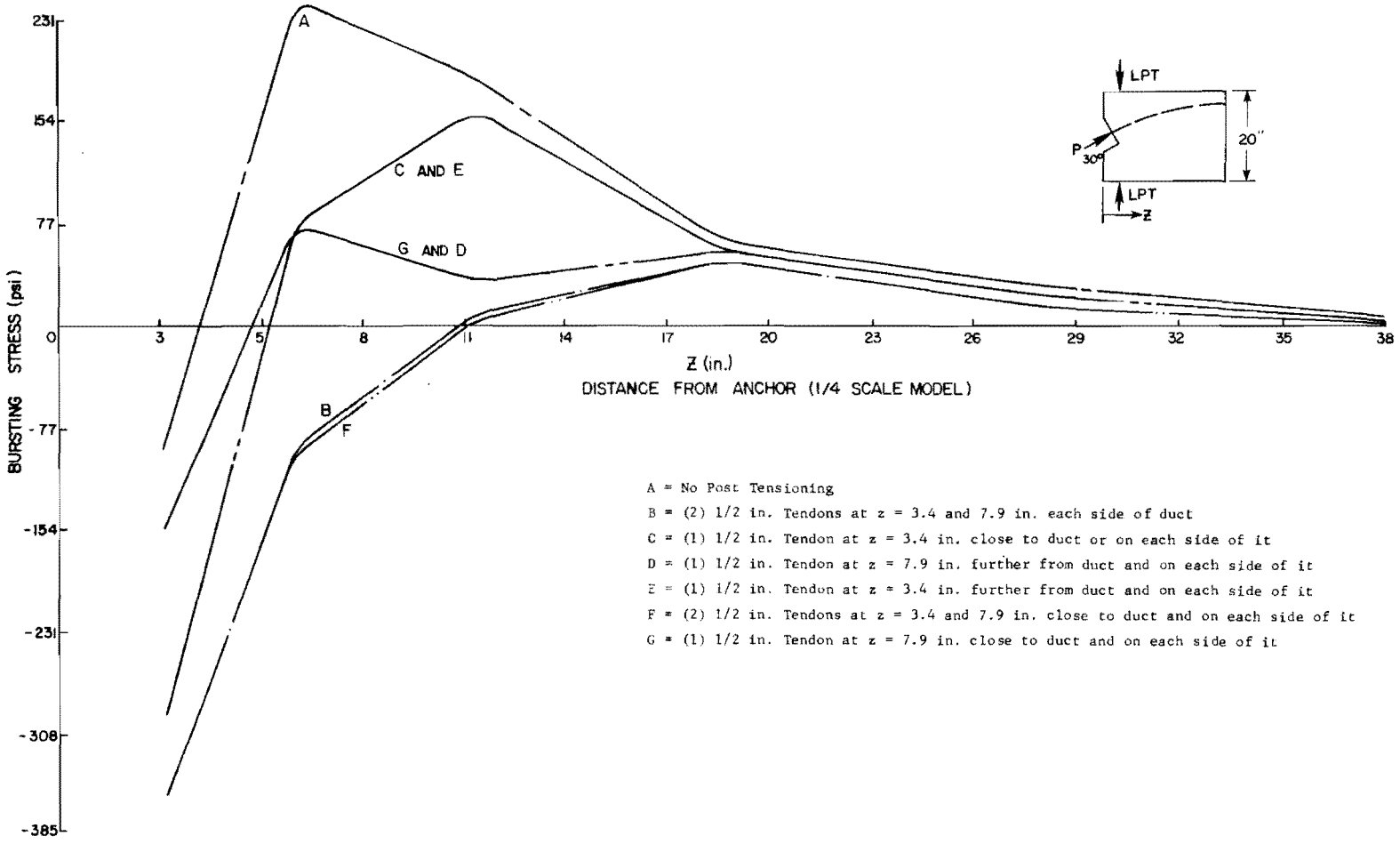

Fig. 3.32 3D FEM analysis--effects of lateral post-tensioning on bursting stress distribution

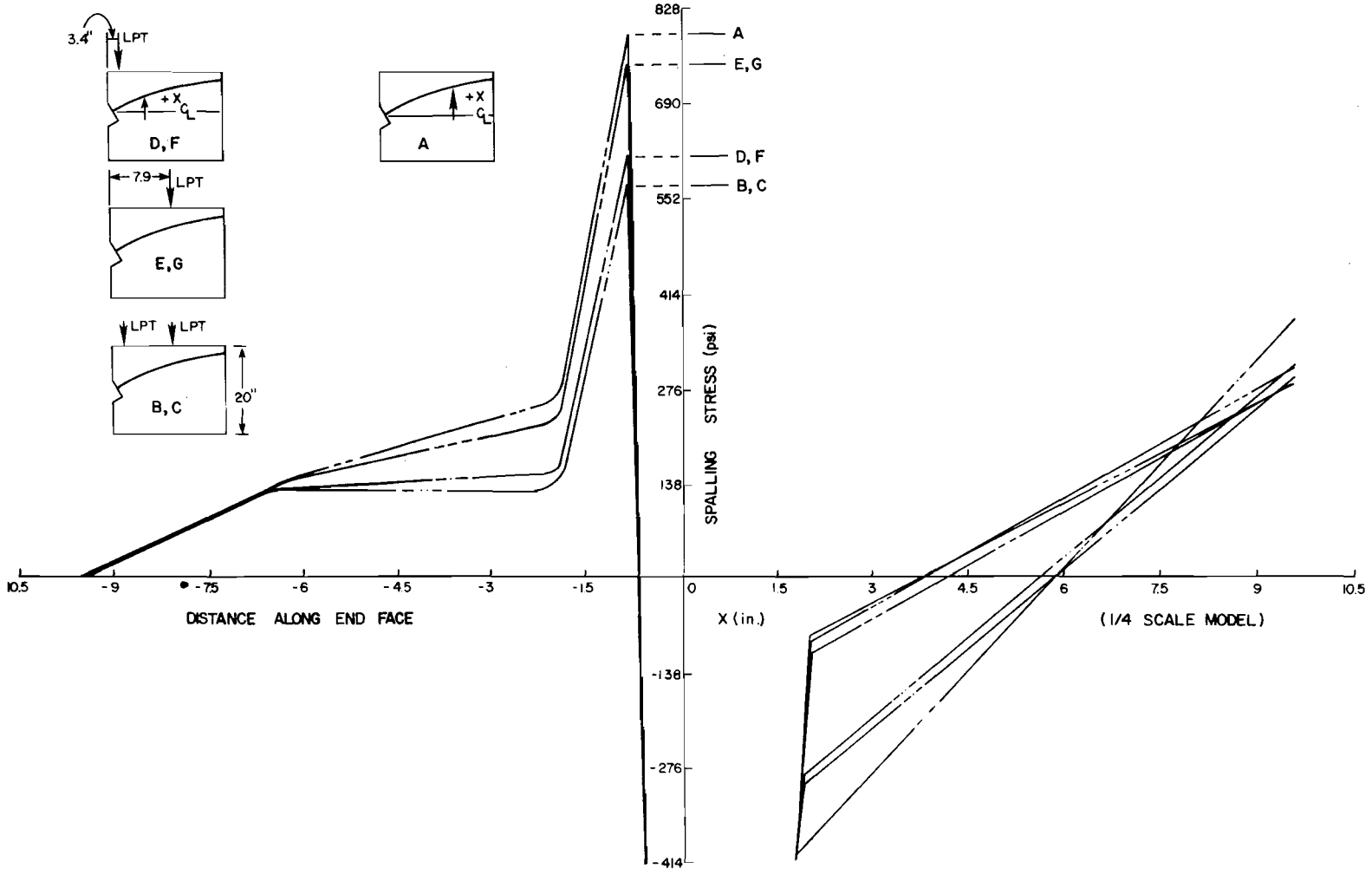

Fig. 3.33 3D FEM analysis--effects of lateral post-tensioning on spalling stress distribution

located near the side face, so placement tolerance is not critical.

Based upon this analysis, specimen FS5A had two 0.5 in. diameter, 270 ksi greased, sheathed (41.3 kip ultimate) vertical prestress tendons placed at a distance of 32 in. from the loaded face. Specimen FS5B had identical tendons placed at a distance of 6 in. from the end face (against the anchor blockout). All vertical tendon pairs were stressed to 60 kips total force before application of the main longitudinal tendon loading to cracking and ultimate. Stressing of the lateral tendons was accomplished using two 30 ton centerhole rams. Load was monitored with load cells atop the rams as shown in Fig. 3.34.

The level of lateral prestress force chosen (60 kips) was selected based on the results of the finite element analyses. If one thinks of the anchorage zone as extending a length equal to the overall depth of the girder (80 in.) the nominal lateral prestress over this zone would be 60000/(80)(12) or approximately 60 psi.

3.4.4.2 FS5A. This specimen had 60 kips lateral post-tensioning at 32 in. from the loaded face and no other supplementary reinforcing. As shown in Fig. 3.35a, first cracking occurred at 460 kips and, although the crack generally followed the tendon path, it seemed to be shifted to a higher position than witnessed in previous tests. The crack propagated from the anchor to the web-flange junction. Once cracking was achieved, the load was released and specimen FS5B tested to failure. This was to ensure that cracking data were obtained for both sides in the event that failure would result in destruction of the specimen as in FS4A.

After completion of testing of FS5B, specimen FS5A was reloaded. At 490 kips, the lower diagonal crack formed at the anchor plate. The upper diagonal formed at 600 kips on the west

(a) FS5A: location of lateral prestress and stressing system

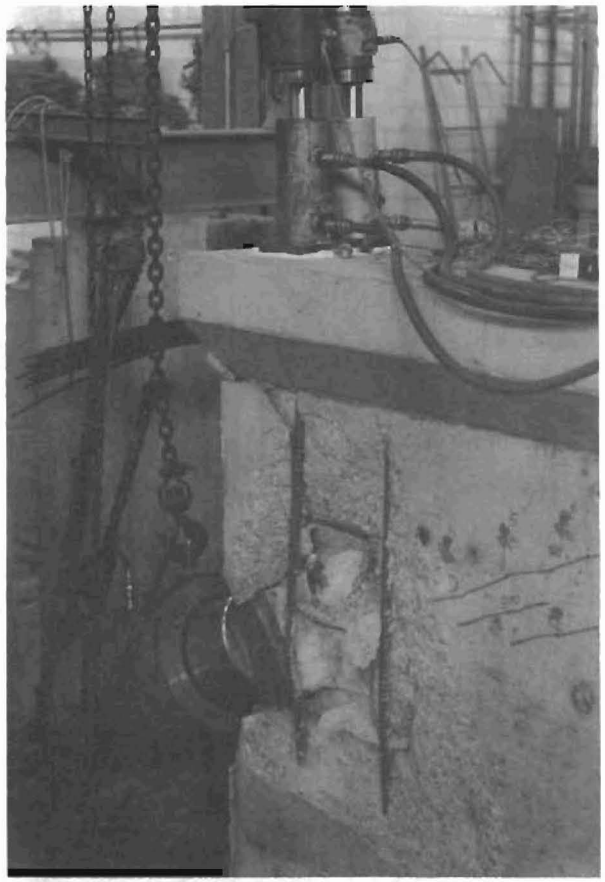

(b) FS5B: lateral prestress as close as possible to end face

Fig. 3.34 Location of lateral prestress

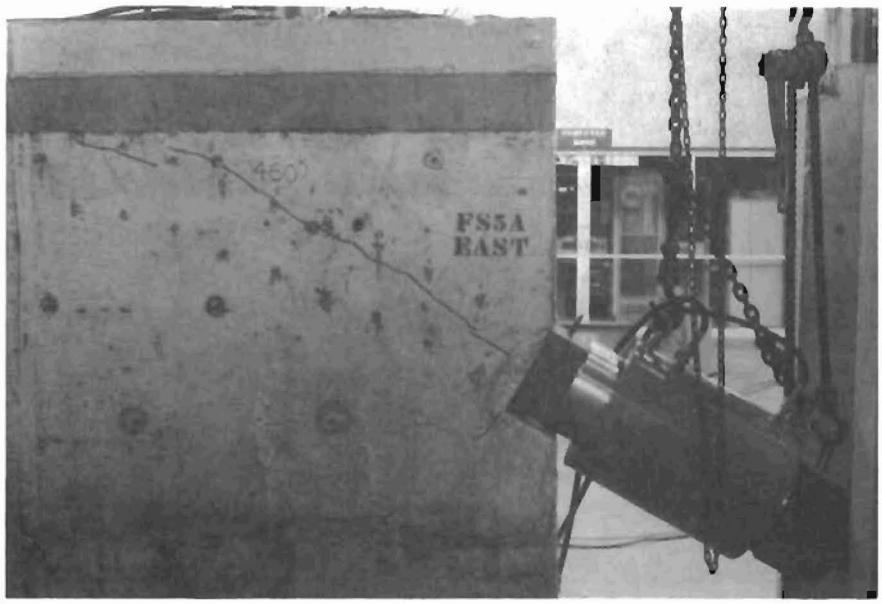

(a) First cracking along tendon path, 460 kips

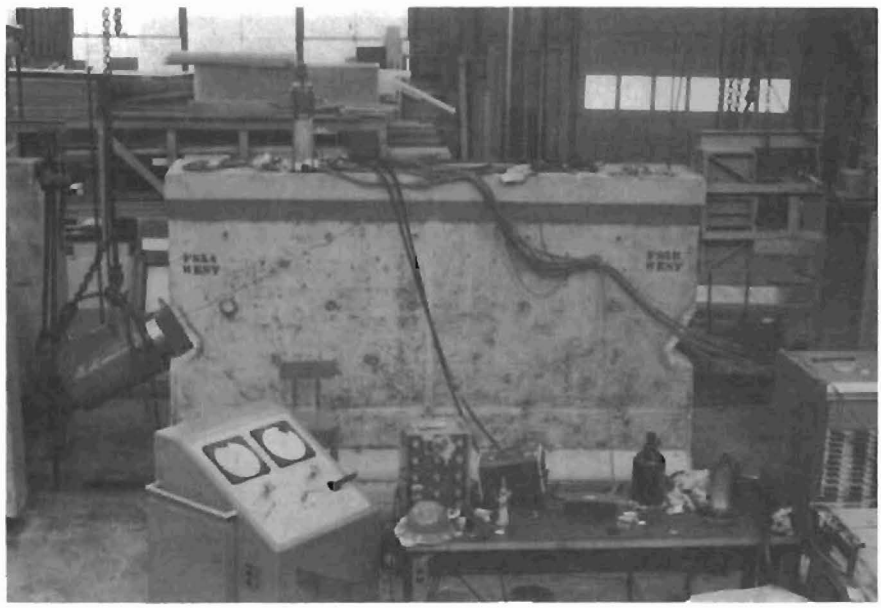

(b) Overall view FS5A showing location of LPT (lateral post-tensioning) jacking system

Fig. 3.35 Failure sequence specimen FS5A

(c) Diagonal cracks, west side

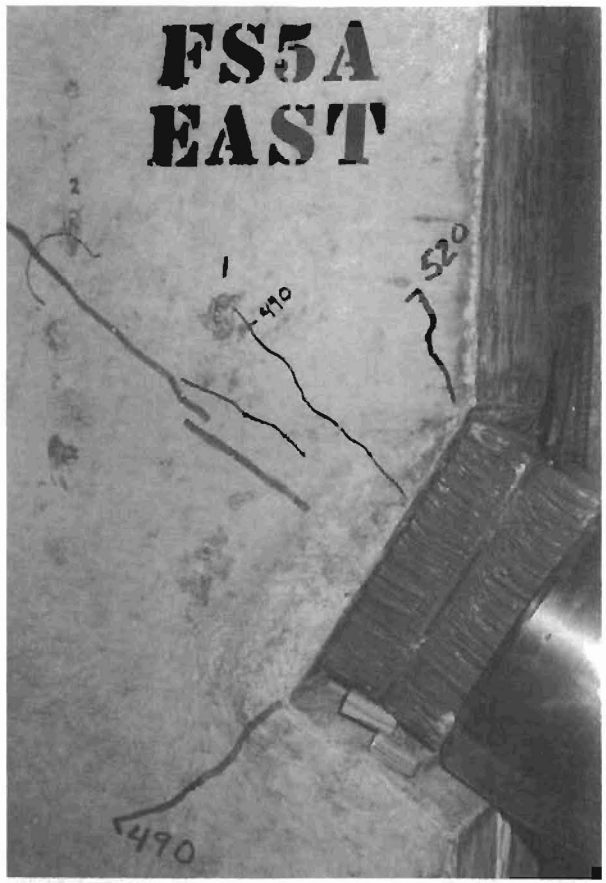

(d) Diagonal cracks, east side

Fig. 3.35 (Continued)

(e) Longitudinal cracks near point of maximum curvature (east side) at 630 kips

(f) Longitudinal cracks near point of maximum curvature (west side)

Fig. 3.35 (continued)

face and at 520 kips on the east face (see Fig. 3.35c and d). Between 630 and 690 kips a series of parallel longitudinal cracks, shown in Fig. 3.35e and f, formed above or below the original tendon path crack. Failure was considered imminent, but at a load of 720 kips the far end flange (which had been repaired after the failure of FS5B) ruptured and no further load could be applied.

3.4.4.3 FS5B. This specimen had 60 kips lateral post-tensioning at 6 in. from the loaded face and no other supplementary reinforcing. As shown in Fig. 3.36, first cracking occurred at 540 kips which was 80 kips above FS5A. Like FS5A, the crack followed the general trend of the tendon path but was shifted upward. Lower diagonal cracks appeared on both sides at 630 kips, and the upper diagonal formed at approximately 790 kips, as shown in Fig. 3.36c and d. No further change took place until 870 kips, at which point multiple longitudinal cracks, some as wide as 0.100 in., formed near the point of maximum curvature, as shown in Fig. 3.36f. These indicated a possible side face blowout similar to FS3B was imminent. The load was maintained, however, until 900 kips, at which point, as shown in Fig. 3.36g, the anchorage zone failed explosively accompanied by a loud explosion which hurled 30 pound pieces of concrete as far as 30 ft. from the specimen. The sudden failure was apparently due to the snapping of the two vertical prestress strands, as shown in Fig. 3.36h. After failure, a distinct cone of crushed concrete was attached to the anchor, as shown in Fig. 3.36i.

3.4.4.4 Strain Distribution. Bursting strain distributions at key load stages are presented in Figs. 3.37 and 3.38. Comparisons to the 3D finite element solutions are given in Figs. 3.39 and 3.40. Figure 3.41 compares the bursting strain distributions of the laterally post-tensioned specimens with that for FS2B where no supplementary reinforcement was provided. The experimental data agree well with the trends predicted by the program, although in

(a) First cracking at 540 kips along tendon path

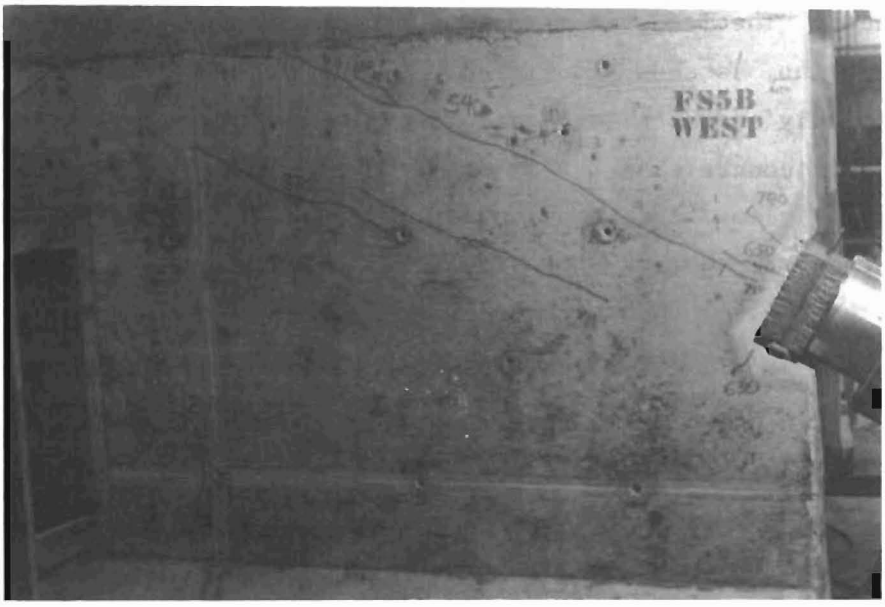

(b) Formation of multiple longitudinal cracks just prior to failure

Fig. 3.36 Failure sequence specimen FS5B

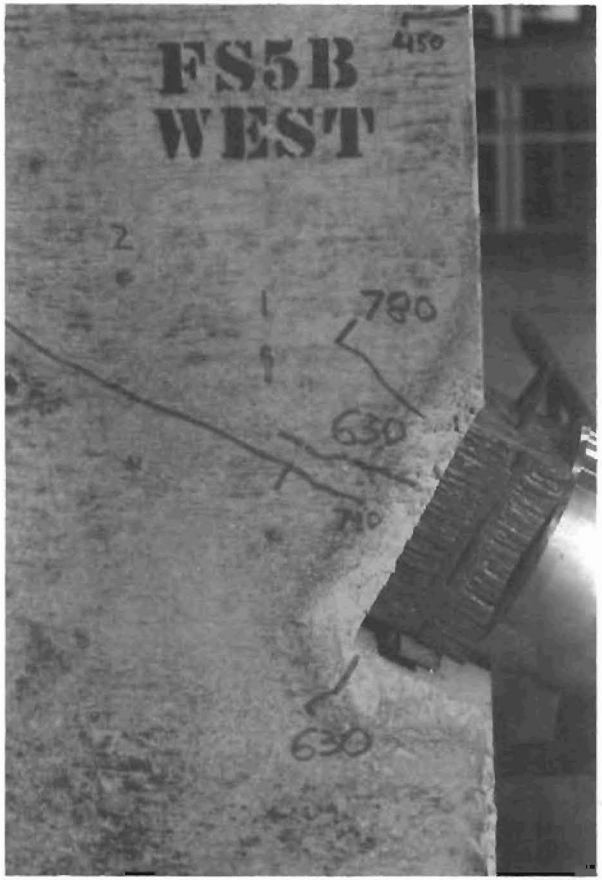

(c) Diagonal cracking, west side

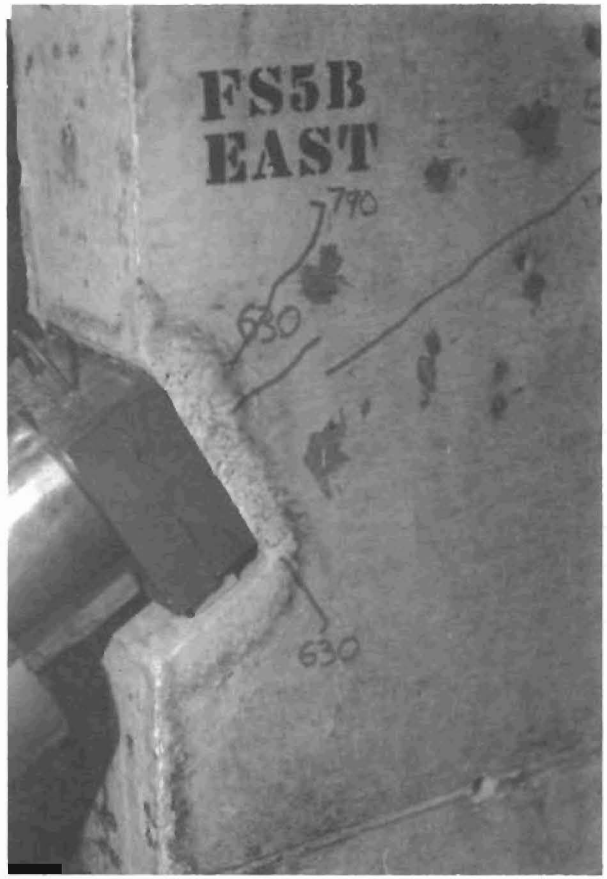

(d) Diagonal cracking, east side

Fig. 3.36 (continued)

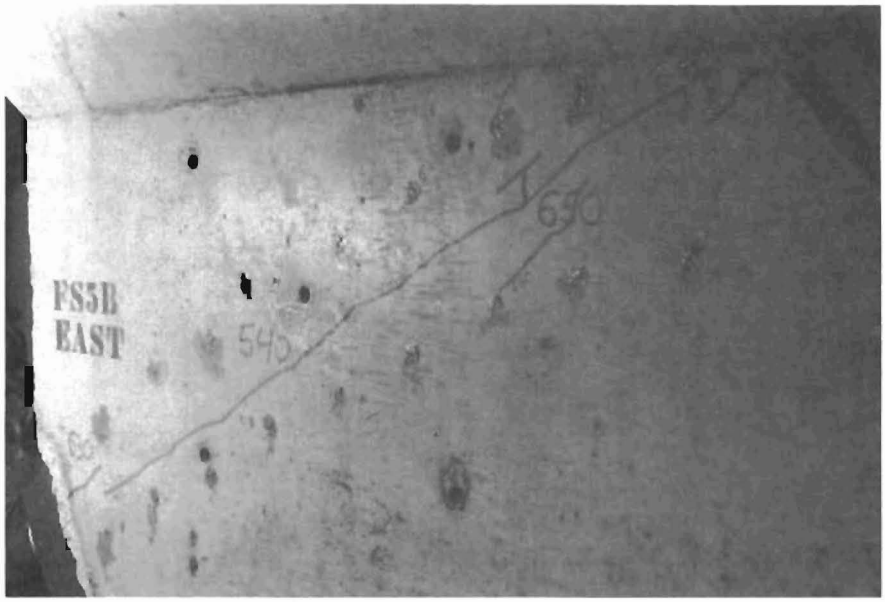

(e) East side at 650 kips

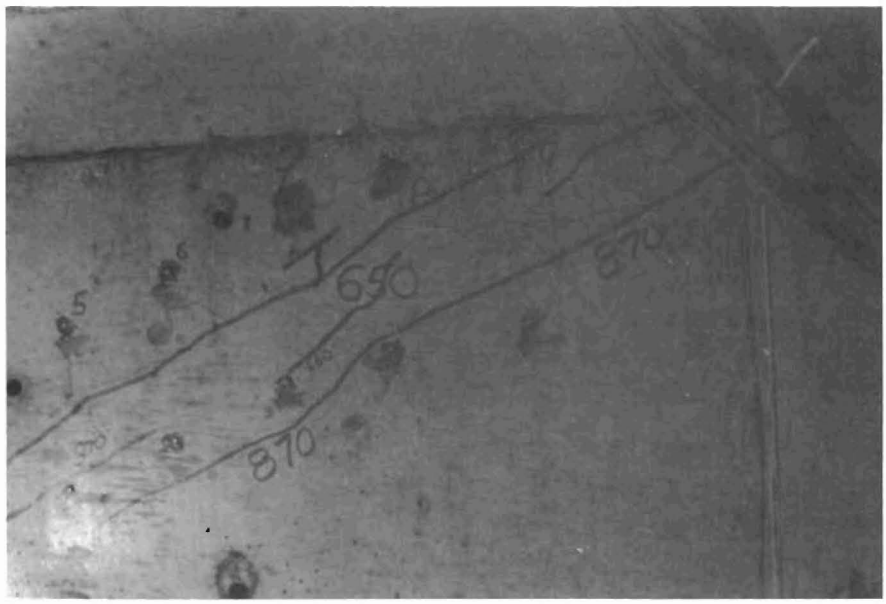

(f) East side just prior to failure

Fig. 3.36 (continued)

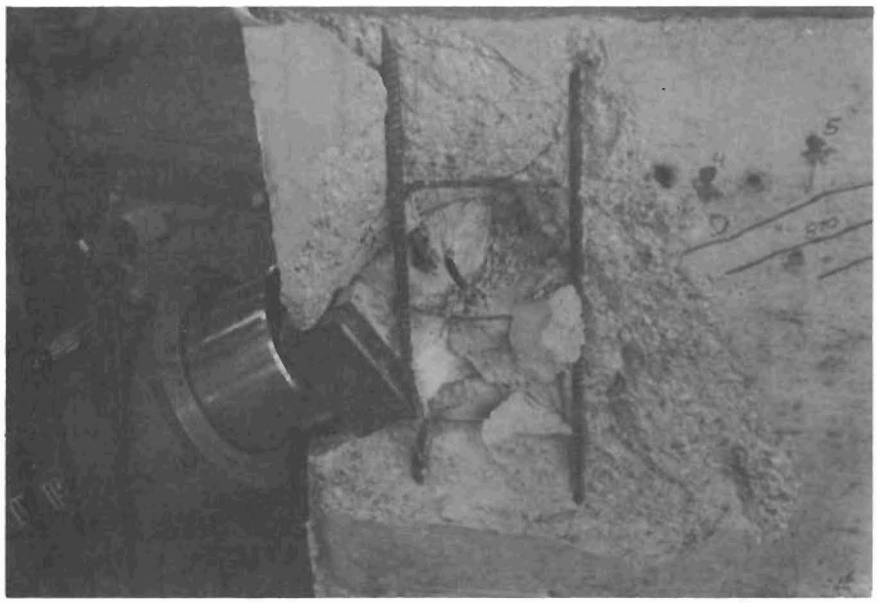

(g) Ultimate failure--explosive rupture of anchorage zone at 900 kips

(h) Failure of lateral prestress tendons initiated explosive failure

Fig. 3.36 (continued)

(i) Cone of crushed concrete, still attached to anchor, removed from specimen after failure

Fig. 3.36 (continued)

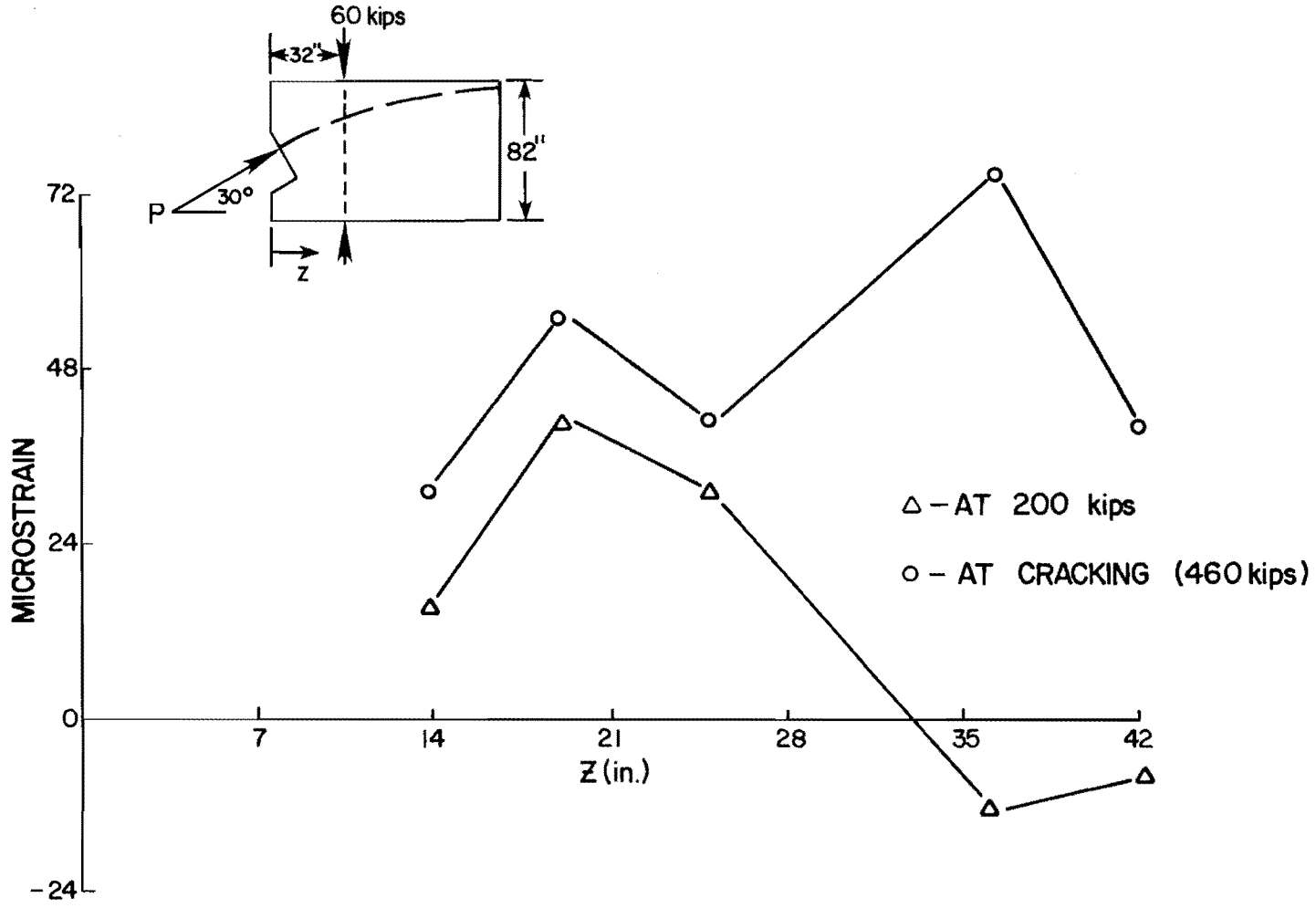

Fig. 3.37 FS5A experimental bursting strain distribution

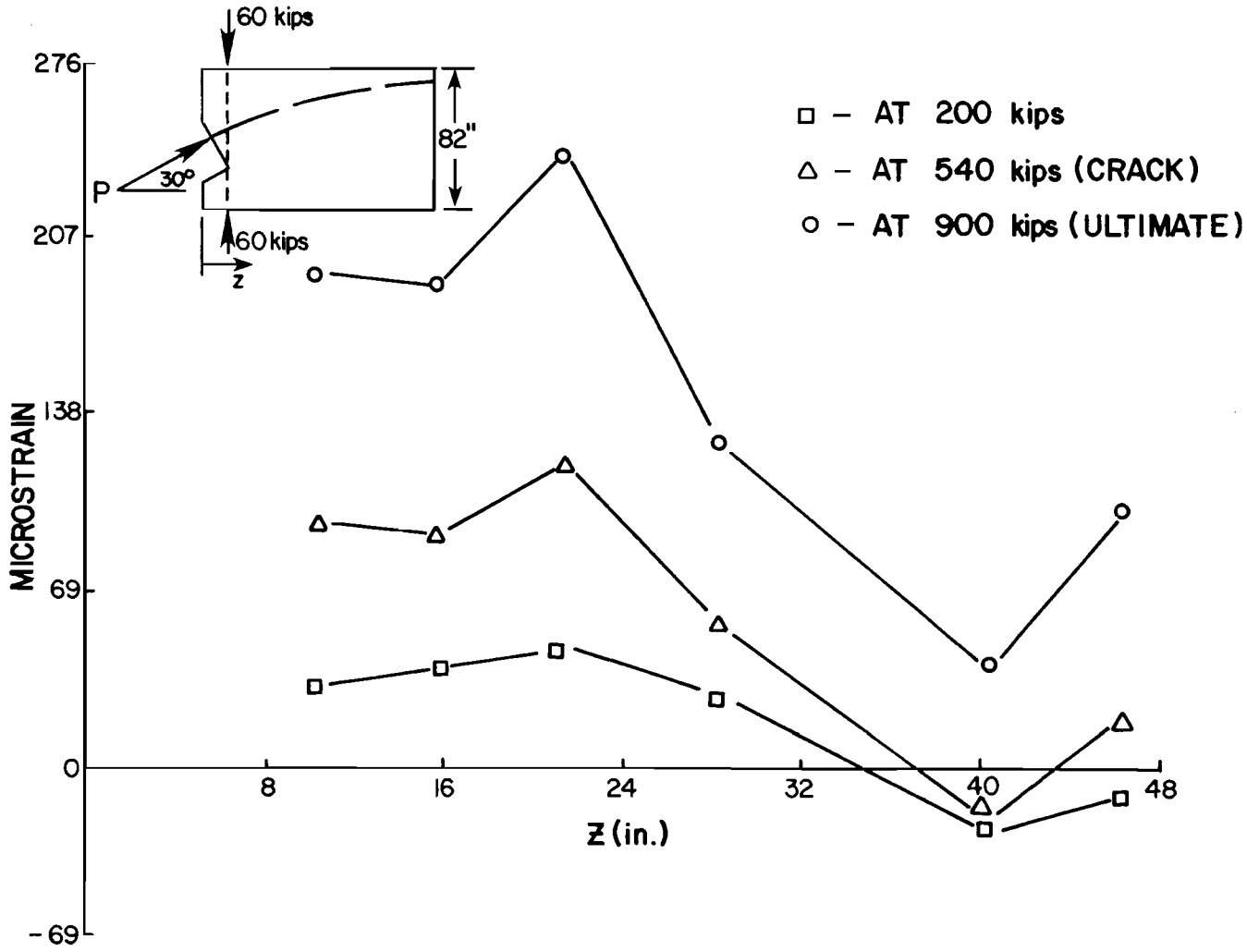

Fig. 3.38 FS5B experimental bursting strain distribution (lateral post-tension series)

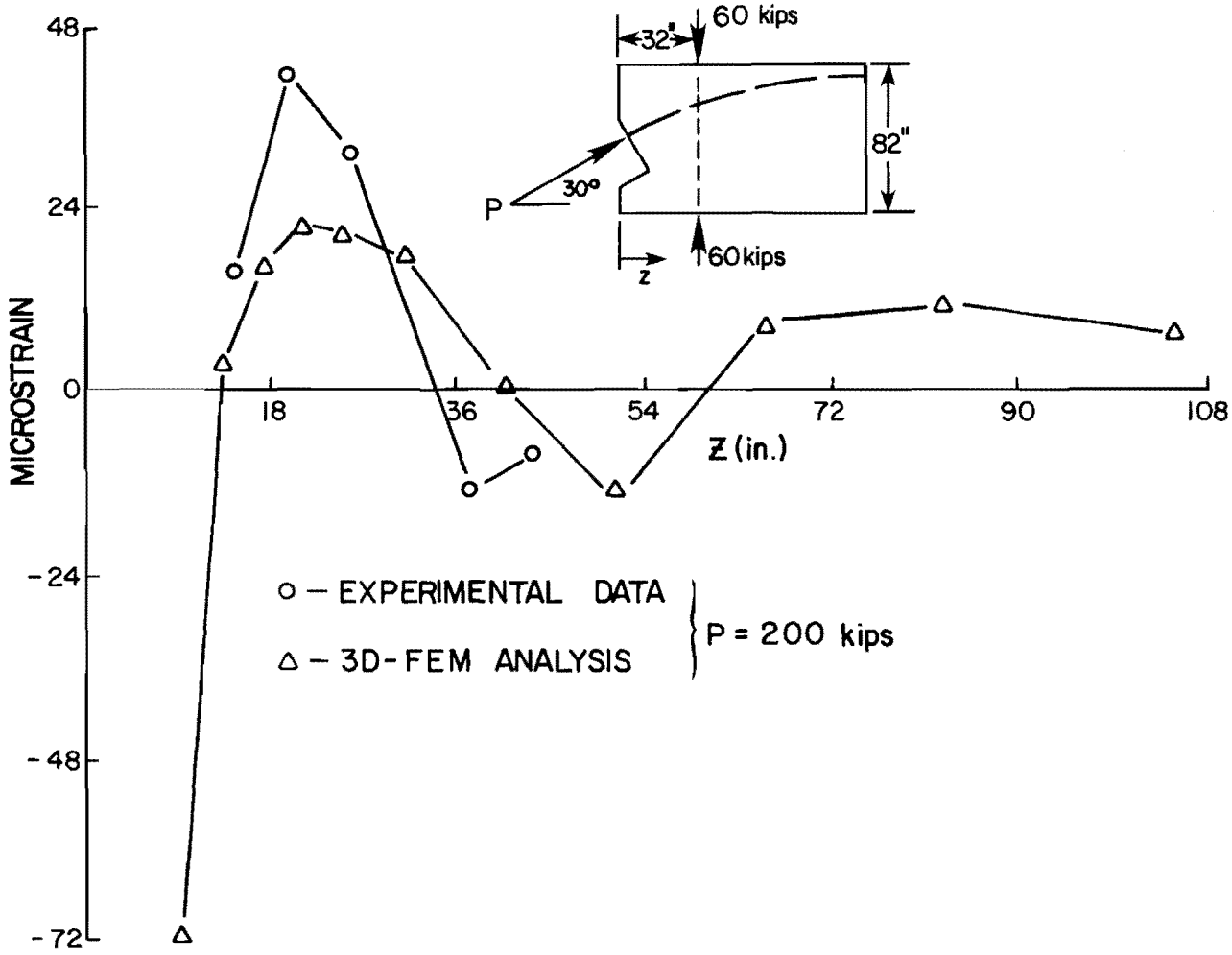

Fig. 3.39 FS5A 3D-FEM vs experimental bursting strain distribution

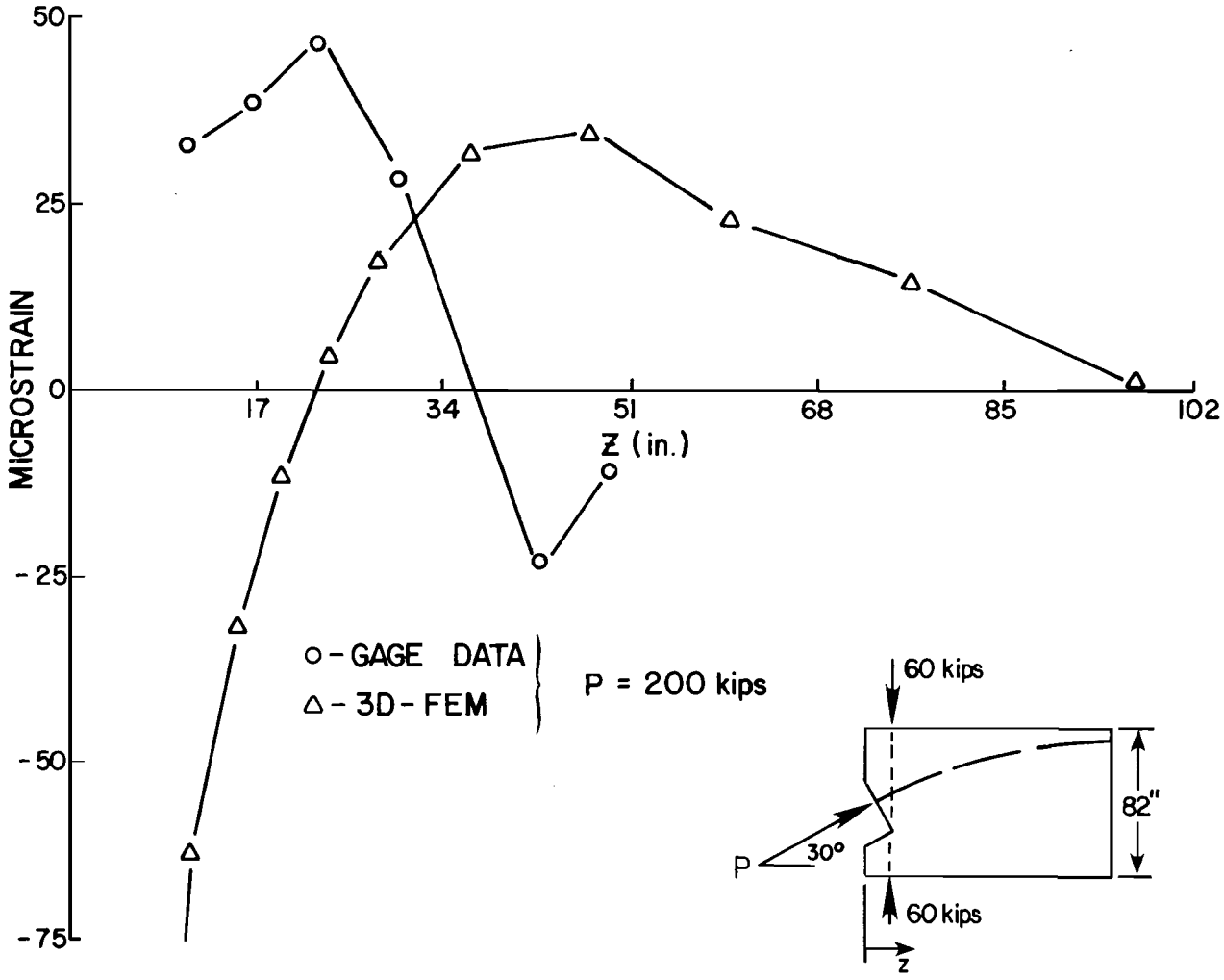

Fig. 3.40 FS5B 3D-FEM vs experimental bursting strain distribution

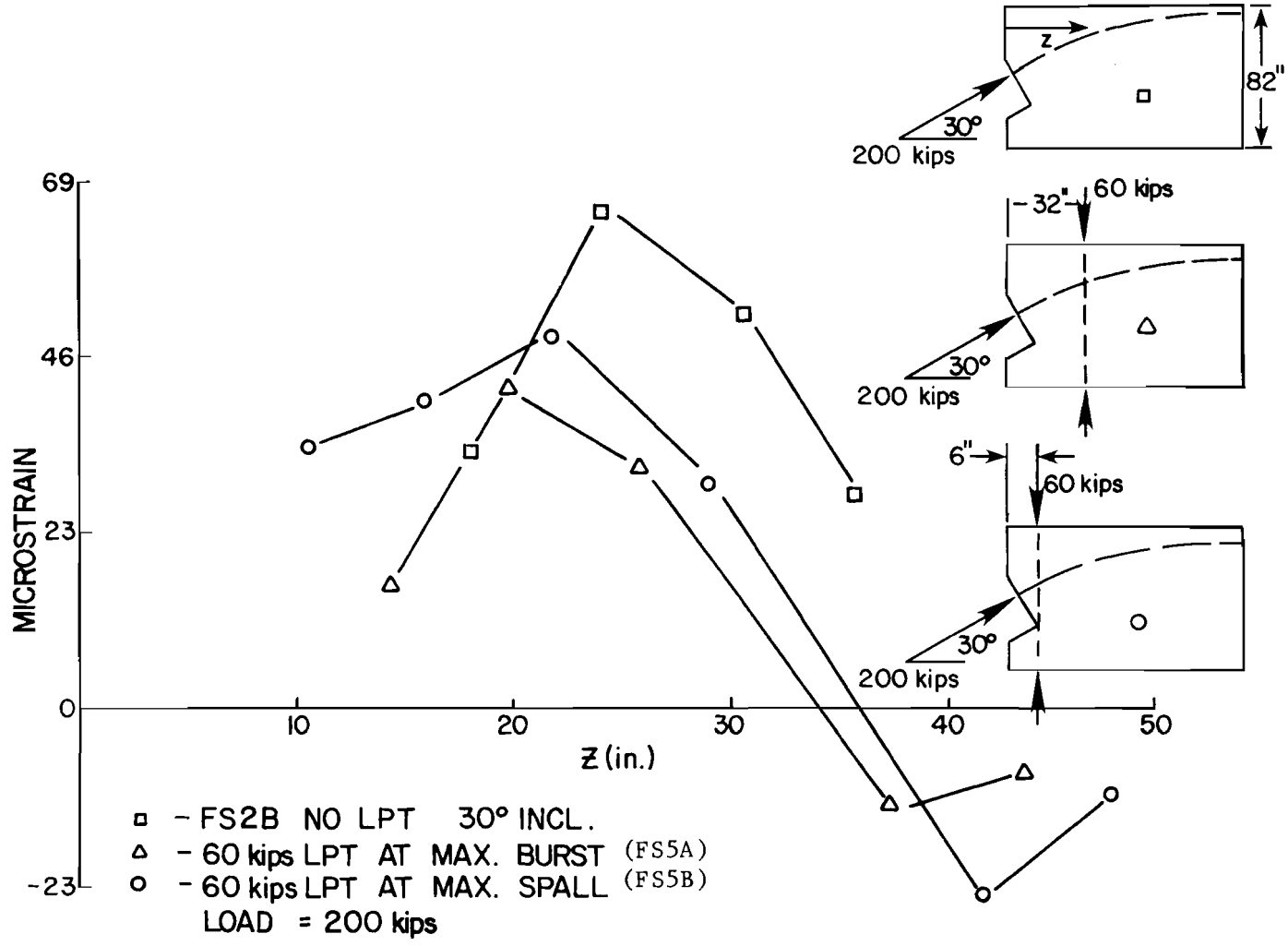

Fig. 3.41 Experimental bursting strain distribution--LPT series

some cases the maximum tensile strain measured physically was higher than the analytical value. Figure 3.41 indicates that the lateral post-tensioning would be expected to reduce bursting strain by about one-third.

Spalling strain distributions are presented in Figs. 3.42 and 3.43 for key load stages. Figure 3.44 compares the various lateral post-tensioning schemes and indicates a similar trend to that predicted analytically: lateral prestress located for maximum precompression of the bursting strain (FS5A) has only slight effect on the spalling distribution; lateral prestress located close to the anchorage produces a significant drop in the maximum spalling strain. Figures 3.45 and 3.46 show a typical comparison between the spalling distribution based on experimental data and that predicted analytically. The excellent correlation was a result of two improvements in the instrumentation following experience with full-scale specimens FS1 through FS4.

(1) Gages were directly wired to the end form so as to place them as close as possible to the end face where the maximum spalling strain occurs.

(2) Dual gages were placed at each location so as to ensure reliability of the data.

It is apparent from this test series that the governing tensile stress in the anchorage zone which initiates formation of the tendon path crack is not the bursting stress as believed by previous researchers. Specimen FS5A, with a lower peak bursting tensile stress (43 percent lower as analytically predicted, 28 percent lower as measured experimentally) than that for FS5B, cracked at a load 15 percent below that for FS5B in which the spalling stresses were precompressed. More likely, it seems that the spalling peak strain offers a better indicator of the load to initiate first cracking. The subject of crack prediction through consideration of the analytically calculated peak spalling strain is discussed in the final report in this series.

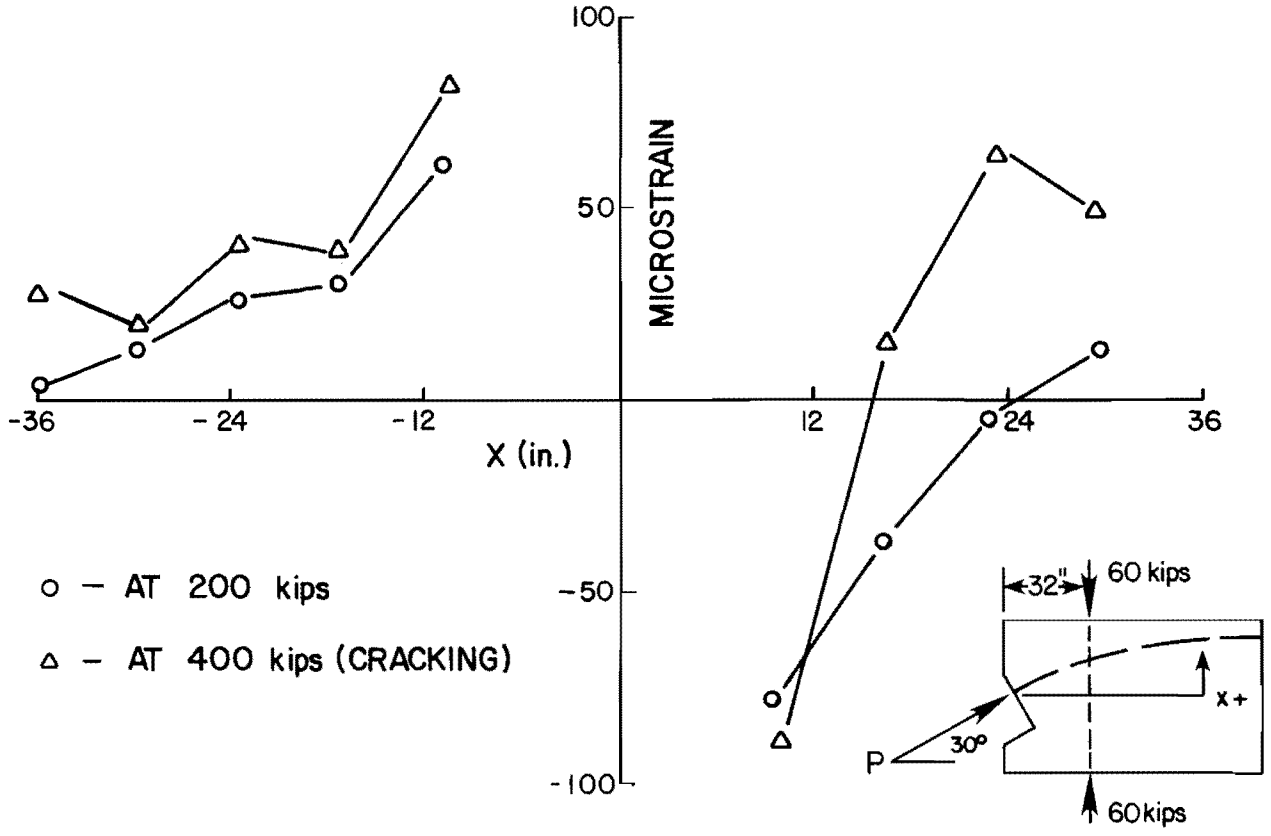

Fig. 3.42 FS5A experimental spalling strain distribution

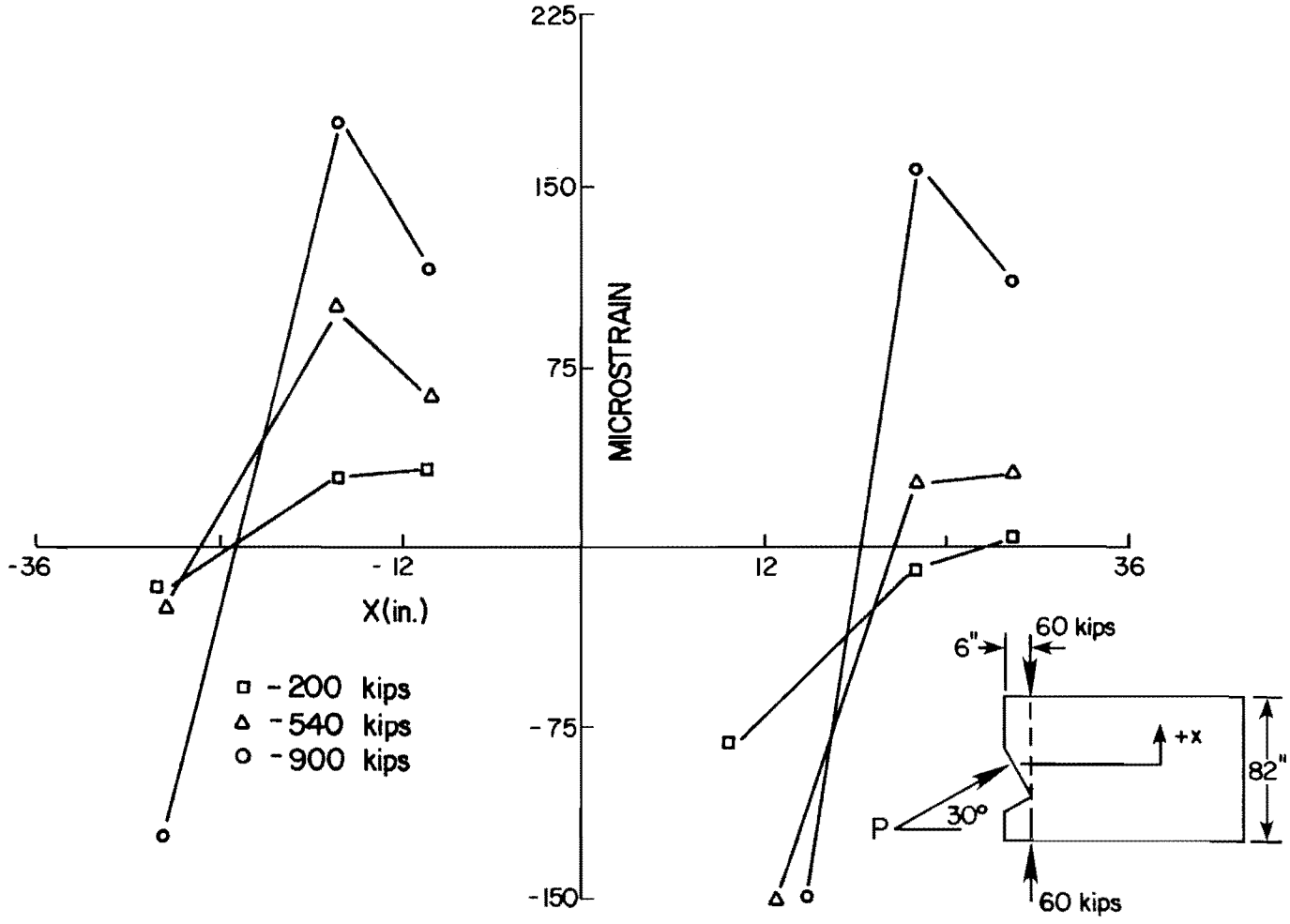

Fig. 3.43 FS5B experimental spalling strain distribution

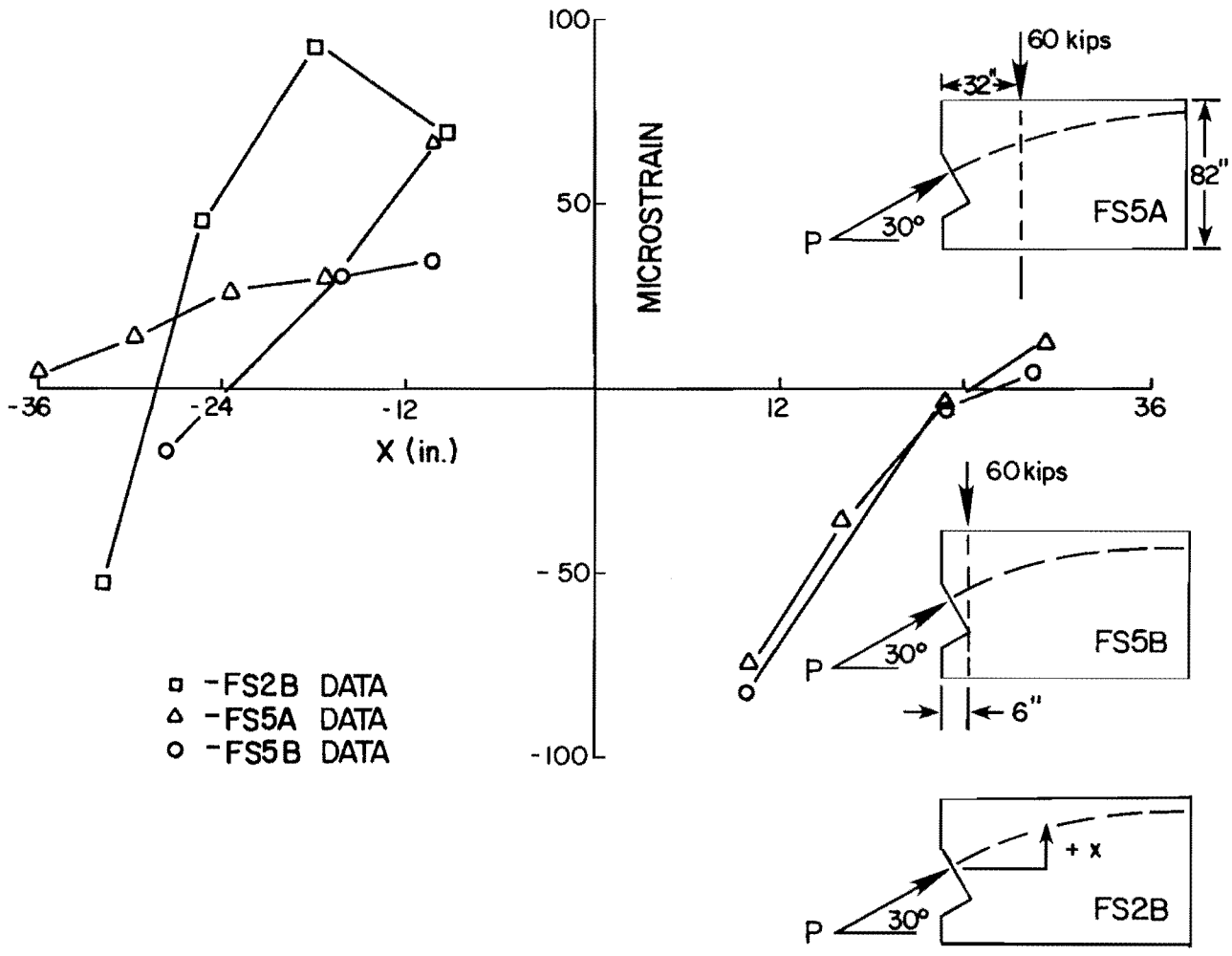

Fig. 3.44 Spalling strain distribution for LPT series tests (load stage P = 200 kips)

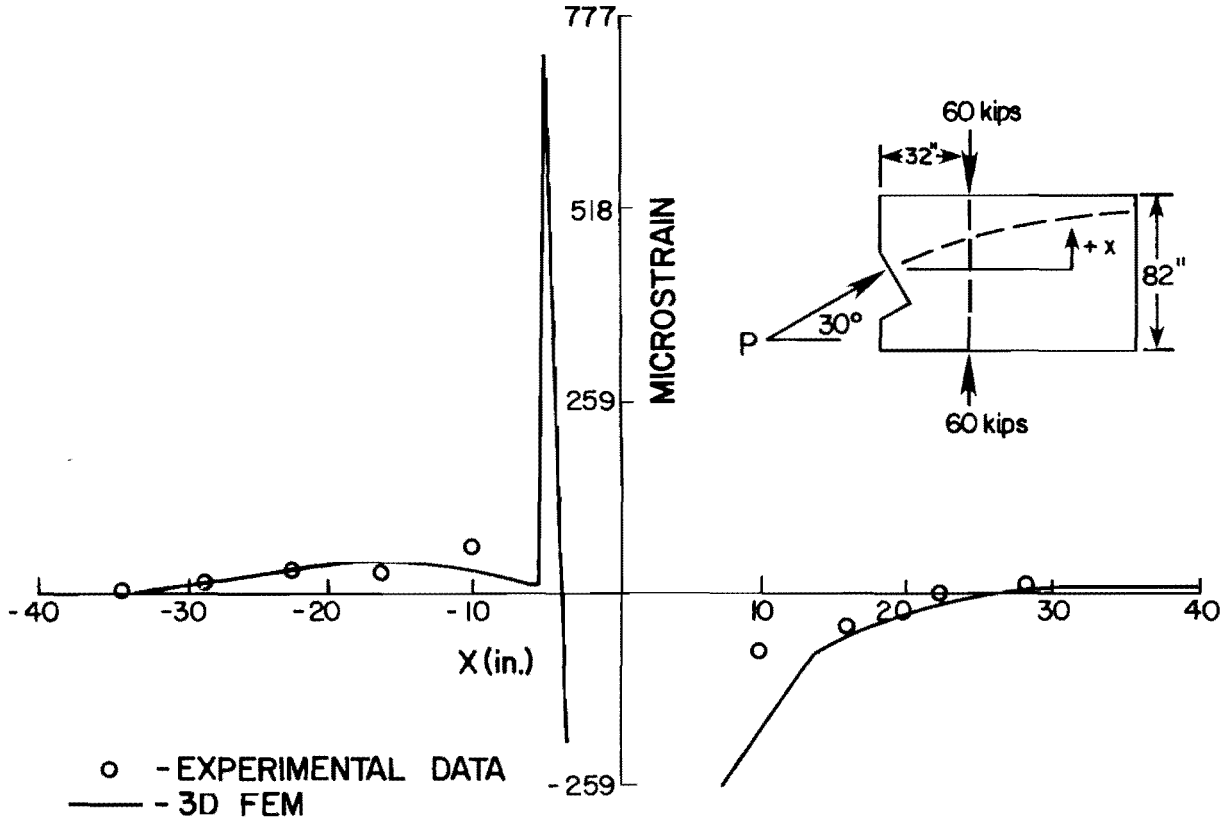

Fig. 3.45 FS5A spalling strain distribution

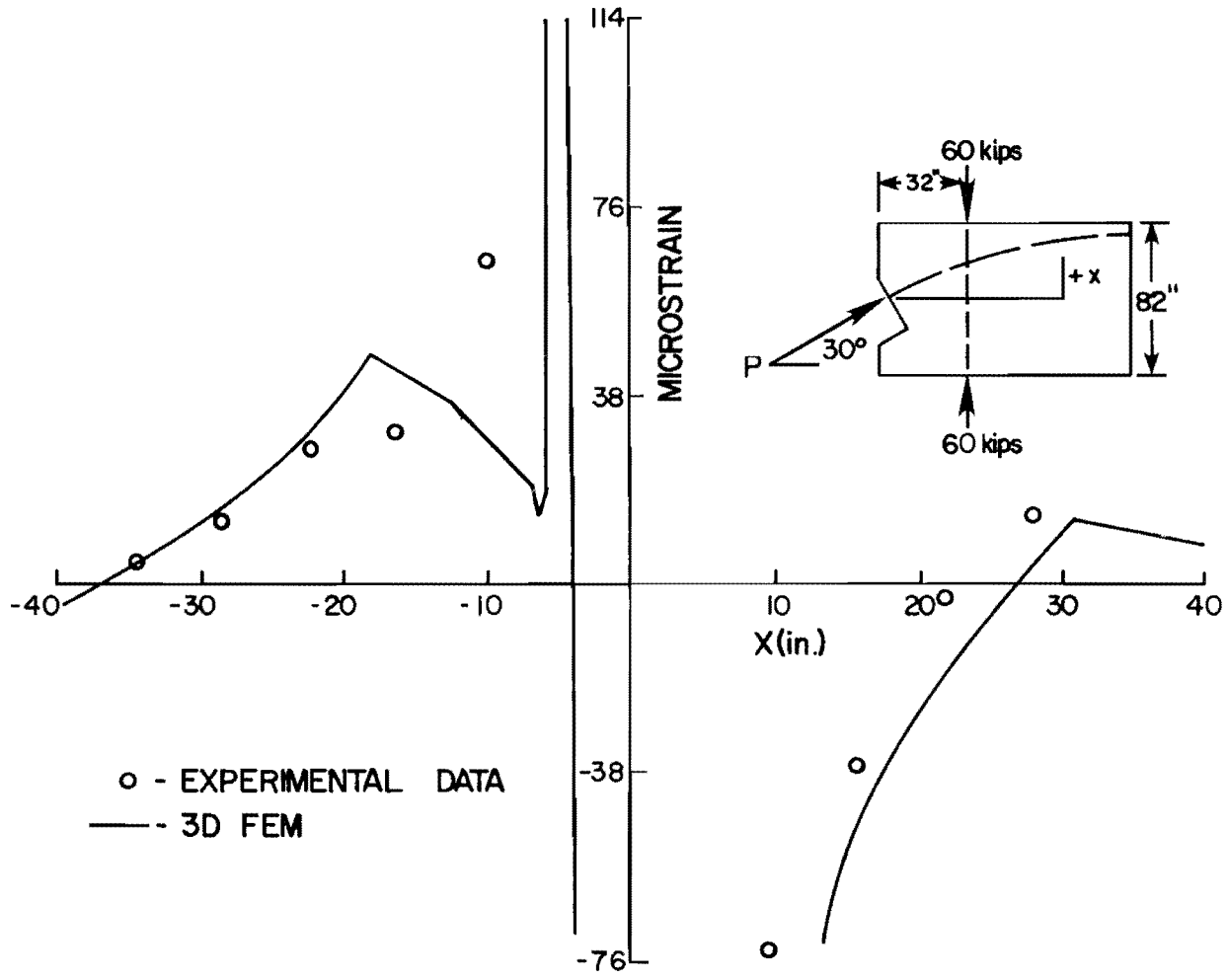

Fig. 3.46 FS5A spalling strain distribution (expanded scale)

3.4.5 Comparison of Supplementary Reinforcing Methods. A summary of the results obtained from the full-scale tests dealing with supplementary anchorage zone reinforcement is presented in Table 3.3. Graphic presentation of the cracking and ultimate load trends is presented in Figs. 3.47 and 3.48. Several conclusions can be drawn:

(1) In general, the addition of supplemental reinforcement, either passive or active, raises the cracking load.

(2) All things considered equal, specimen FS3B (with a 13 in. long spiral fabricated from 1/2 in. diameter, 60 ksi bar stock) exhibited poorer performance than the control specimen (FS2B), which had no supplementary reinforcement. This may have been due to poor concrete or an eccentric (with respect to the centerline) duct in the vicinity of maximum tendon curvature, where failure ultimately occurred.

(3) Lateral prestress located close to the anchor appears to be the most effective means of controlling cracking. The normalized cracking load was 33 percent higher than for the case of an unreinforced anchorage zone, and 25 percent higher than the best performance of the spiral reinforcement. Similar statistics pertain to ultimate behavior as well.

Fig. 3.49 illustrates the efficiency in utilization of reinforcement. Several conclusions can be drawn here:

(1) For a given amount of force ($A_s f_y$) provided by the supplemental reinforcing, the most efficient means of deployment is by means of lateral post-tensioning as close as possible to the anchorage.

(2) Long (26 in.) spirals proved to be no more effective than short spirals (13 in.) in the range investigated. It should be noted that Cooper [9], who used spirals nearly twice the (scaled) length of the long spiral used in this study, reported a significant rise in

TABLE 3.3

FULL-SCALE SPECIMENS WITH SUPPLEMENTAL ANCHORAGE ZONE REINFORCEMENT

Specimen ID	Supplemental Reinforcement	Inclination Θ	f'_c (psi)	f_{sp} (psi)	P_{cr} (kips)	P_{ult} (kips)	$\frac{\ell A_s/2}{10{,}000}$
FS2B	none	30°	4627	455	330	Tendon failure at 620^k	0
FS3A	13" long spiral, 8" ϕ, 2" Pitch 3/8" Bar Stock 60 ksi	30°	4443	470	370	640	138
FS35	13" long spiral, 8" ϕ, 2" Pitch 1/2" bar stock 60 ksi	30°	4550	472	300	590	245
FS4A	26" long spiral, 8" ϕ, 2" Pitch 1/8" bar stock 60 ksi	30°	5200	513	400	650	551.2
FS4B	26" long spiral, 8" ϕ, 2" Pitch 1/2" bar stock 60 ksi	30°	---	---	---	Destroyed with Specimen FS4A	---
FS5A	2-.5" ϕ 270 ksi @32" Vertical prestress = 60^k	30°	5737	544	460	Shear failure at far end deadman at 720^k	4.13
FS5B	2-.5" ϕ 270 ksi @6" Vertical prestress = 60^k	30°	6140	563	540	900	4.13

ℓ = longitudinal extent of supplementary reinforcement (inches)

A_s = total steel area of reinforcement crossing the tendon path (inches^2)

f_y = yield strength of reinforcement (psi)

TABLE 3.3 (Continued)

Specimen ID	$P_{cr}/\sqrt{f'_c}$	P_{cr}/f_{sp}	P_{ud} Upper Diagonal	P_{ud}/f_{sp}	P_{ld} Lower Diagonal	P_{ld}/f_{sp}	$P_{ult}/\sqrt{f'_c}$	P_{ult}/f_{sp}
FS2B	4851	725	---	----	340	747	-----	----
FS3A	5550	787	580	1234	400	851	9602	1361
FS3B	4447	636	480	1017	470	996	8748	1250
FS4A	5547	779	530	1033	400	779	9014	1267
FS4B	----	---	---	----	---	----	----	----
FS5A	6073	845	600	1103	490	845	----	----
FS5B	6891	959	780	1385	630	1119	11486	1599

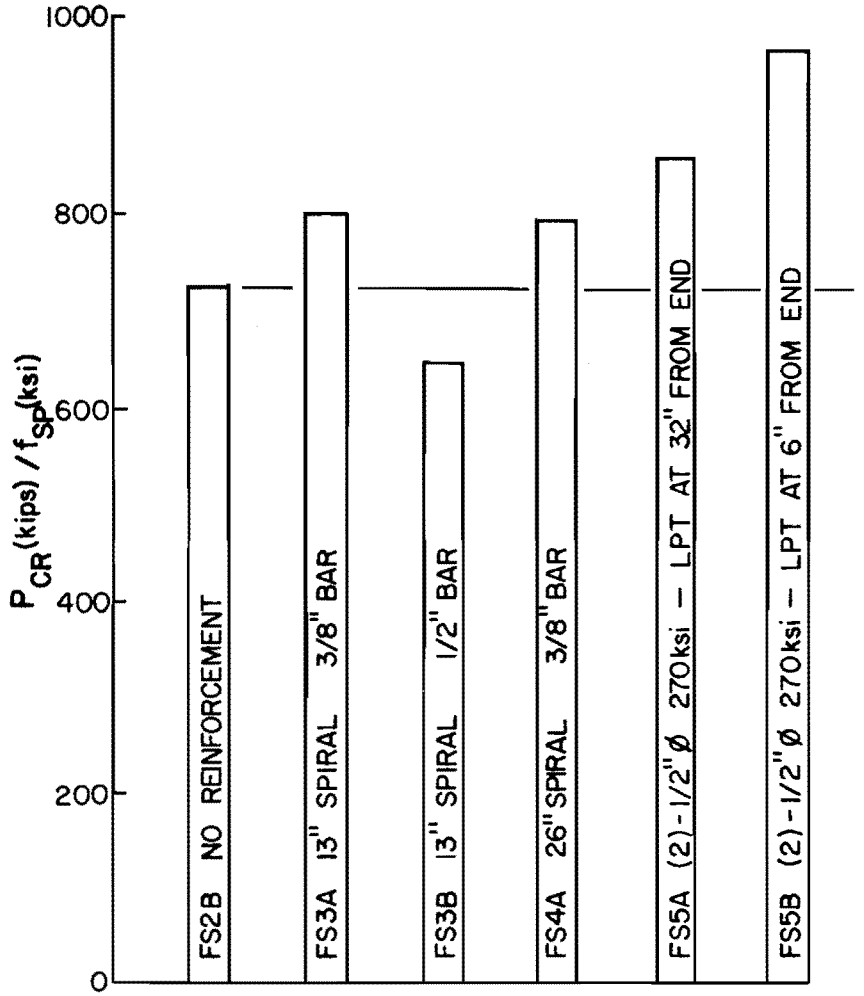

Fig. 3.47 Normalized cracking loads for reinforcement series

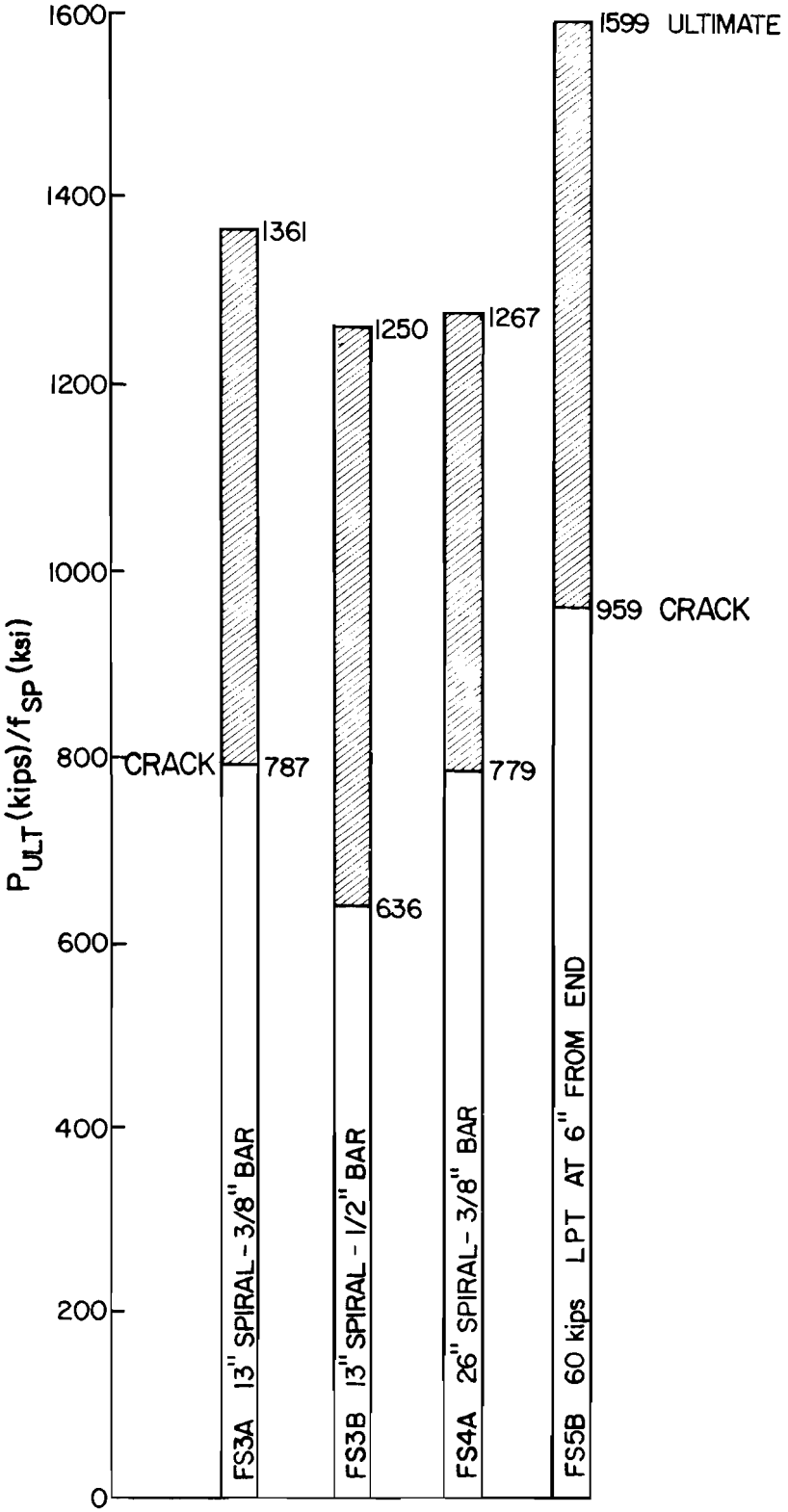

Fig. 3.48 Normalized ultimate loads for reinforcement series

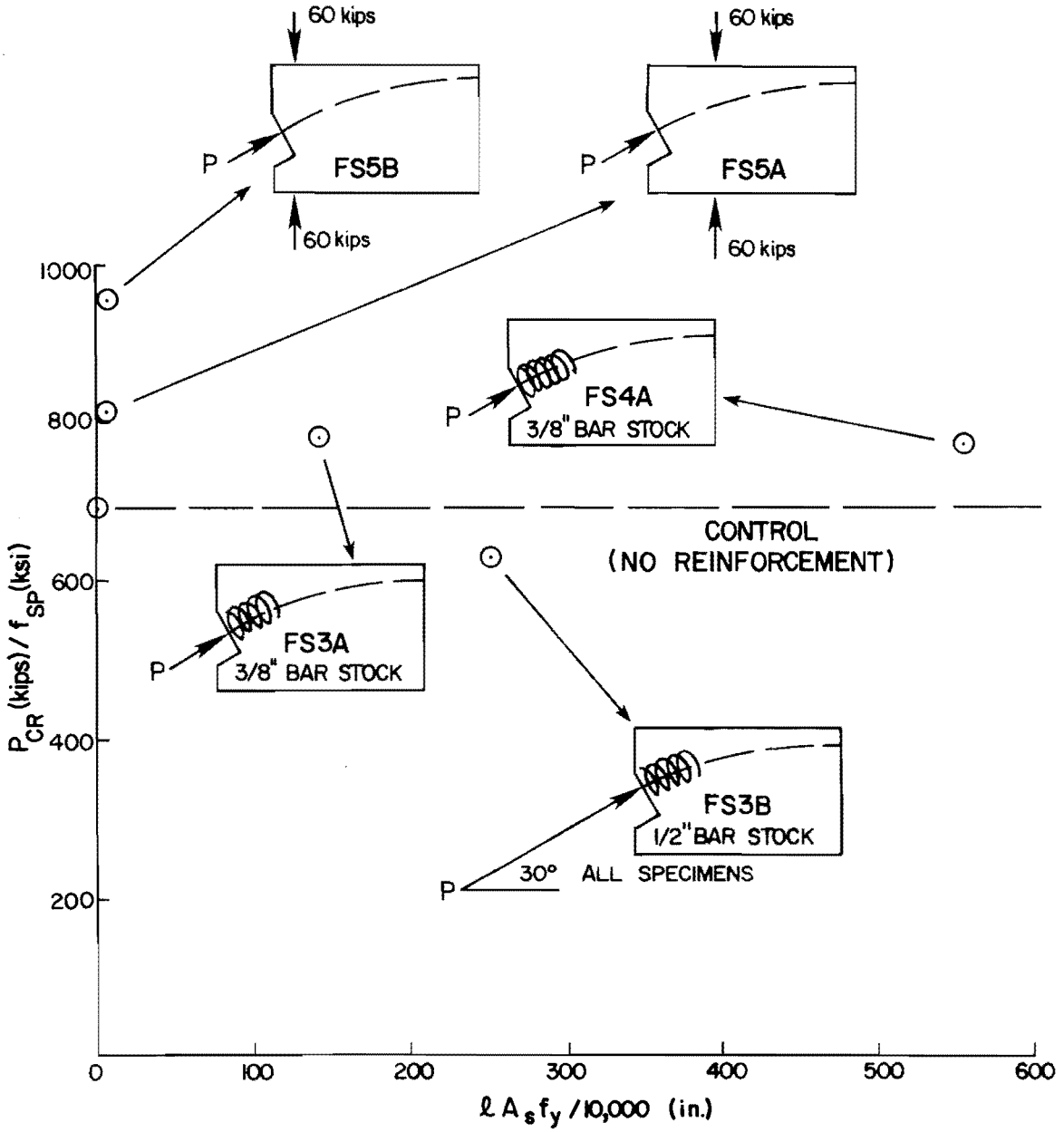

Fig. 3.49 Reinforcement efficiency

cracking loads (for inclined tendon specimens). The reason for this appears to lie in the fact that Cooper's spiral extended through the region of maximum curvature and thus delayed cracking there. Design of specialized reinforcement for this zone is discussed in the final report [2].

(3) Spirals fabricated from 1/2 in. ϕ rod were no more effective than spirals fabricated from 3/8 in. ϕ rod which, for the same spiral diameter and pitch, used only half as much steel.

Table 3.4 summarizes the crack readings taken in the full-scale tests. Normalized (with respect to P_{cr}), crack widths are plotted in Fig. 3.50. The wide black line represents the control specimen FS2B, with no supplemental reinforcement. The following trends were observed:

(1) Crack widths are smaller for specimens with supplementary reinforcement within the section between loaded face and the point of maximum curvature (approximately 1.2a from the loaded face).

(2) Beyond a distance of 1.2a from the loaded face, reinforcement in the vicinity of the anchorage zone appears to have no effect, and the crack widths are roughly equal to those for a specimen with no reinforcement.

(3) Large crack widths for specimen FS3B (13 in. spiral) at 48 in. from the loaded face indicate the onset of a side face rupture at that location.

TABLE 3.4a

AVERAGE CRACK WIDTHS (TENDON PATH) FOR FULL-SCALE SPECIMENS

(ALL READINGS IN 1/1000 IN.)

Vertical Grid Line	Distance from Loaded Face (in.)	FS2B	FS3A		FS3B		FS4A		FS5A		FS5B			
		330k	370k	450k	300k	400k	450k	500k	460k	560k	540k	570k	610k	700k
1	8	5.0	1.0	1.0	2.0	3.5	2.0	3.5	4.5	6.5	3.0	4.0	4.0	6.5
2	16	5.0	2.0	3.0	3.0	6.0	2.0	2.5	9.0	12.0	4.5	6.0	7.5	10.0
3	24	6.0	2.0	5.0	4.0	10.0	4.0	5.0	9.5	14.0	5.5	7.75	9.5	13.0
4	32	6.0	3.5	4.0	5.5	8.0	5.0	8.5	10.0	14.5	7.0	9.5	12.5	15.5
5	40	4.0	3.0	3.0	6.0	11.0	7.0	10.0	12.0	18.5	8.5	12.5	14.0	16.0
6	48	4.0	3.0	5.0	7.5	9.0	6.0	12.0	9.5	12.0	8.0	13.0	13.0	15.5
7	56	3.5	3.0	5.5	7.0	8.0	6.0	8.5	6.0	7.0	6.0	11.5	10.5	12.5
8	64	2.0	2.0	4.5	4.0	3.5	2.0	4.5	---	7.5	7.5	9.5	12.5	15.5
9	72	---	---	---	1.5	9.0	---	---	---	---	---	---	---	---

TABLE 3.4b

NORMALIZED CRACK WIDTHS*

Vertical Grid Line	Distance from Loaded Face (in.)	FS2B	FS3A	FS3B	FS4A	FS5A	FS5B
1	8	15.2	2.7	6.7	4.4	9.8	5.5
2	16	15.2	5.4	10.0	4.4	19.5	8.3
3	24	18.2	5.4	13.3	8.9	20.6	10.2
4	32	18.2	9.5	18.3	11.1	21.7	12.9
5	40	12.1	8.1	20.0	15.6	26.0	15.7
6	48	12.1	8.1	25.0	13.3	20.6	14.8
7	56	10.6	8.1	23.3	13.3	13.0	11.1
8	64	6.0	5.4	13.3	4.4	---	13.8
9	72	---	---	5.0	---	---	---

$$* = \frac{\text{width (1/1000")}}{P_{cr} \text{ (kips)}} \times 1000$$

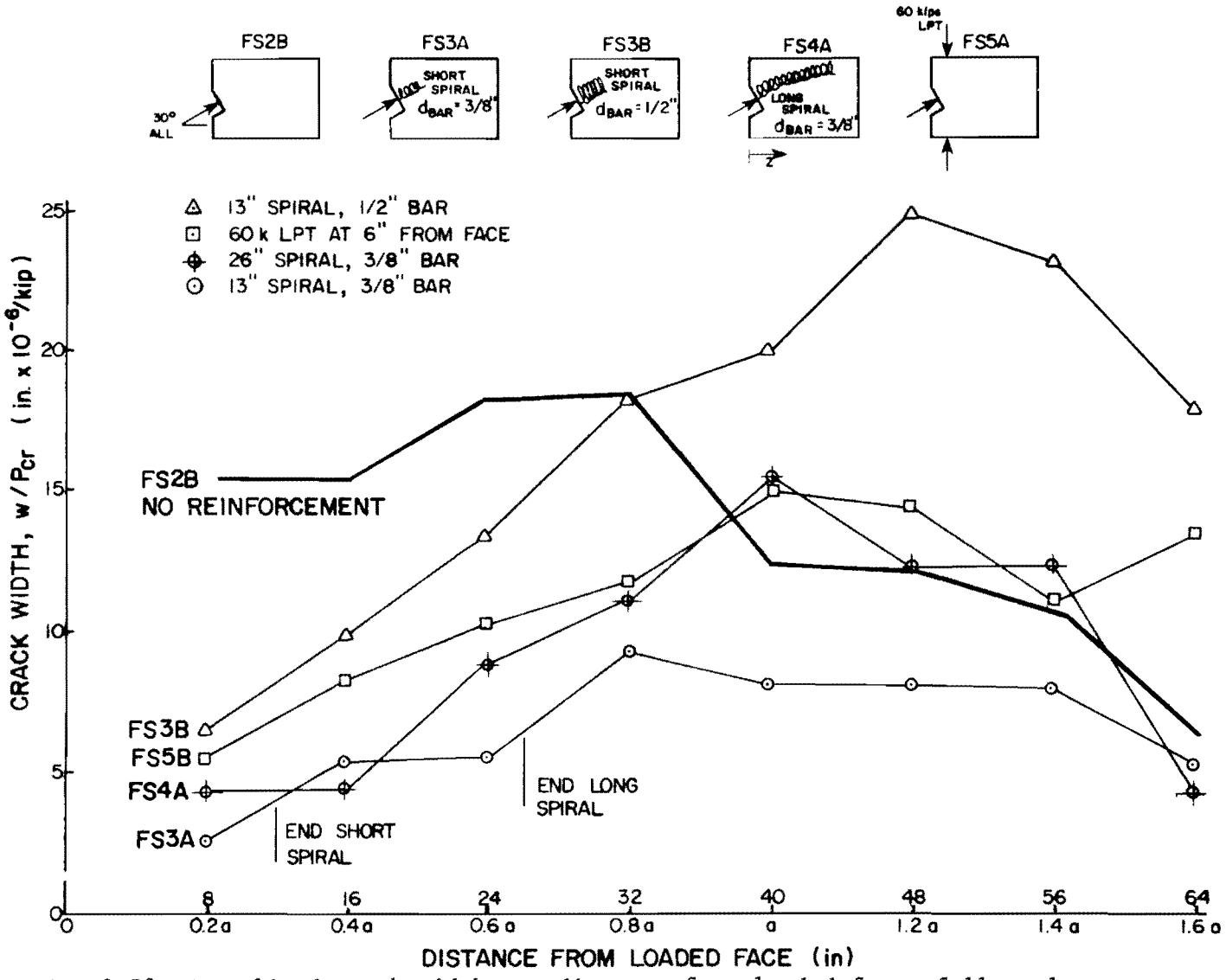

Fig. 3.50 Normalized crack widths vs distance from loaded face--full-scale tests

CHAPTER 4

QUARTER-SCALE I-SECTION MODEL SERIES

4.1 Introduction

Because the full-scale specimens had several geometric changes in comparison to the specimens of the earlier main quarter-scale series, an additional series of six quarter-scale specimens were tested [18] to demonstrate the accuracy of the similitude relationship and to further explore the effect of bearing area noted in the full-scale series. This chapter summarizes the design, fabrication, and testing of these model replicas of the full-scale specimens.

4.2 Specimen Design

The reduced-scale specimens were identified by the following four letter sequence:

MNKL

where
- M = Quarter-scale microconcrete model.
- N = Type of cross section, "I" type or "R" for rectangular section.
- K = Specimen number in this series of tests.
- L = Side of specimen if two tests per specimen, side A or B.

The following correlation existed between model and prototype specimens:

Full-Scale		Model
FS1B	:	MI1A, MR1A
FS1A	:	MI1B, RM1B
FS2B	:	MI2
FS4A	:	MI3

4.2.1 Materials and Details. Dimensions of the quarter-scale models are presented in Fig. 4.1. The flanged specimens were directly scaled from the prototype dimensions of Fig. 3.1. Specimens MR1A and MR1B were rectangular cross sections without flanges. This was to provide a means of comparison with the rectangular model series and directly indicate the effect of the flanges.

Longitudinal dimensions for specimens with straight tendons were chosen to permit two tests per specimen, one at each end. The length of these specimens was 40 in. No evidence of interaction of the test at one end with the subsequent test at the other end was observed. In specimens with inclined tendons, longitudinal dimensions were scaled down from the corresponding full-scale specimens in order to match the relative curvature of the prestressing tendons. Only one test was obtained in each of these specimens which were 32.5 in. long. The scale is clearly illustrated in Fig. 4.2.

4.2.2 Microconcrete. As with the previous models, a specially designed microconcrete was utilized so that material properties such as elastic modulus and load-strain behavior would have scale factors close to unity. The final design was essentially the same as for the first model series with the exception that the water cement ratio was 0.6 rather than 0.7.

A large number of 3 in. by 6 in. cylinders were cast along with each specimen in order that the compressive strength could be checked regularly during the curing period. When the model concrete strength reached the prototype strength, the specimen was tested.

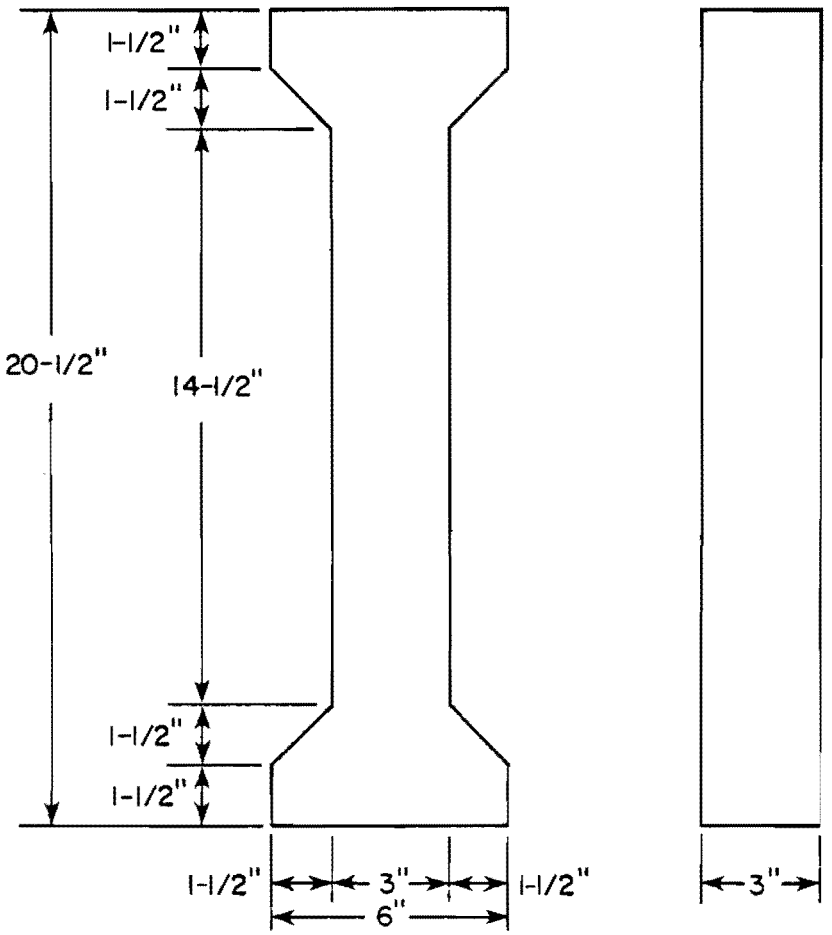

Fig. 4.1 Actual cross section dimensions of models

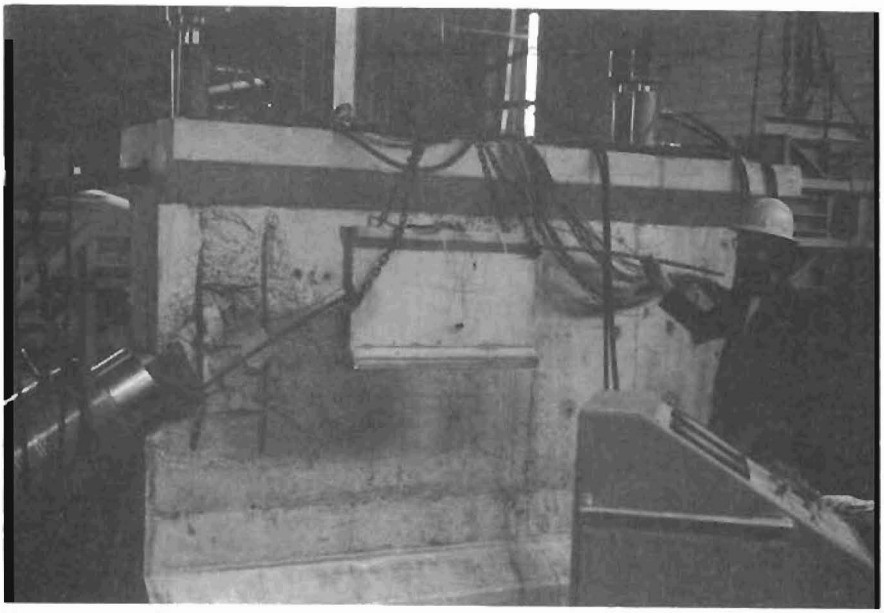

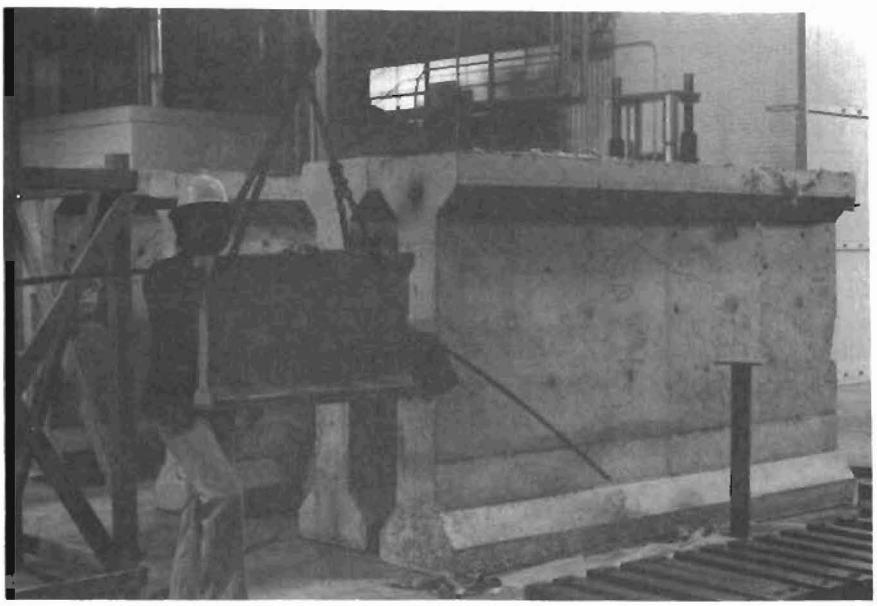

Fig. 4.2 Model dimensions vs prototype dimensions

Despite this procedure, some variations did occur between model and prototype concrete strengths. Split cylinder tests were carried out to determine the indirect tensile strength of the microconcrete for batches corresponding to specimens MI2 and MI3. A number of cylinders corresponding to specimens MR1 and MI1 were defective and could not be tested due to the presence of deep honeycombing. The remaining cylinders were tested in compression. Table 4.1 presents the results of compression and split cylinder tests for the models.

4.2.3 Reinforcement. Model reinforcement was directly scaled from the full-scale cages. U-type stirrups were used in specimens MI1, MI2, and MI3, while closed stirrups matching those used in earlier models were used for specimen MR1. Availability of reinforcing bars and wires led to the typical reinforcing cage shown in Fig. 4.3. Deformed bars (6 mm) were used as stirrups and smooth 13 gage wires were employed as lateral bars. Table 4.2 summarizes similitude requirements with respect to reinforcement and the close degree to which they were met.

Supplemental anchorage zone spiral reinforcement was provided in specimen MI3. Figure 4.4 presents details for both full-scale and model spirals. In order to prevent premature failure at the far end of specimens MI2 and MI3, additional transverse reinforcement was provided consisting of eight 6 mm U-stirrups on 1/2 in. centers in the top flange near the ends.

4.2.4 Anchorage Hardware. For this series of tests, precise replicas of the full-scale bearing-type anchors were fabricated. Miniature trumpets were machined from 1.5 in. diameter bar stock and soldered to the model base plate. Figure 4.5 shows the two types of anchors used. One is the normal commercial type anchor while the other is a reduced bearing area model. Specific dimensions for both model anchors are given in Fig. 4.6. The effective net bearing area for these anchorages was determined as follows:

TABLE 4.1

MICROCONCRETE COMPRESSION AND SPLIT CYLINDER TESTS*
(Second Series)

MODEL	Compressive Strength		Indirect Tensile Strength	
	Average (psi)	Standard Deviation (psi)	Average (psi)	Standard Deviation (psi)
MR1A	56.2	462	no test	---
MR1B	5624	358	no test	---
MI1A	5234	283	no test	---
MI1B	5352	327	no test	---
MI2	5305	425	582	77
MI3	5212	227	606	68

*From 3" by 6" cylinders.

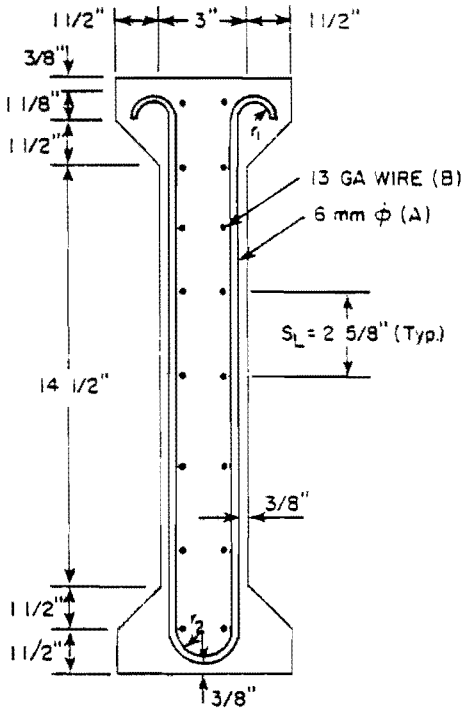

(a) CROSS SECTION

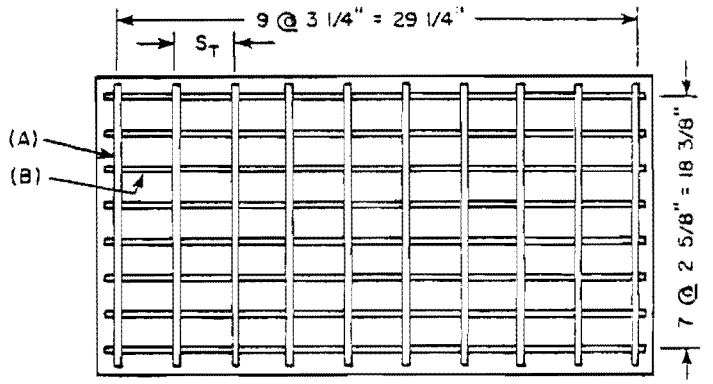

(b) ELEVATION

Fig. 4.3 Passive reinforcement for models

TABLE 4.2 PROTOTYPE AND MODEL REINFORCING CAGES

1/4-SCALE MODELS												
REQUIRED						PROVIDED					
Bars (A) f_y = 60 ksi			Bars (B) f_y = 60 ksi			Bars (A) f_y = 60 ksi			Bars (B) f_y = 36 ksi		
d(in.)	A_s(in.^{2})	S_T(in.)	d(in.)	A_s(in.^{2})	S_L(in.)	d(in.)	A_s(in.^{2})	S_T(in.)	d(in.)	A_s(in.^{2})	S_L(in.)
0.219	0.038	3.25	0.094	0.007	2.63	0.236	0.044	3.25	0.0915	0.0066	2.63

FULL-SCALE SPECIMENS					
Bars (A) f_y = 60 ksi			Bars (B) f_y = 60 ksi		
d(in.)	A_s(in.^{2})	S_T(in.)	d(in.)	A_s(in.^{2})	S_T(in.)
0.375	0.60	13	0.375	0.11	10.5

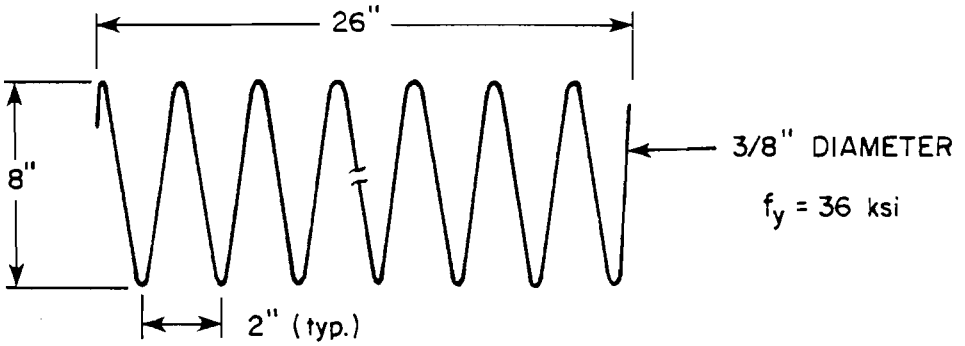

(a) FULL-SCALE SPIRAL

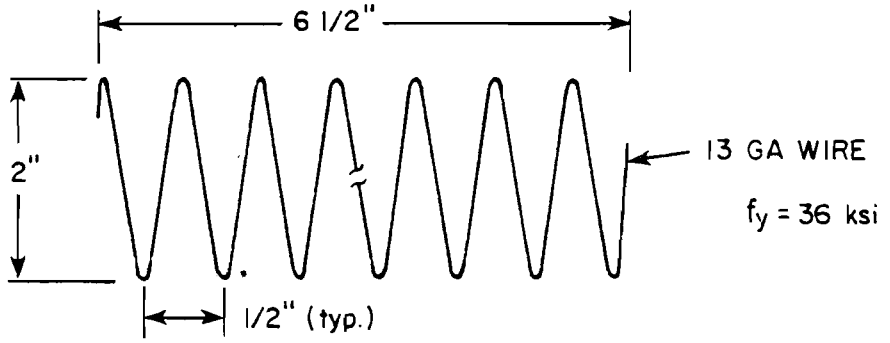

(b) MODEL SPIRAL

Fig. 4.4 Full-scale and model spiral details

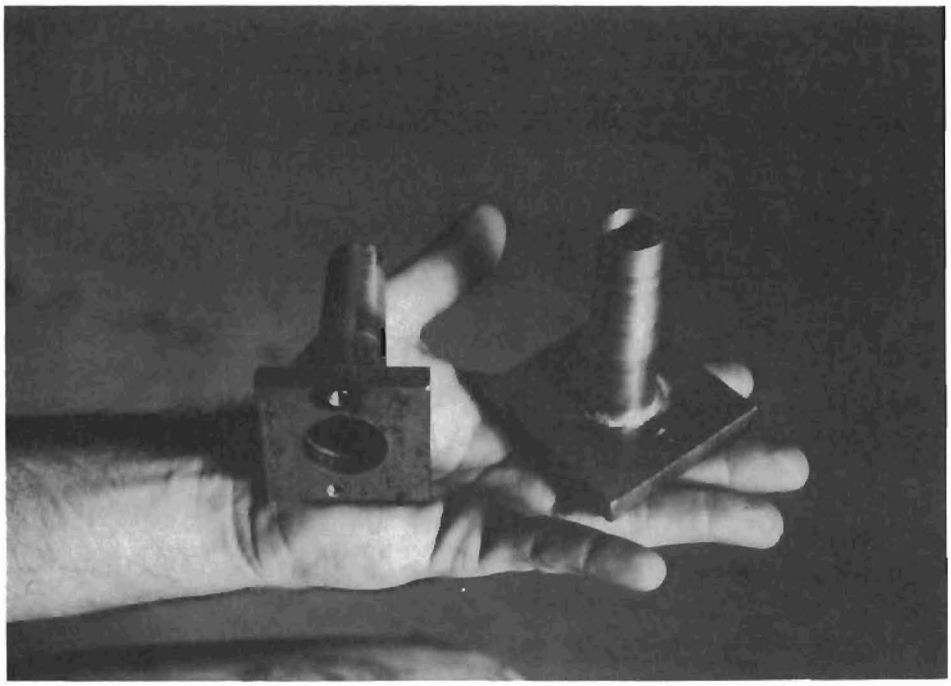

Fig. 4.5 Miniature anchorage hardware

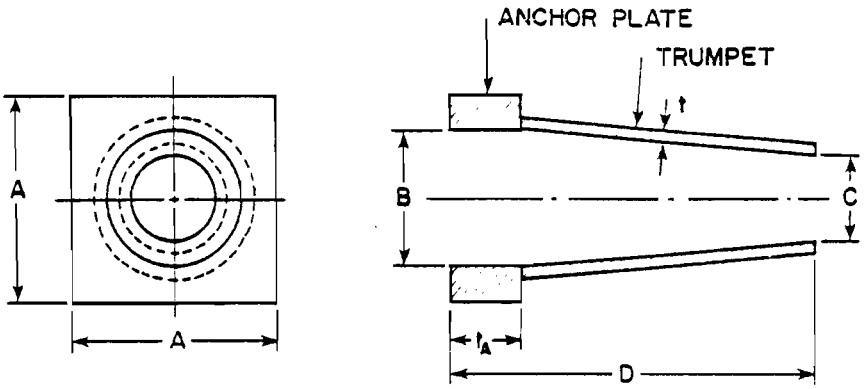

ANCHORAGE HARDWARE

Dimension (in.)	Type I		Type II	
	Prototype	Model	Prototype	Model
A	8.5	2.125	10.5	2.625
B	4.0	1.0	4.0	1.0
C	3.0	0.75	3.0	0.75
D	13.5	3.375	13.5	3.375
t_a	1.5	0.375	1.5	0.375
t	0.0625	0.0156	0.0625	0.0156
Bearing Area A_b	59.68 in^2	3.73 in^2	97.68 in^2	6.11 in^2

Specimen	Anchorage Type
MR1A	II
MR1B	I
MI1A	II
MI1B	I
MI2	II
MI3	II

Fig. 4.6 Anchorage Hardware Details

$$A_b = A^2 - \frac{B^2}{4} \qquad (4.1)$$

where A_b = Effective net bearing area.
A,B = Dimensions shown in Fig. 4.6.

4.2.5 Forms. Two sets of forms were built for casting the models, one for rectangular cross section and the other for I-type cross sections. In order to minimize honeycombing, one side wall in each form was constructed from Plexiglas sheet. The transparency also permitted a visual checking on fabrication tolerances and produced very smooth wall surfaces which enhanced crack observation. Plywood was used for the non-Plexiglas side. Since Plexiglas does not require the application of form oil to break bond, it is recommended that all Plexiglas forms be used for further model studies. In specimens with 30-degree inclined tendons, a special end form with a wooden blockout was provided as shown in Fig. 4.7.

4.2.6 Fabrication, Instrumentation, Test Procedure. With the exception of minor geometry changes in the shear reinforcement cages, all fabrication procedures and instrumentation were identical to those used in the quarter-scale rectangular model series reported in Chapter 2. The loading system again consisted of a 0.6 in. diameter, 270 ksi tendon stressed using a 60 kip centerhole ram. Insertion strainmeters and external Demec points were used to measure strain distribution. Test procedures were identical to those used for the previous model tests with the exception that during the later tests a stethoscope was used to help in detection of first cracking.

4.3 Test Results

4.3.1 Bearing Stress Series. Since all specimens in the first model series were of rectangular cross section, two tests were carried out on this series to compare the effects of flanges. Two tests were obtained from each specimen (MR1A, MR1B, MI1A, and

Fig. 4.7 Attachment of curved tendon to end form

MI1B). Specimens MR1A and MI1A used a precise model of the standard commercial bearing anchor used in the prototype specimens. Specimens MR1B and MI1B used models of the reduced-size anchor used in specimen FS1A. The forces at end "A" were thus applied over a net bearing area of 6.11 $in.^2$, while those at end "B" were applied over a net area of 3.73 $in.^2$.

4.3.1.1 MR1A. This model had a straight tendon, concentric loading, rectangular cross section and a standard anchor corresponding to full-scale specimen FS1B. First cracking occurred, as shown in Fig. 4.8, along the tendon path at 39 kips. This longitudinal crack extended about 2 in. along the tendon, beginning near the loaded face. Elongation of this crack to 3 in. occurred at 46 kips. The lower diagonal crack formed at 48 kips, as shown in Fig. 4.9. The upper diagonal formed at 52 kips. Crack measurements at 48 kips indicated crack widths of 0.002, 0.0015, and 0.001 in. at vertical lines 1, 2, and 3, respectively. Failure occurred in the tendon at a load of 55 kips, 6 percent below the specified ultimate tensile strength of the strand.

Bearing stresses of 6383 psi at first cracking and 9002 psi at failure of the tendon were recorded. The average value of f'_c from cylinder tests was 5612 psi with a standard deviation of 462 psi.

4.3.1.2 MR1B. This model had a straight tendon, concentric loading, rectangular cross section and a reduced anchor corresponding to full-scale specimen FS1A. First cracking occurred at 43 kips on the south side face (Fig. 4.10) and measured 18 in. in length along the tendon path. At 47 kips, a 3 in. crack along the tendon path appeared on the north face. At the same load, the lower diagonal crack formed on the south face (Fig. 4.11a). The upper diagonal formed at 52 kips (Fig. 4.11b).

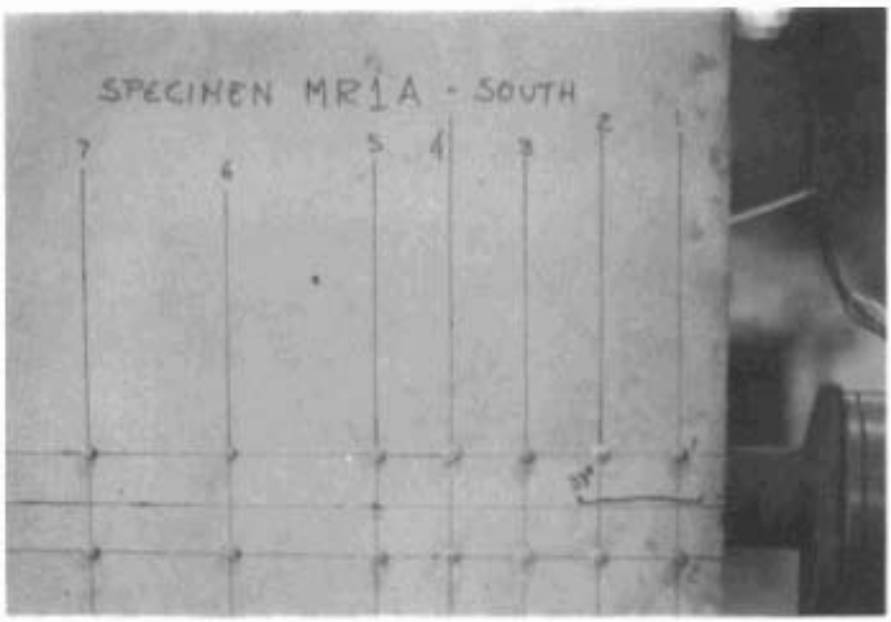

(a)

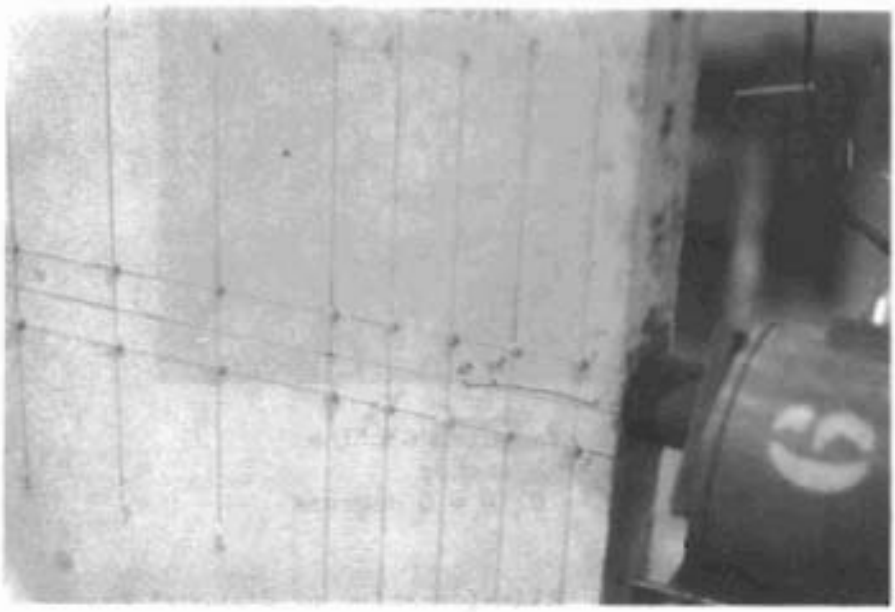

(b)

Rectangular Section
Large Anchor
e = 0; θ = 0 degrees

Fig. 4.8 Specimen MR1A at first cracking

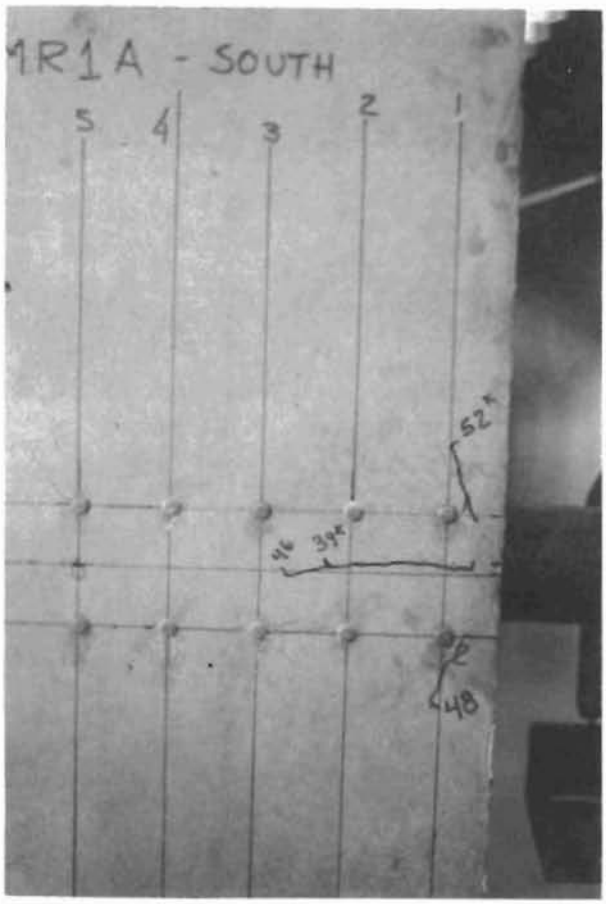

Rectangular Section
Large Anchor
e = 0; θ = 0 degrees

Fig. 4.9 Specimen MR1A--formation of diagonal cracks

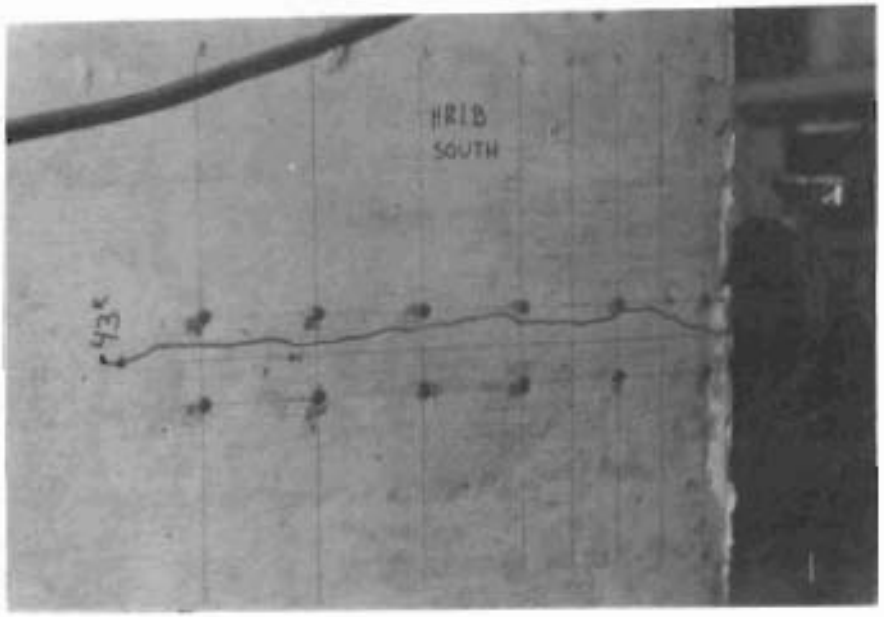

(a)

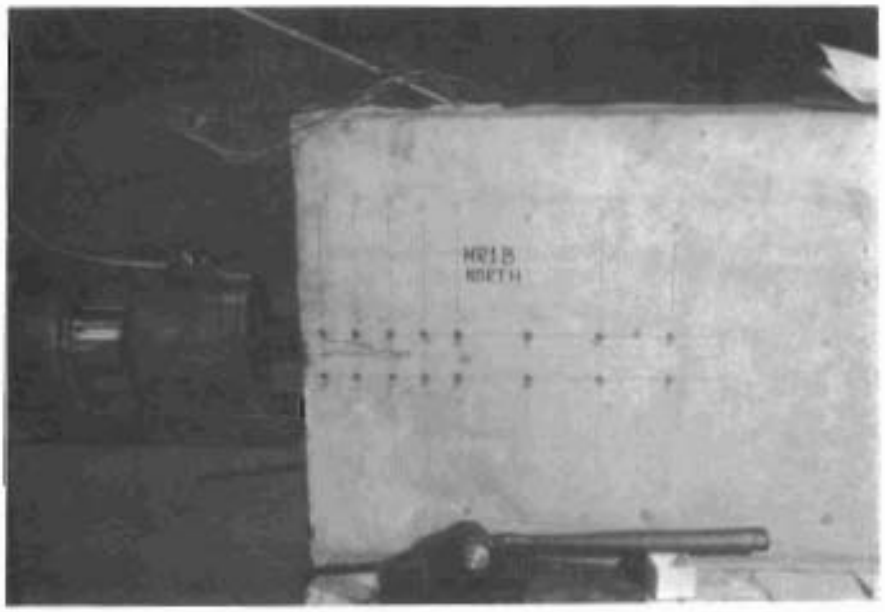

(b)

Rectangular Section
Small Anchor
e = 0; θ = 0 degrees

Fig. 4.10 Specimen MR1B at first cracking

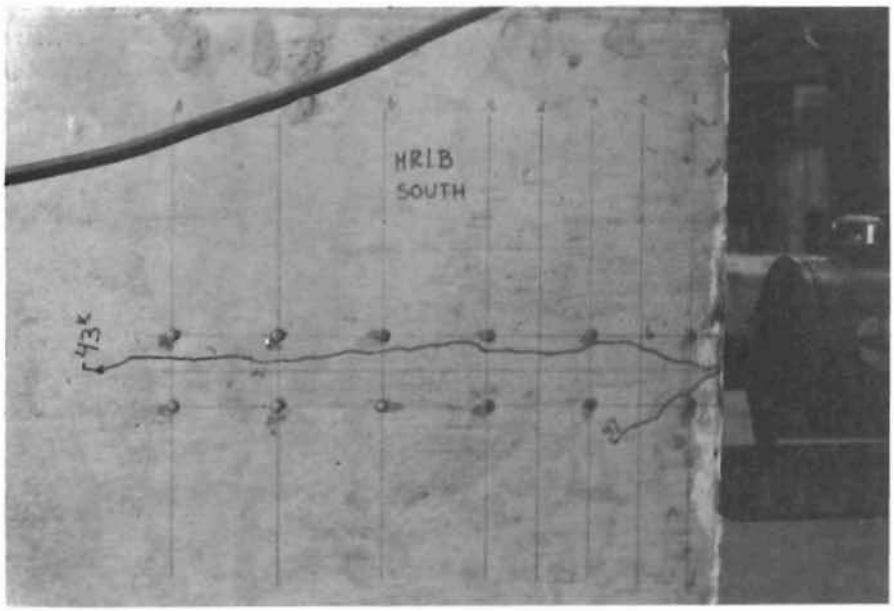

(a)

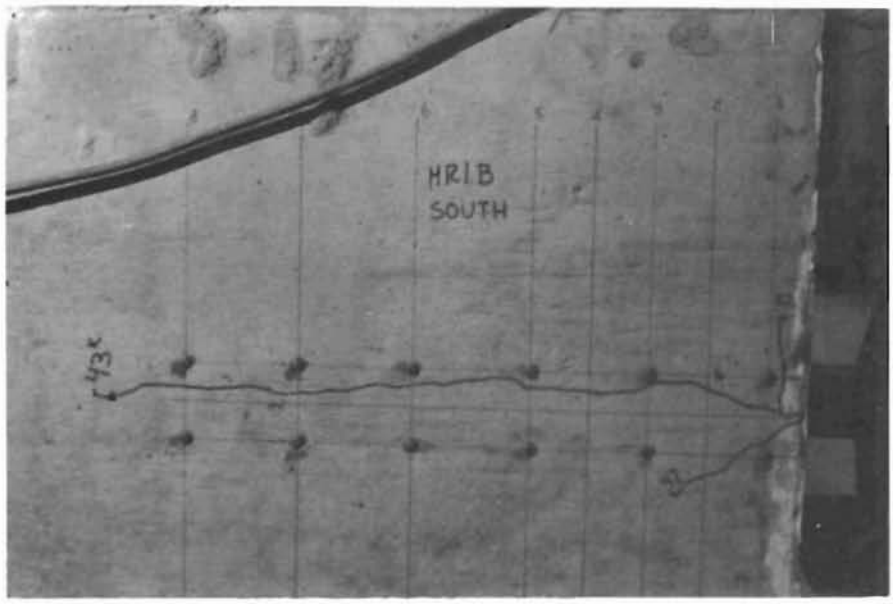

(b) Rectangular Section
Small Anchor
$e = 0$; $\theta = 0$ degrees

Fig. 4.11 Specimen MR1B--formation of diagonal cracks

Crack measurements at 47 kips indicated crack widths of 0.001 in. for the tendon path crack (south) at all vertical line sections, except at line 2 where the crack width was 0.002 in. At 53 kips, an explosive side splitting failure occurred. The failure followed the path of the diagonal cracks (Fig. 4.12). The anchor was forced into the specimen to a depth of 1.5 in., as shown in Fig. 4.13. Bearing stresses of 11,528 psi at first cracking and 14,209 psi at ultimate were developed, despite a value of 5624 psi for f'_c from compression tests (standard deviation 358 psi).

4.3.1.3 MI1A. This model had a straight tendon, concentric loading, I-type section, and a standard anchor corresponding to full-scale specimen FS1B. First cracking was observed at 49 kips (Fig. 4.14a) along the north face and measured 7 in. along the tendon path. At 56 kips, both upper and lower diagonal cracks formed simultaneously (Fig. 4.14b). Until this load stage, no cracks had been observed on the south side. However, at 56 kips, both the tendon path and lower diagonal cracks suddenly appeared (Fig. 4.15). Crack measurements at 49 kips and 54 kips indicated that the crack widths were less than 0.0005 in. in all sections. An explosive side rupture occurred at 59 kips. In addition to the side splitting failure, a deep vertical crack (Fig. 4.16a) at the end face was observed which propagated into and longitudinally along the top flange (Fig. 4.16b). Figure 4.7 shows the cone of crushed concrete beneath the anchor. Note that the anchor was displaced nearly 1.5 in. into the web section at failure.

Bearing stresses of 8020 psi at first cracking and 9656 psi at ultimate were developed. This is contrasted with the compressive cylinder strength of 5234 psi (standard deviation 283 psi).

4.3.1.4 MI1B. This model had a straight tendon, concentric loading, I-type section, and a reduced anchor corresponding to full-scale specimen FS1A. First cracking occurred at 41 kips along the tendon path and measured 7 in. long (Fig. 4.18a). Lower and upper diagonal cracks formed at 46 kips (Fig. 4.18b). Ultimate failure

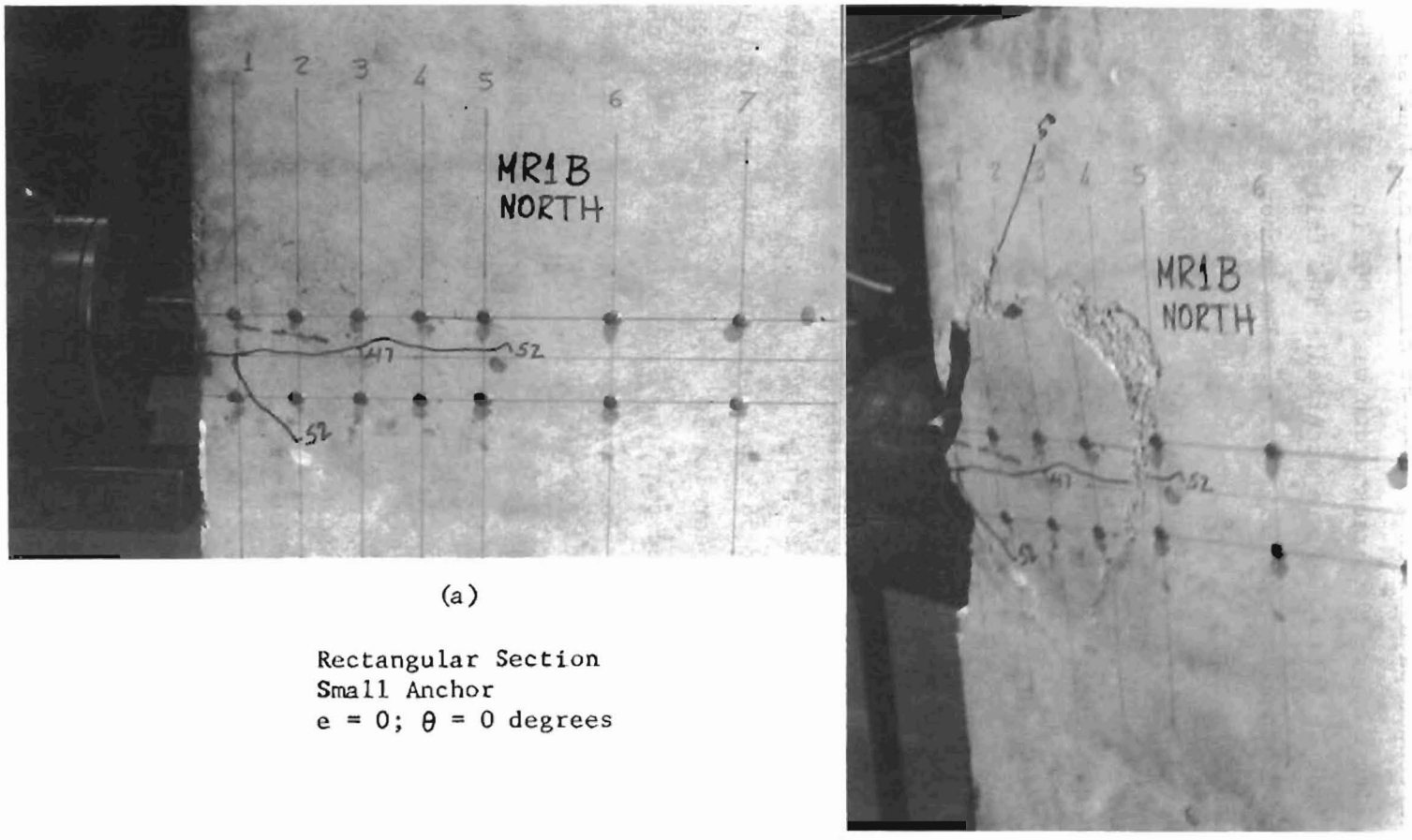

(a)

Rectangular Section
Small Anchor
e = 0; θ = 0 degrees

(b)

Fig. 4.12 Specimen MR1B at failure

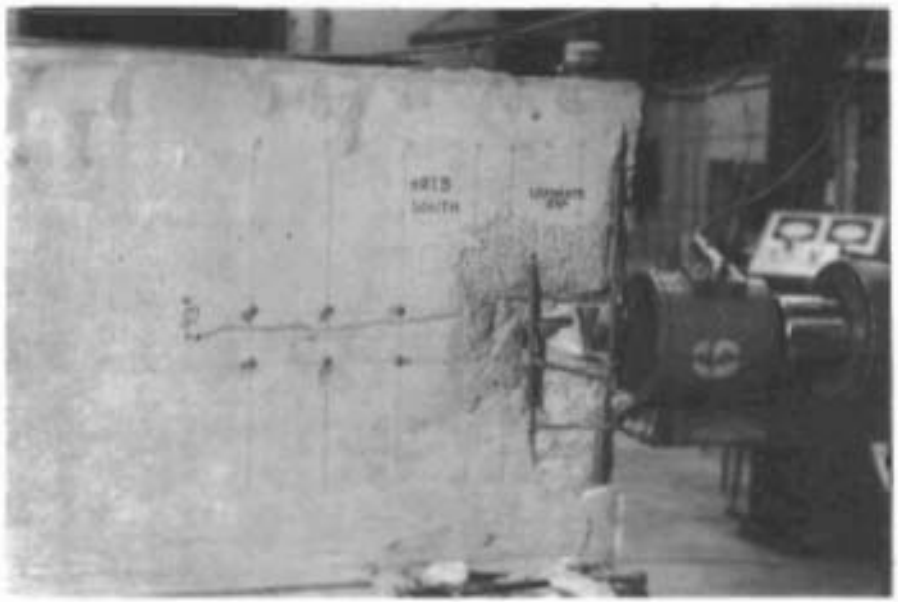

(a)

Rectangular Section
Small Anchor
e = 0; θ = 0 degrees

(b)

Fig. 4.13 Specimen MR1B after concrete failure

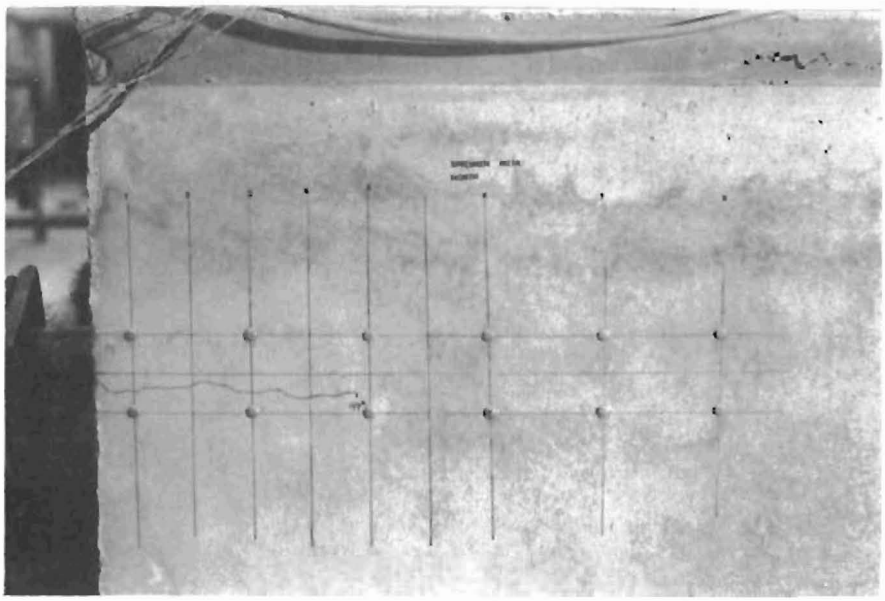

(a)

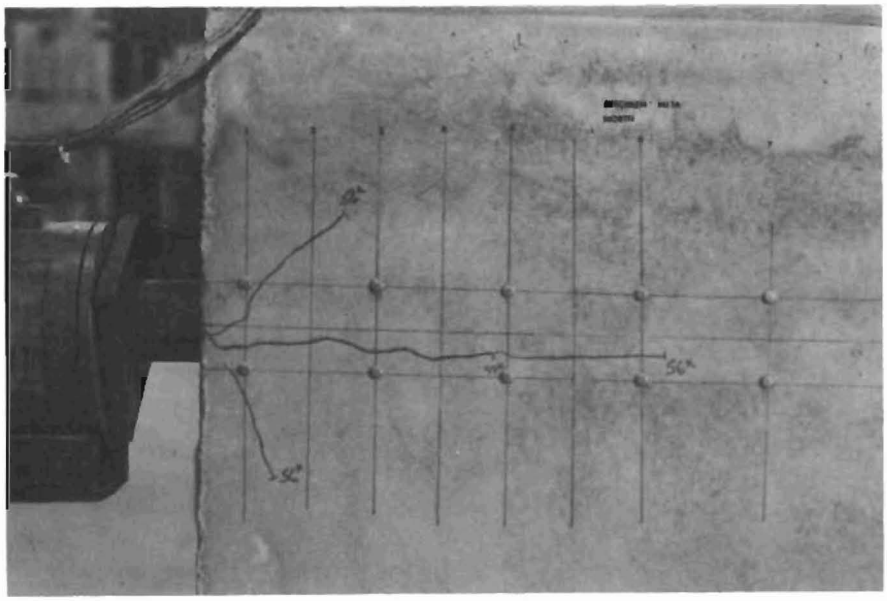

(b)

I-Type Section
Large Anchor
e = 0; θ = 0 degrees

Fig. 4.14 Specimen MI1A--formation of longitudinal and diagonal cracks

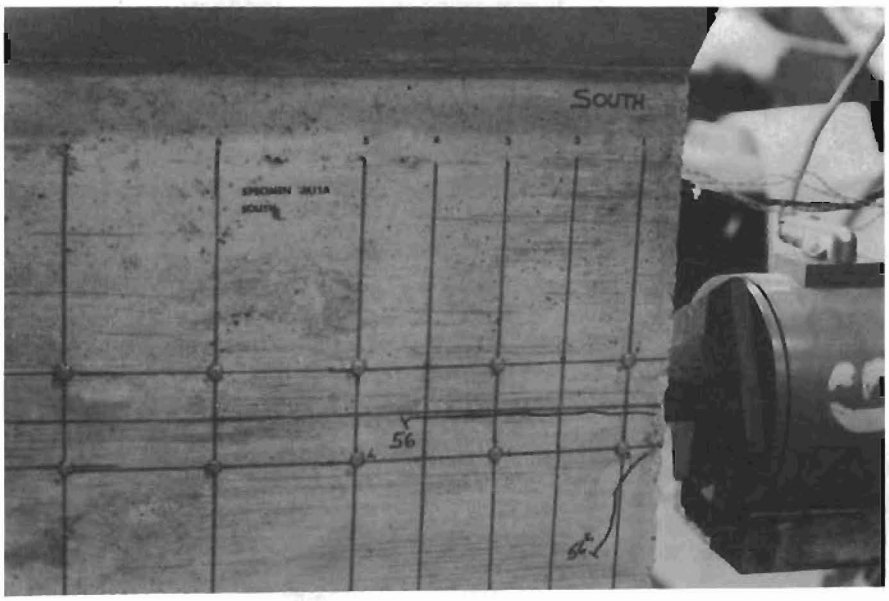

I-Type Section
Large Anchor
e = 0; θ = 0 degrees

Fig. 4.15 Specimen MIlA--crack pattern on south side face

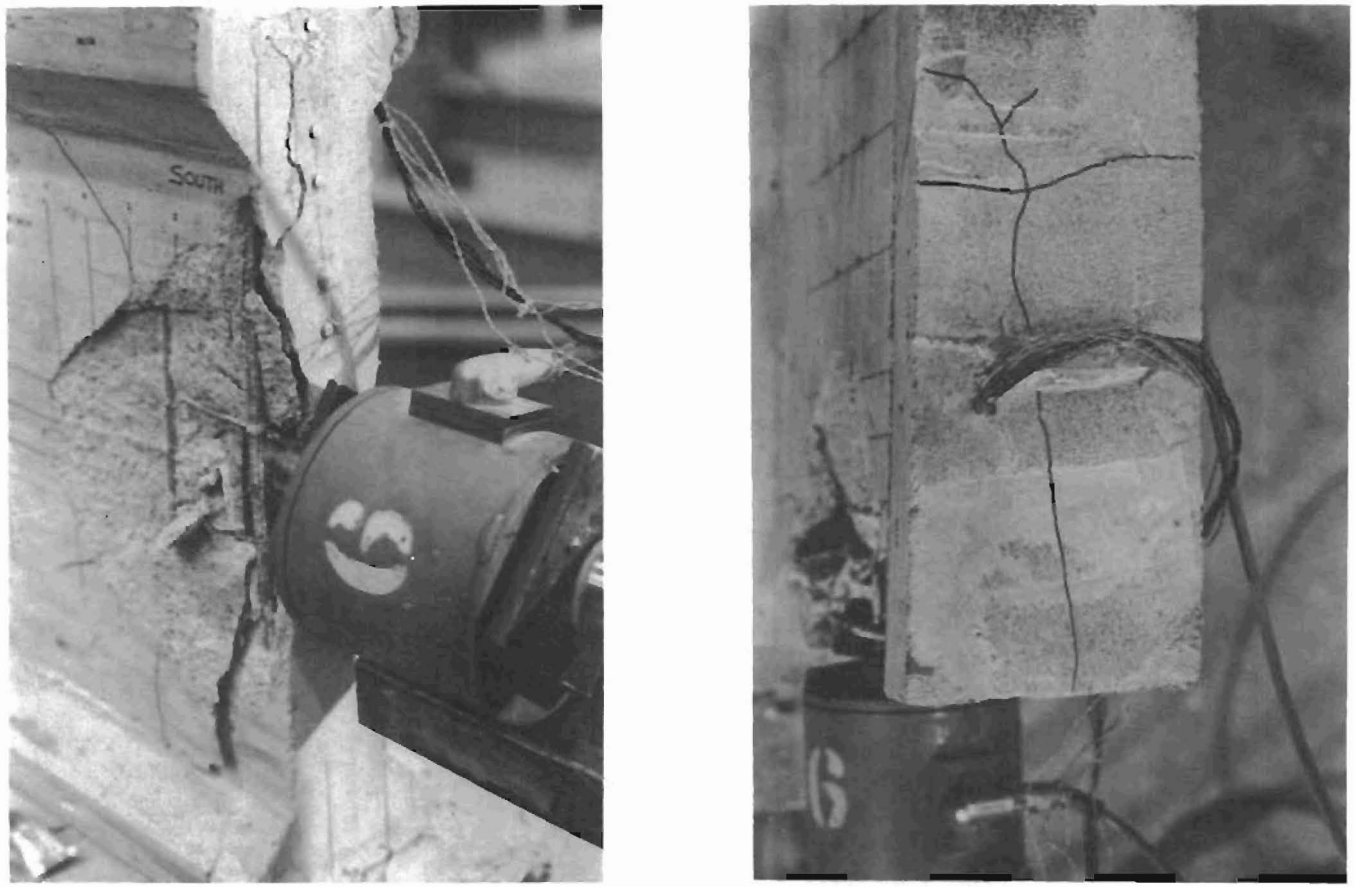

(a) I-Type Section (b)
Large Anchor
e = 0; θ = 0 degrees

Fig. 4.16 Specimen MI1A at failure

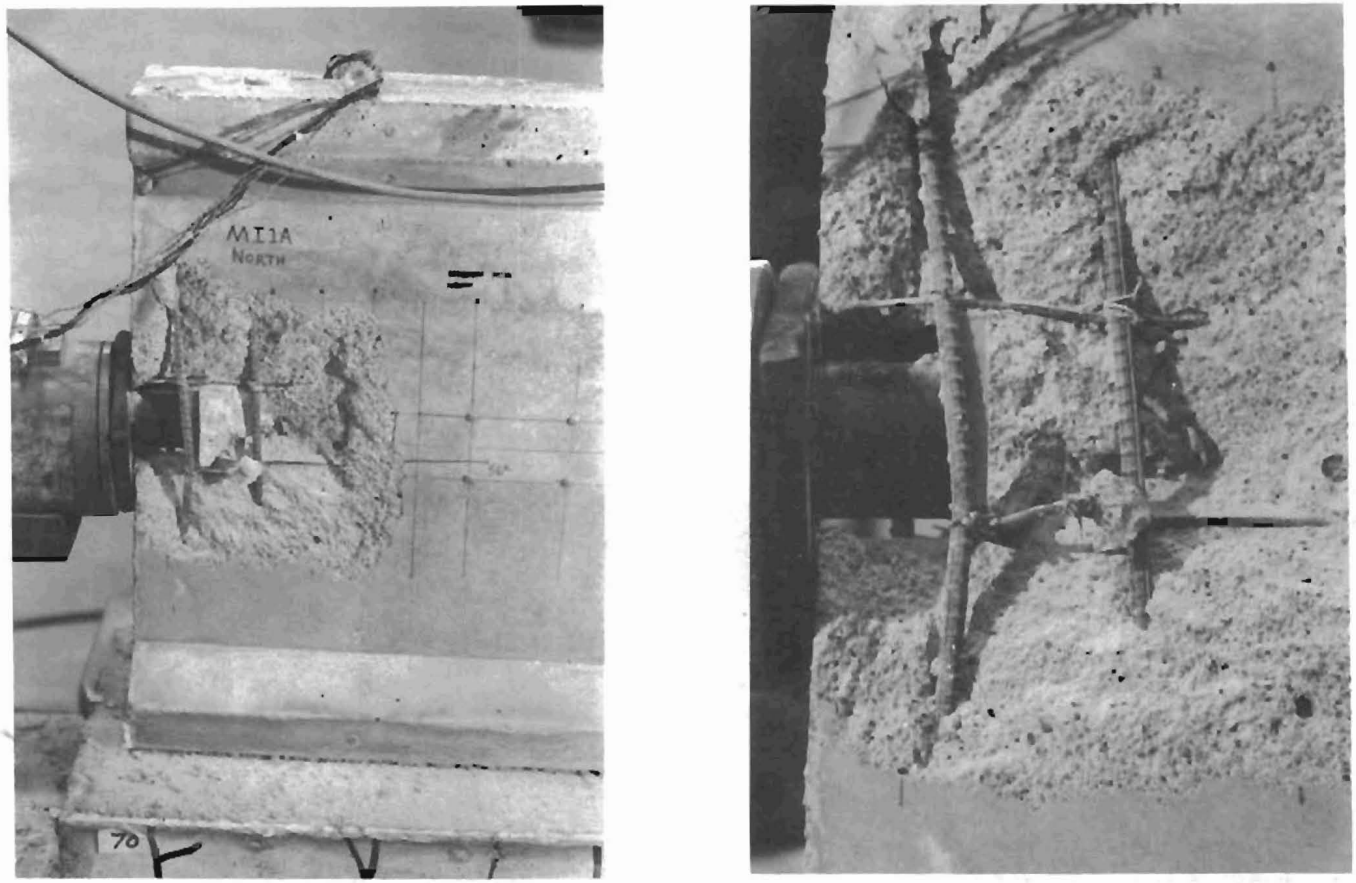

(a) I-Type Section (b)
Large Anchor
e = 0; θ = 0 degrees

Fig. 4.17 Specimen MI1A--formation of concrete cone under anchor

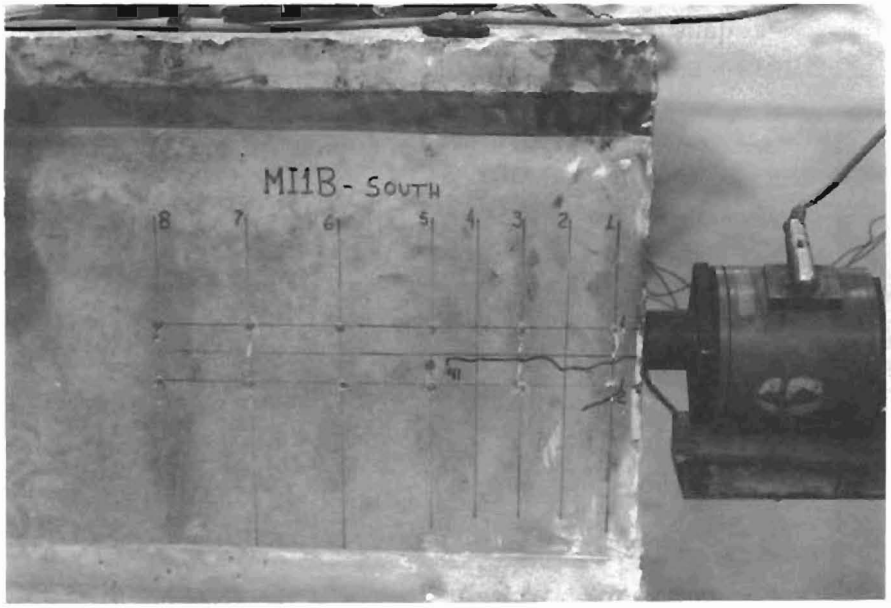

(a)

I-Type Section
Small Anchor
e = 0; θ = 0 degrees

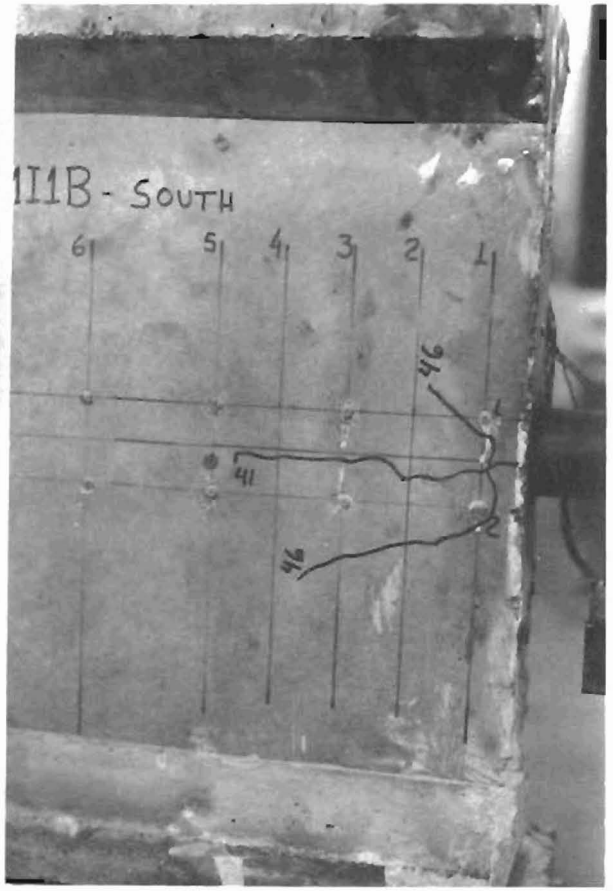

(b)

Fig. 4.18 Specimen MI1B--longitudinal and diagonal cracks

occurred at 50 kips and exhibited an explosive side face rupture similar to that seen in previous tests. Once again a cone of crushed concrete was evidenced beneath the anchor plate (Fig. 4.19).

Bearing stresses of 10,992 psi at cracking and 13,405 psi at ultimate were developed even though cylinder tests indicated an f'_c of 5352 psi (standard deviation 327 psi).

4.3.1.5 Bearing Stress Models--Comparison. The behavior of all four specimens during testing was qualitatively the same. Three stages were always present during the loading sequence:

(a) First cracking, along the tendon path.

(b) Formation of upper and lower diagonal cracks.

(c) Explosive rupture of the side face and accompanying observation of a cone of crushed concrete beneath the anchor.

Since no split cylinder tests could be carried out for these specimens, estimated values for f_{sp} were based on a regression analysis study of all previous microconcrete tests for which split cylinder values were available and indicated:

$$f_{sp} = 0.79(f'_c)^{0.79} \tag{4.2}$$

The estimated values of f_{sp} for these model tests, based on Eq. 4.2 are presented in Table 4.3.

Normalized cracking loads (P_{cr}/f_{sp}) for specimens MI1 and MR1 are compared in Fig. 4.20a. Specimens MR1B and MI1B cracked at exactly the same level of loading. Specimen MR1A, on the other hand, cracked at a load level 11 percent lower than the average while specimen MI1A cracked at a load 18 percent higher than the average. It is surprising to note that MR1A, with a net bearing area nearly twice that of MR1B, cracked at a lower load. Due to the many random variables involved and the reasonable coefficient of variation (12.6 percent), it can be concluded that all four specimens

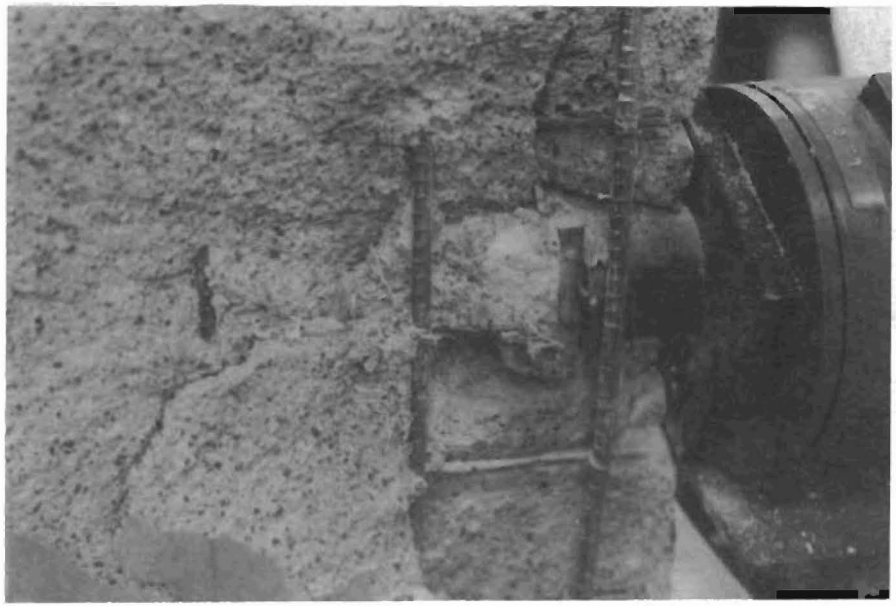

(a)

I-Type Section
Small Anchor
e = 0; θ = 0 degrees

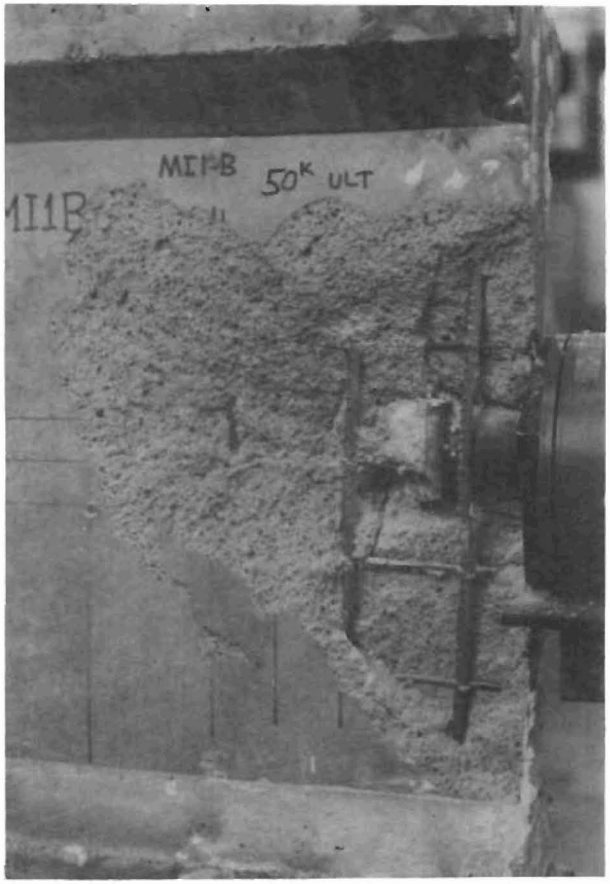

(b)

Fig. 4.19 Specimen MI1B--formation of concrete cone under anchor

TABLE 4.3 EVALUATION OF INDIRECT TENSILE STRENGTH OF MODELS

Model	Average f'_c (psi)	Estimated f_{sp} (psi)
MR1A	5612	723
MR1B	5624	725
MI1A	5234	685
MI1B	5352	697

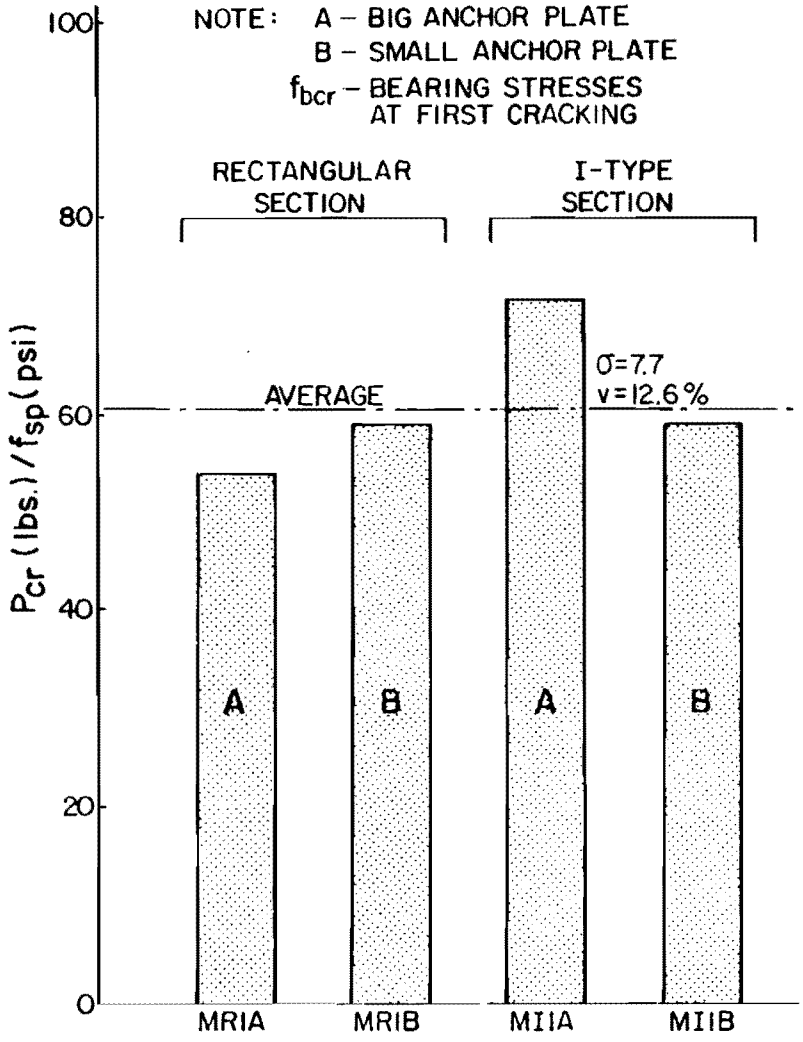

a) Initial cracking load

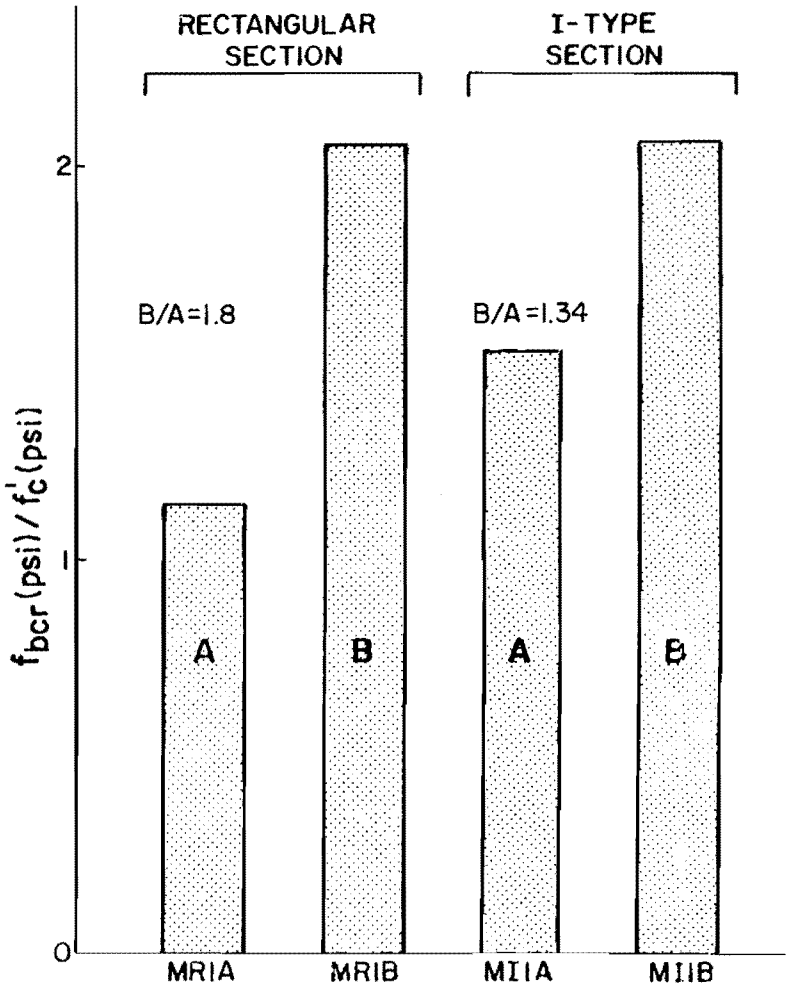

b) Bearing stress

Fig. 4.20 Comparative diagrams of cracking loads and bearing stresses at cracking

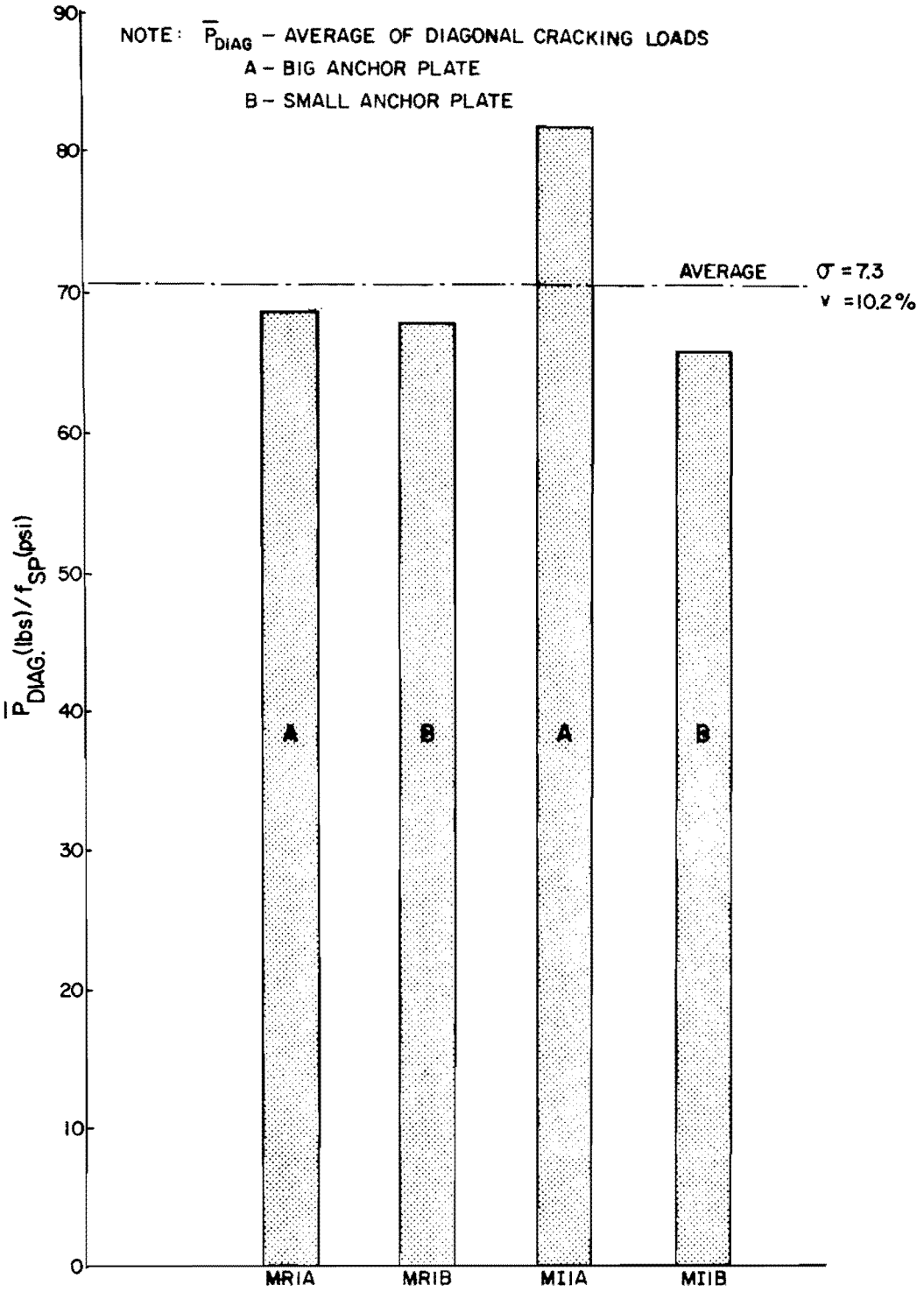

c) Diagonal cracking

Fig. 4.20 (continued)

experienced about the same cracking load and neither the presence of the flanges nor the large difference in bearing areas had any major influence on the cracking loads. Indeed, Fig. 4.20b indicates the average ratio B/A = 1.57, which is almost exactly the ratio of net bearing areas which is 1.64. Thus, bearing area seems to have no effect.

Figure 4.20c shows a comparison between the diagonal cracking load levels for the four specimens. Since lower and upper diagonal cracks formed at different load stages on a few occasions, the average of these stages was used. Specimens MR1A, MR1B, and MI1B reached essentially the same level. Specimen MI1A deviated by about 15 percent from the average. The reasonable coefficient of variation of 10 percent indicates that the diagonal cracking behavior of the specimens, which always occurs after formation of the tendon path crack, was very similar. This indicates that the same mechanism of failure had occurred in each and the bearing-plate area was not a significant variable. Ultimate load stages are compared in Fig. 4.21. The maximum deviation from the average was 12 percent for MI1A and the coefficient of variation was a low 8 percent. A true ultimate load reflecting anchorage zone failure could not be reached for specimen MR1A due to a tendon failure. Results for the other specimens indicated that the small anchor plates had less ultimate capacity than the big plates.

Since crack patterns and quantitative test results were very similar for all four models, it can be concluded that the presence of the flanges and the widely different bearing stresses did not greatly affect the overall performance of the specimens and thus, within the range studied, do not constitute a major variable.

Figure 4.22 shows a comparison between the normalized bearing stress (f_b/f'_c) for the straight tendon models and the ACI limits for permissible bearing stresses, which are given by:

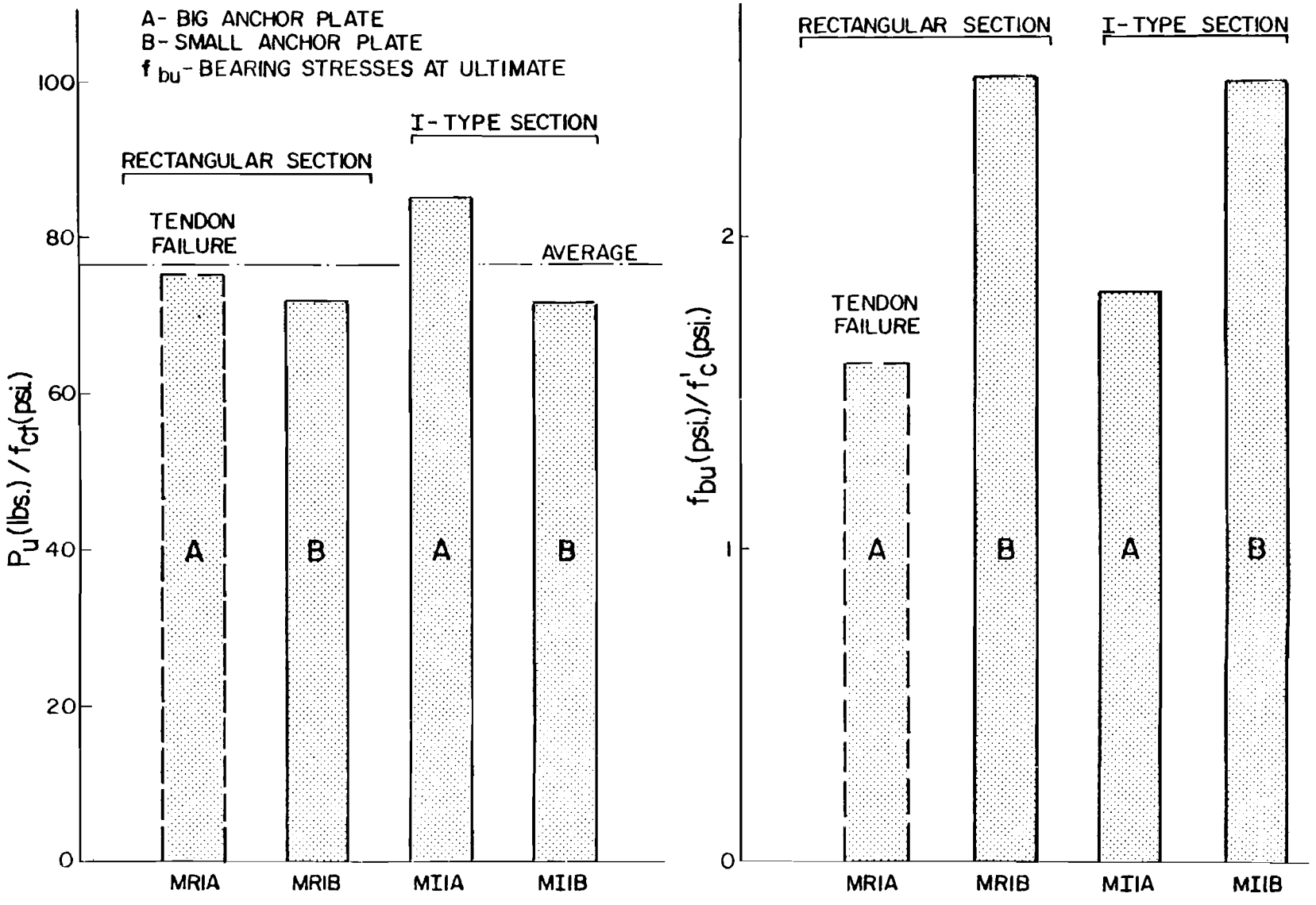

Fig. 4.21 Comparative diagrams of ultimate loads and bearing stresses at ultimate

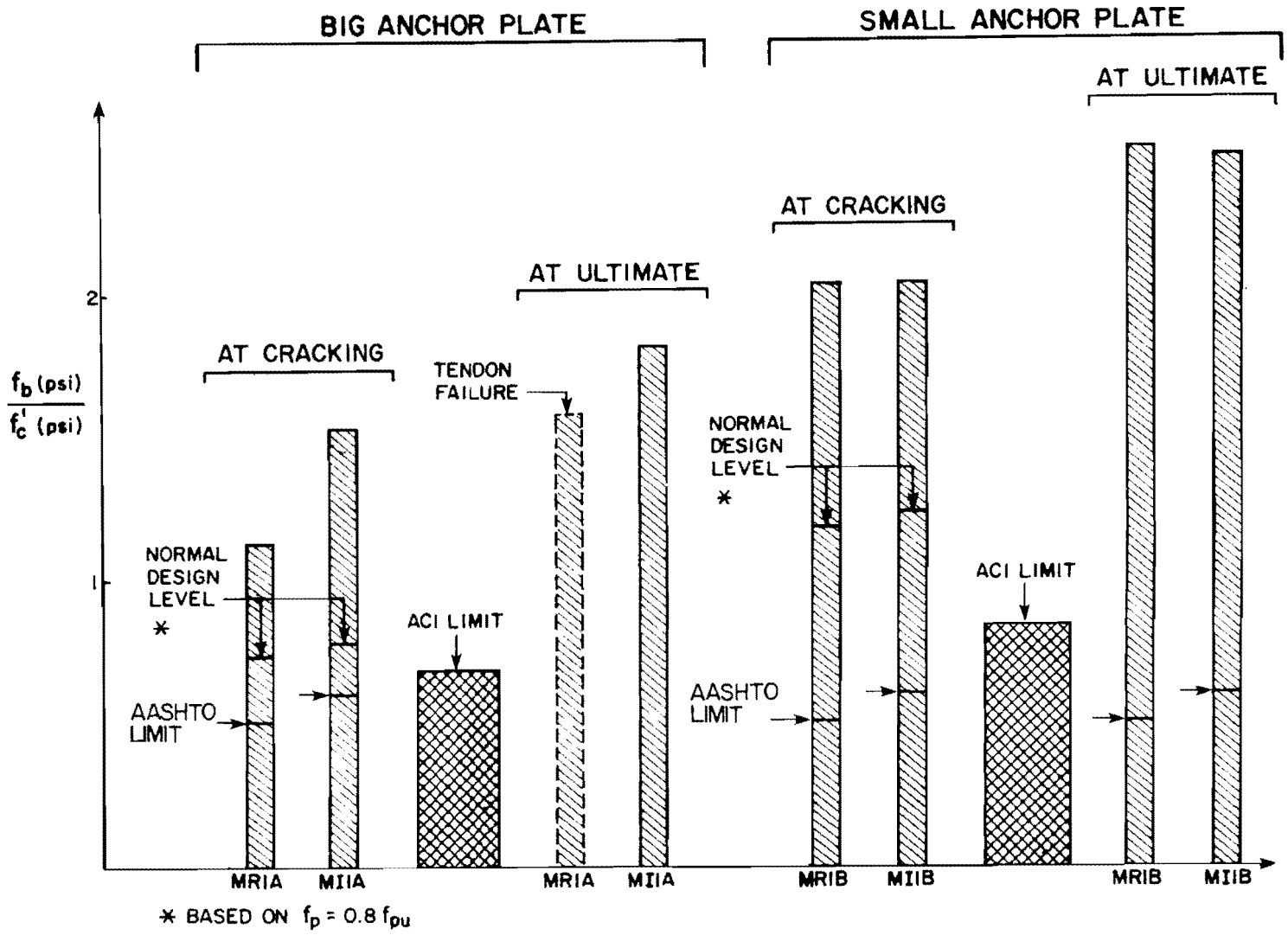

Fig. 4.22 Bearing stresses at cracking and ultimate load stages

$$f_b = 0.6f'_c\sqrt{A_2/A_1} \leq f'_c$$

The areas A_1 and A_2 were taken to be

$$A_2 = 3 \times 3 = 9 \text{ in.}^2$$

$$A_1 = 2.625 \times 2.625 = 6.89 \text{ in.}^2 \text{ (large anchor)}$$

or

$$A_1 = 2.125 \times 2.125 = 4.52 \text{ in.}^2 \text{ (reduced anchor)}$$

This expression, as mentioned in Ref. 1, is based on ultimate bearing capacity from column base-plate tests. For this application, the expression limits bearing stresses to 40 percent and 33 percent, respectively, of the experimentally observed ultimates for the standard and reduced anchors. The AASHTO 3000 psi limiting value is also indicated on Fig. 4.22, and is even more conservative than the ACI expression. Limiting bearing stresses to values such as f'_c (from the ACI building code) or 3000 psi (from the AASHTO specifications) is clearly an over-conservative and insensitive solution to the problem.

It should be emphasized that the ultimate loads achieved in these models were considerably higher than the maximum load that would be anticipated in normal post-tensioning applications. To illustrate the point, a twelve strand 1/2 in. diameter, 270 ksi tendon like the ones used for the full-scale tests would develop 396.5 kips when stressed to the 80 percent ultimate limit for temporary stressing. For the quarter-scale models with identical anchorage conditions, this load would correspond to approximately 25 kips which is less than half the observed ultimate load. The conclusion, therefore, is that for concentric straight tendon loading applications, using bearing-type anchorages similar to those used in the above tests, failure would be governed by the ultimate capacity of the tendons,

not the anchorage zone. On the other hand, it will be shown this conclusion is not applicable for situations involving curved or inclined tendons.

Another important effect which was investigated in this series was the relevance of the top and bottom flanges which had been added to the full-scale specimens (and subsequent models). Figure 4.20 shows very little variation between specimens with or without the flanges. A mean normalized cracking load of 61 with a standard deviation of only 7.7 percent for all tests attests to the small scatter. Similar trends can be seen for ultimate load where even less scatter is evidenced (S.D. = 6.4 percent). It is concluded therefore, that the flange effects can be neglected for specimens where tendon eccentricities are not great.

4.3.2 Inclined Tendon Series. Models MI2 and MI3 were designed for evaluation of the effects of spiral reinforcement as well as for comparison with the full-scale tests. The standard (2.65 × 2.625 in.) model bearing anchors were provided in both specimens. Spiral details for specimen MI3 were presented in Fig. 4.4. One test was performed on each specimen. In both cases, tendons with end eccentricities of 0 in. and 30-degree inclinations were used.

4.3.2.1 MI2. This was a model with a 30-degree inclined tendon, I-type section, standard anchor, and zero eccentricity corresponding to full-scale specimen FS2B. No supplementary anchorage zone reinforcement was provided. First cracking along the tendon path occurred at 30 kips (Fig. 4.23a), beginning at 2.5 in. from the loaded face and extending for about 5 in. At 35 kips, the crack reached the loaded face (Fig. 4.23). The upper diagonal crack formed at 39 kips and continued to propagate up to a load of 46 kips, as shown in Fig. 4.24. The specimen failed at a load of 48 kips, as evidenced by propagation of the upper and lower diagonal cracks and subsequent rupture of the side face (Fig. 4.25).

(a)

(b)

I-Type Section
Large Anchor
e = 0; θ = 30 degrees
No Spiral

Fig. 4.23 Specimen MI2 at first cracking

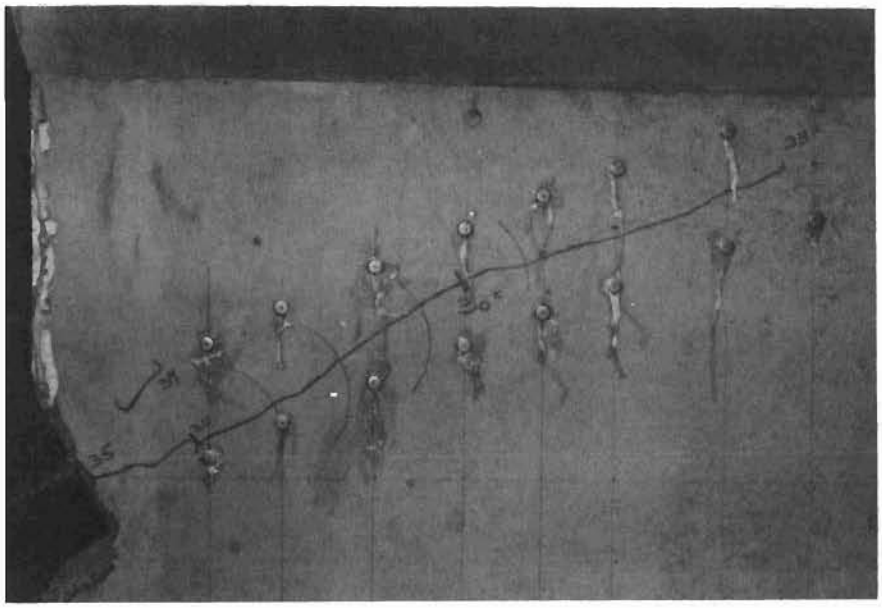

(a)

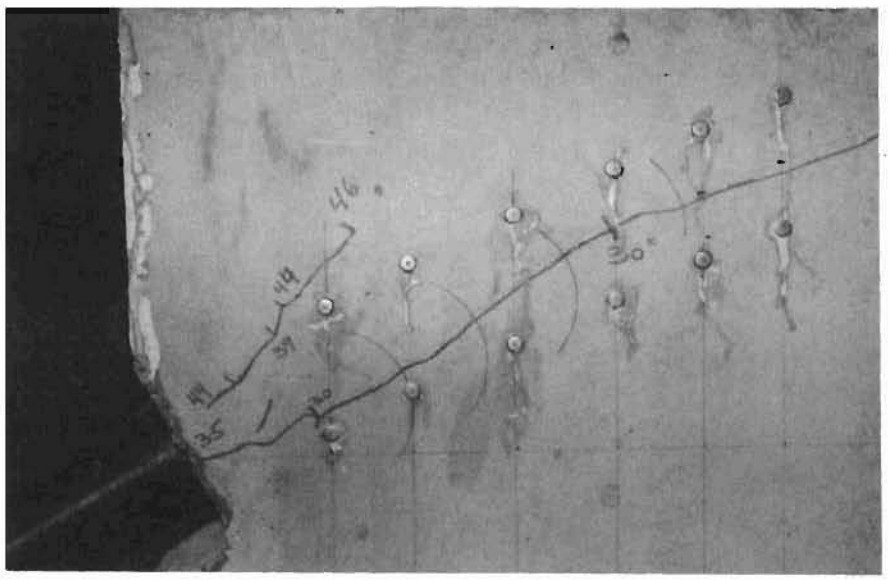

(b)

I-Type Section
Large Anchor
e = 0; θ = 30
No Spiral

Fig. 4.24 Specimen MI2--formation of diagonal cracks

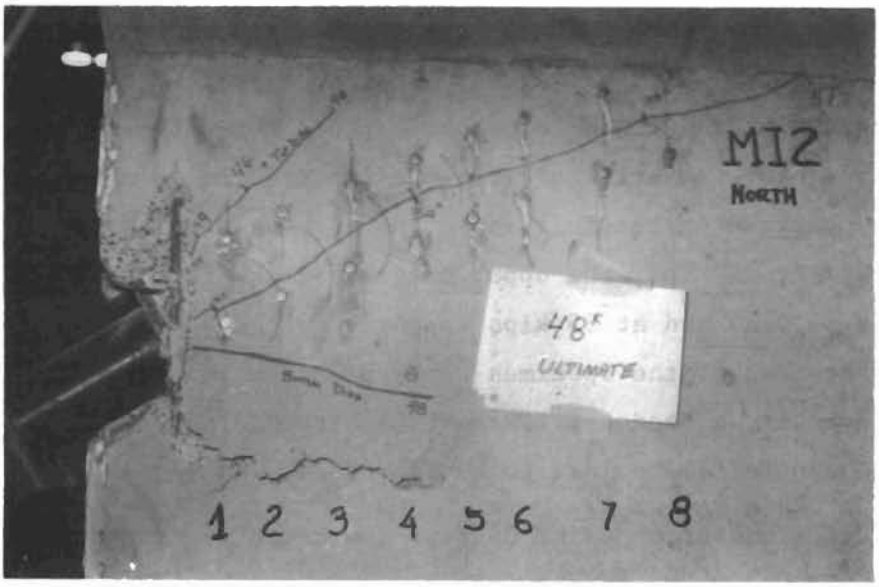

I-Type Section
Large Anchor
e = 0; θ = 30 degrees

Fig. 4.25 Specimen MI2 at failure

Crack measurements at 30 kips indicated crack widths along the tendon path of 0.001, 0.0015, and 0.002 in. at vertical line 1, 2, and 3, and 4, respectively. f'_c averaged 5305 psi with a standard deviation of 425 psi. Indirect tensile strength f_{sp} averaged 582 psi with a standard deviation of 77 psi.

4.3.2.2. MI3. This was a model with a 30-degree inclined tendon, I-type section, standard anchor, and zero eccentricity corresponding to full-scale specimen FS4A. A 2 in. diameter, 6.5 in. long spiral fabricated from 60 ksi, 13 gage wire was included as supplementary reinforcement. First cracking along the tendon path occurred at 37 kips beginning at the loaded face and extending for a distance of 4 in. (Fig. 4.26). At 43 kips, a small crack initiated at the corner of the tendon blockout but did not progress with increasing load. A series of multiple longitudinal cracks (similar to those observed in the full-scale tests) developed as the load was increased. At 47 kips, the upper diagonal crack formed on the south face (Fig. 4.27a) and at 59 kips appeared on the north side. At 61 kips, both sides of the specimen were extensively cracked (Fig. 4.27). However, a tendon failure at 61 kips did not permit anchorage zone ultimate load to be achieved.

Crack measurements at 37 kips indicated tendon path crack widths of 0.001, 0.002, and 0.0015 in. at vertical lines 1, 2, and 3. f'_c averaged 5212 psi with a standard deviation of 227 psi. Indirect tensile strength f_{sp} averaged 606 psi with a standard deviation of 68 psi. This value of f_{sp} was equal to $8.4\sqrt{f'_c}$. For most regular concretes (ready mix) $f_{sp} \leq 6.5\sqrt{f'_c}$, considerably lower. Model trends generally indicated values of f_{sp} between 8 to $10\sqrt{f'_c}$.

4.3.2.3 Comparison. Both specimens with inclined, curved tendons cracked at loads comparatively much lower than the specimens with straight tendons. In fact, the cracking load for inclined tendon specimen MI2 (30 kips) was 39 percent lower than that for

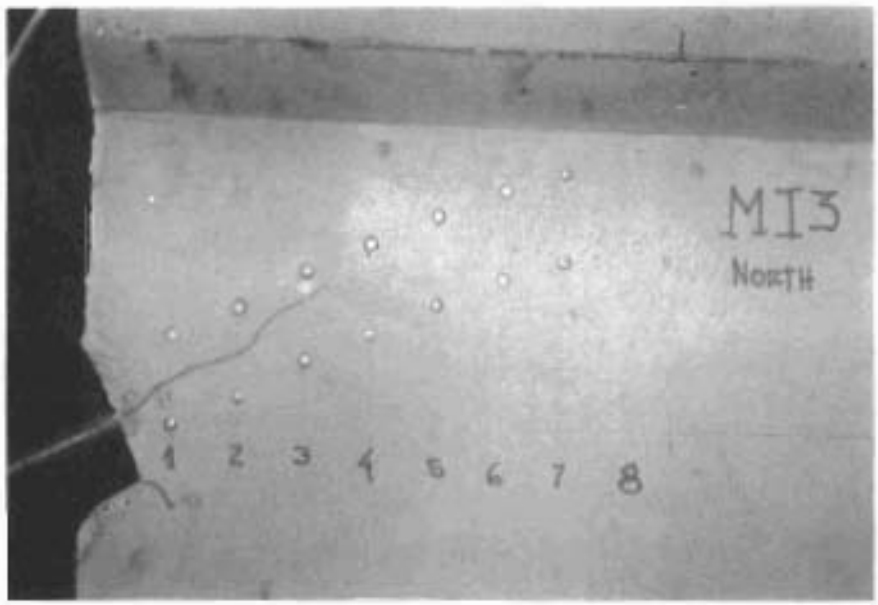

(a)

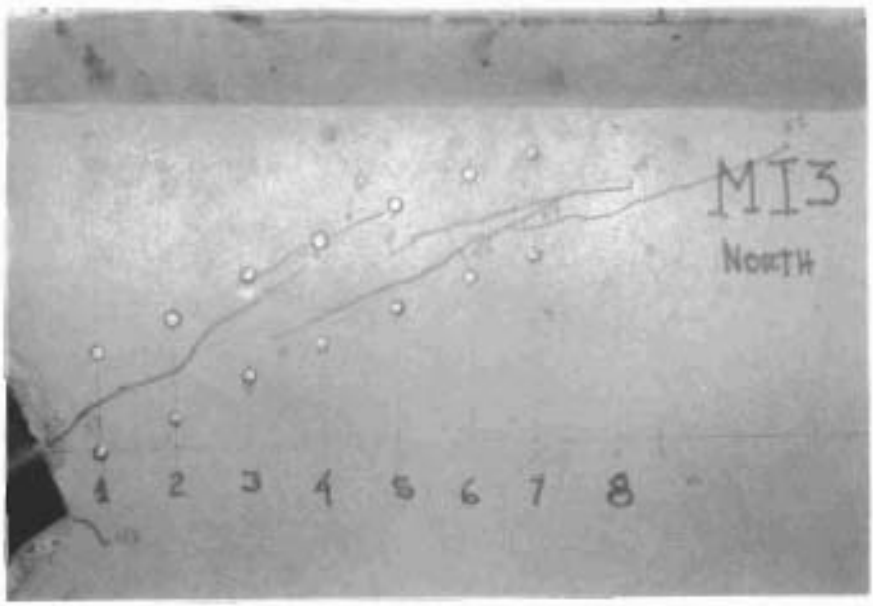

(b)

I-Type Section
Large Anchor
e = 0; θ = 30 degrees
With Spiral

Fig. 4.26 Specimen MI3--development of longitudinal cracks

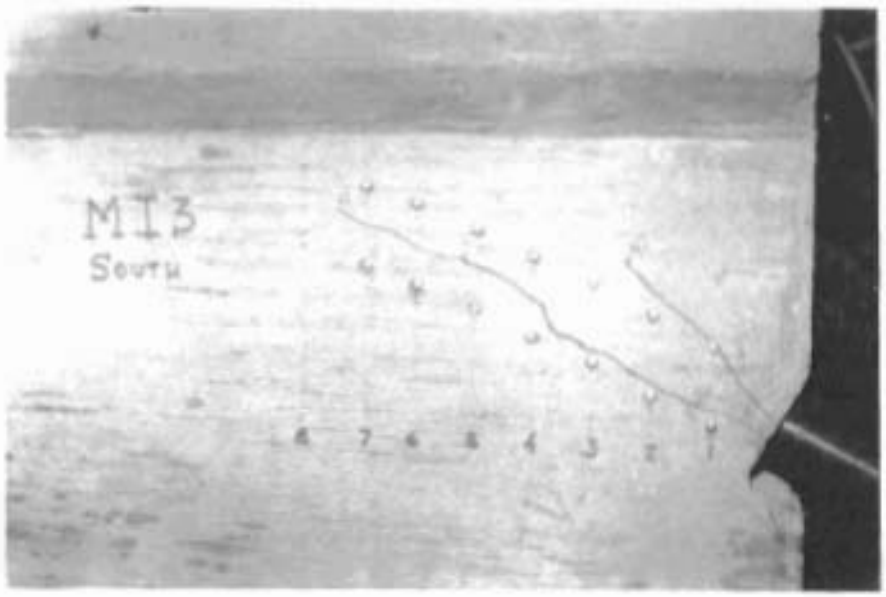

(a)

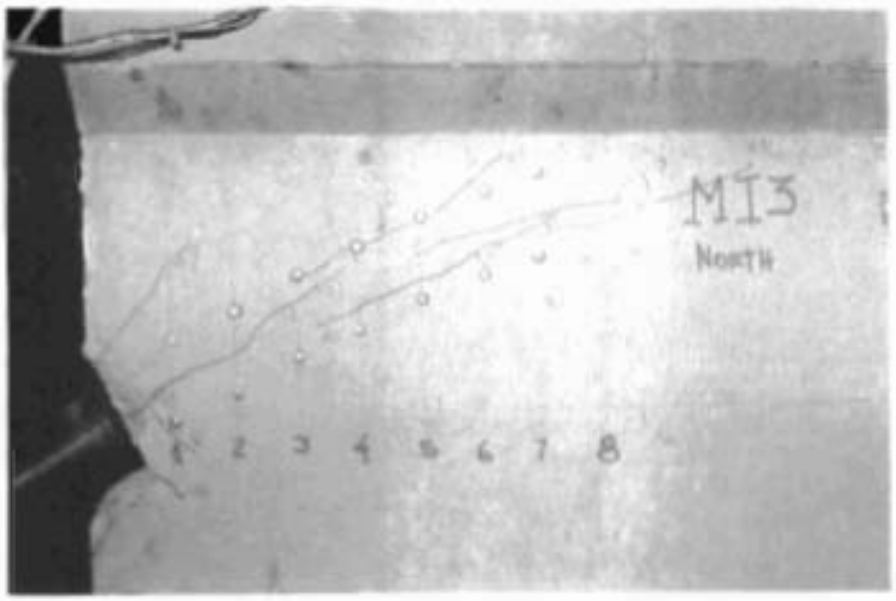

(b)

I-Type Section
Large Anchor
e = 0; θ = 30 degrees
With Spiral

Fig. 4.27 Specimen MI3--formation of diagonal cracks

straight tendon specimen MI1A (49 kips) even though both specimens were otherwise identical and had nearly identical compressive strengths (f'_c).

Both types of inclined tendon specimens exhibited the familiar failure sequence of tendon path cracking, formation of diagonal cracks, and side face rupture in the anchorage zone at failure. The presence of the spiral reinforcement seems to increase the number of longitudinal cracks with corresponding decrease in the individual crack widths. This trend can be observed in Fig. 4.28 which shows average crack widths along the tendon.

The spiral reinforcement had the effect of increasing the cracking load by 17 percent, as illustrated in Fig. 4.29. Unfortunately, a tendon failure occurred in specimen MI3 at 61 kips and failure load for the anchorage zone could not be determined. Figure 4.30 presents a comparison between the two specimens at ultimate. As can be seen, specimen MI3 (with spiral) reached a load 22 percent higher than that for specimen MI2 at the point where the tendon failed. Spiral reinforcement thus (again) appears to be an efficient means of significantly increasing the ultimate capacity of the anchorage zone.

4.4 Similitude Comparison--Results of Model Prototype Tests

A summary of the experimental results for the similitude tests are given in Table 4.4. This section examines the relative cracking and ultimate behavior of both the model and full-scale tests to determine the ability of the models to reproduce behavior seen in the prototype as well as to determine what factors must be taken into account in the interpretation of the model results. In addition to physical cracking and ultimate load data, the models were also instrumented with micro insertion strainmeters, so that relative comparisons of bursting and spalling strain distributions could be made.

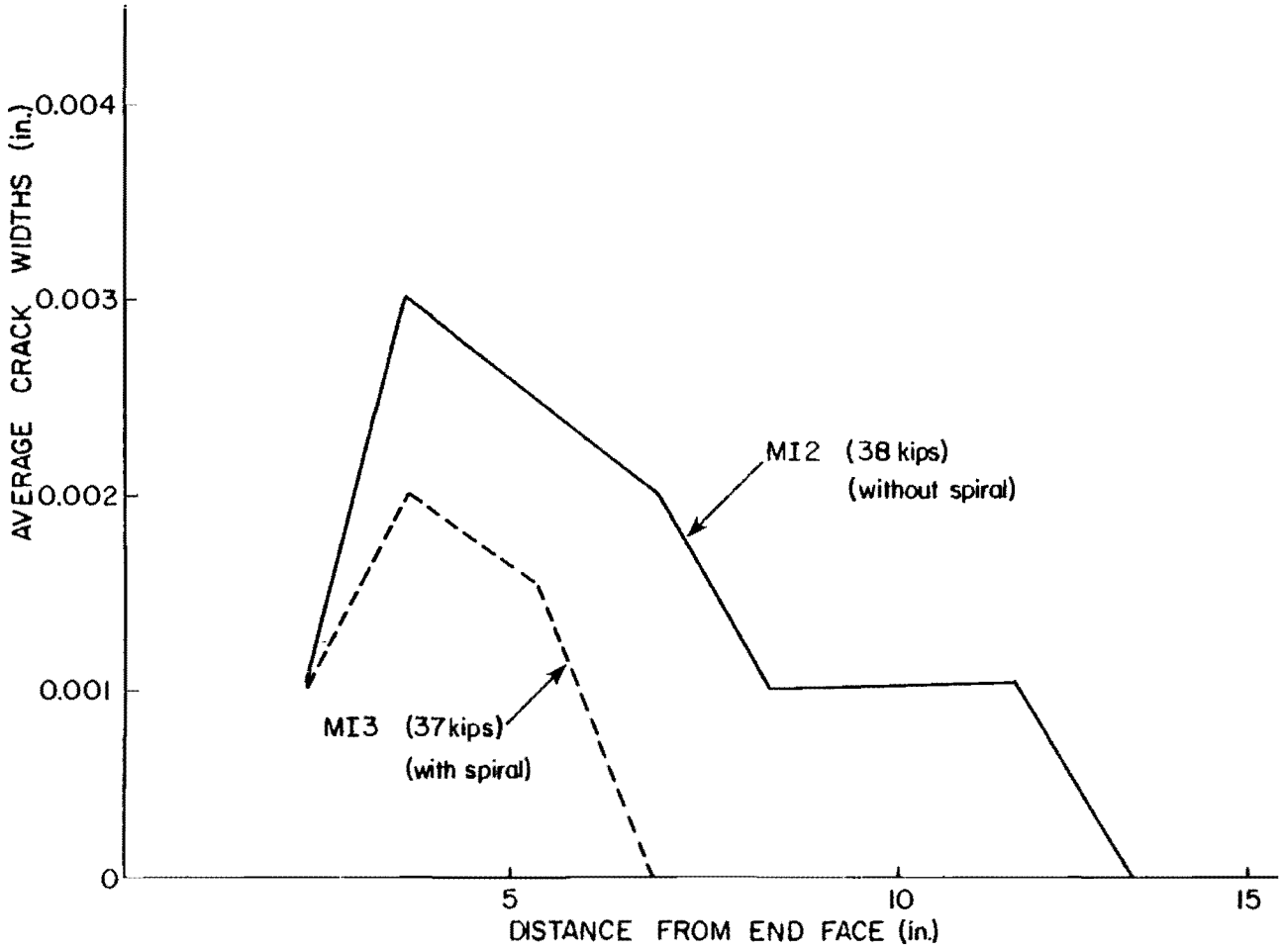

Fig. 4.28 Effects of spiral reinforcement on crack widths

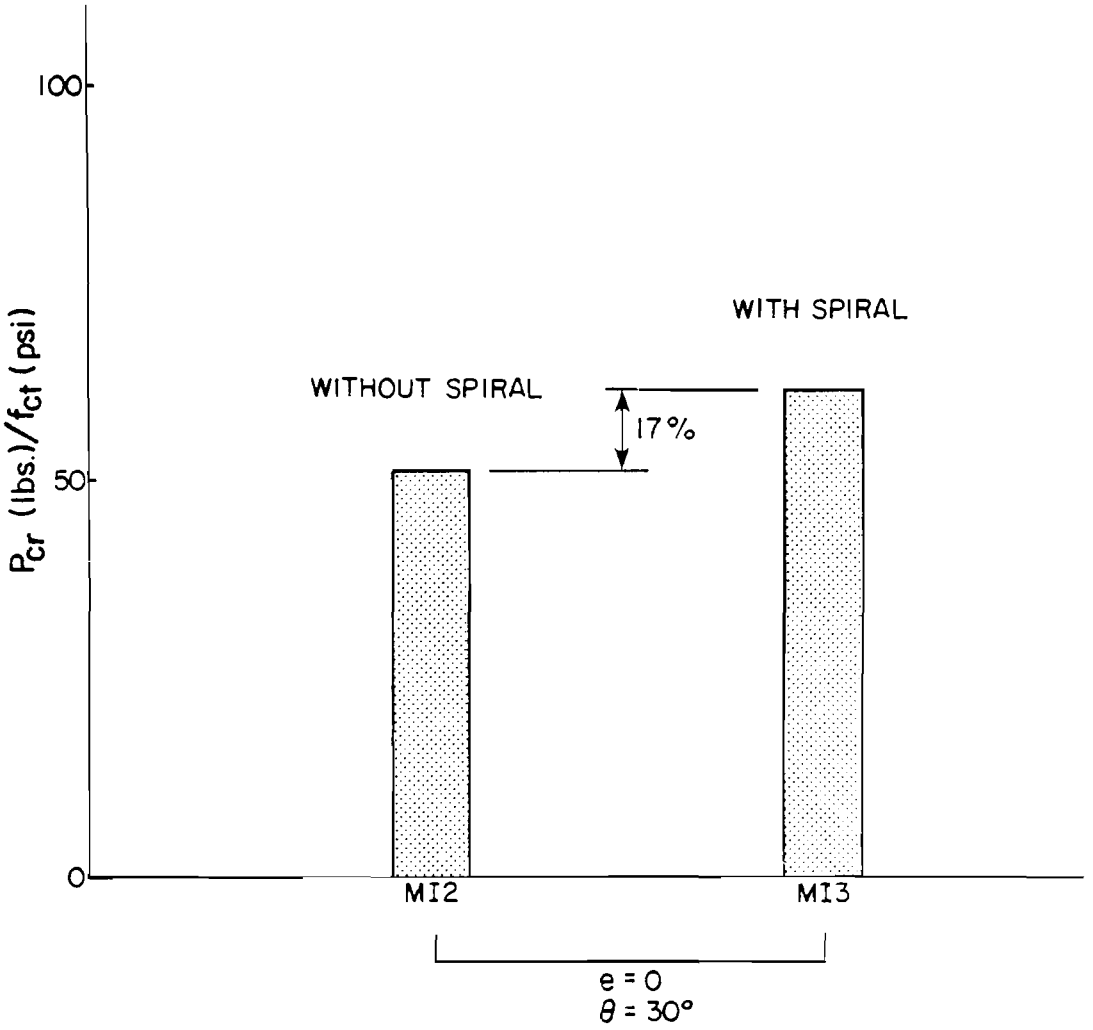

Fig. 4.29 Effect of spiral reinforcement on cracking load

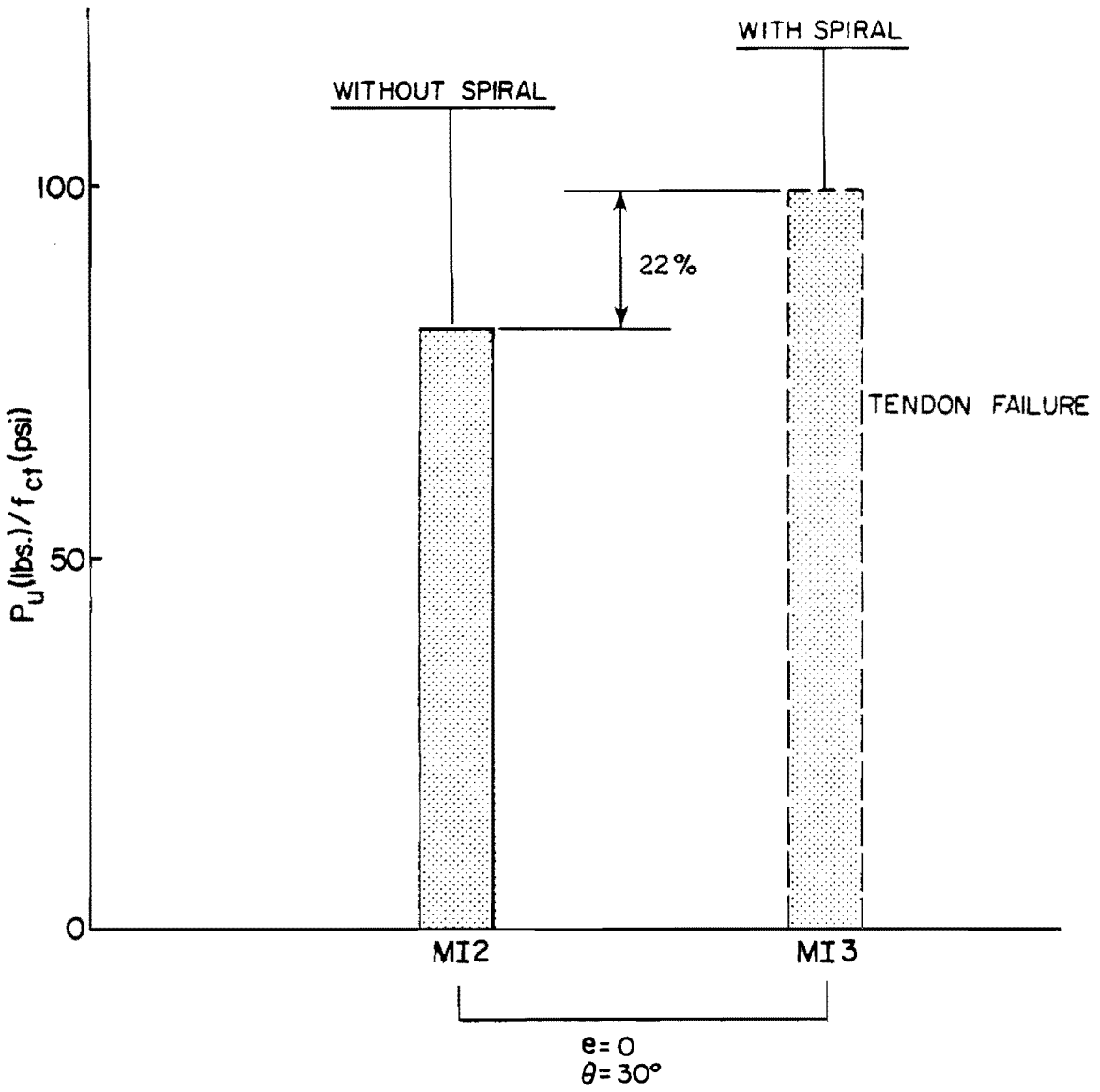

Fig. 4.30 Effect of spiral reinforcement on ultimate capacity

TABLE 4.4 SUMMARY OF TEST RESULTS

Specimen	Type of Cross Section	Type of Tendon Profile	Variable Studied	f'_c (psi)	f_{ct} (psi)	P_{cr} (kips)	P_u (kips)	Type of Failure and Comments
MR1A	Rectangular	Straight e=0; θ=0°	Shape of Cross Section and Bearing Area	5612	723	39	55	Tendon Failure
MR1B	Rectangular	Straight e=0; θ=0°	Shape of Cross Section and Bearing Area	5624	725	43	53	Explosive Side Splitting Failure
MI1A	I-Type	Straight e=0; θ=0°	Bearing Area	5234	685	49	59	Explosive Side Splitting Failure
MI1B	I-Type	Straight e=0; θ=0°	Bearing Area	5352	697	41	50	Explosive Side Splitting Failure
MI2	I-Type	Curved e=0; θ=30°	Curvature	5305	582	30	48	Explosive Side Splitting Failure
MI3	I-Type	Curved e=0; θ=30°	Spiral Reinforcement	5212	606	37	61	Tendon Failure
FS1A	I-Type	Straight e=0; θ=0°	Bearing Area	5034	451	400	--	Not Taken to Ultimate
FS1B	I-Type	Straight e=0; θ=0°	Bearing Area	5783	401	400	--	Not Taken to Ultimate
FS2B	I-Type	Curved e=0; θ=30°	Curvature	4627	455	330	620	Tendon Failure
FS4A	I-Type	Curved e=0; θ=30°	Spiral	5200	513	400	650	Explosive Failure of Anchor Zone

4.4.1 Specimens with Straight Tendons (Bearing Stress Series)

4.4.1.1 Crack Patterns. First cracking was characterized by a crack along the tendon path in both model and full-scale specimens. This longitudinal crack, which initiated at a point approximately the width of the anchor from the loaded face, generally extended to the web-flange junction for inclined tendons, and about five times the width of the anchor for straight tendons. An increase in load led to the formation of upper and lower diagonal cracks, which usually served as an indication of impending failure. These latter cracks were not observed in the two straight tendon prototypes due to tendon capacity limitations in the loading system.

Crack widths for the full-scale specimens were usually wider than those observed in the models (multiplied by a factor of four to account for scale) and were easily observed with the naked eye. On the other hand, the model cracks often needed to be located with a microscope before a visual observation was possible. The use of a stethoscope proved to be of great help as first cracking could actually be heard shortly before it was sighted. Model and full-scale crack widths are compared in Fig. 4.31. The maximum model crack widths, when multiplied by a factor of four, are on the order of 20 percent below those observed in the corresponding full-scale specimen (MI3 to FS4A, MI2 to FS2B).

Figure 4.32 shows cracking loads normalized with respect to f'_c and the scale factor (for load $S^2 = 16$) for models and full-scale specimens. Differences of 50 percent for specimens with the standard commercial anchors, and 36 percent for specimens with the reduced anchors were observed from the model analysis. The important point to be made is that the compressive strength of the concrete is not an appropriate parameter for correlation of cracking loads between model and prototype, especially since the tensile strength (f_{sp}, indirect) of the microconcrete was found to be substantially greater

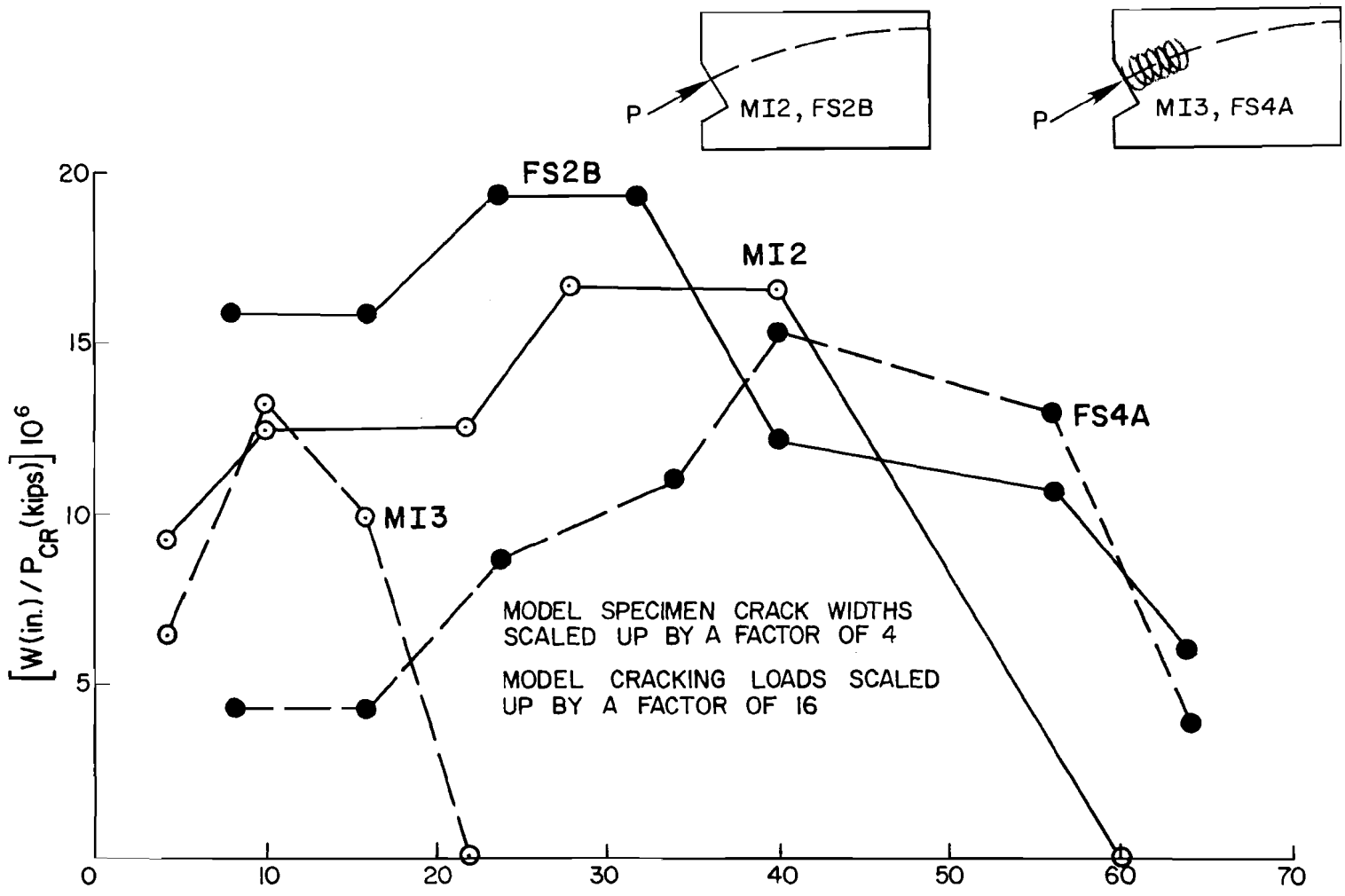

Fig. 4.31 Comparison--full-scale vs model crack widths

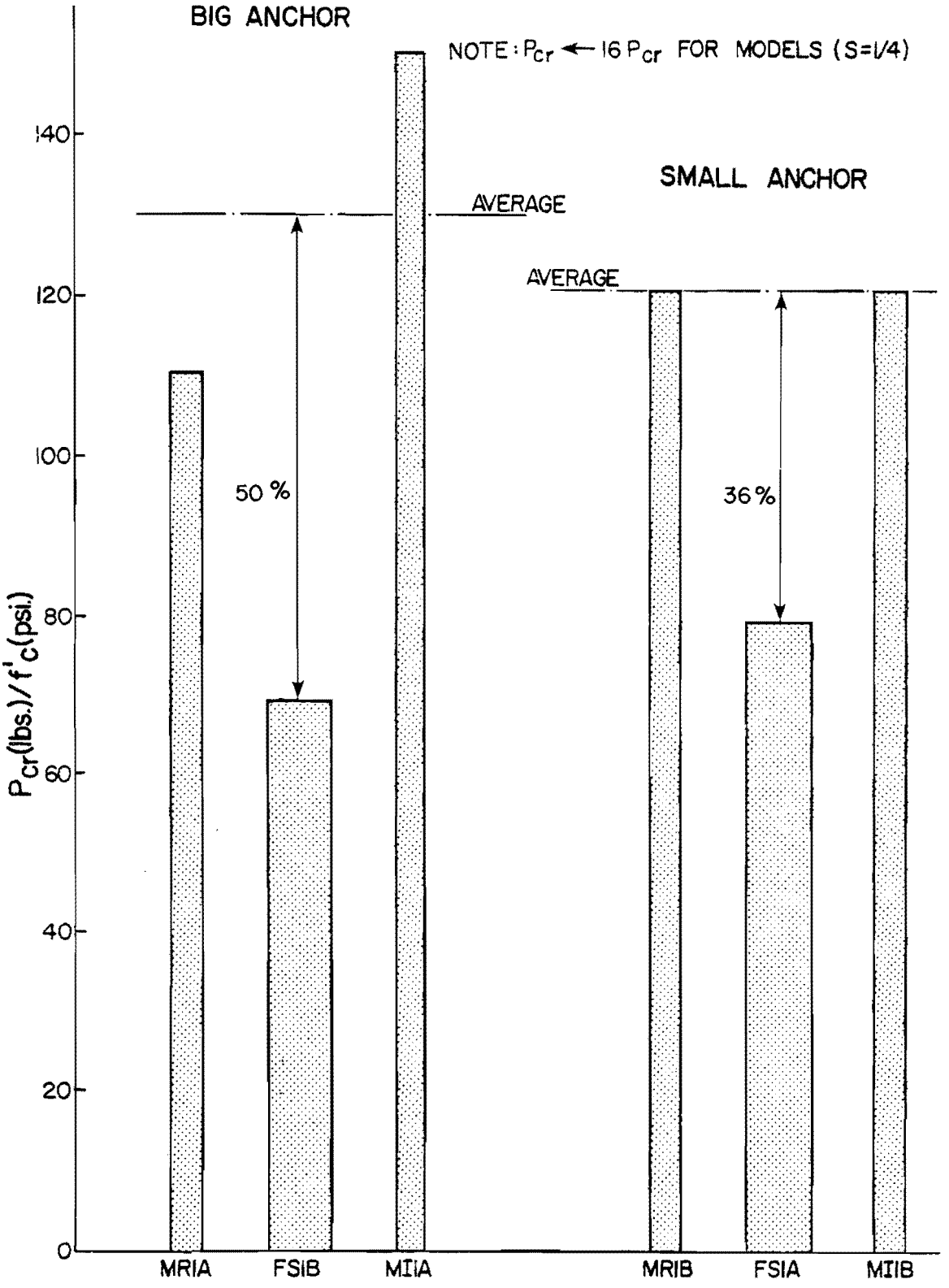

Fig. 4.32 Straight tendon specimens--cracking loads normalized with respect to f'_c

(about 30 percent on the average) than that for the corresponding prototype concrete.

Cracking loads normalized with respect to the indirect tensile strength (f_{sp}) are shown in Fig. 4.33. This shows specimen FS1B (standard anchor) cracked at a level only 1 percent below the average of its companion models. The maximum deviation was 15 percent between FS1B and MR1A (rectangular section). The reduced anchor specimens exhibited very similar cracking loads, with the maximum difference between FS1A and the two models.

The results indicated that the quarter-scale model test results could be used to predict first cracking of full-scale specimens with straight tendons if the indirect tensile strengths were taken into account.

4.4.1.2 Ultimate Load. Since the full-scale specimens could not be taken to failure because of tendon capacity limitations, no comparison could be drawn. However, the model tests suggested that, after the formation of the diagonal cracks, an increase of about 10 percent in the load is sufficient to cause failure in specimens without supplementary reinforcement. The ultimate load stage in the models was characterized by sudden and explosive rupture of the side faces in the anchorage zone, with the accompanying formation of a cone of crushed concrete beneath the anchor.

From the model and full-scale tests, it was concluded that current design criteria, based on permissible bearing stresses, severely underestimate the bearing capacity of the post-tensioned anchorage zone, while paying insufficient attention to the more important tensile stresses.

4.4.2 Specimens with Curved Tendons

4.4.2.1 Crack Patterns. For specimens without spiral reinforcement (MI2, FS2B), the tendon path cracks originated at a point near the loaded face and propagated to a point near the web-flange

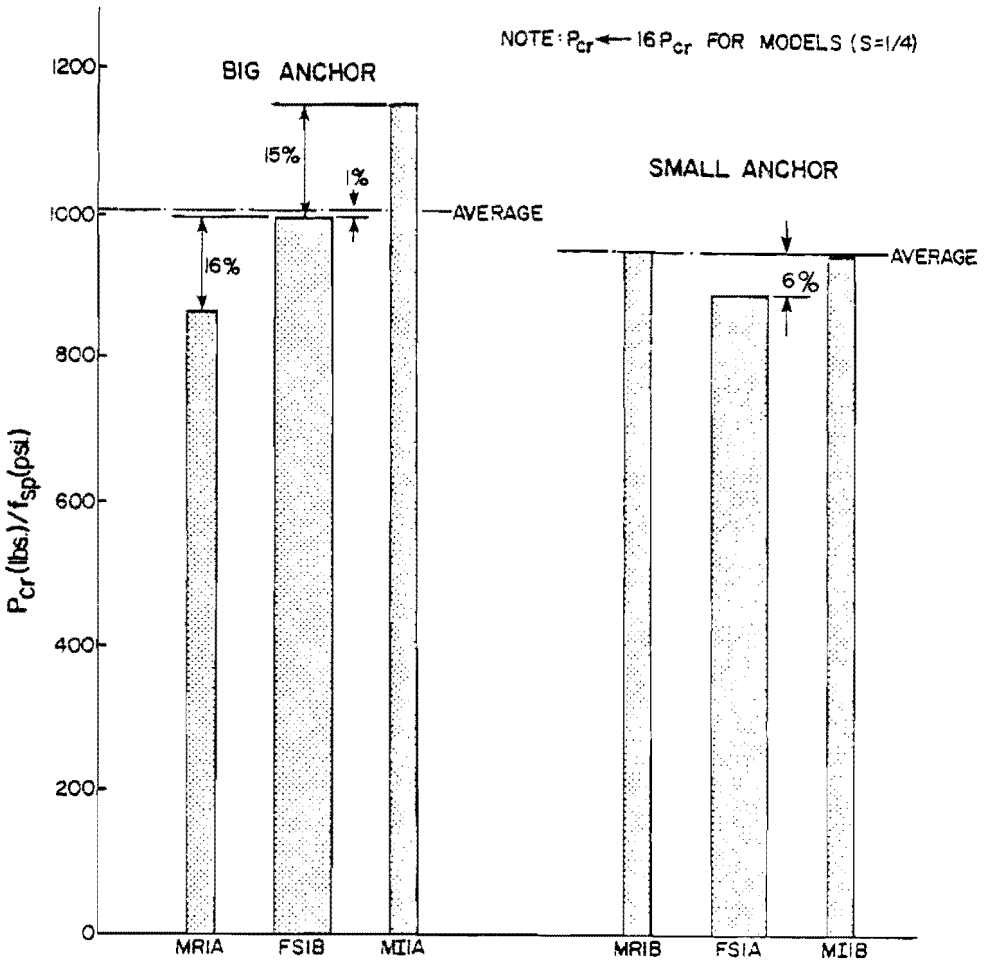

Fig. 4.33 Straight tendon specimens--cracking loads normalized with respect to f_{sp}

junction. Those specimens with spiral reinforcement (MI3, FSA), however, exhibited dissimilar patterns of first cracking. For FS4A (full scale), the crack initiated at the point of maximum curvature and propagated towards the anchor. Specimen MI3 (model) cracked at a load (scaled, normalized) 25 percent above that for FS4A, but with the crack initiating at a point near the loaded face and propagating toward the web-flange junction along the tendon path. In the case of the full-scale specimen, the effect of the spiral was to confine the concrete ahead of the anchor such that cracking first occurred beyond the spiral cutoff point, apparently due to a flattening out of the multiple strand tendon. The model, having a single tendon which developed minimal lateral forces at the point of maximum curvature, cracked in the anchorage zone proper. After first cracking, for both model and prototype the presence of the spiral tended to cause formation of multiple longitudinal cracks at higher load stages. The multiple longitudinal cracks exhibited smaller cracks widths than for corresponding specimens without the spiral.

In most curved tendon specimens, a diagonal crack usually formed below the anchor plate, emanating from the corner blockout at a load well below the formation of the so-called "lower diagonal" crack proper. This is attributed to the extremely high tensile stresses which exist at the reentrant corner.

Figure 4.34 shows a comparison between normalized cracking loads (P_{cr}/f_{sp}) for models and full-scale specimens. As can be seen, the models developed slightly higher cracking loads. Most of this discrepancy can be attributed to the so-called "multistrand effect" which led to premature cracking and side face rupture at the point of maximum tendon curvature.

Radial forces are generated in the concrete along the tendon duct due to the normal component of the prestressing force which exists in curved tendons, as illustrated in Fig. 4.35a. These normal

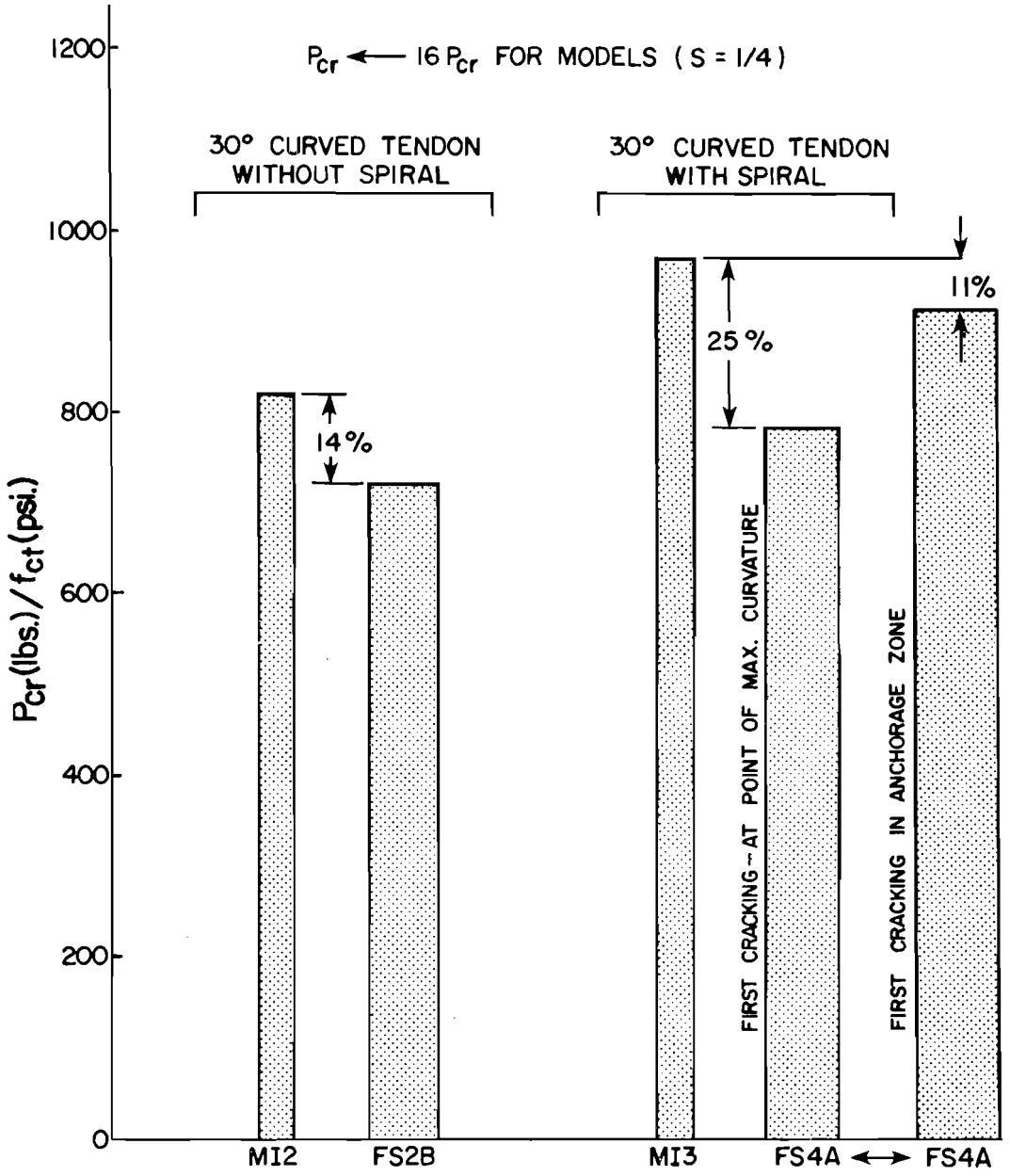

Fig. 4.34 Curved tendon specimens--normalized cracking loads

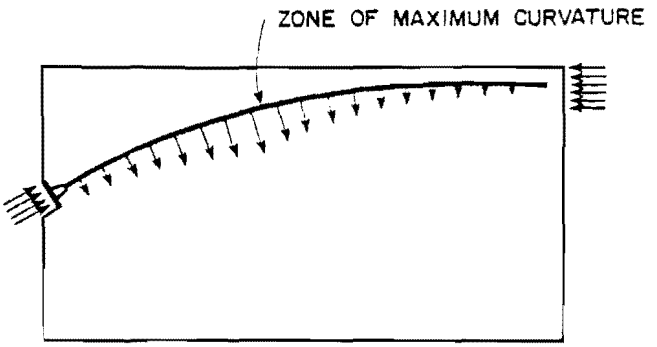

(a) RADIAL FORCES IN THE CONCRETE (ELEVATION)

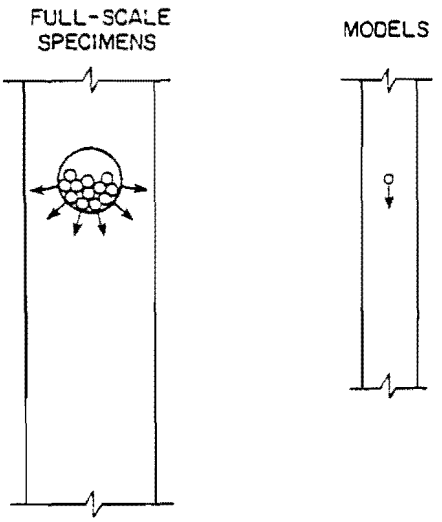

(b) RADIAL FORCES IN THE CONCRETE (CROSS-SECTION)

Fig. 4.35 Multistrand effects

forces which are distributed along the tendon path reach a peak at the point of sharpest curvature and may be computed as F/R where:

F = Post-tension load

R = Radius of curvature at a particular point

If only a two-dimensional loading existed (as idealized to obtain the above formula), the effect could be accurately simulated in the model by using a single strand tendon which followed the same relative curvature as the prototype tendon. However, for the case of a bundled, multiple strand tendon, such as illustrated in Fig. 4.35b, the state of stress also included a large lateral component due to the tendency for the bundle to flatten out. The single unbonded strand used for loading the models was not capable of reproducing this effect.

Depending upon the number of strands in the bundle, the relative size of the duct to the bundle diameter and the position of the duct (i.e., skewed towards one or the other face), the cracking load can be significantly lower than that for an anchorage that was inclined but did not have a curved tendon. As demonstrated with the model tests, it can also be lower than that for a single strand inclined, curved tendon.

Another important point is that when the anchorage zone is equipped with supplemental spiral reinforcement, which tends to confine the concrete and increase the cracking load in the anchorage zone, there is an enhanced tendency for a multistrand failure at the point of maximum tendon curvature if supplemental reinforcement is not present at that point. This is often the case since the maximum curvature often occurs at a point well removed from the anchorage zone.

4.4.2.2 Ultimate Load Stage. Due to the failure of the loading tendon for full-scale specimen FS2B (no spiral), a comparison of ultimate behavior could not be made with specimen MI2. For the two

inclined specimens with spiral reinforcement (FS4A, MI3) the reverse occurred. The tendon for the model failed before ultimate could be reached. Although no direct comparison is possible, Fig. 4.36 shows that ultimate load for the model MI3 would be at least 27 percent higher than that for the prototype FS4A.

4.4.3 Distribution of Transverse Strains. In addition to load behavioral data, a number of the micro insert strainmeters were included in each of the model specimens to see if relatively similar bursting and spalling strain distributions were developed in both model and prototype specimens. Sample results are presented in Figs. 4.37 through 4.40, showing two bursting and two spalling distributions. Load in the prototype specimens was 200 kips, while the load in the models was 1/16 of this or approximately 13 kips. In general, excellent agreement existed considering the expected scatter. Quantitatively, it would be difficult to set a numerical value for the accuracy but qualitatively there is no sharp distinction between the model and prototype data. As previously reported [1], the analytical 3D FEM analysis generated distributions which agreed quite well with both model and full-scale data.

4.5 Developing Similitude

Based upon the results presented in this chapter, the following should be taken into account when extrapolating full-scale anchorage zone behavior from direct model tests:

(1) The tensile strength of the microconcrete is substantially higher than that for the corresponding prototype concrete.

(2) Cracking and ultimate loads must be normalized with respect to the indirect tensile strength when interpreting model test results and for prediction of response in corresponding prototype structures.

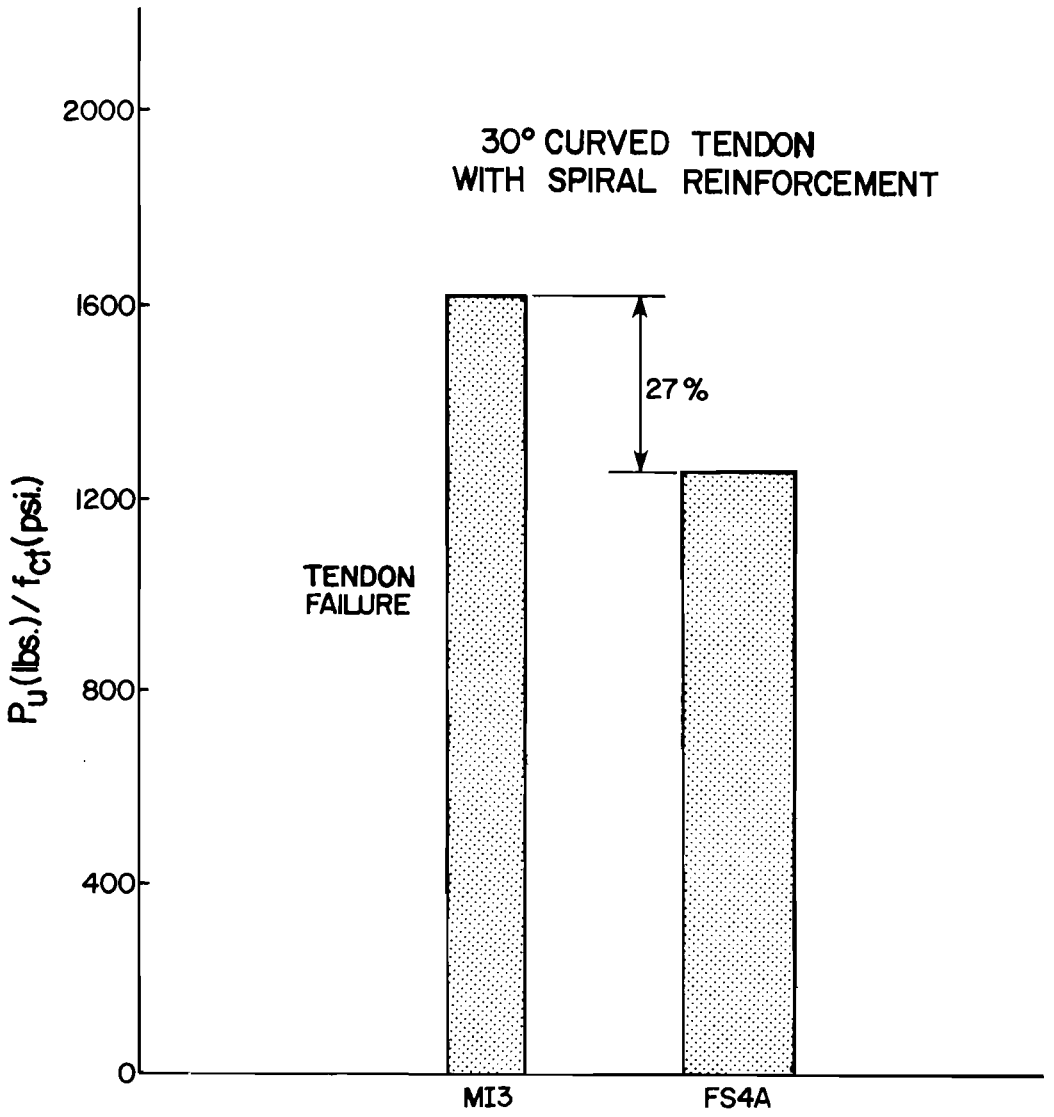

Fig. 4.36 Normalized ultimate loads for specimens with spiral reinforcements

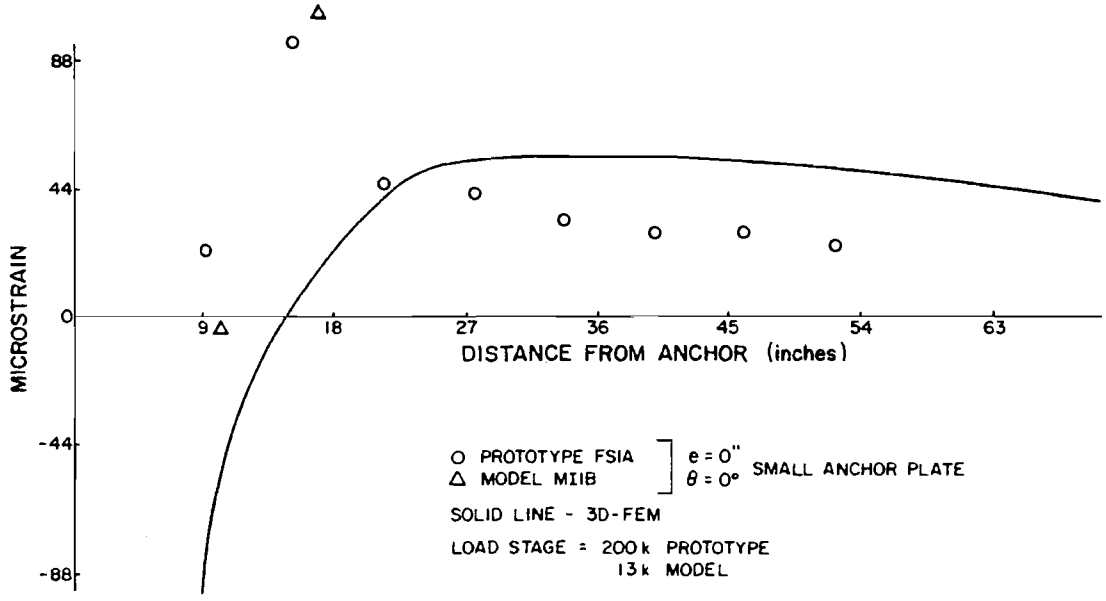

Fig. 4.37 FS1A/MI1B--bursting strain distribution

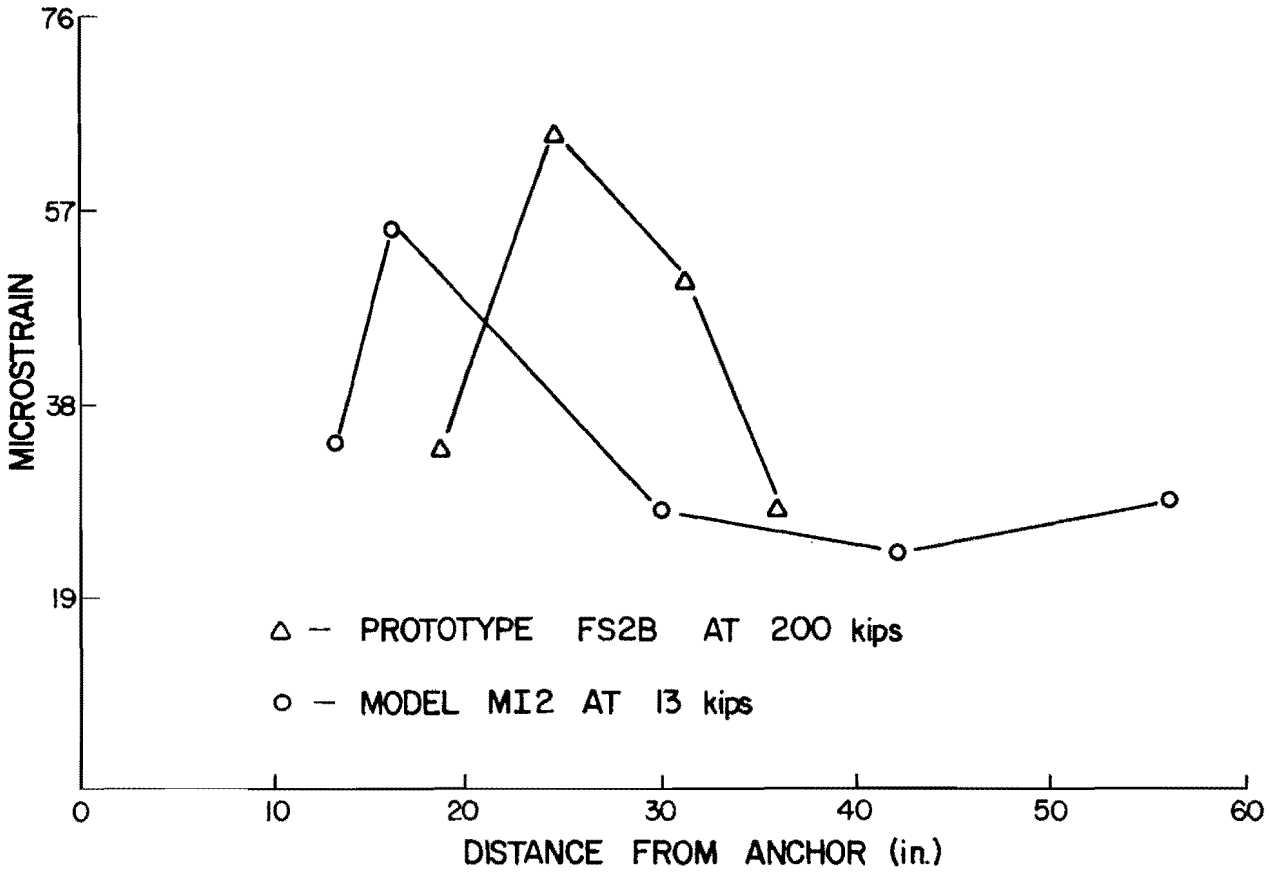

Fig. 4.38 FS2B/MI2--bursting strain distribution (experimental)

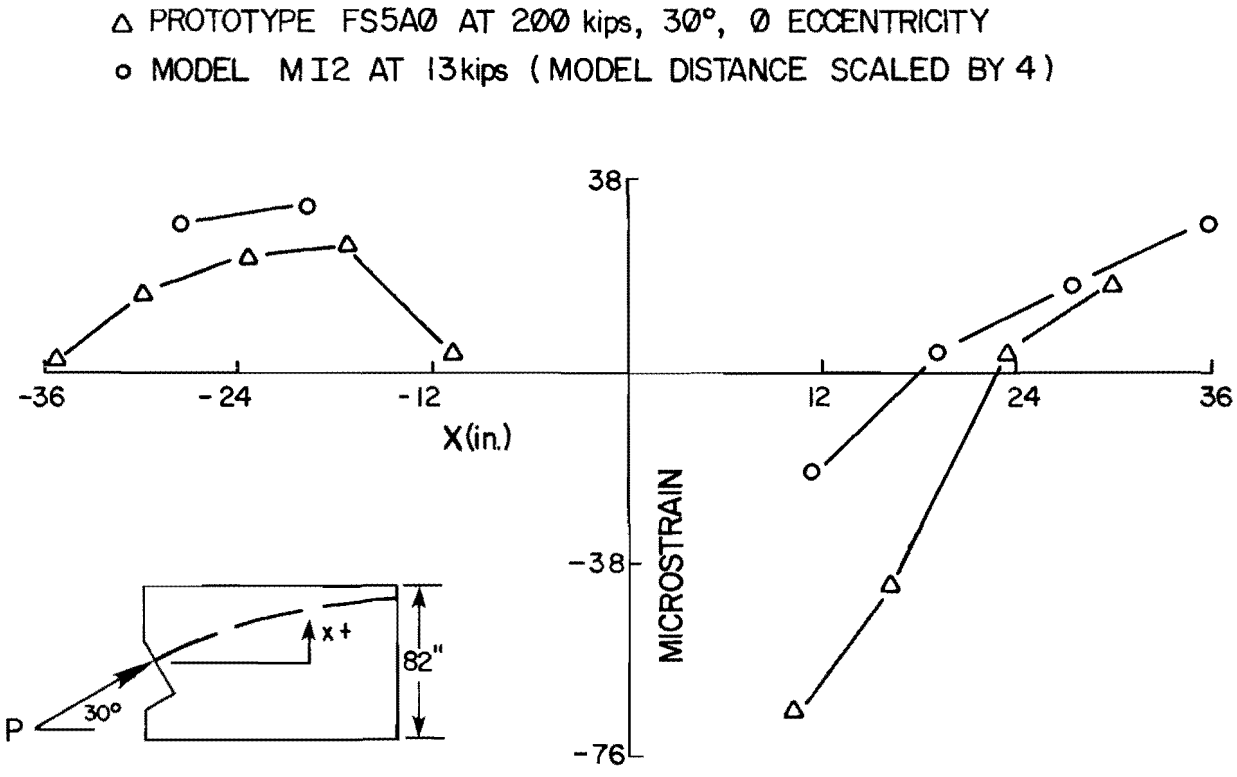

Fig. 4.39 FS5A(no LPT)/MI2--comparison of experimental spalling strain distribution

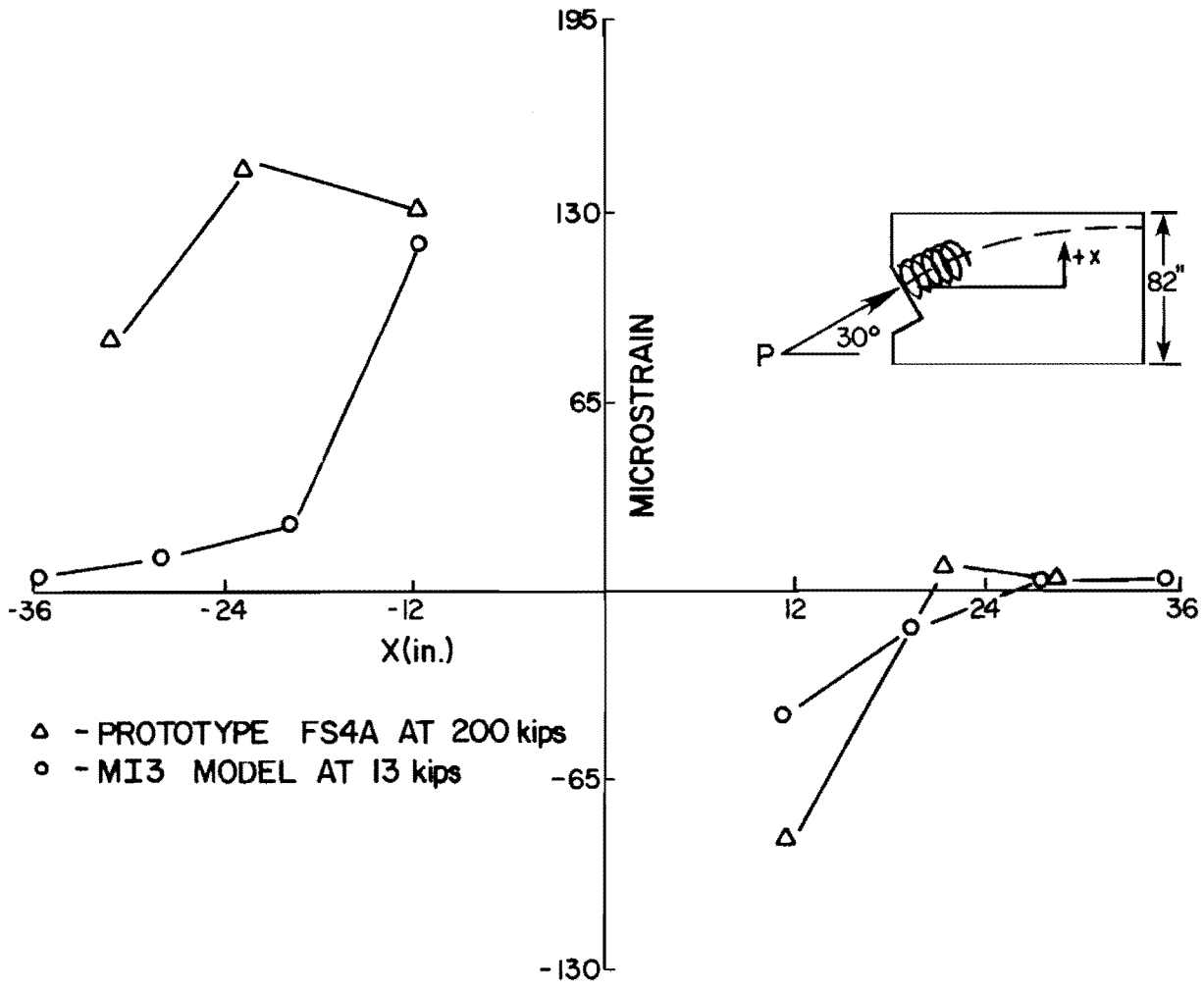

Fig. 4.40 FS4A/MI3 comparison of experimental spalling strain distribution

(3) Excellent reliability (± 10%) can be expected for model tests dealing with straight tendon anchorage zones (including the effects of eccentricity, cover, and bearing area).

(4) Cracking and ultimate loads of multiple strand curved tendon specimens cannot be accurately predicted from single strand curved tendon models. Large lateral forces develop at the point of maximum curvature, due to the flattening out of the multiple strand tendon which can cause side splitting at loads below those that would cause cracking in the anchorage zone.

Accurate reproduction of the multistrand effect in models would require a similar scaled down tendon to that used in the prototype. The main complication is in developing a practical anchorage system for the multiple model strands.

(5) Crack patterns of full-scale specimens are reproduced with reasonable similarity in both straight and curved tendon models. However, crack widths in the models can be 30 to 40 percent smaller (after scaling by 4) than those observed in the full-scale tests.

(6) The formation of the upper and lower diagonal cracks around the anchor is a visual indicator of the proximity of ultimate failure.

(7) The mechanism of failure associated with nonspirally reinforced anchorage zones leads to the formation of a concrete cone under the bearing-plate anchor.

(8) A potential zone for the formation of cracks is located at the corner of the tendon blockout for curved tendon specimens.

(9) Bearing stress is not a governing factor affecting the behavior of post-tensioned anchorage zones in thin web members. Current design criteria based primarily on permissible bearing stresses are inappropriate.

(10) Specimens with inclined tendons crack at load levels considerably lower than those with straight tendons.

(11) The presence of spiral reinforcement changes the cracking pattern from a single tendon path crack to a series of parallel cracks following the tendon which exhibit a significant reduction in the average crack width. In addition, cracking loads can be raised through the use of spiral reinforcement. Spiral effects can be replicated in the models.

(12) For tendons with low eccentricities, the effects of top and bottom flanges on the behavior of the anchorage zone can be neglected. This underscores the localized nature of the anchorage zone stress state.

CHAPTER 5

SUMMARY

5.1 General

The behavioral trends summarized are drawn from three sources reported in detail in this report. These are physical tests of 40 quarter-scale microconcrete models, physical tests of 9 full-scale prototype concrete specimens designed to replicate post-tensioning conditions found in thin web sections, and directly related results of three-dimensional linear elastic finite element computer analyses of many of the physical test specimens. The model test results were found to match the prototype behavior when scaled properly through the use of the geometric scale factor and the measured split cylinder tensile strength of the concrete.

The test specimens used in this investigation differed appreciably from the concentrically loaded symmetrical prisms generally used in previous anchorage tests. These specimens were designed to simulate anchorage zones complicated by thin webs, eccentricity, inclination, and tendon curvature as found in actual applications. Major behavioral differences occur due to these variables.

Various reinforcing schemes (both active and passive) were investigated and the effect of reinforcement placement was evaluated. The prototype tests revealed an interesting additional failure mechanism due to "multistrand" effects. Sections with significant curvature in the tendon profile and with multiple strands in the same duct generated large lateral splitting forces at the point of minimum radius of curvature due to the flattening out of these multiple strands in the tendon within the confines of the duct. This type failure would never occur in concentric tendon tests.

5.2 Conclusions

The results of this study indicate a radical departure from previous characterizations of the behavior of anchorage zones. Specific conclusions drawn from the test series are:

(1) Bursting stress criteria are insufficient for design of anchorage zone reinforcement when the tendon is inclined or eccentric.

(2) Anchorage zone design based upon the ACI anchor bearing stress formula based on the square root of relative bearing areas will yield conservative allowable loads under certain circumstances. However, it cannot be relied upon to be conservative when the tendon is highly eccentric or inclined, or when very thin web sections are used.

(3) Bearing stresses as high as $2.5f'_c$ at ultimate were developed routinely during this study. Specifications limiting allowable bearing stresses to less than f'_c are overly conservative and inappropriate for controlling the complex anchorage phenomena.

(4) The load required to cause formation of the tendon path crack increases with increasing web width. Increasing the angle of inclination, or the eccentricity of the tendon decreases the cracking load.

(5) Tendon path cracks can occur at points well removed from the anchorage zone in sections where the tendon profile has significant curvature and multiple strand tendons are used. This is due to the tendency for the bundle to flatten out within the confines of the duct thus creating lateral forces sufficiently high to cause not only cracking but side face rupture as well.

(6) Anchor geometry can affect the cracking load. Tests using plate, bell, and cone-type anchors indicate the bell-type anchor slightly increases the cracking load over that of a plate-type anchor, while the rigid cone anchor substantially reduces the cracking load. Ultimate loads for plate and cone-type anchors in

specimens with no supplementary reinforcement occurred at loads only nominally above the cracking load. Bell anchors in the same type specimens exhibited ultimate failure at loads approximately 25 percent above that which caused cracking.

(7) In a given web thickness when using passive reinforcement spirals exhibit much better performance than standard orthogonal reinforcing bar mats both for increasing cracking and ultimate load, and in maintaining small crack widths after cracking. The ultimate load for anchorages with spiral reinforcement is as much as 45-60 percent higher than that for anchorages with orthogonal reinforcement (bar grid) with ten times the reinforcement ratio of the spiral.

(8) For a given volumetric percentage of spiral reinforcement, the spirals fabricated from smaller diameter rods were observed to perform better than spirals fabricated from larger rods. While this trend may not be a general rule, it would tend to indicate that for a given quantity, of supplementary reinforcement, spirals fabricated from small bars at a closer pitch are the most efficient.

(9) Within the range investigated in the full-scale tests, long spirals (2t to 2.5t in length affixed to the anchor) performed no better than short spirals (t in length). For the case of the inclined, curved, multiple strand tendons, however, careful attention must be paid to the possibility of cracking along the tendon path at the point of maximum curvature. This point may be well removed from the anchorage zone, and from the influence of any spiral reinforcement in the anchorage zone. Special reinforcement may also be required in that region.

(10) Active reinforcement (lateral post-tensioning) is by far the most efficient means of controlling anchorage zone cracking. A relatively small precompression of 60 psi across the anchorage zone raised the cracking load 33 percent above that for an unreinforced section. This was for a section with an inclined, curved, multiple

strand tendon (assumed to be the worst case to be expected). The optimum location for the lateral prestress is as close to the loaded face as is feasible.

(11) The formation of upper and lower diagonal cracks around the anchor are the visual signals of impending failure. For unreinforced plate anchors a cone of crushed concrete was observed beneath the anchor at failure.

B I B L I O G R A P H Y

1. Stone, W. C., and Breen, J. E.,"Analyses of Post-Tensioned Girder Anchorage Zones,"Research Report No. 208-1, Center for Transportation Research, The University of Texas at Austin, August 1980.

2. Stone, W. C., and Breen, J. E.,"Design of Post-Tensioned Girder Anchorage Zones,"Research Report No. 208-3F, Center for Transportation Research, The University of Texas at Austin, August 1980.

3. Frantz, G. C., "Development of a Microconcrete for a Typical Lightweight Aggregate Concrete," unpublished M.S. thesis, The University of Texas at Austin, August 1970.

4. ACI Committee 444, "Models of Concrete Structures--State-of-the-Art," Concrete International, Vol. 1, No. 1, January 1979, pp. 77-95.

5. Carpenter, J. E., Roll, F., and Zelman, M. I., "Techniques and Materials for Structural Models," Models for Concrete Structures, ACI Publication, No. 24, 1970, pp. 41-64.

6. Litle, W. A., Cohen, E., and Somerville, G., "Accuracy of Structural Models," Models for Concrete Structures, ACI Publication No. 24, 1970, pp. 65-124.

7. Leyendecker, E. V., and Breen, J. E., "Structural Modeling Techniques for Concrete Slab and Girder Bridges," Research Report 94-1, Center for Highway Research, The University of Texas at Austin, August 1968.

8. Aldridge, W. W., and Breen, J. E., "Useful Techniques in Direct Modeling of Reinforced Concrete Structures," Models for Concrete Structures, ACI Publication No. 24, 1970, pp. 125-140.

9. Breen, J. E., Cooper, R. L., and Gallaway, T. M., "Minimizing Construction Problems in Segmentally Precast Box Girder Bridges," Research Report No. 121-6F, Center for Highway Research, The University of Texas at Austin, August 1975.

10. Gergely, P., "Anchorage Systems in Prestressed Concrete Pressure Vessels; Anchorage Zone Problems," Report to Oak Ridge National Laboratory, Contract No. W-7405-eng-26, subcontract No. 2852.

11. Richart, F. E., Brandtzaeg, A., and Brown, R. L., "The Failure of Plain and Spirally Reinforced Concrete in Compression," University of Illinois Engineering Experiment Station, Bulletin No. 190, 1929.

12. Frantz, G. C., "Control of Cracking on the Sides of Large Reinforced Concrete Beams," Ph.D. Dissertation, The University of Texas at Austin, August 1978.

13. Zielinski, T., and Rowe, R. E., "An Investigation of the Stress Distribution in the Anchorage Zones of Post-Tensioned Concrete Members," Cement and Concrete Association, London, Research Report No. 9, September 1960.

14. Zielinski, T., and Rowe, R. E., "The Stress Distribution Associated with Groups of Anchorages in Post-Tensioned Concrete Members," Cement and Concrete Association, Research Report No. 13, London, October 1962; No. 9, London, September 1960.

15. Hawkins, N. M., "The Bearing Strength of Concrete Loaded through Rigid Plates," Magazine of Concrete Research, Vol. 20, No. 62, March 1968.

16. Hawkins, N. M., "The Bearing Strength of Concrete for Strip Loadings," Magazine of Concrete Research, Vol. 22, No. 71, June 1970.

17. Guyon, Y., The Limit State Design of Prestressed Concrete, Vol. II: The Design of the Member, Translated by F. H. Turner, John Wiley & Sons, New York, 1974.

18. Paes-Filho, W. F., "The Behavior of Post-Tensioned Anchorage Zone Models of Thin Web Sections," Masters Thesis, University of Texas at Austin, January 1980.